DUAL PHASE ENGINEERED TISSUE FOR ENHANCED BONE FORMATION

by

Rameshwar Rao

A dissertation submitted in partial fulfillment
of the requirements for the degree of
Doctor of Philosophy
(Biomedical Engineering)
in The University of Michigan
2013

Doctoral Committee:

Associate Professor Jan P. Stegemann, Chair
Professor David H. Kohn
Professor Paul H. Krebsbach
Associate Professor Andrew J. Putnam

To Surbhi,

For her love, support, and guidance.

Acknowledgements

"The Team, the Team, the Team." – Coach Bo Schembechler

At the University of Michigan, we like to live be a famous quote from Coach Bo Schembechler. I have been fortunate to have been a part of an extraordinary team during my graduate studies and I would like to take the time to thank everyone.

First and foremost, to my thesis advisor, Dr. Jan Stegemann – a big thank you. When I first came to Michigan, you took a shot on me when others wouldn't. I really appreciate the time you have spent mentoring me and for always supporting me when I had crazy ideas or wanted to apply for a grant, award, or even medical school. You have always kept my best interests in mind throughout the last four years and have been nothing short of an excellent advisor.

To the rest of my thesis committee – Dr. Andrew Putnam, Dr. David Kohn, and Dr. Krebsbach – each of you have taken countless hours out of your days to discuss science and life with me. Your advice and perspectives have kept me focused and have helped guide my career goals. I appreciate the support and have enjoyed with collaborating with you and your labs over the last few years.

To the members of my lab and all of those that I have collaborated with – it has truly been a pleasure to work with you all and learn from each of you. The list of students that I have been able to work with can go on forever but a big thank you to Rebecca Hortensius, Alexis Peterson, David Caldwell, Jake Ceccarelli, Marina Vigen, Madhu Gudur, Limin Wang, Eiji Saito, Melanie Gupte, Sasha Cai Lesher-Perez, Janani Ramaswamy, Harsha Ramaraju, Tina

Hsiao, Rahul Singh, Niharika Bhatt, Ariana Betts, and Brandan Walters. My apologies to anyone that I left off this list!

I would also like to acknowledge my funding sources – the NIH Tissue Engineering and Regenerative Medicine (TEAM) Training Grant and the NSF Graduate Research Fellowship. Both of these fellowships supported my graduate education and helped advance my career aspirations.

Finally, to the most important member of my team, a big thanks to Surbhi. I would not be in the position without your support!

Table of Contents

List of Figures

List of Tables

List of Appendices

List of Abbreviations

In order of appearance

Bone morphogenetic proteins	BMPs
Vascular endothelial growth factor	VEGF
Transforming growth factor-beta	TGF-β
Extracellular matrix	ECM
Platelet-derived growth factor	PDGF
Fibroblast growth factor	FGF
Food and Drug Administration	FDA
Collagen	COL
Fibrin	FIB
Hydroxyapatite	HA
Mesenchymal stem cells	MSC
Bone marrow-derived mesenchymal stem cells	bmMSC
Adipose-derived stem cells	AdSC
Human umbilical vein endothelial cells	HUVEC
Insulin-like growth factor	IGF
Tumor necrosis factor alpha	TNF-α
Alkaline phosphatase	ALP
Beta-glyocerophosphate	β-GP
Hepatocyte growth factor	HGF
Interleukin-10	IL-10
Endothelial cells	EC
Human dermal microvascular endothelial cells	HMVEC
Endothelial progenitor cells	EPC
Bone marrow endothelial cells	bmEC
Two-Dimensional	2D
Three-Dimensional	3D
Polycaprolactone	PCL
Beta-tricalcium phosphate	β-TCP
Poly(lactide-co-glycolide)	PLGA
Dulbecco's modified Eagle's medium	DMEM
Fetal bovine serum	FBS
Sodium Hydroxide	NaOH
Phosphate buffered saline	PBS
Polydimethylsiloxane	PDMS
Minimum Essential Medium Alpha	αMEM
Orthocresolphthalein complex-one	OCPC
Analysis of variance test	ANOVA
Penicillin and streptomyocin	PS

Endothelial Growth Medium-2	EGM-2
Laser Doppler Perfusion Imaging	LDPI
Region of interest	ROI
Zinc-buffered formalin	Z-Fix
Ethylenediamine tetraacetic acid	EDTA
Tris-buffered saline with Tween 20	TBS-T
Hematoxylin and eosin	H&E
ε-amino caproic acid	ACA
Bovine serum albumin	BSA
Ulex Europaeus Agglutinin I	UEA-1
Micro-Computed Tomography imaging	µCT
Bone volume	BV
Tissue mineral density	TMD
Simulated body fluid	SBF
Modified Dulbecco's modified Eagle's medium	mDMEM
Mineralization medium	MM
Human neonatal dermal fibroblasts	hFBs
Standard error of the mean	SEM
Spectral ultrasound imaging	SUSI
Radiofrequency	RF
Midband fit	MBF
Reagent-grade hydroxyapatite	HA-R
Micro-grade hydroxyapatite	HA-M
Nano-grade hydroxyapatite	HA-N
Grayscale	GS
Magnetic resonance imaging	MRI
Intravascular ultrasound	IVUS
High intensity focused ultrasound	HIFU

ABSTRACT

DUAL PHASE ENGINEERED TISSUE FOR ENHANCED BONE FORMATION

Chair: Dr. Jan Phillip Stegemann

Large bone defects are a significant clinical problem in the United States and worldwide. “Non-unions” are fractures that fail to heal due to a lack of blood supply to the defect site. In our approach to bone regeneration, we create modular engineered tissues (“microbeads”) designed to form bone, and combine them with a surrounding vascularizing tissue to generate a dual-phase injectable matrix for enhanced bone formation. In the first Aim, human bone marrow mesenchymal stem cells (bmMSC) or human adipose stem cells (AdSC) were embedded in collagen/fibrin (COL/FIB) or collagen/fibrin/hydroxyapatite (COL/FIB/HA) microbeads. Both cell types mineralized microbeads, indicating differentiation towards the osteogenic lineage. The second Aim used a co-culture model of bmMSC and human umbilical vein endothelial cells in COL/FIB composite hydrogels to create a vasculogenic matrix. Cell ratio and matrix composition were varied in a systematic manner. Vascular network formation increased in vitro with increasing fibrin content in composite materials, although the 40/60 COL/FIB and pure fibrin materials exhibited similar responses. Hydroxyapatite (HA) was found to recover endothelial network formation in unconstrained hydrogels. Over 7 days of dorsal subcutaneous implantation in nude mice, these matrices exhibited increasing neovascularization, though there was no significant effect of HA. The final Aim combined osteogenic microbeads with a surrounding vasculogenic matrix to evaluate the effect of this dual-phase tissue in vivo. Both vasculogenesis and osteogenesis were examined in a subcutaneous bone formation model in the mouse at 4 and 8 weeks. Blood flow measured by Doppler imaging was not significantly different between any conditions at any time point, except at 8 weeks where the vasculogenic matrix alone was lower than all other groups. Micro-computed tomography of ectopic bone demonstrated significantly higher bone volume in the osteogenic microbead condition at 4 weeks and both the blank and osteogenic microbead conditions at 8 weeks, compared to the dual osteogenic/vasculogenic condition. These data suggest an inhibitory effect of the vasculogenic component on bone formation in the non-ischemic model. Dual-phase implants may be more effective in ischemic orthotopic bone regeneration models, and these results demonstrate that such constructs can be designed, fabricated, and delivered for therapeutic use.

CHAPTER 1

Introduction

1.1 – Background of the Thesis

Large bone defects are a significant clinical problem in the United States and worldwide. According to 2006 data from the U.S. Health and Cost and Utilization Project (HCUP), there are approximately one million hospital admissions related to appendicular skeletal-tissue injuries each year in the United States [1]. Bone injuries and fractures require over 500,000 grafting procedures and account for over $26 billion of healthcare costs in the U.S. annually, and skull and facial fractures contribute an additional $1.3 billion to the annual health care cost. Importantly, approximately 10% of the total fractures in the U.S. are complicated by impaired healing, non-unions or delayed unions. “Non-unions” are defined as broken bones that fail to heal while “delayed unions” are fractures that take longer than usual to heal. A main cause of delayed and non-union is tissue instability and lack of nutrient supply around the defect site, since both stability and vascularization are required for the normal bone healing process. Some bones, such as the head of the femur and the wristbones, have limited vasculature to provide necessary proteins, vitamins, and calcium required for healing [2], and these bones therefore tend to be more susceptible to non-unions.

Although the natural healing response can lead to physiological bone remodeling, non-unions and large-scale traumatic bone injuries require surgical intervention. Autografts, allografts, and xenografts are currently used as treatment options, but these are associated with complications including donor site morbidity, disease transmission, and immunological rejection.

The current gold standard for large bone defect repair therefore uses a tissue autograft from the patient [3]. These grafts contain the proper cell types, matrix, and vasculature necessary for proper bone regrowth in the injured area. However, autografts require a secondary operative procedure that can lead to complications such as pain and donor-site morbidity. Allografts using tissue from human donors are also commonly used but are associated with an increased risk of disease transmission and failure rate over long-term use, relative to autografts [4]. Xenografts involve the transplantation of bone tissue from species other than humans; however, they also present the risk of disease transmission after implantation. Futher, xenografts must undergo sterilization processes that cause the loss of osteoinductive factors within the grafting material. One major drawback of both allografts and xenografts is the potential for immune rejection after implantation.

Medullary rods and internal fixation using metallic devices is sometimes an option to enhance bone healing. However, these approaches require permanent implants that are not remodeled by the patient and are susceptible to fatigue fracture over long-term use [5]. Bonding of such metallic devices to adjacent bone is challenging. Attempts to modify the surfaces of implants with bioceramics and mineralized coatings have shown some success, but these surface conditioning techniques can lead to decreased durability of the device [5]. Local stress shielding caused by metallic implants can also lead to a reduction in bone density and can require revision surgeries [6]. Vascularization of regions supported by metallic implants is also limited [5].

The problems associated with transplanted grafts and stabilization strategies have resulted in an increasing interest in improved bone graft substitutes and bone tissue engineering solutions. Current osteobiologic approaches provide a scaffold material that is designed to allow growth and proliferation of host cells. Many approaches also include osteogenic growth factors, and in

particular the bone morphogenetic proteins (BMPs), to enhance bone formation in large defects [7]. The commercially available Medtronic INFUSE® Bone Graft combines recombinant human BMP-2 with an absorbable collagen sponge, and has been used widely in the clinic [8]. The product is currently approved for selected spinal fusion, intramedullary fixation, and sinus augmentation procedures, and it has had a dramatic effect on treatment of particularly difficult bone healing indications. However, concerns have been raised about the degree of control of BMP-2 release from the product and potentially serious reactions when the product is used off-label such as ectopic bone formation, nerve damage, edema and inflammation [9-11]. Most recently, the possibility that BMP is cancer promoting has further clouded the view of how these products are best used [12-14]. The limitations and potential complications associated with these early osteobiologic treatments has driven development of even more biologically-based approaches, which included living cells to provide more refined control over bone formation.

Bone tissue engineering aims to mimic and recreate native tissue through the combination of cells, scaffolds, and inductive factors [15]. Numerous studies have employed osteoconductive matrices to transplant both osteoprogenitor cells and osteoinductive factors to enhance healing in bone defect sites. Modular tissue engineering embraces advances in material science and biology to create individual cellular microenvironments and assemble them in desired geometries to create functional tissues [16]. Although limited to non-load bearing applications, injectable scaffolds provide beneficial properties to large bone injuries such as the ability to serve as shape-filling matrices, biodegradability, and in situ formation. Therefore, injectable modular tissue engineering can be employed for a minimally invasive bone regeneration therapy that allows for bone regeneration and restoration of proper function.

Combinatorial tissue engineering therapies using osteogenic and vasculogenic components have been previously investigated with mixed results. Patel et. al combined vascular endothelial growth factor (VEGF) and BMP-2 recombinant delivery at fixed concentrations (12 µg/scaffold and 2 µg/scaffold, respectively) in a rat cranial defect model [17]. The combination of both growth factors did not achieve a significant increase in bone formation at 12 weeks compared to the BMP-2 alone condition. Furthermore, Young et. al varied doses of VEGF and BMP-2 at decreased concentrations compared to Patel et al., but achieved similar results [18]. Finally, Schonmeyr et. al showed co-delivery of VEGF and BMP-2 inhibited bone formation of rat bone marrow-derived mesenchymal stem cells (bmMSCs) as VEGF inhibited any osteogenic effects of BMP-2 in their system [19]. Taken together, these studies indicate that growth factor delivery may not be a suitable method of treating critical sized bone defects.

1.2 - Cell-Seeded Hydrogel Microbeads

In contrast to traditional tissue engineering techniques in which cells are seeded onto a scaffold, modular tissue engineering aims to fabricate engineered tissues through the assembly of cell-seeded biomimetic structures [20]. Tissue subunits, or "modules," are utilized to generate larger tissue structures that have been employed for orthopedic, vascular, and numerous other applications. Methods such as micro-fabrication of cell-laden hydrogels [21, 22], cell printing [23, 24], or the creation of cell sheets [25, 26] have been employed in modular tissue engineering applications. Current work in the formation of cell-seeded hydrogels includes creating collagen microspheres in small droplets and through water-in-oil emulsion techniques [27, 28]. Cheng et. al utilized two different types of microspheres fabricated in this method to assemble larger tissue structures with compartmentalized cell phenotypes [29].

Cell-seeded hydrogel microenvironments have been previously utilized as cell delivery vehicles for orthopedic applications. There is a need for better bone repair strategies for healing of complex fractures, non-unions, tumor resected sites, and periodontal defects, which together constitute over 4 million procedures per year worldwide [30]. Kim et. al developed biomimetic collagen-apatite microspheres through a water-in-oil emulsion technique that served as microcarriers for rat bone marrow derived stem cells [28]. Although these structures did not encapsulate cells directly, they demonstrated favorable adhesion properties for cells and upregulation of alkaline phosphatase activity, an osteogenic marker, as well as gene expression for osteogenic genes such as osteocalcin. Other work has utilized RGD-modified alginate microspheres to deliver a co-culture of human bone marrow stromal cells with endothelial cells into mouse femoral defect model [31]. The implantation of these hydrogel microspheres demonstrated bone regeneration and promoted mineralization of delivered cells.

1.3 - Vasculature

Capillaries

Microcirculation exists within each organ and tissue as vessel structures called capillaries [32]. Compared to arteries, arterioles, veins, and venules, capillaries have the smallest diameter; on the order of 5 – 10 μm. Capillaries form vascular networks that allow fluids to exchange gasses, metabolites, and waste products to and from tissues. Capillaries are composed of a single layer of endothelial cells and these cells form a narrow tube that allows for the passage of red blood cells one at a time. Blood flow through capillaries can be controlled by local and systemic signals such as nitric oxide.

Three types of capillaries exist: continuous, fenestrated, and discontinuous. Continuous capillaries are found in the muscle, lung, and central nervous system and are held together by tight, or occluding, junctions. These capillaries only allow the passage of relatively small molecules between adjacent endothelial cells. Fenestrated capillaries have small pores across their walls that allow small molecular weight proteins to diffuse through their pores. These types of capillaries can be found in endocrine glands and in the kidney. Finally, discontinuous capillaries, which are found in the liver, spleen, and bone marrow, tend to have larger diameters than other capillary types and are more irregularly shaped. These vessels have a discontinuous basal lamina and utilize gaps between cells to allow for the movement of cells and proteins.

Pericytes

Pericytes are relatively undifferentiated cells that surround continuous capillaries that function to provide vascular support and stability. Through physical and chemical signaling from endothelial cells, pericytes can contract to regulate blood flow through the capillary. Pericytes are characterized by their expression of smooth muscle actin and vimentin, a protein found in the cytoskeleton. Bone marrow derived mesenchymal stem cells can act as pericytes when co-cultured with endothelial cells and can also differentiate towards pericytes if exogenous transforming growth factor-beta (TGF-β) is added to the culture media [33, 34].

Angio- and vasculogenesis

Neovascularization can be classified into two general categories: vasculogenesis and angiogenesis. Vasculogenesis is the creation of new vessels in situ with the assembly of endothelial cells. Angiogenesis, on the other hand, involves the sprouting of new capillaries from

existing vasculature. Both processes are critical during the wound healing response and have been implicated for bone tissue engineering applications. In either case, vessel development involves formation, stabilization, branching, remodeling, and pruning [35].

During the formation of a nascent vascular network, VEGF plays a critical role in regulating initial vessel formation. Endothelial cells combine and form tubular-like structures under the influence of VEGF. These newly created vessels are formed in a hypoxic environment which induces further angiogenesis. Mural cells such as fibroblasts and mesenchymal stem cells are then recruited to the nascent vessels and stabilize their structures by depositing extracellular matrix (ECM). Numerous factors such as platelet-derived growth factor (PDGF) [36], Tie receptors [37], and TGF-β1 [38] are involved in stabilizing newly formed vessels and in differentiating mesenchymal stem cells towards the pericytic lineage. Vessels then continue to elongate, branch, anastomose with other vascular networks, and remodel into specialized segments. Various ECM components and signaling pathways are involved in the continued proliferation and differentiation of endothelial cells and mural cells. Proteases such as matrix metalloproteinases-2, 3, and 9 and proangiogeneic growth factors such as VEGF and fibroblast growth factor (FGF) have also been demonstrated to be involved with these functions in vessel maturation [35].

1.4 - Overarching Hypothesis

We hypothesized that the use of a dual-phase injectable matrix consisting of osteogenic and vasculogenic components will prove to be superior to either component alone in the ability to form vascularized bone *in vivo*. The approaches that will be used are summarized in Figure 1.1.

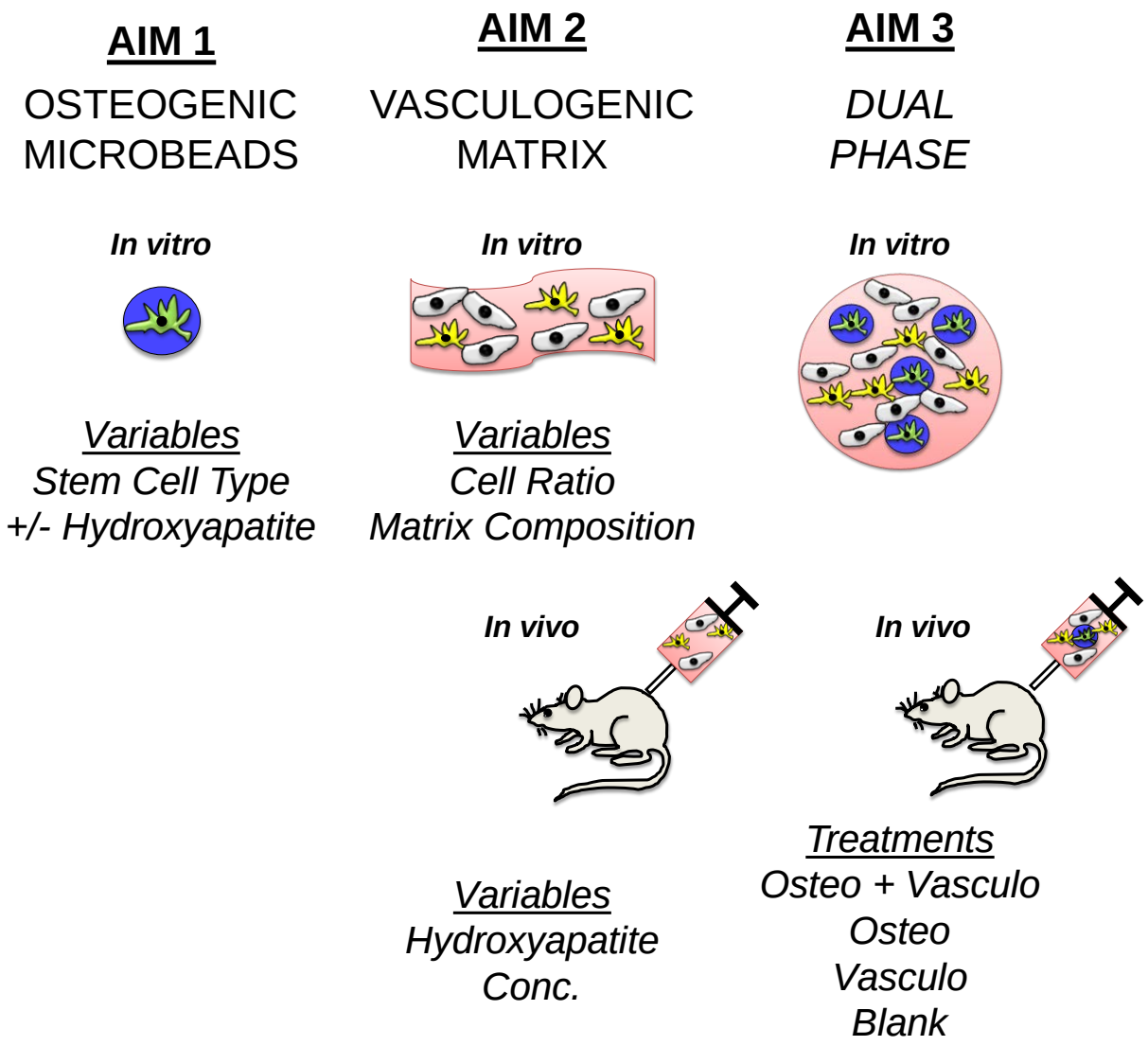

Figure 1.1 – Dual-Phase Engineered Tissue for Enhanced Bone Formation.

1.5 – Specific Aims

Aim 1: Formation of osteogenic microbeads

Modular tissue engineering approaches will be applied to generate three-dimensional hydrogel cell microenvironments composed of collagen/fibrin or collagen/fibrin/hydroxyapatite and will be seeded with either human adipose-derived stem cells or human bone marrow-derived mesenchymal stem cells and differentiated towards the osteogenic lineage. The goal will be to

compare and contrast the osteogenic ability of bone-marrow derived mesenchymal stem cells and adipose derived stem cells in our composite protein-ceramic microbeads.

Aim 2: Generation of a vasculogenic matrix

Subaim 2.1: Co-culture system in composite collagen/fibrin hydrogels - Human mesenchymal stem cells and human umbilical vein endothelial cells will be co-cultured in collagen/fibrin composite gels to create a vasculogenic matrix upon implantation. The relationship between matrix stiffness and network formation will be investigated.

Subaim 2.2: Addition of hydroxyapatite into the vasculogenic matrix – Hydroxyapatite will be systematically added into composite collagen/fibrin hydrogels to prevent cell-mediated compaction and provide proangiogenic cues in an attempt to maintain endothelial network formation in unconstrained culture. *In vitro* and *in vivo* studies will be conducted to investigate the effect of hydroxyapatite on vasculogenesis.

Aim 3: Dual-Phase Engineered Tissue for Enhanced Bone Formation

Osteogenic microbeads will be dispersed throughout the vasculogenic matrix and the resulting *in vitro* model will be utilized to show endothelial network formation by human umbilical vein endothelial cells around osteogenic microbeads. This dual-phase engineered tissue will then be implanted into a mouse subcutaneous model to investigate whether the combination of osteogenic and vasculogenic components demonstrate enhanced bone formation over either component alone. The goal will be demonstrate *in vivo* potential of our system.

1.6 – Translational Potential

Recalcitrant bone defects are of significant clinical concern as large bone defects fail to heal. Numerous bone void fillers are currently available on the market to combat these deficiencies; however, they lack the ability to completely regenerate tissue that is similar to native bone in terms of function and structure. This project utilizes Food and Drug Administration (FDA)-approved biomaterials and cells types with translational potential (Figure 1.2). A further discussion and the clinical indications are shown below.

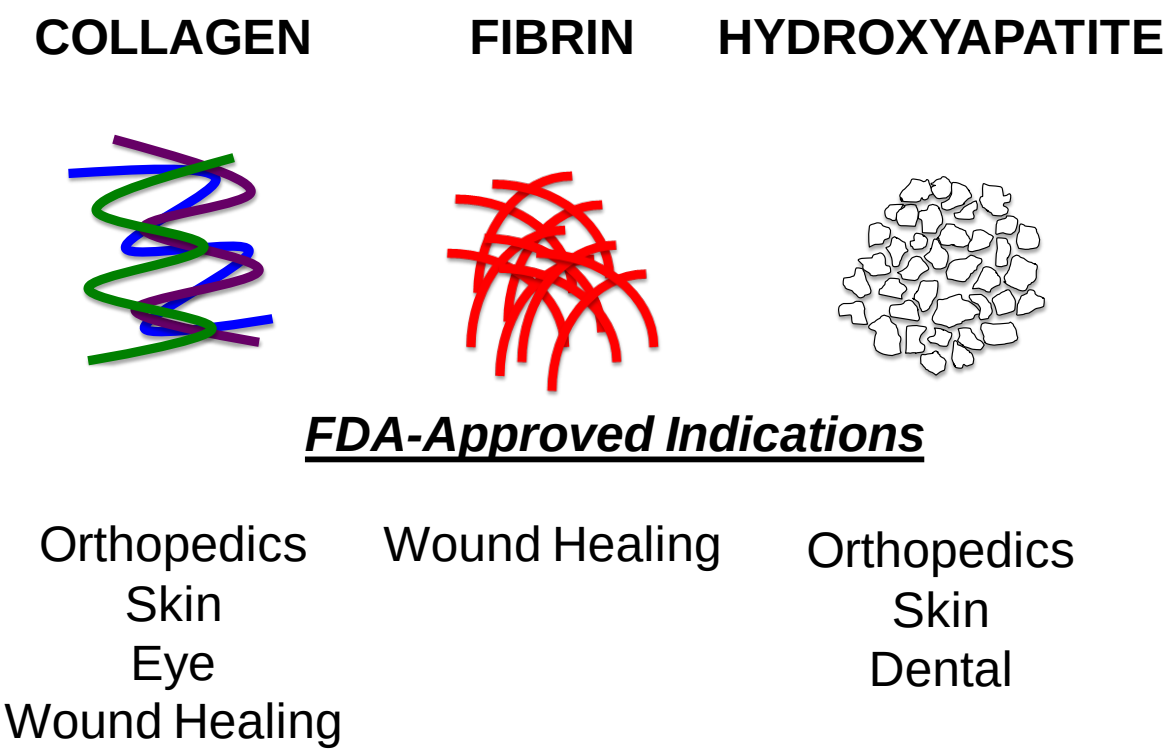

Figure 1.2 – Food and Drug Administration (FDA) approved indications for the biomaterials utilized.

Biomaterials

The ideal scaffolding material for use in bone tissue engineering would be osteoconductive, osteoinductive, biocompatible, and biodegradable and would only serve as a template for bone regeneration [39]. Osteoconductivity refers to a material's ability to support

cell attachment and migration on and through the scaffold. This feature is important in not only creating a bone-bonding interface with host bone and implant but in also allowing host cells to infiltrate, interact with, and remodel the implant. Osteoinductivity describes a material's ability to induce undifferentiated stem cells towards the osteogenic lineage. The chosen biomaterial should elicit an appropriate immune response and the host should be able to interact and remodel implanted matrices. Natural biomaterials provide beneficial properties for bone tissue engineering applications in their ability to be osteoconductive and osteoinductive as well as biodegradable.

Collagen type I (COL) is the most abundant protein in the human body and constitutes the majority of the ECM in tissues such as bone, tendon, skin, and cornea [40]. Collagen molecules are composed of a triple-helical structure and its subunits are organized with –(glycine-X-Y) - repeats where X and Y can be proline, hydroxyproline, lysine, hydroxylysine or other amino acids. 30% of collagen is composed of glycine, the smallest amino acid. Its small structure allows collagen fibrils to wind into α-helices by minimizing steric hindrance. Collagen quaternary structure involves the self-assembly of tropocollagen into an entropically favorable form of collagen fibrils.

Collagen is widely used as a biomaterial as it supports cell attachment and proliferation and contains favorable mechanical properties. Recent studies have illustrated the osteoinductive potential of collagen towards human bone marrow mesenchymal stem cells [41, 42]. Moreover, collagen exhibits favorable mechanical properties that allow it to be handled and formed into desired geometries [40]. Collagen has FDA-approved indications as skin filler (CosmoDerm, Evolence) [43, 44], eye filler to treat glaucoma (AquaFlow) [45], wound dressing (Oasis, Integra, E-Z-Derm) [46], and bone (Infuse) [9-12].

Fibrinogen, the precursor of fibrin (FIB), is a 340 kDa protein that regularly circulates in the bloodstream and is one of the proteins involved in the wound healing cascade [47, 48]. Under normal physiological conditions, fibrinogen remains soluble and aggregation is prevented by the α and β subunits. Following vessel injury, numerous reactions take place allowing for the release of the enzyme thrombin, which cleaves the two subunits. Thrombin also activates factor XIII which crosslinks adjacent fibrin structures. Fibrin monomers then polymerize to form a network of fibers allowing for the stabilization of a clot.

Fibrin hydrogels have been fabricated for numerous tissue engineering applications [49]. Cells can be added directly into the fibrinogen precursor and the mixture can form a hydrogel without appreciable cell death. Fibrin concentrations and gel structure can be modified to direct cell phenotype and stem cell differentiation [50]. Owing to its intrinsic properties in the wound healing cascade, fibrin can be utilized in angiogenic and vasculogenic applications [51, 52]. Matrix metalloproteinases, cell-secreted proteinases, have been shown to be critical in the remodeling of fibrin to successfully create stable vessels. Fibrin was first approved for clinical use in the U.S. in 1998 and there are currently 7 commercially available fibrin products with indications as hemostats, sealants, and adhesives [49, 53].

Hydroxyapatite (HA) is the mineral component of bone and is present in a crystalline form throughout the collagen structure [32]. HA can provide an osteoconductive and osteoinductive environment for stem cell differentiation while increasing the mechanical properties of the underlying substrate [54, 55]. These changes in material properties can be achieved through creating a scaffold derived of HA or by incorporating synthetic particles throughout another material. HA has clinical indications in bone (Bonesource, Interpore, Pro Osteon, Collagraft) [56-58] and skin (Radiesse) [59].

Cell Types

The cell types utilized in this dissertation have direct clinical potential as they can potentially be obtained from both autologous and allogeneic sources. Mesenchymal stem cells (MSC) are a multipotent cell type found in numerous tissues of the body and are characterized by their ability to proliferate in an undifferentiated state and their potential to differentiate into various cell types [60, 61]. MSCs can be isolated from bone marrow (bmMSC), adipose tissue (AdSC), muscle, peripheral blood, cord blood, and the placenta. These different tissues yield MSC that have different proliferative and multipotency profiles. Furthermore, age and disease stage are critical factors that can affect MSC function. Both autologous and allogenic MSC are currently being investigated for their use in clinical applications.

Endothelial cells are present within every blood vessel in the human body. These cells can self-assemble into vascular tubes when cultured in materials such as collagen and fibrin. Vessel formation can also occur under the guidance of pro-angiogenic factors such as VEGF and FGF. Endothelial cells can be extracted from numerous tissue sources such as umbilical cords, dermal tissue, and from the saphenous vein [62]. Human umbilical vascular endothelial cells (HUVEC) can be extracted from umbilical cords through a collagenase digestion and macrovascular endothelial cells can be isolated. HUVEC can form capillary-like structures when co-cultured with stromal cells such as fibroblasts or mesenchymal stem cells. Secreted factors from the MSC such as VEGF and MMPs allow migration of HUVEC through matrices allowing them to combine and form tubule structures.

A more complete review of both osteogenic and endothelial cell types is presented in Chapter 2.

1.7 – Preview of the Thesis

Chapter 2 provides an in-depth review of cell-based approaches to vascularized bone tissue engineering. Basic bone biology, osteogenic and endothelial cell types, *in vitro* co-culture models, and *in vivo* bone formation and bone regeneration models are discussed throughout the review. Chapter 3 (Aim 1) describes the creation of collagen/fibrin composite three-dimensional cell-seeded hydrogel microenvironments that support the osteogenic differentiation of mesenchymal stem cells. The differentiation potential of adipose-derived stem cells and bone marrow mesenchymal stem cells are compared in both collagen/fibrin and collagen/fibrin/hydroxyapatite microbeads. Chapter 4 (Aim 2.1) presents the formation of a vasculogenic matrix composed of collagen and fibrin that supports endothelial network formation of human umbilical vein endothelial cells that are co-cultured with bone marrow mesenchymal stem cells. Cell ratio and matrix composition are varied and matrix stiffness is investigated as a potential cause behind the obtained results. Both *in vitro* and *in vivo* studies are conducted in Chapter 5 (Aim 2.2) to study the addition of hydroxyapatite and its effect on endothelial network formation and cell-mediated compaction within the vasculogenic matrix previously developed. The osteogenic microbeads and the vasculogenic matrix are then combined in Chapter 6 (Aim 3). An *in vitro* model is utilized to demonstrate endothelial network formation around the microbeads. The dual-phase engineered tissue is then implanted into an *in vivo* mouse subcutaneous model and ectopic bone formation is studied over a period of 8 weeks. The results and key findings are then summarized in Chapter 7 and the broader impacts of this work and its future clinical potential are discussed.

1.8 – References

1. HCUP Healthcare Cost and Utilization Project, Agency for Healthcare Research and Quality. 2006.

2. Soucacos PN, Dailiana Z, Beris AE, Johnson EO. Vascularised bone grafts for the management of non-union. Injury 37, S41, 2006.

3. Khan Y, Yaszemski MJ, Mikos AG, Laurencin CT. Tissue engineering of bone: material and matrix considerations. J Bone Joint Surg Am 90,36, 2008.

4. Wheeler DL, Enneking WF. Allograft bone decreases in strength in vivo over time. Clin Orthop Relat Res 435, 36, 2005.

5. Schroeder JE, Mosheiff R. Tissue engineering approaches for bone repair: concepts and evidence. Injury 42, 609, 2011.

6. Sayyidmousavi A, Bougherara H. Investigation of stress shielding around the Stryker Omnifit and Exeter periprosthetic hip implants using an irreversible thermodynamic-based model. J Biomed Mater Res B Appl Biomater 100, 1416, 2012.

7. Barr T, McNamara AJ, Sándor GK, Clokie CM, Peel SA. Comparison of the osteoinductivity of bioimplants containing recombinant human bone morphogenetic proteins 2 (Infuse) and 7 (OP-1). Oral Surg Oral Med Oral Pathol Oral Radiol Endod 109, 531, 2010.

8. McKay WF, Peckham SM, Badura JM. A comprehensive clinical review of recombinant human bone morphogenetic protein-2 (INFUSE Bone Graft). Int Orthop 31, 729, 2007.

9. Carreon LY, Glassman SD, Brock DC, Dimar JR, Puno RM, Campbell MJ. Adverse events in patients re-exposed to bone morphogenetic protein for spine surgery. Spine 33, 391, 2008.

10. Shahlaie K, Kim KD. Occipitocervical fusion using recombinant human bone morphogenetic protein-2: adverse effects due to tissue swelling and seroma. Spine 33, 2361, 2008.

11. Epstein NE. Pros, cons, and costs of INFUSE in spinal surgery. Surg Neurol Int 2, 10, 2011.

12. Carragee EJ, Hurwitz EL, Weiner BK. A critical review of recombinant human bone morphogenetic protein-2 trials in spinal surgery: emerging safety concerns and lessons learned. Spine J 11, 471, 2011.

13. Carragee EJ, Baker RM, Benzel EC, Bigos SJ, Cheng I, Corbin TP, Deyo RA, Hurwitz EL, Jarvik JG, Kang JD, Lurie JD, Mroz TE, Oner FC, Peul WC, Rainville J, Ratliff JK, Rihn JA,

Rothman DJ, Schoene ML, Spengler DM, Weiner BK. A biologic without guidelines: the YODA project and the future of bone morphogenetic protein-2 research. Spine J 12, 877, 2012.

14. Even J, Eskander M, Kang J. Bone morphogenetic protein in spine surgery: current and future uses. J Am Acad Orthop Surg 20, 547, 2012.

15. Langer R, Vacanti JP. Tissue engineering. Science 260, 920, 1993.

16. Nichol JW, Khademhosseini A. Modular Tissue Engineering: Engineering Biological Tissues from the Bottom Up. Soft Matter 5, 1312, 2009.

17. Patel ZS, Young S, Tabata Y, Jansen JA, Wong ME, Mikos AG. Dual delivery of an angiogenic and an osteogenic growth factor for bone regeneration in a critical size defect model. Bone 43, 931, 2008.

18. Young S, Patel ZS, Kretlow JD, Murphy MB, Mountziaris PM, Baggett LS, Ueda H, Tabata Y, Jansen JA, Wong M, Mikos AG. Dose effect of dual delivery of vascular endothelial growth factor and bone morphogenetic protein-2 on bone regeneration in a rat critical-size defect model. Tissue Eng Part A 15, 2347, 2009.

19. Schönmeyr BH, Soares M, Avraham T, Clavin NW, Gewalli F, Mehrara BJ. Vascular endothelial growth factor inhibits bone morphogenetic protein 2 expression in rat mesenchymal stem cells. Tissue Eng Part A 16, 653, 2010.

20. Nichol

21. Tejavibulya N, Youssef J, Bao B, Ferruccio T-M, Morgan JR. Directed self-assembly of large scaffold-free multi-cellular honeycomb structures. Biofabrication 3, 034110, 2011.

22. Tekin H, Tsinman T, Sanchez JG, Jones BJ, Camci-Unal G, Nichol JW, et al. Responsive Micromolds for Sequential Patterning of Hydrogel Microstructures. Journal of the American Chemical Society 133, 12944, 2011.

23. Jakab K, Norotte C, Marga F, Murphy K, Vunjak-Novakovic G, Forgacs G. Tissue engineering by self-assembly and bio-printing of living cells. Biofabrication 2, 022001, 2010.

24. Mironov V, Boland T, Trusk T, Forgacs G, Markwald RR. Organ printing: computer-aided jet-based 3D tissue engineering. Trends in Biotechnology 21, 157, 2003.

25. Elloumi-Hannachi I, Yamato M, Okano T. Cell sheet engineering: a unique nanotechnology for scaffold-free tissue reconstruction with clinical applications in regenerative medicine. Journal of Internal Medicine 267, 54, 2010.

26. Kelm JM, Fussenegger M. Scaffold-free cell delivery for use in regenerative medicine☆. Advanced Drug Delivery Reviews 62, 753, 2010.

27. Chan BP, Hui TY, Yeung CW, Li J, Mo I, Chan GCF. Self-assembled collagen–human mesenchymal stem cell microspheres for regenerative medicine. Biomaterials 28, 4652, 2007.

28. Kim HW, Gu H-J, Lee H-H. Microspheres of Collagen-Apatite Nanocomposites with Osteogenic Potential for Tissue Engineering. Tissue Engineering 13, 965, 2007.

29. Cheng HW, Luk KDK, Cheung KMC, Chan BP. In vitro generation of an osteochondral interface from mesenchymal stem cell–collagen microspheres. Biomaterials 32, 1526, 2011.

30. Al-Munajjed AA, Plunkett NA, Gleeson JP, Weber T, Jungreuthmayer C, Levingstone T, Hammer J, O'Brien FJ. Development of a biomimetic collagen-hydroxyapatite scaffold for bone tissue engineering using a SBF immersion technique. Journal of Biomedical Materials Research Part B: Applied Biomaterials 90B, 584, 2009

31. Grellier M, Granja PL, Fricain J-C, Bidarra SJ, Renard M, Bareille R, et al. The effect of the co-immobilization of human osteoprogenitors and endothelial cells within alginate microspheres on mineralization in a bone defect. Biomaterials 30, 3271, 2009.

32. Ross MH, Pawlina W. Histology: A Text and Atlas. Philadelphia: Lippincott Williams & Wilkins, 218, 2010.

33. Rao RR, Peterson AW, Ceccarelli J, Putnam AJ, Stegemann JP. Matrix composition regulates three-dimensional network formation by endothelial cells and mesenchymal stem cells in collagen/fibrin materials. Angiogenesis 15, 253, 2012.

34. Tsigkou O, Pomerantseva I, Spencer JA, Redondo PA, Hart AR, O'Doherty E, Lin Y, Friedrich CC, Daheron L, Lin CP, Sundback CA, Vacanti JP, Neville C. Engineered vascularized bone grafts. Proc Natl Acad Sci U S A 107, 3311, 2010.

35. Jain RK. Molecular regulation of vessel maturation. Nat Med 9, 685, 2003.

36. Hellström M, Gerhardt H, Kalén M, Li X, Eriksson U, Wolburg H, Betsholtz C. Lack of pericytes leads to endothelial hyperplasia and abnormal vascular morphogenesis. J Cell Biol 153, 543, 2001.

37. Yancopoulos GD, Davis S, Gale NW, Rudge JS, Wiegand SJ, Holash J. Vascular-specific growth factors and blood vessel formation. Nature 407, 242, 2000.

38. Pepper MS. Transforming growth factor-beta: vasculogenesis, angiogenesis, and vessel wall integrity. Cytokine Growth Factor Rev 8, 21, 1997.

39. Lanza R, Langer R, Vacanti JP. Principles of Tissue Engineering. Elsevier Academic Press, 2007.

40. Cen L, Liu W, Cui L, Zhang W, Cao Y. Collagen tissue engineering: development of novel biomaterials and applications. Pediatr Res 63, 492, 2008.

41. Salasznyk RM, Williams WA, Boskey A, Batorsky A, Plopper GE. Adhesion to Vitronectin and Collagen I Promotes Osteogenic Differentiation of Human Mesenchymal Stem Cells. J Biomed Biotechnol 2004, 24, 2004.

42. Kundu AK, Putnam AJ. Vitronectin and collagen I differentially regulate osteogenesis in mesenchymal stem cells. Biochem Biophys Res Commun 347, 347, 2006.

43. Bauman L. CosmoDerm/CosmoPlast (human bioengineered collagen) for the aging face. Facial Plast Surg 20, 125, 2004.

44. Solish NJ. Assessment of recovery time for the collagen products Dermicol-P35 27G and 30G. J Am Acad Dermatol 62, 824, 2010.

45. Demeter S, Hailey D. Non-penetrating glaucoma surgery using AquaFlow(TM)collagen implants. Issues Emerg Health Technol 22, 1, 2001.

46. Bello YM, Falabella AF, Eaglstein WH. Tissue-engineered skin. Current status in wound healing. Am J Clin Dermatol 2, 305, 2001.

47. Rowe SL, Stegemann JP. Microstructure and mechanics of collagen-fibrin matrices polymerized using ancrod snake venom enzyme. J Biomech Eng 131, 061012, 2009.

48. Lord ST. Molecular mechanisms affecting fibrin structure and stability. Arterioscler Thromb Vasc Biol 31, 494, 2011.

49. Breen A, O'Brien T, Pandit A. Fibrin as a delivery system for therapeutic drugs and biomolecules. Tissue Eng Part B Rev 15, 201, 2009.

50. Davis HE, Miller SL, Case EM, Leach JK. Supplementation of fibrin gels with sodium chloride enhances physical properties and ensuing osteogenic response. Acta Biomater 7, 691, 2011.

51. Carrion B, Huang CP, Ghajar CM, Kachgal S, Kniazeva E, Jeon NL, Putnam AJ. Recreating the perivascular niche ex vivo using a microfluidic approach. Biotechnol Bioeng 107, 1020, 2010.

52. Kachgal S, Putnam AJ. Mesenchymal stem cells from adipose and bone marrow promote angiogenesis via distinct cytokine and protease expression mechanisms. Angiogenesis 14, 47, 2011.

53. Spotnitz WD. Fibrin sealant: past, present, and future: a brief review. World J Surg 34, 632, 2010.

54. Gleeson JP, Plunkett NA, O'Brien FJ. Addition of hydroxyapatite improves stiffness, interconnectivity and osteogenic potential of a highly porous collagen-based scaffold for bone tissue regeneration. Eur Cell Mater 20, 218, 2010.

55. Yoshikawa H, Myoui A. Bone tissue engineering with porous hydroxyapatite ceramics. J Artif Organs 8,131, 2005.

56. Friedman CD, Costantino PD, Takagi S, Chow LC. BoneSource hydroxyapatite cement: a novel biomaterial for craniofacial skeletal tissue engineering and reconstruction. J Biomed Mater Res 43, 428, 1998.

57. Jensen SS, Aaboe M, Pinholt EM, Hjørting-Hansen E, Melsen F, Ruyter IE. Tissue reaction and material characteristics of four bone substitutes. Int J Oral Maxillofac Implants 11, 55, 1996.

58. Block JE, Thorn MR. Clinical indications of calcium-phosphate biomaterials and related composites for orthopedic procedures. Calcif Tissue Int 66, 234, 2000.

59. Jacovella PF. Use of calcium hydroxylapatite (Radiesse) for facial augmentation. Clin Interv Aging 3, 161, 2008.

60. Augello A, Kurth TB, De Bari C. Mesenchymal stem cells: a perspective from in vitro cultures to in vivo migration and niches. Eur Cell Mater 20, 121, 2010.

61. Rosenbaum AJ, Grande DA, Dines JS. The use of mesenchymal stem cells in tissue engineering: A global assessment. Organogenesis 4, 23, 2008.

62. Hendrickx B, Vranckx JJ, Luttun A. Cell-based vascularization strategies for skin tissue engineering. Tissue Eng Part B Rev 17, 13, 2011.

CHAPTER 2

Cell-Based Approaches to the Engineering of Vascularized Bone Tissue

2.1 The Physiology of Bone

Composition and Architecture at the Micro- and Macro-scale

Bone is one of the main connective tissues in the human body. It is characterized by a collagenous extracellular matrix (ECM) that is extensively mineralized with hydroxyapatite (Ca10(PO4)6(OH)2) [1], which is found as plate-like structures 20-80 nm in length [2]. Hydroxyapatite contributes to the high density and strength of bone which in turns provides both support and protection to the other tissues and organs of the body. The mineral component of bone is both reactive and soluble, allowing turnover and remodeling within the bone structure. Bone tissue also contains a variety of other ionic species such as carbonate and magnesium, which are liberated to the systemic circulation as bone remodels. Bone therefore serves as an important storage depot for ions, including calcium and phosphate, which play roles in homeostatic regulation and metabolic function.

The proteinaceous ECM of bone is composed primarily of collagen type I, with lesser amounts of collagen type V and a variety of noncollagenous proteins [3]. Proteoglycans found in bone include chondroitin sulfate and keratin sulfate, which consist of a core protein surrounded by glycosaminoglycans and are found throughout the bone structure. Several key bone-associated proteins such as osteonectin, osteopontin, bone sialoprotein I and II, and osteocalcin play regulatory roles in bone formation and cellular attachment. In addition, the bone tissue

environment includes potent growth factors and cytokines, including insulin-like growth factors (IGF), tumor necrosis factor alpha (TNF-α), transforming growth factor-beta (TGF-β), and bone morphogenetic proteins, which direct cell differentiation and proliferation. The microenvironment in bone therefore is comprised of a complex combination of physical and chemical cues that orchestrate tissue function in both health and disease.

There are two main types of bone structure: cortical (also called compact) and trabecular (also called cancellous or spongy) [4]. Cortical bone is stiffer and more organized than trabecular bone and forms a compact, dense layer that surrounds the trabecular tissue in the long bones. Cortical bone consists of highly organized concentric structures called osteons that serve as the tissue's anatomical and functional unit. Osteons are supplied with blood form the marrow through Haversian canals, whereas Volkmann's canals move blood between osteons. Trabecular tissue is found in the interior of bones and is also highly vascular. Trabecular bone is less dense and stiff compared to compact bone, due to the large marrow cavities it contains. The red marrow within trabecular bone contains hematopoietic progenitor cells that are responsible for the production of the cells of the blood, as well as a small population of stem cells that can give rise to mesenchymal tissues, including new bone. The marrow itself is also highly vascularized and provides nutrients to the surrounding bone.

There are four primary cell types in bone tissue: osteoprogenitor cells, osteoblasts, osteocytes, and osteoclasts [3]. Osteoprogenitor cells reside in the marrow, periosteum, and bone canals. When environmental signals initiate the processes that require bone formation, such as tissue growth or repair, these progenitors migrate, proliferate, and differentiate into osteoblasts. The primary function of osteoblasts is to secrete the protein ECM of bone, which subsequently becomes mineralized to form new bone tissue. Found on the outer lining of bone, these cells can

either remain inactive on the surface of bones or become osteocytes. Alkaline phosphatase (ALP) activity serves as a marker of their action. BMPs play an important role in the regulation of osteoblast differentiation and activity. As bone is formed, osteoblasts become trapped in the matrix, and they alter their phenotype to become osteocytes, which account for the majority of the cells in bone. These cells fill spaces called lacunae in the osteons and communicate to one another through channels called canaliculi, maintaining the bone under homeostasis. Osteoclasts are bone-resorbing cells that are activated during bone injury and remodeling, and their function is to digest bone. The balance of growth, remodeling, and repair that is important in maintaining skeletal function is maintained by the orchestrated action of these cell types.

The Vascular Supply to Bone

Bone is a highly metabolic tissue requiring an abundant vascular supply throughout its structure for homeostasis, growth and remodeling. It is estimated that bone tissue uses approximately 10 to 20% of resting cardiac output [5]. A dual blood supply exists in both flat and long bones, through major arteries surrounding the bones [6]. Long bones have a nutrient foramen in both the diaphysis (midsection of bone) and epiphysis (end of long bone), which are openings in the hard tissue to allow blood vessels to pass through and reach the marrow cavities. Smaller epiphyseal and metaphyseal arteries arising from surroundings joints connect with capillaries throughout the diaphysis. In the outer areas of cortical bone, capillaries that run through the Volkmann's canals split into smaller arterioles that enter Haversian canals and in turn connect with surrounding skeletal muscle. Blood and waste drainage through the venous supply closely follows the nutrient arteries through bone. As flat bones do not contain diaphyses, metaphyses, or epiphyses, the dual blood supply runs adjacent to the plates of flat bones

providing areas for nutrient and waste exchange along the bone structure. The highly vascularized structure of bone allows the high demand of nutrient, waste, and ion transfer to be satisfied throughout the tissue and maintains normal development, growth, and remodeling of bone.

The Bone Healing Process

Injury to bone results in a cascade of events that allows the tissue to regenerate in a manner in which functionally developed tissue is recreated. These processes are triggered when skeletal integrity and local vasculature are disrupted at the defect site. Tissue damage initiates the bone healing response, which encompasses an initial inflammatory response, followed by intramembranous bone formation, endochondral bone formation, and finally bone remodeling (Figure 2.1).

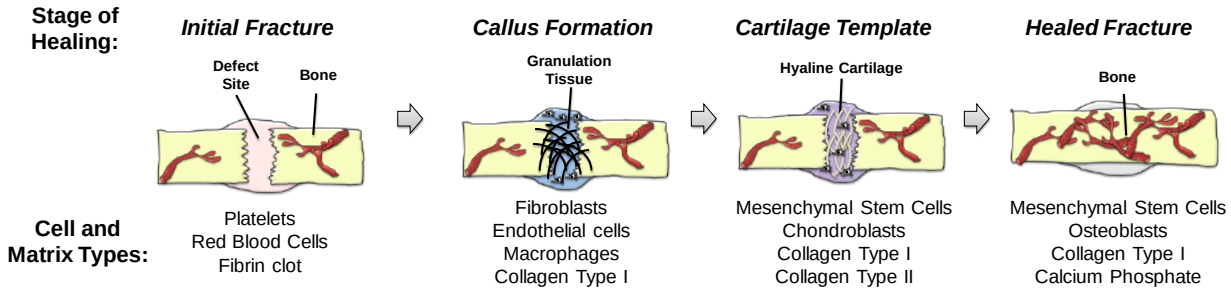

Figure 2.1 – Schematic of the process of bone fracture healing, showing the major cell and matrix types involved at each stage.

Angiogenesis is the formation of new blood vessels and is a critical component of the bone healing process, as it is required for the transport of nutrients, wastes, and cells to and from the injured site. Lack of angiogenesis has been cited as one of the primary causes of delayed- and non-unions. The capillary networks formed during the inflammatory phase of healing are typically transient in nature and are incapable of forming the functional vasculature required to heal non-unions. Evidence of this observation has been provided in a rat distraction osteogenesis

model where administration of anti-angiogenic drugs during osteogenesis caused fibrous tissue formation and resulted in non-union [7].

Immediately after a bone fracture, ruptured blood vessels in the injured area constrict and a clot is formed to prevent further bleeding [3]. The resulting lack of blood supply causes a local hypoxic environment. Fibroblasts migrate towards the injured site to deposit initial extracellular matrix and generate granulation tissue. The lack of oxygen acts as a signal for local endothelial cells to proliferate and chondroblasts to differentiate from bone marrow stem cells, forming a bridge of hyaline cartilage between the ends of the injury site. The chondroblasts subsequently become hypertrophic and express pro-angiogenic factors, including vascular endothelial growth factors (VEGF) and fibroblast growth factors (FGF), causing blood vessels to further extend into the cartilaginous matrix. The presence of new blood vessels allows osteoprogenitor and hematopoietic cells to be transported to the wounded area, where they differentiate in the ossification center to form bone and bone marrow, respectively. In the final stages of healing, the local osteoprogenitor cells differentiate into osteoblasts to produce functional bone.

2.2 Cell Types used in Engineering of Vascularized Bone Tissue

The general approach to creating vascularized bone tissue is to combine an osteogenic cell type with an endothelial cell type, as shown schematically in Figure 2.2. For regeneration of defects, 3D hydrogel- or solid scaffold-based approaches are often used, though 2D co-culture models have been used to study the healing process. There are now a range of possible osteogenic cell sources, including bone marrow-derived mesenchymal stem cells, adipose-derived stem cells, or mature osteoblasts. Similarly, a variety of endothelial cell types or their progenitors can be used. The cell types most commonly applied are described briefly below.

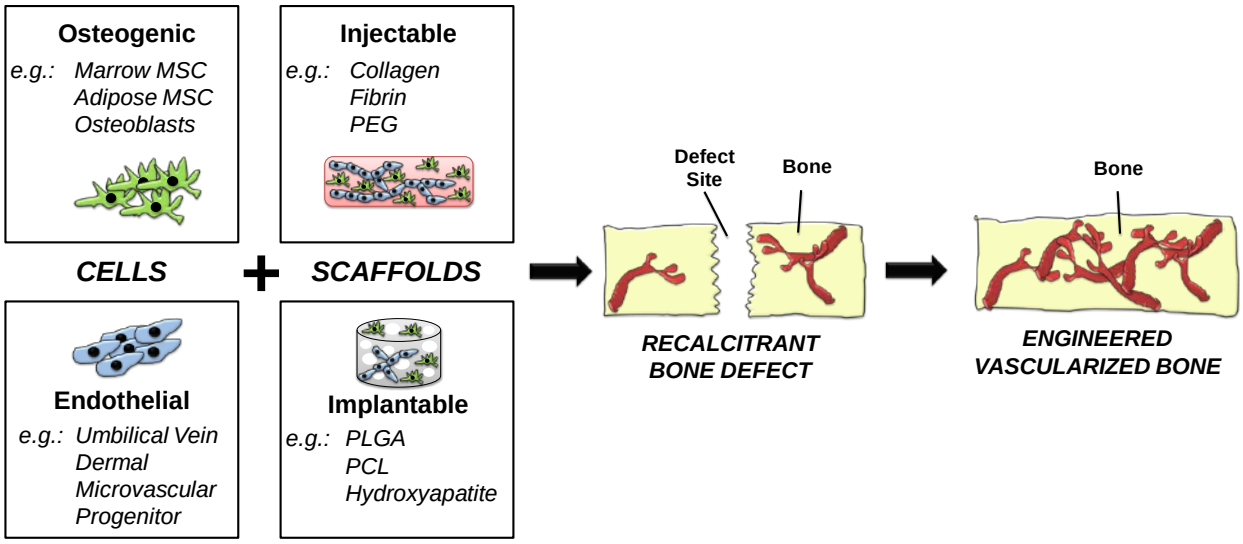

Figure 2.2 – Schematic of cell-based approaches to engineering vascularized bone tissue. Cells and scaffolds are combined to treat large and recalcitrant defects.

Osteogenic Cell Types

Mesenchymal stem cells (MSC) are a multipotent cell type found in numerous tissues of the body. They are characterized as stem cells based on their ability to proliferate in an undifferentiated state and their potential to differentiate into various mesenchymal cell lineages [8, 9]. MSC are commonly isolated from bone marrow (bmMSC) and adipose tissue (AdSC), though they have also been extracted from a variety of other tissues, including umbilical cord, placental tissue, cord blood, amniotic fluid, and the periosteum [10-12]. These different tissues yield MSC that have different proliferative and multipotency profiles. Furthermore, age and disease stage are critical factors that can affect MSC function and potential.

MSC differentiation can be controlled by exogenous factors including hormones, growth factors, and extracellular matrix molecules. In vitro, bmMSC have been shown to differentiate towards bone, cartilage, muscle, adipose tissue, and tendon [13]. In particular, osteogenesis of bmMSC is commonly induced in vitro by adding dexamethasone, beta-glyocerophosphate (β-

GP), and ascorbic acid to the culture media [14-17]. Dexamethasone, a glucocorticoid, induces transcription of osteogenic factors such as bone sialoprotein [18] and the α5 integrin, an activator of Runx-2, ALP, and collagen I mRNA expression [19]. Ascorbic acid is an important cofactor in collagen formation, the most abundant protein in the ECM of bone, and increases ALP expression. Typically, ascorbic-2-phosphate is used in osteogenic studies as it is more stable in cell culture (pH = 7.4, 37ºC, and 5% CO2) conditions [20]. Cell-secreted ALP hydrolyzes supplemented β-GP to form the inorganic phosphate that aids in matrix mineralization [21]. Furthermore, growth factors such as TGF-β1, TGF-β2, TGF-β3, and BMPs can be exogenously applied in specific concentrations to differentiate bmMSC towards both the osteogenic and chondrogenic lineages. MSC differentiation can also be directed through matrix identity, matrix stiffness mechanical stimulation, substrate stiffness and nanotopographical cues [22-26]. The ability to control the phenotype of these progenitor cells makes them a valuable resource for tissue engineering approaches to bone regeneration.

Autologous bmMSC have advantages when designing cell-based therapies, because they avoid issues of immune rejection and can be harvested from patients using relatively simple surgical procedures. Clinical studies have been performed in which autologous bmMSC were purified from bone marrow aspirates, followed by ex vivo expansion and subsequent re-implantation as therapies for graft-versus-host-disease, liver disease, bone fractures, heart failure, and multiple sclerosis [27]. Biopsy from the iliac crest is the most widely used procedure for obtaining bone marrow from which bmMSC can be purified. However, this method is associated with donor site pain and other types of morbidity. Furthermore, bone marrow aspirates contain bmMSC at a frequency of only 0.001-0.01% of total marrow cells, and therefore yield a

relatively low number of bmMSC after isolation. For these reasons, other sources of MSC have been examined and developed for cell-based therapies.

Allogeneic cells and tissues typically elicit a host immune reaction upon implantation. This response can be managed through pharmacological immune suppression, but may also cause an array of undesired side effects. Interestingly, it has been suggested that bmMSC are hypoimmunogenic relative to other cell types, and therefore that they may be useful for therapeutic purposes even in the absence of immune modulation [28, 29]. Studies have shown that bmMSC can inhibit T-cell proliferation through the secretion of soluble factors such as hepatocyte growth factor (HGF), TGF-β1, and interleukin-10 (IL-10) [30-32]. It is thought that these growth factors and cytokines create an immunosuppressive environment around bmMSC, resulting in a delayed and attenuated immune response. Allogeneic bmMSC offer the great advantage that they could be produced in large quantities for therapeutic use, allowing more comprehensive quality control of both safety and function. The possibility of using these cells without immunosuppression makes them very attractive for cell-based therapies.

Adipose-derived stem cells (AdSC) are a subtype of MSC that are derived from fat tissue. They are considered separately here because of the great interest in their use, engendered by the ease of isolating them from adipose tissue and their associated translational potential [33]. These cells can be isolated from liposuction aspirates or other biopsies [34, 35], and have been shown to differentiate into a variety of mesenchymal cell lineages including bone [36, 37], fat [38, 39], and cartilage [40-42]. Similar to bmMSC, AdSC have been shown to possess immunomodulatory properties allowing for inhibition of inflammatory cytokines [43, 44].

Osteoblasts are the secretory cells that form the collagen matrix present within the bone structure. These cells also secrete non-collageneous proteins such as osteocalcin, osteopontin,

and osteonectin, which participate in the mineralization process required to create mature bone. Osteoblasts also play a primary role in fracture healing. They are recruited towards fracture sites and deposit matrix to achieve the appropriate geometry required to fill the defect. In tissue engineering applications, primary osteoblasts [45, 46], osteoblast cell lines [47, 48], and pre-osteoblast cell lines [49-51] have typically been used to demonstrate efficacy in up-regulating osteogenic genes in vitro and bone formation in vivo. The use of primary osteoblasts in bone regeneration has the advantage that cell differentiation is not required, but an autologous source would be required. However, these cells have limited proliferative capacity in vitro and therefore present challenges in obtaining a sufficient quantity of cells to achieve a therapeutic effect [52].

Endothelial Cell (EC) Types

Endothelial cells (EC) line the blood vessels and are present throughout the vasculature in the human body [53, 54]. These cells have the ability to self-assemble into vascular tubes when isolated and then cultured in protein materials such as collagen and fibrin [55, 56]. Vessel formation can also occur under the guidance of pro-angiogenic factors such as VEGF, FGF, HGF, and platelet-derived growth factor (PDGF) [57, 58].

Endothelial cells can be extracted from numerous tissue sources, including umbilical cords, dermal tissue, and the saphenous vein [54]. A commonly used macrovascular cell type is human umbilical vascular endothelial cells (HUVEC), which can be isolated from discarded umbilical cords through a facile collagenase digestion procedure. HUVEC can form capillary-like structures when co-cultured in 3D matrices with stromal cells, including fibroblasts [59], MSC [56, 60], and AdSC [61]. Secreted factors from the MSC, such as VEGF and MMPs, allow migration of HUVEC through matrices, thereby enabling the cells to combine and form tubular

structures. Human dermal microvascular endothelial cells (HMVEC) are an alternate endothelial cell source for the engineering of vascularized tissue that can be isolated from neonatal foreskin [62] or adult skin capillaries [63]. HMVEC have been shown to create vessel-like structures in vitro when co-cultured with stromal cell types such as fibroblasts [64], and have yielded perfused vessels in vivo [65]. An advantage of HMVEC is that they potentially represent an autologous cell source for therapeutic neovascularization.

Endothelial progenitor cells (EPC) have also been studied for their ability to form capillary-like structures in vivo when co-cultured with stromal cells [66]. EPC are a somewhat heterogeneous cell type that can be derived from a number of sources including from adult bone marrow, adult peripheral blood, and umbilical cords. There are two types of EPC which can be obtained from peripheral blood: late outgrowth and early outgrowth, which differ in their culture times, proliferative potential, and gene expression [67]. Au et al. [68] showed that EPC derived from umbilical cord blood and EPC derived from adult peripheral blood can both form vessels in vivo when co-cultured with fibroblasts, but the stability and density of the vessels differed. EPC can be obtained from adult humans, and therefore they offer the potential of an autologous stem cell use in engineered tissues.

Other sources of EC such as those isolated directly from the bone marrow (bmEC) [69] and EC derived from an original progenitor cell source such as AdSC [70] or bmMSC [71] are being explored, including as sourced in vascularized bone tissue engineering applications. While these cell types are less commonly used, they have potential advantages in terms of ease of procurement and use as an allogeneic cell source. However, the methods for consistently isolating these cells are still being developed, and the full functional characterization of these sources as vasculogenic EC are not yet complete.

2.3 In Vitro Co-Culture Models of Vascularized Bone Formation

A variety of two-dimensional (2D) experimental models have been employed to study the mechanisms of both osteogenesis and angio/vasculogenesis, with the aim of understanding the relationships and interactions between various cell types in vitro. Early co-culture studies established a synergistic relationship between endothelial cell types and osteoblastic cell types. Co-culturing these cell types together caused an upregulation of the activity of the osteogenic marker ALP in bmMSC, AdSCs, and osteoblasts [72-75]. Increased ALP expression requires direct contact between the two cell types, allowing for gap junctional communication between HUVEC and osteoblasts [75]. It has also been suggested that ALP mRNA is stabilized by p38 mitogen-activated protein kinase expressed by EC in the system [76]. However the contribution of EC to osteogenesis is complex, and other 2D co-culture models have shown downregulation of osteogenic factors such as Runx2 and osteocalcin [77, 78].

Other work has demonstrated a positive effect of EC on both bmMSC and osteoblast proliferation [79], putatively through inactivation of the proapoptotic protein BAD [80]. Conversely, MSC and osteoblasts secrete pro-angiogenic factors such as VEGF [81], causing upregulation of the VEGF receptor in EC, which in turn increases ALP expression in bmMSC and osteoblasts [82]. The sonic hedgehog pathway is implicated as one of the main signaling pathways that control both angiogenesis and osteogenesis in these co-culture models [83]. The secretion of proangiogenic factors from bmMSC has also been suggested to be differentiation-state dependent, such that osteogenically induced bmMSC show reduced secretion of VEGF and FGF-2, leading to a decrease in EPC chemotaxis [84]. Other studies have investigated the effects of modulating cell ratio, cell type, and culture medium in order to optimize both osteogenic and angiogenic conditions of the two cell types [85-89].

Three-dimensional (3D) co-culture systems using a variety of natural and synthetic biomaterials have also been employed as systems to study concurrent angio-/vasculogenesis and osteogenesis. Three-dimensional spheroid co-culture of bmMSC and HUVEC was shown to produce well-organized 3D vascular structures in vitro [90]. Further, the authors observed an increase in ALP expression in the bmMSC/HUVEC co-culture system compared to a control (bmMSC/fibroblast) co-culture system. These effects were attributed to enhanced activation of Wnt signaling as evidenced by β-catenin expression, as well as upregulation of BMP signaling through elevated pSmad 1/5/8 expression.

Similarly, 3D solid scaffold-based co-culture systems have been investigated. Santos et al cultured HMVEC with osteoblasts on fiber-mess scaffolds composed of a blend of corn starch and polycaprolactone (PCL) scaffolds and observed alignment of EC and expression of collagen IV, an endothelial basement membrane protein, after 21 days of culture [91]. Further gene expression analysis showed upregulation of key osteogenic and angiogenic genes such as collagen I, VEGF, ALP, and VCAM-1. Direct cell-cell contact between the two cell types promoted increased VEGF secretion and high expression of the gap junction protein connexin 43 was detected at the osteoblast-HUVEC interface. These data suggest that heterotypic intercellular crosstalk between the two cell types impacts their respective gene expression profiles. Beta-tricalcium phosphate (β-TCP) scaffolds were assessed for their ability to support both HUVEC and bmMSC co-cultures as shown in Figure 2.3 [92]. In this study, the authors investigated the effects of mono- or co-cultured bmMSC and HUVEC at various ratios (bmMSC:HUVEC ratios of 5:1, 1:1, and 5:1). This system was permissive to both bmMSC and HUVEC proliferation,

vessel-like structure formation by the HUVEC, and upregulation of ALP.

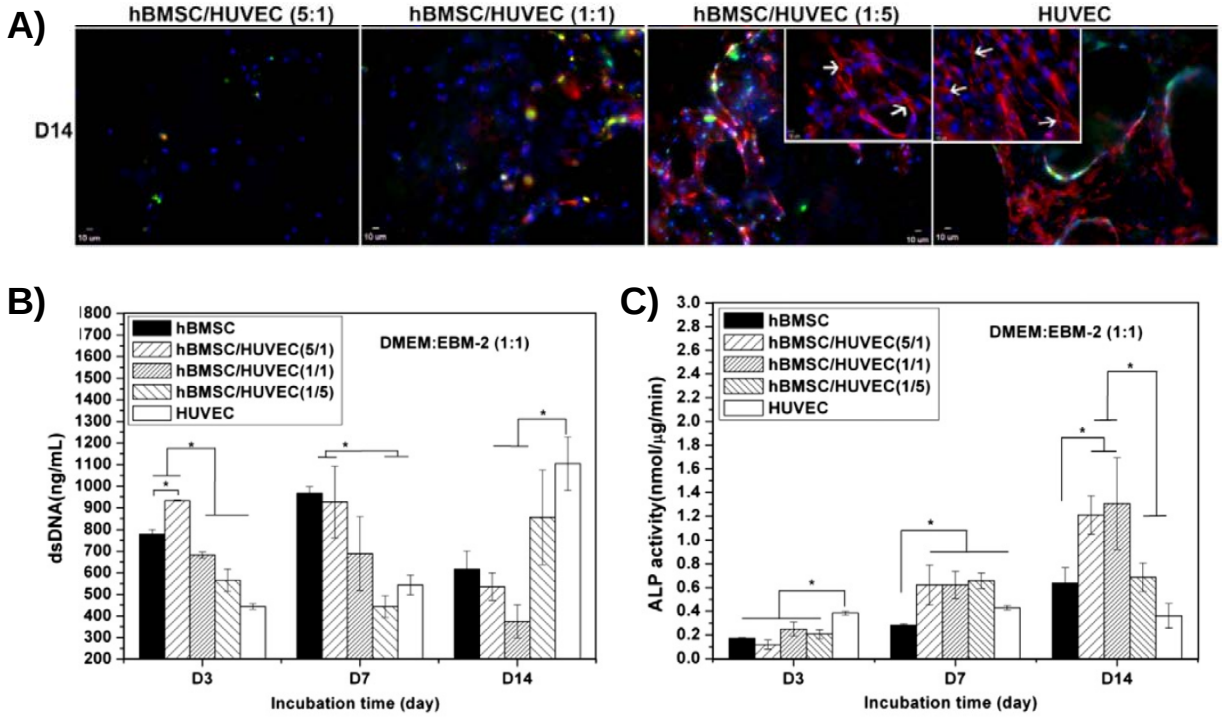

Figure 2.3 – In vitro co-culture models of vascularized bone formation. (A) Kang et al showed endothelial network formation by HUVEC on β-tricalcium phosphate scaffolds after 14 days of co-culture with bmMSC. CD31 is labeled red and cell nuclei are labeled blue. Scale bar = 10 μm. (B and C) Both cell proliferation and alkaline phosphatase expression were modulated in co-culture conditions. All panels were adapted from [92]. Copyright 2013 Elsevier B.V.

Poly(lactide-co-glycolide) (PLGA) scaffolds have also been employed as scaffolds to support co-cultures of bmMSC and EPC. Nukavarapu et. al observed increases in BMP-2 and VEGF gene expression as well as ALP expression on macro-porous scaffolds fabricated from PLGA microspheres [93]. Moreover, other scaffolding materials such as PCL [69] and polyester-urethane [94] can support co-cultures of bmMSC and EC.

2.4 In Vivo Regeneration of Vascularized Bone Tissue

Combined osteogenic/angiogenic cell-based co-culture systems have been applied to generating vascularized bone tissue in both ectopic and orthotropic sites in vivo. After demonstrating that HMVEC increase osteogenic differentiation of bmMSC through the secretion of BMP-2, Kaigler et al investigated the co-transplantation of HMVEC and bmMSC on PLGA scaffolds into the dorsal region of SCID mice and monitored ectopic bone formation after 8 weeks [95]. The authors observed no differences between total blood vessel content in the implants containing both cell types, compared to implants with bmMSC alone. However, there was a significant increase in bone formation in the HMVEC+bmMSC condition, compared to the bmMSC alone implants. In another study, examination of culture conditions of HUVEC and bmMSC in vitro suggested that vasculogenesis needed to be induced prior to osteogenesis [96]. The two cell types were then cultured for 6 weeks on decellularized bone grafts and implanted subcutaneously into nude mice, which resulted in bone formation.

Scaffold-less co-transplantation of bmMSC and HUVEC has also been investigated as a means of generating ectopic bone formation [97]. A dense cell sheet was constructed by seeding bmMSC in a monolayer and inducing the cells towards the osteogenic phenotype. HUVEC were then seeded on top of the bmMSC cell layer, which created a vessel-like network within the cell sheet. After transplantation of the co-cultured cell sheet into nude mice, immunohistochemical analysis demonstrated expression of the bone marker osteocalcin, and integration of transplanted HUVEC with host vasculature. Ectoptic osteogenesis has also been evaluated through the co-transplantation of EPC and bmMSC on collagen fiber mesh scaffolds into nude mice subcutaneously [98]. Neovasculature and total bone area, as measured by capillary density and histological analysis, were both increased in the co-culture group compared to the bmMSC only

condition after 12 weeks of implantation. Ectopic bone formation has also been achieved in a large animal model. Geuze et al combined EPC and bmMSC on biphasic calcium phosphate scaffolds and implanted them intramuscularly into a goat model [99]. The authors observed significant increases in bone formation in the co-culture condition compared to acellular controls, however there was no significant difference in bone generation compared to the bmMSC alone group. Similar results were observed by Fedorovich et al using goat bmMSC and goat blood-derived EPC in a subcutaneous ectopic bone model in nude mice [100].

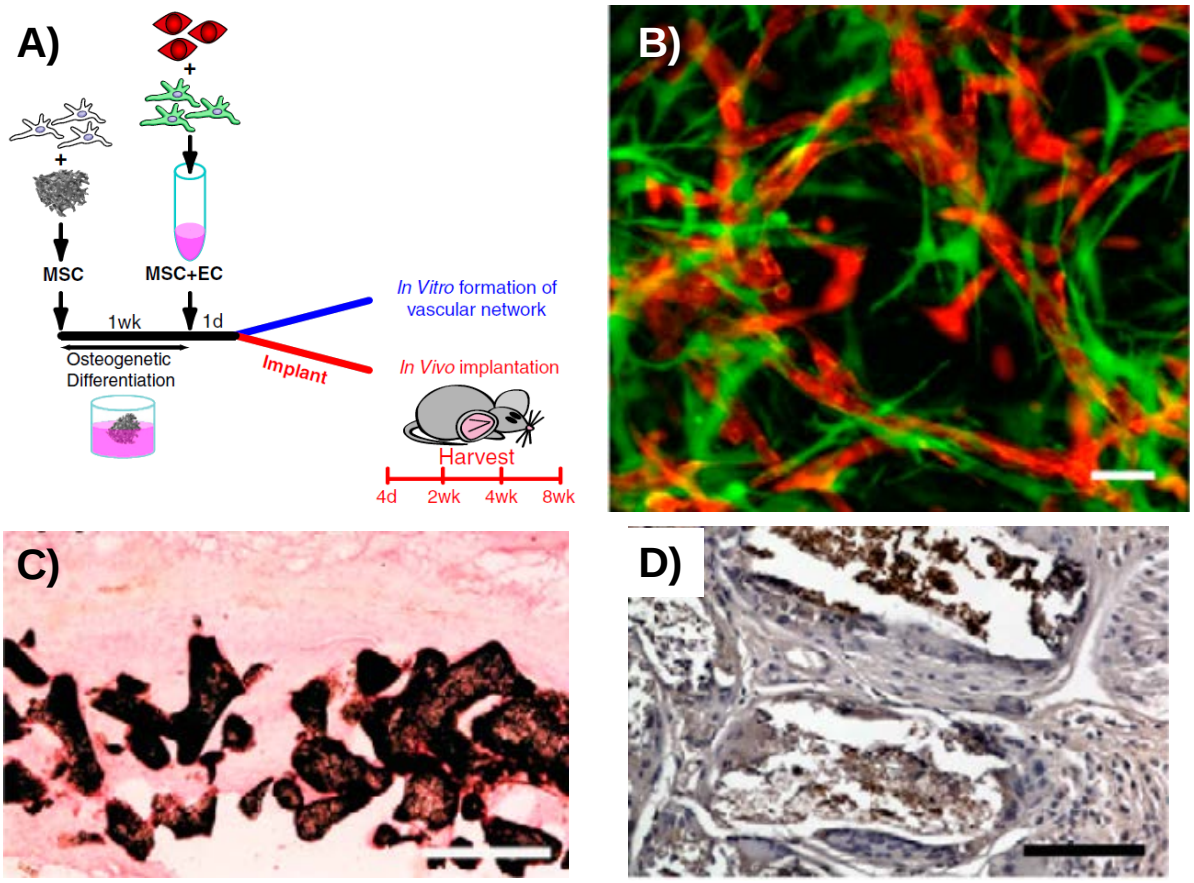

Figure 2.4 - In vivo regeneration of vascularized bone tissue. (A) Tsikgou et al seeded bmMSC on PLGA scaffolds and pre-differentiated them towards the osteogenic lineage prior to embedding the scaffolds in a collagen-fibronectin hydrogel containing a bmMSC and HUVEC co-culture. (B) In vitro formation of vessel-like structures after 21 days of culture. MSC (eGFP) and HUVEC (tdTomato) were transduced with a lentivirus to fluorescently label the cells. Scale bar = 50 µm. (C) Von Kossa staining after 8 weeks of subcutaneous implantation in immunodeficient mice. Calcium deposition was observed on the pore surfaces of the implanted scaffold. Scale bar = 500 µm. (D) Osteocalcin, a late marker of osteogenesis, was also present throughout the scaffold. Scale bar = 100 µm. All panels are adapted from [101]. Copyright 2010 National Academy of Sciences of the United States of America.

An interesting approach to engineering vascularized bone grafts was demonstrated by Tsigkou et al [101]. Bone marrow MSC were first seeded onto porous PLGA scaffolds and predifferentiated toward the osteogenic lineage for one week of in vitro culture (Figure 2.4). The scaffolds were then seeded with a collagen-fibronectin hydrogel containing HUVEC and bmMSC, and were implanted subcutaneously into SCID mice. Seeded HUVEC were shown to

connect with host vasculature, and ectopic bone formation and expression of osteocalcin was achieved after 8 weeks of implantation.

Orthotopic models in animals have also demonstrated the potential of MSC and EC co-cultures systems to regenerate bone, but the results have been mixed. Calvarial defects in rodents are a common orthotopic model. Early studies by Kaigler et al combined bmMSC and HMVEC on PLGA scaffolds to assess bone regeneration in a rat cranial defect model [102]. Bone mineral density of the bmMSC+HMVEC group was significantly higher after 6 weeks compared to the bmMSC alone condition, but was not statistically different after 12 weeks post-implantation. Conversely, bone volume was not statistically different after 6 weeks of implantation, but was significantly higher in the co-culture condition after 12 weeks. Koob et. al also used calvarial defects in SCID mice to study the effect of bmMSC+HUVEC co-cultures that were embedded in fibrin/Matrigel hydrogels and then seeded onto decalcified bone scaffolds [103]. Human EC were successfully transplanted into the mice, as demonstrated by positive human CD31 staining. However, the dual (MSC+HUVEC) group showed no significant increase in either capillary or bone formation in the implant site, relative to controls. This result was attributed to a lack of direct contact between implanted HUVEC and bmMSC as well as the contribution of endogenous angiogenesis from the host, which enabled comparable bone formation in controls. In a separate study, pre-differentiation of AdSC toward the bone lineage and co-transplantation with HUVEC on PCL/PLGA/TCP scaffolds yielded different results [104]. More rapid and more extensive bone regeneration was observed in the AdSC+HUVEC group compared to the AdSC alone condition, indicating a beneficial response to the addition of HUVEC. In a study using EPC+bmMSC co-cultures on PLGA scaffolds, no significant increase in neovascularization was observed compared to the bmMSC alone group [105]. Further, the dual group did not yield

improved bone regeneration compared to the bmMSC or EPC groups, which the authors attributed to low transplantation efficiency of EPC in vivo.

Femoral defects are another orthotopic model that has been used to study osteogenesis induced by bmMSC+EC co-cultures. In this model, co-transplantation of bmMSC and HUVEC embedded within alginate microspheres enhanced bone regeneration compared to the bmMSC alone condition, suggesting a synergistic response of HUVEC with transplanted bmMSC [106]. Co-transplantation of EPC and bmMSC on fibronectin-coated β-TCP scaffolds also showed promising results [107]. Both neovascularization and bone volume fraction were increased in the dual group compared to the cell types individually at the early time points of one and four weeks. Importantly, after 8 weeks, bone quality was significantly higher in the EPC+bmMSC group, as measured by ultimate load measurements, indicating a potential benefit of generating highly vascularized engineered bone.

2.5 Summary and Conclusions

The healing of large bone defects remains a particular clinical challenge due to the need to establish vascularization in appropriate conjunction with bone regeneration. Approaches to this problem using growth factor and gene delivery have shown some promise, but results have been variable, and consistently robust regeneration has not been achieved. Only cells can create new bone and new vasculature, and therefore cell-based therapies are particularly promising for the treatment of large bone defects where the native cellular component may be absent. Numerous cell types in this application, including bone marrow mesenchymal stem cells, adipose-derived stem cells, osteoblasts, umbilical vein endothelial cells, dermal microvascular

endothelial cells, and endothelial progenitor cells. Each cell type presents its own advantages and disadvantages, particularly in their capacity to be used as an autologous or allogeneic source.

In vitro 2D co-cultures models have provided a deeper mechanistic understanding of the crosstalk between MSC and EC that is critical to regenerating mature and stable tissue. For example, expression of ALP, an osteogenic protein, by MSC is increased when they are co-cultured with EC. At the same time MSC secrete VEGF, which induces local EC to form primitive tubular networks. Similarly, in vitro 3D co-cultures using various natural and synthetic biomaterials have provided proof-of-concept studies to demonstrate cell survival and maintenance of both osteogenic and angiogenic phenotypes. Furthermore, these scaffolds have served as materials to transplant cells in vivo in both ectopic bone formation and orthotopic bone regeneration models. The transplantation of MSC and EC co-cultures in vivo has shown promising results in generating vascularized bone and in regenerating higher quality bone faster compared to transplanting either cell type alone.

This review has endeavored to summarize the key cellular components and processes involved in regenerating vascularized bone tissue, and how biologists and bioengineers have attempted to mimic these processes in vitro and in vivo. It is clear that an interplay between osteogenic and vasculogenic cells is required to create vascularized bone, and the studies summarized above have provided insight into these interactions. The 2D and 3D studies that have been performed to date suggest that targeting of vasculogenesis concomitantly with osteogenesis can lead to more rapid, robust, and mature bone formation. However these early approaches need to be validated in pre-clinical large animal models, before they can be investigated in humans. The ability to generate well-vascularized bone tissue in vivo will expedite clinical translation of cell-based approaches to bone tissue engineering.

2.6 References

1. Clarke B. Normal bone anatomy and physiology. Clin J Am Soc Nephrol 2008;3 Suppl 3:S131-9.

2. Sommerfeldt DW, Rubin CT. Biology of bone and how it orchestrates the form and function of the skeleton. Eur Spine J 2001;10:S86-95.

3. Ross MH, Pawlina W. Histology: A Text and Atlas. Philadelphia: Lippincott Williams & Wilkins; 2010. p 218-53.

4. Downey PA, Siegel MI. Bone biology and the clinical implications for osteoporosis. Phys Ther 2006;86:77-91.

5. Khurana JS, Safadi FF. Bone Structure, Development and Bone Biology. Essentials in Bone and Soft-Tissue Pathology 2010. p. 1-15.

6. Buck DW 2nd, Dumanian GA. Bone biology and physiology: Part I. The fundamentals. Plast Reconstr Surg 2012;129:1314-20.

7. Fang TD, Salim A, Xia W, Nacamuli RP, Guccione S, Song HM, Carano RA, Filvaroff EH, Bednarski MD, Giaccia AJ, Longaker MT. Angiogenesis is required for successful bone induction during distraction osteogenesis. J Bone Miner Res 2005;20:1114-24.

8. Augello A, Kurth TB, De Bari C. Mesenchymal stem cells: a perspective from in vitro cultures to in vivo migration and niches. Eur Cell Mater 2010;20:121-33.

9. Rosenbaum AJ, Grande DA, Dines JS. The use of mesenchymal stem cells in tissue engineering: A global assessment. Organogenesis 2008;4:23-7.

10. Bieback K, Wuchter P, Besser D, Franke W, Becker M, Ott M, Pacher M, Ma N, Stamm C, Klüter H, Müller A, Ho AD; START-MSC consortium. Mesenchymal stromal cells (MSCs): science and f(r)iction. J Mol Med 2012;90:773-82.

11. Motaln H, Schichor C, Lah TT. Human mesenchymal stem cells and their use in cell-based therapies. Cancer 2010;116:2519-30.

12. van Gastel N, Torrekens S, Roberts SJ, Moermans K, Schrooten J, Carmeliet P, Luttun A, Luyten FP, Carmeliet G. Engineering vascularized bone: osteogenic and proangiogenic potential of murine periosteal cells. Stem Cells 2012;30:2460-71.

13. Pittenger MF, Mackay AM, Beck SC, Jaiswal RK, Douglas R, Mosca JD, Moorman MA, Simonetti DW, Craig S, Marshak DR. Multilineage potential of adult human mesenchymal stem cells. Science 1999;284:143-7.

14. Vater C, Kasten P, Stiehler M. Culture media for the differentiation of mesenchymal stromal cells. Acta Biomater 2011;7:463-77.

15. Davis HE, Rao RR, He J, Leach JK. Biomimetic scaffolds fabricated from apatite-coated polymer microspheres. J Biomed Mater Res A 2009;90:1021-31.

16. Wang L, Stegemann JP. Thermogelling chitosan and collagen composite hydrogels initiated with beta-glycerophosphate for bone tissue engineering. Biomaterials 2010;31:3976-85.

17. Wang L, Stegemann JP. Glyoxal crosslinking of cell-seeded chitosan/collagen hydrogels for bone regeneration. Acta Biomater 2011;7:2410-7.

18. Ogata Y, Yamauchi M, Kim RH, Li JJ, Freedman LP, Sodek J. Glucocorticoid regulation of bone sialoprotein (BSP) gene expression. Identification of a glucocorticoid response element in the bone sialoprotein gene promoter. Eur J Biochem 1995;230:183-92.

19. Hamidouche Z, Fromigué O, Ringe J, Häupl T, Vaudin P, Pagès JC, Srouji S, Livne E, Marie PJ. Priming integrin alpha5 promotes human mesenchymal stromal cell osteoblast differentiation and osteogenesis. Proc Natl Acad Sci U S A. 2009;106:18587-91.

20. Takamizawa S, Maehata Y, Imai K, Senoo H, Sato S, Hata R. Effects of ascorbic acid and ascorbic acid 2-phosphate, a long-acting vitamin C derivative, on the proliferation and differentiation of human osteoblast-like cells. Cell Biol Int 2004;28:255-65.

21. Chung CH, Golub EE, Forbes E, Tokuoka T, Shapiro IM. Mechanism of action of beta-glycerophosphate on bone cell mineralization. Calcif Tissue Int 1992;51:305-11.

22. Li D, Zhou J, Chowdhury F, Cheng J, Wang N, Wang F. Role of mechanical factors in fate decisions of stem cells. Regen Med 2011;6:229-40.

23. Rehfeldt F, Engler AJ, Eckhardt A, Ahmed F, Discher DE. Cell responses to the mechanochemical microenvironment--implications for regenerative medicine and drug delivery. Adv Drug Deliv Rev 2007;59:1329-39.

24. Carpentier B, Layrolle P, Legallais C. Bioreactors for bone tissue engineering. Int J Artif Organs 2011;34:259-70.

25. Mauney JR, Volloch V, Kaplan DL. Role of adult mesenchymal stem cells in bone tissue engineering applications: current status and future prospects. Tissue Eng 2005;11:787-802.

26. Hidalgo-Bastida LA, Cartmell SH. Mesenchymal stem cells, osteoblasts and extracellular matrix proteins: enhancing cell adhesion and differentiation for bone tissue engineering. Tissue Eng Part B Rev 2010;16:405-12.

27. Salem HK, Thiemermann C. Mesenchymal stromal cells: current understanding and clinical status. Stem Cells 2010;28:585-96.

28. Yi T, Song SU. Immunomodulatory properties of mesenchymal stem cells and their therapeutic applications. Arch Pharm Res 2012;35:213-21.

29. Abumaree M, Al Jumah M, Pace RA, Kalionis B. Immunosuppressive properties of mesenchymal stem cells. Stem Cell Rev 2012;8:375-92.

30. Aggarwal S, Pittenger MF. Human mesenchymal stem cells modulate allogeneic immune cell responses. Blood 2005;105:1815-22.

31. Shi M, Liu ZW, Wang FS. Immunomodulatory properties and therapeutic application of mesenchymal stem cells. Clin Exp Immunol 2011;164:1-8.

32. Yagi H, Soto-Gutierrez A, Parekkadan B, Kitagawa Y, Tompkins RG, Kobayashi N, Yarmush ML. Mesenchymal stem cells: Mechanisms of immunomodulation and homing. Cell Transplant 2010;19:667-79.

33. Gir P, Oni G, Brown SA, Mojallal A, Rohrich RJ. Human adipose stem cells: current clinical applications. Plast Reconstr Surg 2012;129:1277-90.

34. Lee K, Chan CK, Patil N, Goodman SB. Cell therapy for bone regeneration--bench to bedside. J Biomed Mater Res B Appl Biomater 2009;89:252-63.

35. Zeve D, Tang W, Graff J. Fighting fat with fat: the expanding field of adipose stem cells. Cell Stem Cell 2009;5:472-81.

36. Bodle JC, Hanson AD, Loboa EG. Adipose-derived stem cells in functional bone tissue engineering: lessons from bone mechanobiology. Tissue Eng Part B Rev 2011;17:195-211

37. Correia C, Bhumiratana S, Yan LP, Oliveira AL, Gimble JM, Rockwood D, Kaplan DL, Sousa RA, Reis RL, Vunjak-Novakovic G. Development of silk-based scaffolds for tissue engineering of bone from human adipose-derived stem cells. Acta Biomater 2012;8:2483-92.

38. Brayfield CA, Marra KG, Rubin JP. Adipose tissue regeneration. Curr Stem Cell Res Ther 2010;5:116-21.

39. Wang W, Cao B, Cui L, Cai J, Yin J. Adipose tissue engineering with human adipose tissue-derived adult stem cells and a novel porous scaffold. J Biomed Mater Res B Appl Biomater 2013;101:68-75.

40. Hildner F, Albrecht C, Gabriel C, Redl H, van Griensven M. State of the art and future perspectives of articular cartilage regeneration: a focus on adipose-derived stem cells and platelet-derived products. J Tissue Eng Regen Med 2011;5:e36-51.

41. Cheng NC, Estes BT, Young TH, Guilak F. Genipin-crosslinked cartilage-derived matrix as a scaffold for human adipose-derived stem cell chondrogenesis. Tissue Eng Part A 2013;19:484-96.

42. Estes BT, Diekman BO, Gimble JM, Guilak F. Isolation of adipose-derived stem cells and their induction to a chondrogenic phenotype. Nat Protoc 2010;5:1294-1311.

43. Cui L, Yin S, Liu W, Li N, Zhang W, Cao Y. Expanded adipose-derived stem cells suppress mixed lymphocyte reaction by secretion of prostaglandin E2. Tissue Eng 2007;13:1185-95.

44. De Miguel MP, Fuentes-Julián S, Blázquez-Martínez A, Pascual CY, Aller MA, Arias J, Arnalich-Montiel F. Immunosuppressive properties of mesenchymal stem cells: advances and applications. Curr Mol Med 2012;12:574-91.

45. Burdick JA, Anseth KS. Photoencapsulation of osteoblasts in injectable RGD-modified PEG hydrogels for bone tissue engineering. Biomaterials 2002;23:4315-23.

46. Benoit DS, Durney AR, Anseth KS. Manipulations in hydrogel degradation behavior enhance osteoblast function and mineralized tissue formation. Tissue Eng 2006;12:1663-73.

47. Rodrigues SC, Salgado CL, Sahu A, Garcia MP, Fernandes MH, Monteiro FJ. Preparation and characterization of collagen-nanohydroxyapatite biocomposite scaffolds by cryogelation method for bone tissue engineering applications. J Biomed Mater Res A 2012 (in press).

48. Müller U, Imwinkelried T, Horst M, Sievers M, Graf-Hausner U. Do human osteoblasts grow into open-porous titanium? Eur Cell Mater 2006;11:8-15.

49. Ignatius A, Blessing H, Liedert A, Schmidt C, Neidlinger-Wilke C, Kaspar D, Friemert B, Claes L. Tissue engineering of bone: effects of mechanical strain on osteoblastic cells in type I collagen matrices. Biomaterials 2005;26:311-18.

50. Khatiwala CB, Kim PD, Peyton SR, Putnam AJ. ECM compliance regulates osteogenesis by influencing MAPK signaling downstream of RhoA and ROCK. J Bone Miner Res 2009;24:886-98.

51. Gibon E, Batke B, Jawad MU, Fritton K, Rao A, Yao Z, Biswal S, Gambhir SS, Goodman SB. MC3T3-E1 osteoprogenitor cells systemically migrate to a bone defect and enhance bone healing. Tissue Eng Part A 2012;9-10:986-73.

52. Jayakumar P, Di Silvio L. Osteoblasts in bone tissue engineering. Proc Inst Mech Eng H 2010;224:1415-40.

53. Khan OF, Sefton MV. Endothelialized biomaterials for tissue engineering applications in vivo. Trends Biotechnol 2011;29:379-87.

54. Hendrickx B, Vranckx JJ, Luttun A. Cell-based vascularization strategies for skin tissue engineering. Tissue Eng Part B Rev 2011;17:13-24.

55. Lokmic Z, Mitchell GM. Engineering the microcirculation. Tissue Eng Part B Rev 2008;14:87-103.

56. Rao RR, Peterson AW, Ceccarelli J, Putnam AJ, Stegemann JP. Matrix composition regulates three-dimensional network formation by endothelial cells and mesenchymal stem cells in collagen/fibrin materials. Angiogenesis 2012;15:253-64.

57. Zhang G, Suggs LJ. Matrices and scaffolds for drug delivery in vascular tissue engineering. Adv Drug Deliv Rev 2007;59:360-73.

58. Nomi M, Atala A, Coppi PD, Soker S. Principals of neovascularization for tissue engineering. Mol Aspects Med 2002;23:463-83.

59. Kniazeva E, Putnam AJ. Endothelial cell traction and ECM density influence both capillary morphogenesis and maintenance in 3-D. Am J Physiol Cell Physiol 2009;297:C179-87.

60. Kachgal S, Carrion B, Janson IA, Putnam AJ. Bone marrow stromal cells stimulate an angiogenic program that requires endothelial MT1-MMP. J Cell Physiol 2012;227:3546-55.

61. Grainger SJ, Putnam AJ. Assessing the permeability of engineered capillary networks in a 3D culture. PLoS One 2011;6:e22086.

62. Davison PM, Bensch K, Karasek MA. Isolation and growth of endothelial cells from the microvessels of the newborn human foreskin in cell culture. J Invest Dermatol 1980;75:316-21.

63. Richard L, Velasco P, Detmar M. A simple immunomagnetic protocol for the selective isolation and long-term culture of human dermal microvascular endothelial cells. Exp Cell Res 1998;240:1-6.

64. Eckermann CW, Lehle K, Schmid SA, Wheatley DN, Kunz-Schughart LA. Characterization and modulation of fibroblast/endothelial cell co-cultures for the in vitro preformation of three-dimensional tubular networks. Cell Biol Int 2011;35:1097-110.

65. Nör JE, Peters MC, Christensen JB, Sutorik MM, Linn S, Khan MK, Addison CL, Mooney DJ, Polverini PJ. Engineering and characterization of functional human microvessels in immunodeficient mice. Lab Invest 2001;81:453-63.

66. Melero-Martin JM, Khan ZA, Picard A, Wu X, Paruchuri S, Bischoff J. In vivo vasculogenic potential of human blood-derived endothelial progenitor cells. Blood 2007;109:4761-8.

67. Young PP, Vaughan DE, Hatzopoulos AK. Biologic properties of endothelial progenitor cells and their potential for cell therapy. Prog Cardiovasc Dis 2007;49:421-9.

68. Au P, Daheron LM, Duda DG, Cohen KS, Tyrrell JA, Lanning RM, Fukumura D, Scadden DT, Jain RK. Differential in vivo potential of endothelial progenitor cells from human umbilical cord blood and adult peripheral blood to form functional long-lasting vessels. Blood 2008;111:1302-5.

69. Choong CS, Hutmacher DW, Triffitt JT. Co-culture of bone marrow fibroblasts and endothelial cells on modified polycaprolactone substrates for enhanced potentials in bone tissue engineering. Tissue Eng 2006;12:2521-31.

70. Correia C, Grayson W, Eton R, Gimble JM, Sousa RA, Reis RL, Vunjak-Novakovic G. Human adipose-derived cells can serve as a single-cell source for the in vitro cultivation of vascularized bone grafts. J Tissue Eng Regen Med 2012 (in press).

71. Zhang R, Gao Z, Geng W, Yan X, Chen F, Liu Y. Engineering vascularized bone graft with osteogenic and angiogenic lineage differentiated bone marrow mesenchymal stem cells. Artif Organs 2012;36:1036-46.

72. Villars F, Guillotin B, Amédée T, Dutoya S, Bordenave L, Bareille R, Amédée J. Effect of HUVEC on human osteoprogenitor cell differentiation needs heterotypic gap junction communication. Am J Physiol Cell Physiol 2002;282:C775-85.

73. Laranjeira MS, Fernandes MH, Monteiro FJ. Reciprocal induction of human dermal microvascular endothelial cells and human mesenchymal stem cells: time-dependent profile in a co-culture system. Cell Prolif 2012;45:320-34.

74. Wang J, Ye Y, Tian H, Yang S, Jin X, Tong W, Zhang Y. In vitro osteogenesis of human adipose-derived stem cells by coculture with human umbilical vein endothelial cells. Biochem Biophys Res Commun 2011;412:143-9.

75. Stahl A, Wenger A, Weber H, Stark GB, Augustin HG, Finkenzeller G. Bi-directional cell contact-dependent regulation of gene expression between endothelial cells and osteoblasts in a three-dimensional spheroidal coculture model. Biochem Biophys Res Commun 2004;322:684-92.

76. Hager S, Lampert FM, Orimo H, Stark GB, Finkenzeller G. Up-regulation of alkaline phosphatase expression in human primary osteoblasts by cocultivation with primary endothelial cells is mediated by p38 mitogen-activated protein kinase-dependent mRNA stabilization. Tissue Eng Part A 2009;15:3437-47.

77. Xue Y, Xing Z, Hellem S, Arvidson K, Mustafa K. Endothelial cells influence the osteogenic potential of bone marrow stromal cells. Biomed Eng Online 2009;8:34.

78. Guillotin B, Bareille R, Bourget C, Bordenave L, Amédée J. Interaction between human umbilical vein endothelial cells and human osteoprogenitors triggers pleiotropic effect that may support osteoblastic function. Bone 2008;42:1080-91.

79. Leszczynska J, Zyzynska-Granica B, Koziak K, Ruminski S, Lewandowska-Szumiel M. Contribution of endothelial cells to human bone-derived cells expansion in coculture. Tissue Eng Part A 2013;19:393-402.

80. Steiner D, Lampert F, Stark GB, Finkenzeller G. Effects of endothelial cells on proliferation and survival of human mesenchymal stem cells and primary osteoblasts. J Orthop Res 2012;30:1682-9.

81. Kaigler D, Krebsbach PH, Polverini PJ, Mooney DJ. Role of vascular endothelial growth factor in bone marrow stromal cell modulation of endothelial cells. Tissue Eng 2003;9:95-103.

82. Grellier M, Ferreira-Tojais N, Bourget C, Bareille R, Guillemot F, Amédée J. Role of vascular endothelial growth factor in the communication between human osteoprogenitors and endothelial cells. J Cell Biochem 2009;106:390-8.

83. Dohle E, Fuchs S, Kolbe M, Hofmann A, Schmidt H, Kirkpatrick CJ. Sonic hedgehog promotes angiogenesis and osteogenesis in a coculture system consisting of primary osteoblasts and outgrowth endothelial cells. Tissue Eng Part A 2010;16:1235-7.

84. Hoch AI, Binder BY, Genetos DC, Leach JK. Differentiation-dependent secretion of proangiogenic factors by mesenchymal stem cells. PLoS One 2012;7:e35579.

85. Bidarra SJ, Barrias CC, Barbosa MA, Soares R, Amédée J, Granja PL. Phenotypic and proliferative modulation of human mesenchymal stem cells via crosstalk with endothelial cells. Stem Cell Res 2011;7:186-97.

86. Ma J, van den Beucken JJ, Yang F, Both SK, Cui FZ, Pan J, Jansen JA. Coculture of osteoblasts and endothelial cells: optimization of culture medium and cell ratio. Tissue Eng Part C Methods 2011;17:349-57.

87. Kolbe M, Xiang Z, Dohle E, Tonak M, Kirkpatrick CJ, Fuchs S. Paracrine effects influenced by cell culture medium and consequences on microvessel-like structures in cocultures of mesenchymal stem cells and outgrowth endothelial cells. Tissue Eng Part A 2011;17:2199-212.

88. Pedersen TO, Blois AL, Xue Y, Xing Z, Cottler-Fox M, Fristad I, Leknes KN, Lorens JB, Mustafa K. Osteogenic stimulatory conditions enhance growth and maturation of endothelial cell microvascular networks in culture with mesenchymal stem cells. J Tissue Eng. 2012;3(1):2041731412443236.

89. Thébaud NB, Siadous R, Bareille R, Remy M, Daculsi R, Amédée J, Bordenave L. Whatever their differentiation status, human progenitor derived - or mature - endothelial cells induce osteoblastic differentiation of bone marrow stromal cells. J Tissue Eng Regen Med 2012;6:e51-60.

90. Saleh FA, Whyte M, Genever PG. Effects of endothelial cells on human mesenchymal stem cell activity in a three-dimensional in vitro model. Eur Cell Mater 2011;22:242-57.

91. Santos MI, Unger RE, Sousa RA, Reis RL, Kirkpatrick CJ. Crosstalk between osteoblasts and endothelial cells co-cultured on a polycaprolactone-starch scaffold and the in vitro development of vascularization. Biomaterials. 2009;30:4407-15.

92. Kang Y, Kim S, Fahrenholtz M, Khademhosseini A, Yang Y. Osteogenic and angiogenic potentials of monocultured and co-cultured human-bone-marrow-derived mesenchymal stem cells and human-umbilical-vein endothelial cells on three-dimensional porous beta-tricalcium phosphate scaffold. Acta Biomater 2013;9:4906-15.

93. Nukavarapu SP, Amini AR. Optimal scaffold design and effective progenitor cell identification for the regeneration of vascularized bone. Conf Proc IEEE Eng Med Biol Soc 2011;2011:2464-7.

94. Buschmann J, Welti M, Hemmi S, Neuenschwander P, Baltes C, Giovanoli P, Rudin M, Calcagni M. Three-dimensional co-cultures of osteoblasts and endothelial cells in DegraPol foam: histological and high-field magnetic resonance imaging analyses of pre-engineered capillary networks in bone grafts. Tissue Eng Part A 2011;17:291-9.

95. Kaigler D, Krebsbach PH, West ER, Horger K, Huang YC, Mooney DJ. Endothelial cell modulation of bone marrow stromal cell osteogenic potential. FASEB J 2005;19:665-7.

96. Correia C, Grayson WL, Park M, Hutton D, Zhou B, Guo XE, Niklason L, Sousa RA, Reis RL, Vunjak-Novakovic G. In vitro model of vascularized bone: synergizing vascular development and osteogenesis. PLoS One 2011;6:e28352.

97. Mendes LF, Pirraco RP, Szymczyk W, Frias AM, Santos TC, Reis RL, Marques AP. Perivascular-like cells contribute to the stability of the vascular network of osteogenic tissue formed from cell sheet-based constructs. PLoS One 2012;7:e41051.

98. Usami K, Mizuno H, Okada K, Narita Y, Aoki M, Kondo T, Mizuno D, Mase J, Nishiguchi H, Kagami H, Ueda M. Composite implantation of mesenchymal stem cells with endothelial progenitor cells enhances tissue-engineered bone formation. J Biomed Mater Res A 2009;90:730-41.

99. Geuze RE, Wegman F, Oner FC, Dhert WJ, Alblas J. Influence of endothelial progenitor cells and platelet gel on tissue-engineered bone ectopically in goats. Tissue Eng Part A 2009;15:3669-77.

100. Fedorovich NE, Haverslag RT, Dhert WJ, Alblas J. The role of endothelial progenitor cells in prevascularized bone tissue engineering: development of heterogeneous constructs. Tissue Eng Part A 2010;16:2355-67

101. Tsigkou O, Pomerantseva I, Spencer JA, Redondo PA, Hart AR, O'Doherty E, Lin Y, Friedrich CC, Daheron L, Lin CP, Sundback CA, Vacanti JP, Neville C. Engineered vascularized bone grafts. Proc Natl Acad Sci U S A 2010;107:3311-6.

102. Kaigler D, Krebsbach PH, Wang Z, West ER, Horger K, Mooney DJ. Transplanted endothelial cells enhance orthotopic bone regeneration. J Dent Res 2006;85:633-7.

103. Koob S, Torio-Padron N, Stark GB, Hannig C, Stankovic Z, Finkenzeller G. Bone formation and neovascularization mediated by mesenchymal stem cells and endothelial cells in critical-sized calvarial defects. Tissue Eng Part A 2011;17:311-21.

104. Kim JY, Jin GZ, Park IS, Kim JN, Chun SY, Park EK, Kim SY, Yoo J, Kim SH, Rhie JW, Cho DW. Evaluation of solid free-form fabrication-based scaffolds seeded with osteoblasts and human umbilical vein endothelial cells for use in vivo osteogenesis. Tissue Eng Part A 2010;16:2229-36.

105. He J, Decaris ML, Leach JK. Bioceramic-mediated trophic factor secretion by mesenchymal stem cells enhances in vitro endothelial cell persistence and in vivo angiogenesis. Tissue Eng Part A 2012;18:1520-28.

106. Grellier M, Granja PL, Fricain JC, Bidarra SJ, Renard M, Bareille R, Bourget C, Amédée J, Barbosa MA. The effect of the co-immobilization of human osteoprogenitors and endothelial cells within alginate microspheres on mineralization in a bone defect. Biomaterials 2009;30:3271-8.

107. Seebach C, Henrich D, Kähling C, Wilhelm K, Tami AE, Alini M, Marzi I. Endothelial progenitor cells and mesenchymal stem cells seeded onto beta-TCP granules enhance early vascularization and bone healing in a critical-sized bone defect in rats. Tissue Eng Part A 2010;16:1961-70.

CHAPTER 3

Osteogenic Differentiation of Adipose-derived and Marrow-derived Mesenchymal Stem Cells in Modular Protein/Ceramic Microenvironments

3.1 Introduction

Improved therapies for the regeneration of bone are needed to achieve full repair of recalcitrant and large fractures. Through the combination of cells, materials, and signaling molecules, tissue engineering aims to create biomimetic tissue constructs to both regenerate and replace damaged tissue [1]. Numerous sources of stem and progenitor cells [2] have been used in bone tissue engineering applications including embryonic [3], umbilical cord [4], and dental pulp [5]. However, bone marrow-derived mesenchymal stem cells (bmMSC) and adipose-derived stem cells (AdSC) [6] are the most commonly studied cell types for orthopaedic applications and both have demonstrated the ability to regenerate bone *in vivo* [7,8]. Further, both of these cell types has specific advantages in their use; bmMSC have been suggested to have immunomodulatory properties [9] and therefore can be used as an allogeneic source. AdSC have the advantage that they are an easily obtained autologous cell source [10]. A number of recent studies have directly compared the osteogenic potential of these two cell types, however the results are context-dependent and more work is needed to determine the utility of these cells in specific applications [11-15].

Natural biomaterials such as collagen [16-18], fibrin [19,20], and chitosan [21,22] have been proposed as osteoconductive materials for engineering and regenerating bone. Ceramics such as β-tricalcium phosphate [18], calcium carbonate [23], bioglass [24], or coatings created by simulated body fluid [25] have been combined with these materials to enhance the mechanical properties and osteoinductivity of the matrices. In particular, incorporation of hydroxyapatite (HA), the principal mineral component of native bone, has proven to be an effective strategy to provide stem cell-specific cues that aid in the formation of biomimetic composite structures for the engineering of bone [15, 27, 28].

Modular tissue engineering has emerged as a scheme for applying a "bottom-up" approach to fabricate engineered tissues [29]. Cell-seeded, modular hydrogel microenvironments ("microbeads") can be individually cultured, differentiated, and then later combined to create macroscopic tissue constructs with defined architecture. In bone tissue engineering, recent studies have used gelatin microcarriers to support osteogenic differentiation of human amniotic fluid mesenchymal stem cells which were then combined to create bone tissue constructs [30]. Other studies have used alginate microbeads to differentiate human embryonic stem cells towards the osteoblast lineage [31]. Previous work in our lab has used various natural biomaterials including chitosan, fibrin, collagen, and agarose to create cell-seeded microenvironments through a water-in-oil emulsion process [32-34]. Pure protein microbeads have been difficult to fabricate using this process because they are difficult to harvest and are fragile. To circumvent this issue, the collagen matrix can be supplemented with agarose to generate composite microbeads for osteogenic differentiation of encapsulated bmMSC [35]. However, the inclusion of agarose, a polysaccharide not found in bone, limits the application of such microbeads in bone repair.

In this study, we generated pure protein microbeads by combining collagen (COL) and fibrin (FIB) for bone repair applications. Particulate HA was also added to the microbeads to increase the density of microbead preparations, thereby facilitating harvesting during the production process. Our primary goal was to directly compare the osteogenic differentiation of bmMSC and AdSC in COL/FIB and COL/FIB/HA microbeads. These modular cell-based hydrogel microenvironments could provide utility in generating natural biomaterial based approaches to bone regeneration.

3.2 – Materials and Methods

Collagen/Fibrin Microbead Fabrication

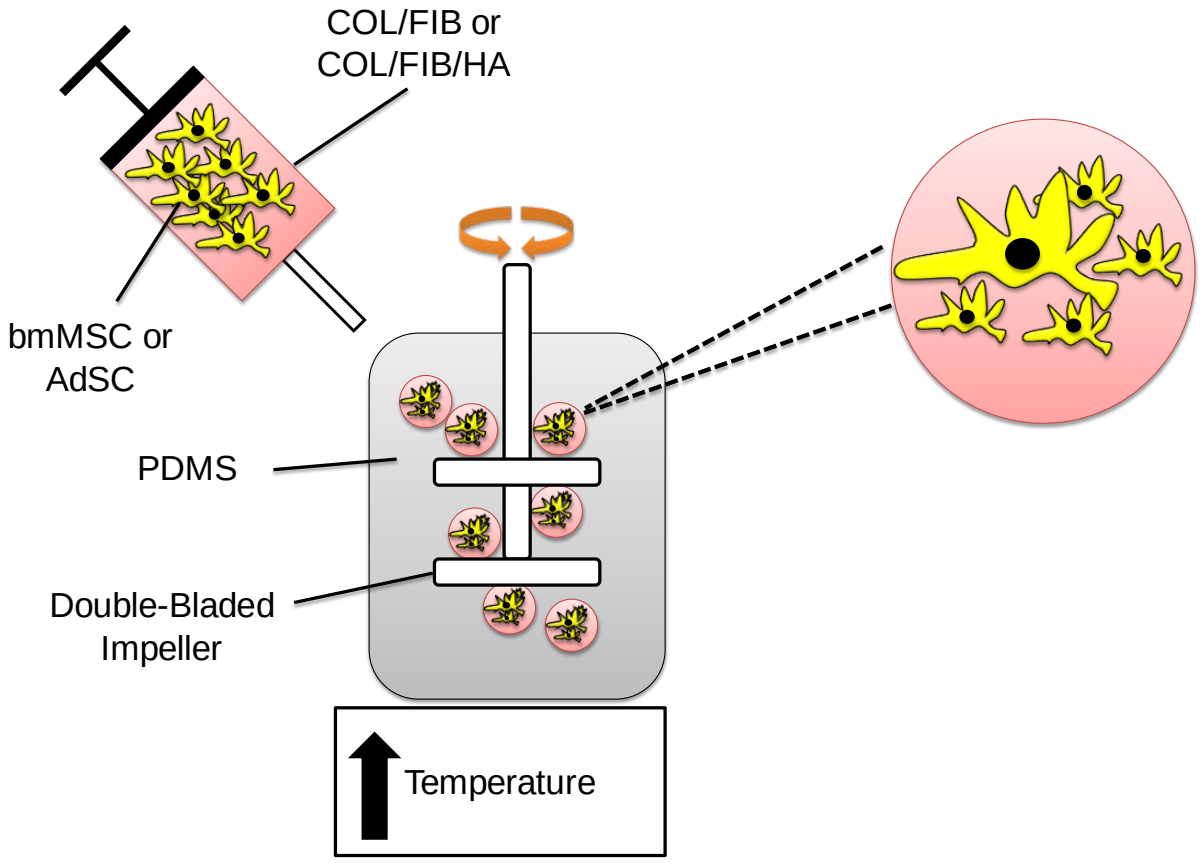

Figure 3.1 – Schematic of microbead fabrication process. COL/FIB and COL/FIB/HA microbeads were formed through a water-in-oil emulsification process which resulted in spheroidal cell-seeded hydrogel microenvironments.

Microbeads composed of 50/50 (mass ratio) collagen/fibrin (COL/FIB) were generated through a water-in-oil emulsion technique as shown in Figure 3.1. Bovine Type I COL (MP Biomedicals, Solon, OH, USA) was dissolved in 0.02 N acetic acid at a concentration of 4.0 mg/ml and bovine fibrinogen (Sigma Aldrich, St. Louis, MO USA) was dissolved at 4.0 mg/ml clottable protein in serum-free Dulbecco's modified Eagle's medium (DMEM; Thermo Scientific, Logan, UT, USA). COL (1.25 mg/ml) and FIB (1.25 mg/ml) were then added to a mixture containing 10% fetal bovine serum (FBS; Life Technologies, Grand Island, NY, USA), 10% 5X-concentrated DMEM (starting concentration), 5% 0.1 N sodium hydroxide (NaOH), 2% bovine thrombin (1 UT/ml; Sigma), and 1 mM glyoxal (Sigma) at 4°C. The remaining volume For HA-containing microbeads, 2.5 mg/ml of HA in 1X DMEM was sonicated for 1 hour prior to incorporation to ensure homogenous distribution throughout the microbeads [36]. The HA was then added directly into the pre-gel mixture.

The pre-gel mixture was then quickly pipetted into a pre-cooled bath of 100 cSt polydimethylsiloxane (PDMS; Xiameter, Dow Corning, Midland, MI) and stirred with a double-bladed impeller set at 700 RPM. After 5 minutes of mixing at 0°C, the temperature was then raised to 37°C to initiate co-polymerization and gelation of the COL and FIB. Microbeads were collected from the oil phase by centrifuging the mixture at 200X g and washing three times for 10 minutes per wash with phosphate buffered saline (PBS; Life Technologies) containing Pluronic L101 (BASF, Florham Park, NJ, USA) in order to separate the beads from the oil phase and remove excess oil.

Microbead Imaging, Size and Size Distribution Quantification

For light microscopy imaging, microbeads were stained with EZBlue Coomasie reagent overnight and imaged with an Olympus IX15 Microscope system (Olympus America, Center

Valley, PA, USA). Confocal reflectance microscopy using a laser scanning microscope (Olympus) was used to acquire images of the microbead architecture. Microbead diameter was analyzed using ImageJ software (National Institute of Health, Bethesda, MD, USA) and size and size distribution of the microbeads were quantified.

Cell Culture

Human marrow-derived mesenchymal stem cells (bmMSC; Lonza Inc., Walkersville, MD, USA) and human adipose-derived stem cells (AdSC; Lonza) were grown in Minimum Essential Medium Alpha (αMEM) supplemented with 10% bmMSC-Qualified FBS and 1% penicillin/streptomyocin (Life Technologies). bmMSC were used at passage 6 and AdSC were used at passage 5, corresponding to two subculture periods after arrival. Cells were added directly into the pre-gel mix at a concentration of 1.0 X 10^6 cells/ml to promote even cell distribution throughout the beads. Microbeads were cultured statically in 15 ml centrifuge tubes (Corning Incorporated, Corning, NY, USA) with 3 ml of media.

Cell Viability Studies

Cell viability was assessed using a vital stain kit (Live/Dead®, Life Technologies). At days 1 and 7, cell-seeded microbeads were collected and washed three times in sterile PBS for 10 min/wash. Microbeads were then incubated in a solution containing 4.0 μm calcein-AM and 4.0 μm ethidium homodimer-1 in PBS at 37°C for 35 min. Microbeads were again washed three times in PBS, and then imaged using a laser scanning confocal microscope (Olympus). Percent viability was calculated by comparing the total green-stained cells (live) to the total red-stained cells (dead).

Osteogenic Differentiation

For osteogenic studies, cell-seeded microbeads were cultured in either complete medium (growth) or osteogenic medium composed of complete medium supplemented with 10 mM β-glycerophosphate (Sigma), 50 µg/ml ascorbic acid 2-phosphate (Sigma), and 100 nM dexamethasone (Sigma) for 14 days. Microbead samples were collected at days 1, 3, 7, and 14 and flash-frozen in in liquid N_2 and stored at -80°C. To analyze cell proliferation and alkaline phosphatase (ALP) activity, microbeads were dissolved overnight in 10 mM Tris-HCl (Sigma) containing 0.6 mg/ml collagenase Type I (MP Biomedicals), 0.2% IGEPAL (Sigma), and 2 mM phenylmethanesulfonylfluoride (Sigma). DNA content was then assessed using a commercially available DNA assay (PicoGreen®, Life Technologies). Alkaline phosphatase activity was quantified by adding 20 µl of the sample lysate to a 100 µl of 0.5 M 2-amino-2-methyl-1-popanol (Sigma) with 5.0 mM p-nitrophenol phosphate substrate (Sigma) at a pH of 10.3 and read spectrophotometrically at 405 nm [22]. Total calcium secretion was analyzed using the OCPC method as described [36]. Briefly, microbead samples were dissolved overnight in 1.0 N acetic acid and 10 µl of the sample was incubated in 0.05 mg/ml of OCPC solution in ethanolamine, boric acid, and 8-hydroxyquinoline buffer (Sigma) for 10 min. Samples were read against a standard curve with known calcium values at 565 nm.

Statistical Analysis

All values are represented as mean +/- standard deviation. N = 4 independent samples were used for the osteogenic differentiation studies. DNA content and calcium secretion data were normalized to day 1 values from within each condition. A one-way analysis of variance test

(ANOVA) and a two-way ANOVA with a Tukey's post hoc analysis were used to determine significance between conditions and groups. A value of $p < 0.05$ was used to determine statistical significance.

3.3 - Results

Acellular Microbead Morphology, Size, and Size Distribution

Figure 3.2 depicts acellular COL/FIB microbeads directly after fabrication and shows their regular spheroidal morphology (panels A-D). Coomasie staining allowed for visualization of microbeads under light microscopy, and microbeads containing HA were dark due to the attenuation of light passing through the microbeads. Hydroxyapatite remained well-dispersed and homogeneous throughout the microbeads. Confocal reflectance imaging allowed for the visualization of the microbead architecture (panels E, F). COL/FIB microbeads exhibited a fibrillar structure whereas the COL/FIB/HA microbeads was observed to have homogenous distribution of hydroxyapatite throughout and within its fibrillar structure. The addition of HA did not significantly affect the average size of the microbead populations, and both had an average diameter of approximately 130 +/- 25 μm, with a relatively narrow size distribution (panels G, H)

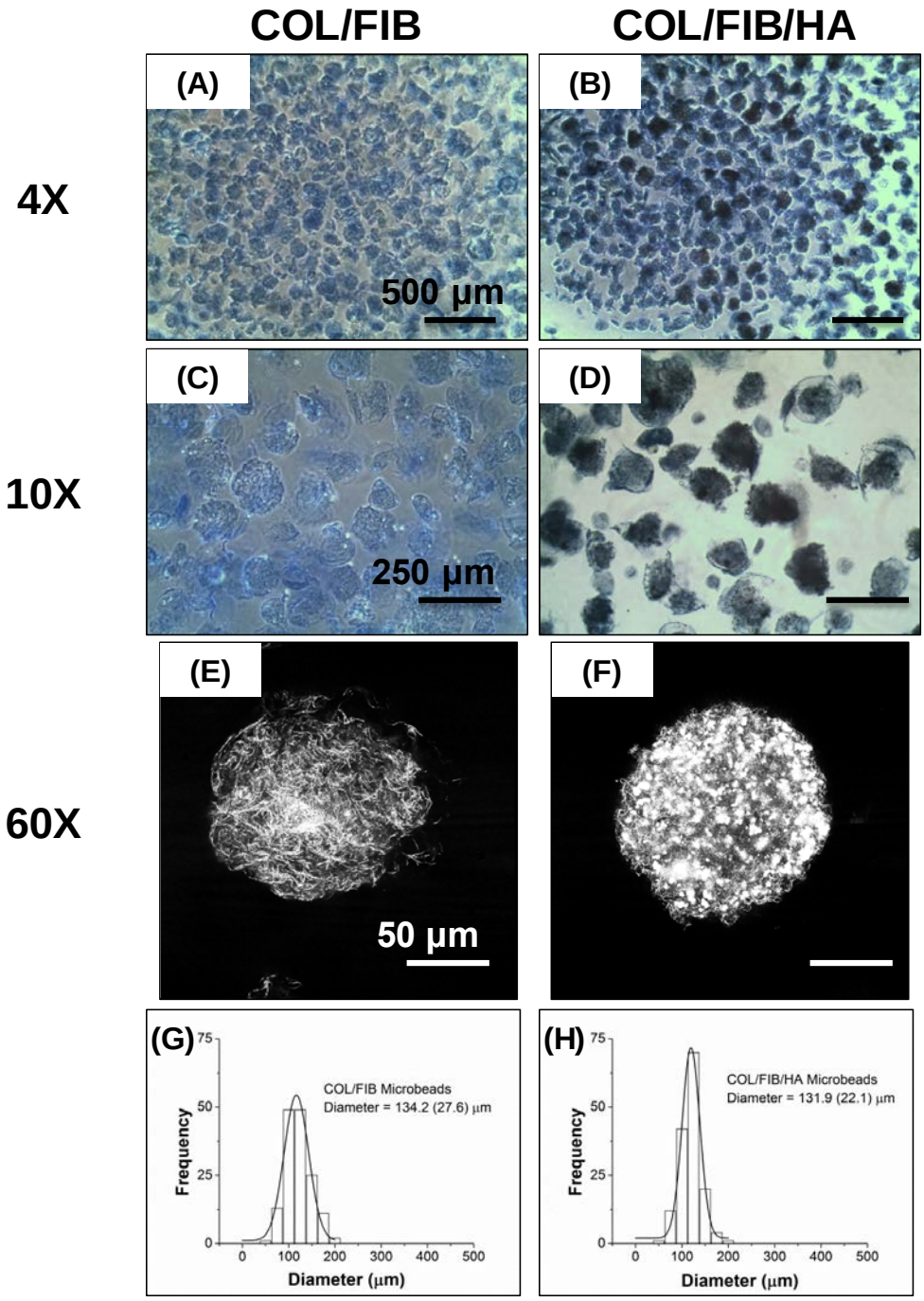

Figure 3.2 – Morphology and size distribution of acellular microbeads. Coomasie Blue staining allowed for visualization of microbeads under light microscopy (A-D). Microbeads that formed were spherical. Images of the matrix microarchitecture of microbeads obtained through confocal reflectance microscopy (E,F). Confocal reflectance imaging demonstrated the fibrillar nature of the COL/FIB microbeads and homogenous dispersion of the HA throughout the microbeads. Histograms of the size distribution of microbeads (G,H). The size and size distribution did not change with the addition of HA into the microbeads. Scale bar = 500 µm (A,B), 250 µm (C,D), 50 µm (E,F).

Cell Viability

Cell viability of bmMSC or AdSC in COL/FIB or COL/FIB/HA beads was assessed at days 1 and 7, and vital staining of microbeads is shown in Figure 3.3. Viability remained high (>90%) at both time points in all conditions as seen by the abundant green staining and low red staining. By day 7, the morphology of the embedded cells began to change as they spread throughout both the matrix and mineral phases of the microbeads.

Confocal Reflectance Imaging of Cell-Seeded Microbeads

Characterization of matrix architecture was performed using confocal reflectance microscopy, as shown in the representative imaged in Figure 3.4. Changes in matrix architecture in cell-seeded microbeads were tracked over a 7 day culture period. At day 1, individual fibers were visible within the collagen/fibrin microbeads. However, by day 7, both COL/FIB and COL/FIB/HA microbeads became denser and the fibrillar structure of the matrix was less evident. The mineral phase could be discerned in HA-containing microbeads, but did not change over the 7 day culture period.

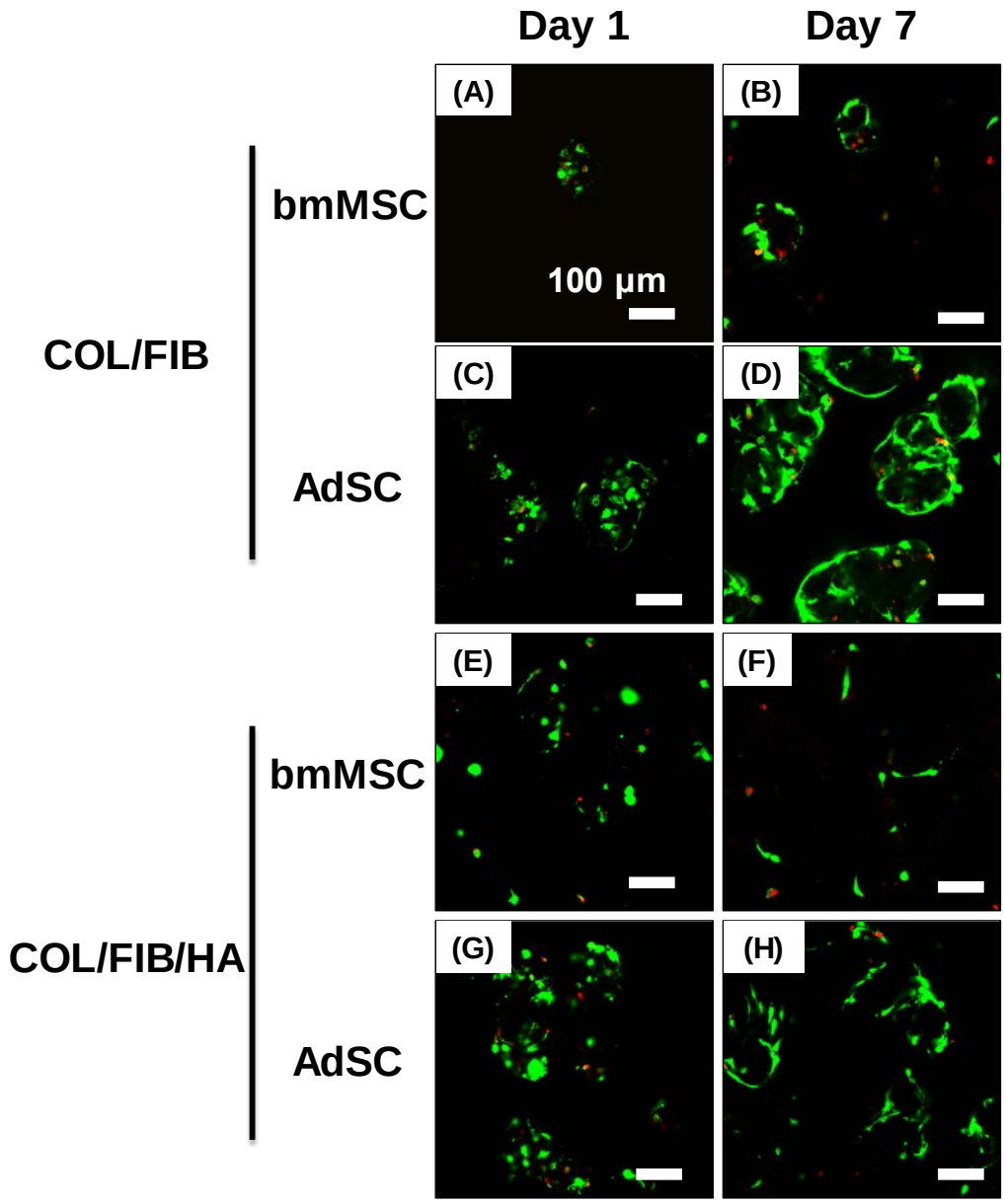

Figure 3.3 – Cell viability of bmMSC or AdSC in COL/FIB or COL/FIB/HA microbeads at days 1 and 7. High viability (green staining) was observed in all conditions at all time points. bmMSC COL/FIB (A,B), AdSC COL/FIB (C,D), bmMSC COL/FIB/HA (E,F), AdSC COL/FIB/HA (G,H). Scale bar = 100 µm.

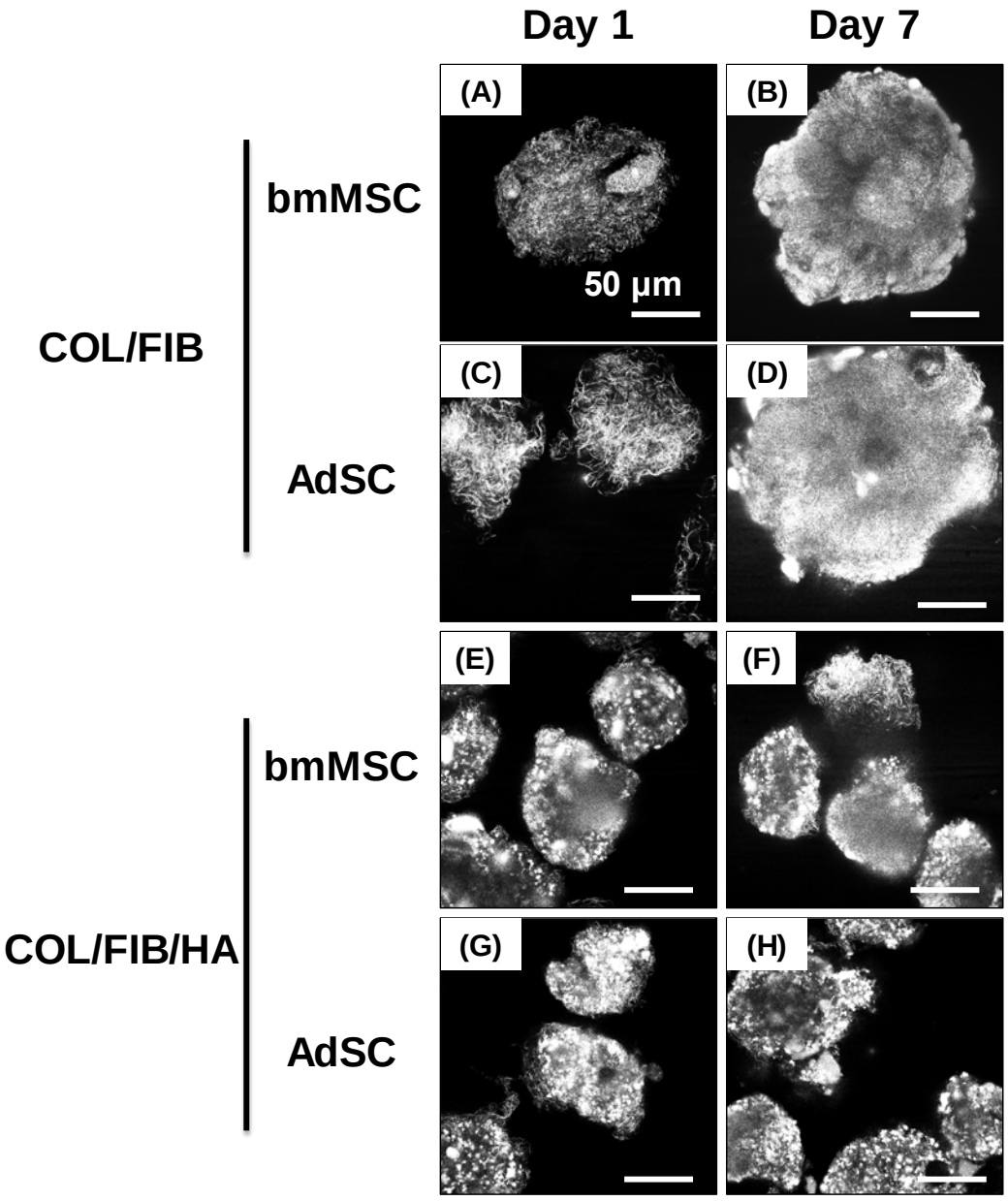

Figure 3.4 – Confocal reflectance imaging of bmMSC or AdSC in COL/FIB or COL/FIB/HA microbeads at days 1 and 7. The fibrillar nature of the cell-seeded COL/FIB microbeads was visible after 1 day of culture. COL/FIB microbeads aggregated and the fibrillar structure was less visible after 7 days in culture. HA remained evenly dispersed for 7 days in cell-seeded COL/FIB/HA microbeads. bmMSC COL/FIB (A,B), AdSC COL/FIB (C,D), bmMSC COL/FIB/HA (E,F), AdSC COL/FIB/HA (G,H). Scale bar = 50 µm.

Osteogenic Differentiation

Figure 3.5 shows DNA, ALP, and calcium secretion data for both bmMSC and AdSC in COL/FIB and COL/FIB/HA microbeads after 14 days in either growth or osteogenic media. In

growth medium, there were no significant differences in DNA content at day 7; however, the bmMSC COL/FIB/HA group exhibited significantly higher DNA content compared to the other conditions at day 14. In osteogenic media, the AdSC COL/FIB group showed higher DNA content relative to the other conditions at day 7; however, there were no significant differences at day 14.

ALP activity in microbeads was significantly higher at day 3 in the bmMSC COL/FIB/HA formulation compared to the bmMSC COL/FIB microbeads. The bmMSC COL/FIB/HA microbeads showed significantly higher ALP activity when cultured in osteogenic media, as compared to growth media. Both AdSC COL/FIB and bmMSC COL/FIB/HA had statistically greater ALP activity than the bmMSC COL/FIB microbeads when cultured in osteogenic media.

Calcium deposition markedly increased at day 14 in both the bmMSC COL/FIB and AdSC COL/FIB microbeads in osteogenic media, relative to microbeads cultured in growth media. However, there were no significant differences in calcium deposition between any of the conditions in osteogenic media at day 14.

A full list of the statistical results generated from two-way ANOVA analyses is provided in the tables in Figure 3.6.

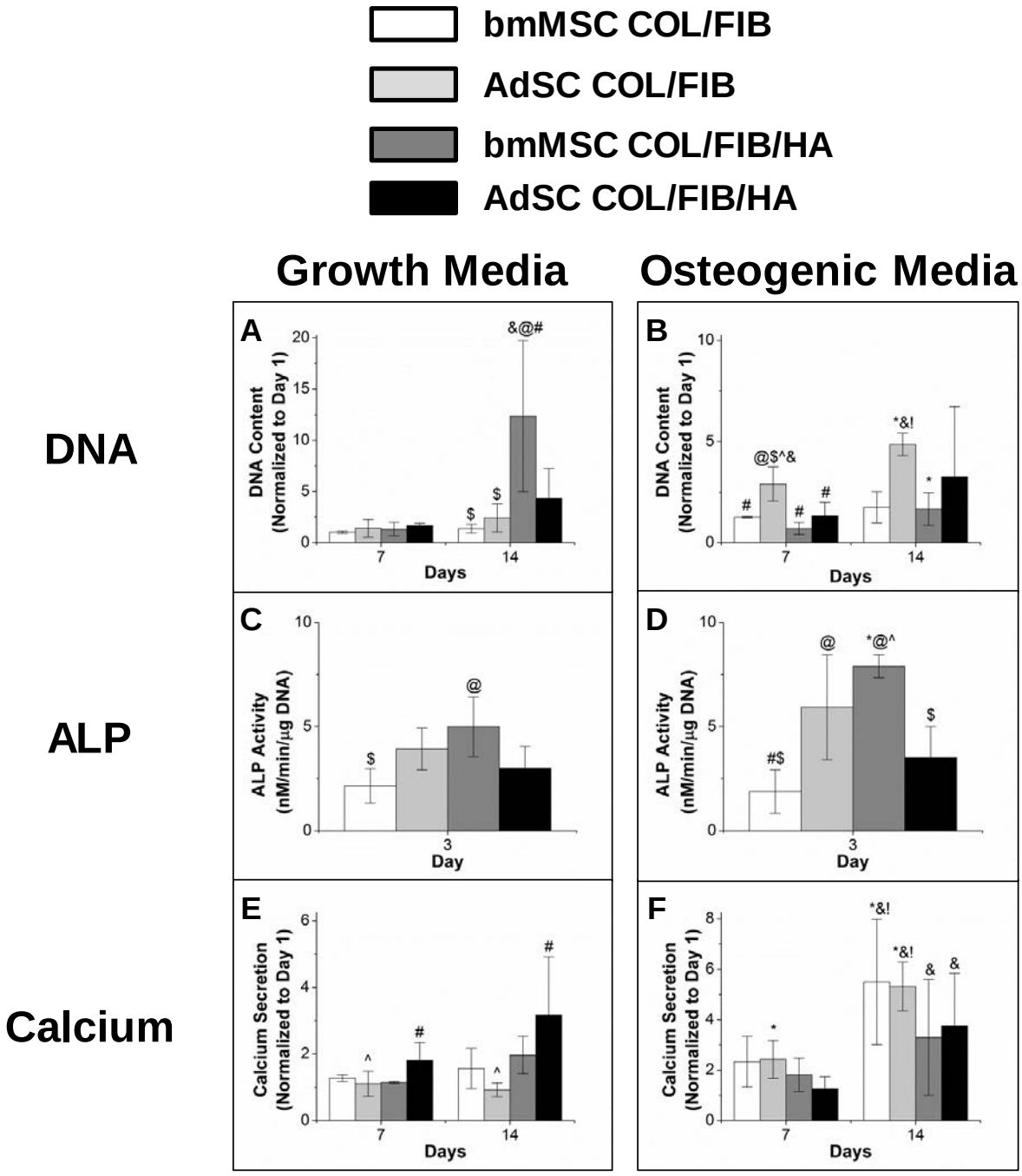

Figure 3.5 – Cell function and osteogegenic differentiation in microbeads. DNA Content in growth Media (A) and osteogenic media (B), alkaline phosphatase activity in growth media (C) and osteogenic media (D), and calcium secretion in growth media (E) and ostegenic media (F). (*) denotes statistical significance against growth condition. (@) denotes statistical significance against MSC COL/FIB. (#) denotes statistical significance against ASC COL/FIB. ($) denotes statistical significance against MSC COL/FIB/HA. (^) denotes statistical significance against ASC COL/FIB/HA. (&) denotes statistical significance against Day 1. (!) denotes statistical significance against Day 7.

DNA	*Day 7*		*Day 14*	
	Significant	p value	Significant	p value
bmMSC vs. AdSC	X	0.001		0.671
Growth vs. Osteo		0.460		0.128
COL/FIB vs. COL/FIB/HA		0.110		0.057

ALP	*Day 3*	
	Significant	p value
bmMSC vs. AdSC		0.656
Growth vs. Osteo		0.057
COL/FIB vs. COL/FIB/HA		0.087

Calcium	*Day 7*		*Day 14*	
	Significant	p value	Significant	p value
bmMSC vs. AdSC		0.962		0.710
Growth vs. Osteo	X	0.014	X	0.0003
COL/FIB vs. COL/FIB/HA		0.247		0.663

Figure 3.6 – Two-way Analysis of Variance (ANOVA) results.

3.4 - Discussion

This study has demonstrated that a simple water-in-oil emulsion process can be used to create modular microenvironments consisting of native extracellular matrix proteins supplemented with a ceramic phase. The addition of hydroxyapatite into the microbeads increased the yield that was harvested, but did not alter the size or size distribution of the microbeads. COL/FIB and COL/FIB/HA microbeads were spheroidal and approximately 130 µm +/- 25 µm in diameter. In this range of microbead sizes, a defined number of cells can be encapsulated within each bead, but cells can also spread and interact with the microbead matrix.

Further, this size allows sufficient mass transfer through the microbead matrix to the embedded cells, since the maximum diffusion path for nutrients through tissues has been suggested to be only 150-200 μm [37]. Although not explored in this study, the microbead size and distribution can be controlled by modulating the impeller speed, oil viscosity and other fabrication process parameters [32,33].

Analysis of cell viability showed that both bmMSC and AdSC survived the embedding process and remained viable over at least a week in culture. Furthermore, after 7 days both bmMSC and AdSC exhibited a spread morphology indicating that they associated with the COL and FIB extracellular matrix components. Inclusion of HA in the microbeads did not alter either cell type's viability or morphology. In addition, confocal reflectance microscopy allowed the microarchitecture of microbeads to be visualized. The fibrillar structure of the microbeads became denser over time, suggesting that the microbeads were compacted by the embedded cells, a phenomenon that is commonly observed when cells are seeded within natural biomaterials [38]. Taken together, these findings suggest that the microbead environment is conducive to maintenance of living cells and allows them to retain their active functions.

Comparison of bmMSC and AdSC osteogenic differentiation in COL/FIB and COL/FIB/HA microbeads suggested that theses cell types are mostly similar in their responses. Two-way ANOVA found no significant differences between AdSC and bmMSC in their DNA content, ALP activity, or calcium secretion over two weeks of culture in either growth or osteogenic media. Moreover, we did not observe any significant differences between the COL/FIB and COL/FIB/HA matrices in any of the assays, indicating that the addition of HA did not cause any detrimental effects to stem cell differentiation throughout the culture period. ALP activity, an early osteogenic marker, was somewhat elevated in the bmMSC COL/FIB/HA

group, suggesting potential osteoinductive effects of the COL/FIB microbeads. Calcium secretion, a late osteogenic marker, increased in both bmMSC and AdSC in COL/FIB microbeads in osteogenic media compared to growth media. There were no differences in calcium secretion of either bmMSC or AdSC in COL/FIB/HA microbeads in the two media types, presumably because these matrices already contained a large amount of exogenous mineral [39].

The modular microbead technology we have demonstrated is aimed at developing new minimally invasive techniques for bone repair. Fabrication of microbeads can be easily scaled up to create larger populations of microbeads in a controlled batch process. Cell-seeded microbeads can be pre-differentiated towards the osteogenic phenotype, collected, concentrated into a paste, and then injected into a defect site in a minimally invasive manner. The advantages of such a cell-based therapy are particularly important in treating recalcitrant bone wounds and non-unions, where the delivery of appropriately functional cells may be a key to achieving regeneration.

3.5 - References

1. Langer R, Vacanti JP. Tissue engineering. Science 260, 920, 1993.

2. Szpalski C, Barbaro M, Sagebin F, Warren SM. Bone Tissue Engineering: Current Strategies and Techniques-Part II: Cell Types. Tissue Eng Part B Rev 18, 258, 2012.

3. Domev H, Amit M, Laevsky I, Dar A, Itskovitz-Eldor J. Efficient Engineering of Vascularized Ectopic Bone from Human Embryonic Stem Cell-Derived Mesenchymal Stem Cells. Tissue Eng Part A 2012.

4. Thein-Han W, Xu HH. Collagen-calcium phosphate cement scaffolds seeded with umbilical cord stem cells for bone tissue engineering. Tissue Eng Part A 17, 2943, 2011.

5. Atari M, Caballé-Serrano J, Gil-Recio C, Giner-Delgado C, Martínez-Sarrà E, García-Fernández DA, Barajas M, Hernández-Alfaro F, Ferrés-Padró E, Giner-Tarrida L. The enhancement of osteogenesis through the use of dental pulp pluripotent stem cells in 3D. Bone 50, 930, 2012.

6. Lee K, Chan CK, Patil N, Goodman SB. Cell therapy for bone regeneration--bench to bedside. J Biomed Mater Res B Appl Biomater 89, 252, 2009.

7. Wang J, Yang Q, Mao C, Zhang S. Osteogenic differentiation of bone marrow mesenchymal stem cells on the collagen/silk fibroin bi-template-induced biomimetic bone substitutes. J Biomed Mater Res A 2012.

8. Hattori H, Masuoka K, Sato M, Ishihara M, Asazuma T, Takase B, Kikuchi M, Nemoto K, Ishihara M. Bone formation using human adipose tissue-derived stromal cells and a biodegradable scaffold. J Biomed Mater Res B Appl Biomater 76, 230, 2006.

9. English K, Mahon BP. Allogeneic mesenchymal stem cells: agents of immune modulation. J Cell Biochem 8, 1963, 2011.

10. Gir P, Oni G, Brown SA, Mojallal A, Rohrich RJ. Human adipose stem cells: current clinical applications. Plast Reconstr Surg 129, 1277, 2012.

11. Strioga M, Viswanathan S, Darinskas A, Slaby O, Michalek J. Same or Not the Same? Comparison of Adipose Tissue-Derived Versus Bone Marrow-Derived Mesenchymal Stem and Stromal Cells. Stem Cells Dev 2012.

12. Shafiee A, Seyedjafari E, Soleimani M, Ahmadbeigi N, Dinarvand P, Ghaemi N. A comparison between osteogenic differentiation of human unrestricted somatic stem cells and mesenchymal stem cells from bone marrow and adipose tissue. Biotechnol Lett 33, 1257, 2011.

13. Miyazaki M, Zuk PA, Zou J, Yoon SH, Wei F, Morishita Y, Sintuu C, Wang JC. Comparison of human mesenchymal stem cells derived from adipose tissue and bone marrow for ex vivo gene therapy in rat spinal fusion model. Spine 33, 863, 2008.

14. Noël D, Caton D, Roche S, Bony C, Lehmann S, Casteilla L, Jorgensen C, Cousin B. Cell specific differences between human adipose-derived and mesenchymal-stromal cells despite similar differentiation potentials. Exp Cell Res 314, 1575, 2008.

15. De Ugarte DA, Morizono K, Elbarbary A, Alfonso Z, Zuk PA, Zhu M, Dragoo JL, Ashjian P, Thomas B, Benhaim P, Chen I, Fraser J, Hedrick MH. Comparison of multi-lineage cells from human adipose tissue and bone marrow. Cells Tissues Organs 174, 101, 2003.

16. Gao TJ, Lindholm TS, Kommonen B, Ragini P, Paronzini A, Lindholm TC.Enhanced healing of segmental tibial defects in sheep by a composite bone substitute composed of tricalcium phosphate cylinder, bone morphogenetic protein, and type IV collagen. J Biomed Mater Res 32, 505, 1996.

17. Jégoux F, Goyenvalle E, Cognet R, Malard O, Moreau F, Daculsi G, et al. Reconstruction of irradiated bone segmental defects with a biomaterial associating MBCP+®, microstructured collagen membrane and total bone marrow grafting: An experimental study in rabbits. Journal of Biomedical Materials Research Part A 91A, 1160, 2009.

18. Guda T, Walker JA, Singleton BM, Hernandez JW, Son JS, Kim SG, Oh DS, Appleford M, Ong JL, Wenke JC. Guided bone regeneration in long bone defects with a structural hydroxyapatite graft and collagen membrane. Tissue Eng Part A 2012.

19. Le Nihouannen D, Saffarzadeh A, Aguado E, Goyenvalle E, Gauthier O, et al. Osteogenic properties of calcium phosphate ceramics and fibrin glue based composites. J Mater Sci Mater Med 18, 225, 2007.

20. Davis HE, Miller SL, Case EM, Leach JK. Supplementation of fibrin gels with sodium chloride enhances physical properties and ensuing osteogenic response. Acta Biomater 7, 691, 2011.

21. Muzzarelli RA, Biagini G, Bellardini M, Simonelli L, Castaldini C, Fratto G. Osteoconduction exerted by methylpyrolidinone chitosan in dental surgery. Biomaterials 14, 39, 1993

22. Wang L, Stegemann JP. Glyoxal crosslinking of cell-seeded chitosan/collagen hydrogels for bone regeneration. Acta Biomater 7, 2410, 2011.

23. Koo KT, Polimeni G, Qahash M, Kim CK, Wikesjö UM.Periodontal repair in dogs: guided tissue regeneration enhances bone formation in sites implanted with a coral-derived calcium carbonate biomaterial. J Clin Periodontol 32,104, 2005.

24. Jones JR. Review of bioactive glass- from Hench to hybrids. Acta Biomater 2012.

25. Rao RR, He J, Leach JK. Biomineralized composite substrates increase gene expression with nonviral delivery. J Biomed Mater Res A 94, 344, 2010.

26. Hunter KT, Ma T. In vitro evaluation of hydroxyapatite-chitosan-gelatin composite membrane in guided tissue regeneration. J Biomed Mater Res A 2012

27. Gleeson JP, Plunkett NA, O'Brien FJ. Addition of hydroxyapatite improves stiffness, interconnectivity and osteogenic potential of a highly porous collagen-based scaffold for bone tissue regeneration. Eur Cell Mater. 20, 218, 2010.

28. Yoshikawa H, Myoui A. Bone tissue engineering with porous hydroxyapatite ceramics. J Artif Organs 8,131, 2005.

29. Nichol JW, Khademhosseini A. Modular Tissue Engineering: Engineering Biological Tissues from the Bottom Up. Soft Matter 5, 1312, 2009.

30. Chen M, Wang X, Ye Z, Zhang Y, Zhou Y, Tan WS. A modular approach to the engineering of a centimeter-sized bone tissue construct with human amniotic mesenchymal stem cells-laden microcarriers. Biomaterials 32, 7532, 2011.

31. Tang M, Chen W, Weir MD, Thein-Han W, Xu HH. Human embryonic stem cell encapsulation in alginate microbeads in macroporous calcium phosphate cement for bone tissue engineering. Acta Biomater 8, 3436, 2012.

32. Chen Z, Wang L, Stegemann JP. Phase-separated chitosan-fibrin microbeads for cell delivery. J Microencapsul 28, 344, 2011.

33. Batorsky A, Liao J, Lund AW, Plopper GE, Stegemann JP. Encapsulation of adult human mesenchymal stem cells within collagen-agarose microenvironments. Biotechnol Bioeng 92, 492, 2005.

34. Wang L, Rao RR, Stegemann JP. Matrix-Enhanced Stem Cells Embedded in Chitosan-Collagen Microbeads. Cells, Tissues, Organs 2012 (Submitted)

35. Lund AW, Bush JA, Plopper GE, Stegemann JP. Osteogenic differentiation of mesenchymal stem cells in defined protein beads. J Biomed Mater Res B Appl Biomater 87, 213, 2008.

36. Gudur M, Rao RR, Hsiao YS, Peterson AW, Deng CX, Stegemann JP. Noninvasive, Quantitative, Spatiotemporal Characterization of Mineralization in Three-Dimensional Collagen Hydrogels Using High-Resolution Spectral Ultrasound Imaging. Tissue Eng Part C 18, 935, 2012.

37. Novosel EC, Kleinhans C, Kluger PJ. Vascularization is the key challenge in tissue engineering. Adv Drug Deliv Rev 63, 300, 2011.

38. Fernandez P, Bausch AR. The compaction of gels by cells: a case of collective mechanical activity. Integr Biol (Camb) 1, 252, 2009.

39. Davis HE, Rao RR, He J, Leach JK. Biomimetic scaffolds fabricated from apatite-coated polymer microspheres. J Biomed Mater Res A 90, 1021, 2009.

CHAPTER 4

Matrix Composition Regulates Three-Dimensional Network Formation by Endothelial Cells and Mesenchymal Stem Cells in Collagen/Fibrin Materials

4.1 Introduction

Angiogenesis and vasculogenesis are biological processes that are vital to developing and regenerating tissues [1]. Vasculogenesis is the *de novo* formation of neovessels through the assembly of endothelial cells into a tube, followed by stabilization and maturation into a blood vessel. Angiogenesis creates new vessels via the sprouting of new capillaries from existing vasculature. When tissues are transplanted, these processes are critical in enabling the transport of nutrients and waste products and achieving integration of the transplanted tissue with the host vasculature [2, 3]. The field of tissue engineering has encountered a particular challenge in creating large tissue constructs that can be transplanted without subsequent loss of tissue viability, since the limit of effective diffusive transport has been suggested to be only 150-200 μm [4]. The interior regions of large implanted tissues therefore become necrotic due to the lack of a functional vascular supply to provide convective transport [5]. Stimulating the rapid creation of a functional vascular supply by either vasculogenesis or angiogenesis is a key to maintaining tissue viability post-implantation [6].

A number of experimental investigations have demonstrated that important aspects of vasculogenesis can be recapitulated in vitro [7-9]. Recent studies have focused on the

interactions of human umbilical vein endothelial cells (HUVEC) with stromal cells in generating vessel-like structures [10-12]. In such co-culture systems, stromal cells have been suggested to act as pericytes that provide paracrine factors to induce the formation of vessel structures and also stabilize neovessels by providing mechanical support [13, 14]. In vivo evidence suggests that the lack of a stromal cell component leads to pathological vessel formation characterized by hyperplasia and irregular HUVEC morphology [15, 16].

Co-cultures of HUVEC and bone marrow-derived mesenchymal stem cells (bmMSC) have been used as a model of vasculogenesis and it has been shown that bmMSC can function as pericytes to promote vessel formation and maturation [17-19]. In this role, bmMSC secrete specific pro-angiogenic cytokines [20, 21] and control the permeability of neovessels through regulation of cell-cell adherens junctions [22, 23]. The ratio of HUVEC to bmMSC has been shown to affect cell function and capillary morphogenesis. Lower HUVEC:bmMSC ratios have been associated with higher cell metabolic activity in vitro, though higher ratios increase the proportion of CD31+ cells [24]. In vivo, lower ratios have been associated with an increased vasculogenic response [25], and functional prevascular networks have been observed in vivo at even very low (2:99) ratios [26]. Although the effect of HUVEC:bmMSC ratio is not yet clear, it is likely to be one of the contributing factors in determining the rate and degree of vasculogenesis.

Vasculogenesis has been studied in a variety of extracellular matrix systems in vitro. Collagen and fibrin are of particular interest in this context because of their prominent role as wound healing proteins [27, 28]. Studies in which collagen and fibrin were combined as composite matrices have suggested that collagen delays neovessel formation in a dose-dependent manner [29]. Previous work in our lab has shown that collagen/fibrin composite materials have

mechanical properties distinct from either of the pure components alone, even at equivalent total protein concentrations [30, 31]. The effects of matrix concentration and stiffness on capillary morphogenesis have recently been investigated using pure extracellular matrix components of different compositions and stiffness [32-34]. These studies have shown that the degree of vascularization can be modulated by the properties of the surrounding matrix, and have suggested an inverse relationship between matrix stiffness and the degree of neovessel formation.

In the present study, we systematically examined vasculogenesis by HUVEC-bmMSC co-cultures in vitro using well defined three-dimensional (3D) matrices made of collagen and fibrin. Our goal was to determine the relative role of cell ratio and matrix composition in a controlled environment that incorporated both pure and composite formulations of matrix proteins of relevance in wound healing. In particular, we varied the HUVEC:bmMSC ratio and the collagen/fibrin proportion of the surrounding matrix and quantified the degree of vessel-like structure formation. The mechanical properties of the extracellular matrices were assessed using rheometry to provide measures of the stiffness of the matrix. Our findings demonstrate that collagen/fibrin matrices supported vasculogenesis in vitro, but the degree of vessel-like structure formation was dependent on matrix composition. Further experiments in which matrix mechanical properties were varied revealed a clear correlation between matrix stiffness and the degree of vasculogenesis. These studies highlight key features of the extracellular milieu that regulate neovessel formation, which may provide insight into the biological process of vasculogenesis. In addition this knowledge may be applied to promoting neovascularization of transplanted tissues.

4.2 – Materials and Methods

Cell Culture

Human bone marrow-derived mesenchymal stem cells (bmMSC; Lonza Inc., Walkersville, MD) were cultured in Dulbecco's modified Eagle's medium (low glucose DMEM; Thermo Scientific; Logan, UT) supplemented with 10% bmMSC-qualified fetal bovine serum (FBS; Invitrogen, Carlsbad, CA) and 1% penicillin and streptomyocin (PS; Invitrogen). bmMSC were used between passages 6-8. Media was changed every other day.

Human umbilical vein endothelial cells (HUVEC) were isolated from harvested umbilical cords as previously described [20]. Briefly, umbilical veins were irrigated with sterile phosphate buffered saline (PBS) and then incubated with 0.1% collagenase (Type I, Worthington Biochemical, Lakewood, NJ) at 37°C for 20 min. The digestion product was collected, the vein was washed with PBS, and the resulting suspension was centrifuged. The cell pellet was re-suspended in Endothelial Growth Medium-2 (EGM-2, Lonza) and plated into flasks. After 24 hours, the cells were washed with PBS to remove residual erythrocytes. HUVEC were cultured in EGM-2 and used at passage 4. Culture medium was changed every other day.

Fabrication of Three-Dimensional Collagen-Fibrin Gels

Collagen (COL) and fibrin (FIB) composite gels were fabricated as previously described [31], and the process is shown schematically in Figure 4.1.

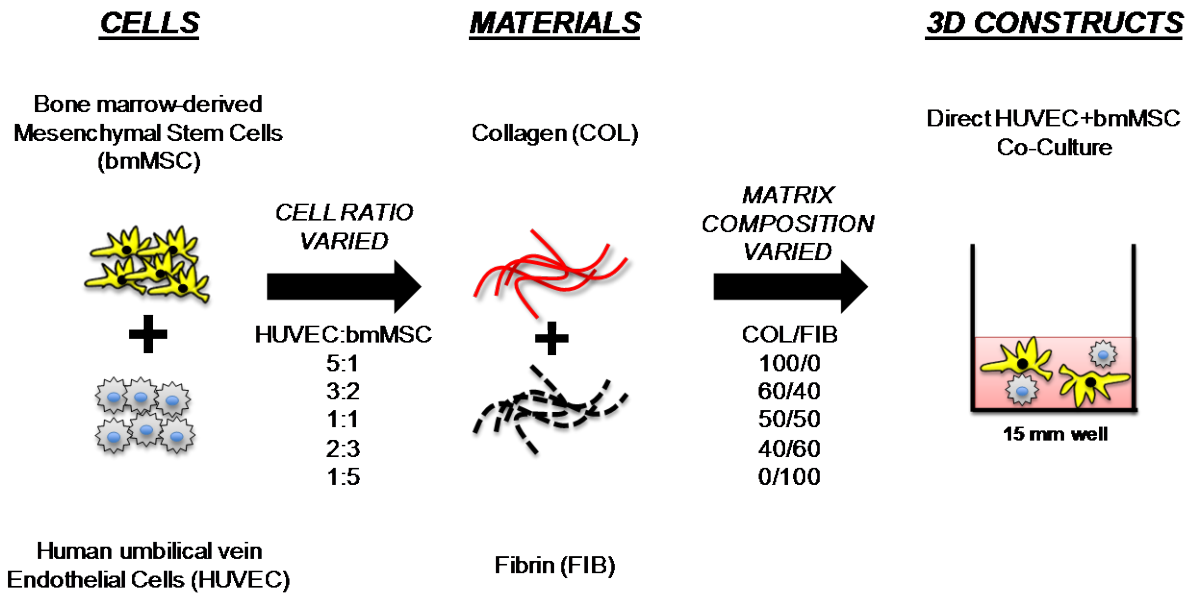

Figure 4.1 – Schematic of composite matrix fabrication and parameters varied in experimental design.

Briefly, 4.0 mg/ml Type I COL (MP Biomedicals, Solon, OH) was dissolved in 0.02 N acetic acid and 4.0 mg/ml bovine fibrinogen (Sigma Aldrich, St. Louis, MO) was dissolved in DMEM. Cell-seeded COL/FIB composite gels were created by suspending HUVEC and bmMSC in a mixture with 10% FBS, 10% 5X-concentrated DMEM (starting concentration), 5% 0.1 N NaOH, 2% bovine thrombin (0.1 UT/ml; Sigma), COL, and fibrinogen at 4°C. COL and fibrinogen volumes were varied to generate COL/FIB composite gels at mass ratios of 100/0 (pure COL), 60/40, 50/50, 40/60, and 0/100 (pure FIB) at a constant total protein concentration of 2.5 mg/ml. 1X-concentrated DMEM was used to fill the final volume to 100%. The suspension was then pipetted into a 24-well plate and allowed to gel at 37°C for 45 min. The resulting gels contained homogenously distributed HUVEC and bmMSC embedded directly within the protein matrix. Cells were embedded in the gels in all five COL/FIB concentrations at HUVEC:bmMSC ratios of 5:1, 3:2, 1:1, 2:3, and 1:5. The total cell concentration of all gels was kept constant at 6.0×10^5 cells/ml. After fabrication cell-seeded gels were cultured for 7 days at 37 °C and 5% CO_2.

The first experimental series examined the effects of cell ratio and relative matrix composition using the parameter described above. In subsequent studies, a cell ratio of 1:1 HUVEC-bmMSC and a matrix composition of 40/60 COL/FIB were used. The effect of total protein concentration on vasculogenesis was evaluated by creating COL/FIB gels with total protein concentrations of 1.25 mg/ml, 2.5 mg/ml, and 5.0 mg/ml using a stock collagen solution of 4.0 mg/ml and stock fibrinogen solutions of 4.0 and 20.0 mg/ml. To examine the effect of matrix stiffness independently from matrix concentration, the small dialdehyde glyoxal was used to crosslink 40/60 COL/FIB composite gels. Glyoxal was added at 1.0 mM directly to the pre-gelled matrix solution containing 1:1 HUVEC:bmMSC and gelation was initiated by incubating the mixture at 37°C for 45 minutes. Gels were then washed three times for 10 minutes each in PBS to remove unreacted glyoxal and medium was added.

Vasculogenesis Assay

HUVEC were labeled with a fluorescent protein (mCherry; Clontech, Mountain View, CA) as previously described to allow visualization and quantification of vessel-like networks [17]. A retroviral expression system (Orbigen Inc., San Diego, CA) was used to achieve stable expression of the mCherry gene by HUVEC. At days 1, 3, 5, and 7 post-fabrication, gels were imaged on a fluorescent microscope system (Olympus America Inc., Center Valley, PA). Five representative images of each sample were taken at each time point. The images were analyzed using the Angiogenesis Module in Metamorph Premier software (Molecular Devices Inc., Sunnyvale, CA) as previously described [20]. Minimum width, maximum width, and intensity over background were set to discriminate vessel-like structures within the images. The total length of formed vessel-like structures was then calculated.

Confocal Imaging of HUVEC, bmMSC, and Matrix Architecture

To determine the relative positions of the different cell types in 3D composite matrices, bmMSC were retrovirally transduced to achieve expression of GFP, using the same methods as for mCherry transfection (Orbigen Inc., San Diego, CA), and were co-embedded with mCherry labeled HUVEC. Images were acquired using a laser scanning confocal microscope (Olympus America Inc., Center Valley, PA). Separate image scans were taken to identify the HUVEC and bmMSC, and these sections were combined to determine co-localization of the cell types. Image scans were captured in a horizontal plane containing vessel-like structures. Images of the matrix architecture were obtained using confocal reflectance microcopy at a wavelength of 488 nm. These images are included in the Supplementary Data 4.5.

Cell Viability and Proliferation

Cell viability was assessed using a vital staining kit (Live/Dead®, Molecular Probes, Eugene, OR) as previously described [35]. Briefly, gels were washed three times in sterile PBS for 10 min and then incubated at 37°C for 45 min in a solution containing 4.0 µm calcein-AM and 4.0 µm ethidium homodimer-1 in PBS. After three subsequent PBS washes, gels were imaged using a laser scanning confocal microscope (Olympus). Viability was quantified using ImageJ software (National Institute of Health, Bethesda, MD).

To quantify cell proliferation during the culture period, the total DNA content of gels was determined and run against a standard curve. Gels were washed three times in phosphate buffered saline for 10 minutes per wash and were then extracted using 4.0 M guanidine

hydrochloride solution. DNA analysis was performed on samples at days 0, 1, 3, and 7 of culture using a commercially available DNA assay (PicoGreen®, Invitrogen Inc.).

Gel Rheology

The mechanical properties of acellular COL/FIB composite gels were determined by gel rheometry (AR-G2, TA Instruments, New Castle, DE) [36]. Pre-mixed COL/FIB matrix solutions were loaded onto a Peltier stage precooled to 10 °C. A 20 mm steel parallel plate was used at a gap height of 1000 μm. A temperature ramp over 2 minutes was performed to raise the temperature of the system to 37°C. A time sweep was then conducted for 45 minutes at 37°C at 1% strain and at an oscillation frequency of 1 radian/second to simulate the gelation conditions used in the vasculogenesis assay. Reported storage (G') and loss (G'') moduli were generated from the average of the last 5 minutes of the time sweeps.

Statistical Analysis

All quantitative analyses were processed using a one-way Analysis of Variance using Tukey's post-hoc analysis. Statistical significance was set at $p < 0.05$. Numerical values are presented as mean +/- standard deviation; n = 3 for HUVEC-bmMSC cell ratio vasculogenic assays, n = 4 for cell proliferation studies, n = 5 for all rheological data, n = 4 for protein concentration and glyoxal vasculogenic assays, and n = 4 for cell viability studies.

4.3 - Results

Effect of Matrix Composition

COL/FIB composite matrices were fabricated at COL/FIB compositions of 100/0, 60/40, 50/50, 40/60, and 0/100. Figure 4.2 shows representative images of these materials seeded with

cells at a 1:5 HUVEC-bmMSC ratio (panels A-E) and examined after 7 days in culture. In general, the degree of vessel-like network formation clearly increased with increasing fibrin content in the composite gels. Figure 4.2F shows quantification of the total network length over time in culture. The trend for increased network development over time is evident and all five matrix compositions showed significantly higher values ($p<0.05$) of both total network length and the number of segments at day 7 compared to day 1. By day 7, the length for all composite matrix compositions were significantly higher than the pure collagen (100/0) group. At day 7 the pure fibrin (100/0) group had statistically higher values ($p < 0.05$) of network length compared to the 60/40, 50/50, and 0/100 matrix compositions. However, there was no statistical difference in either total network length or the number of segments between pure fibrin and the 40/60 matrix composition.

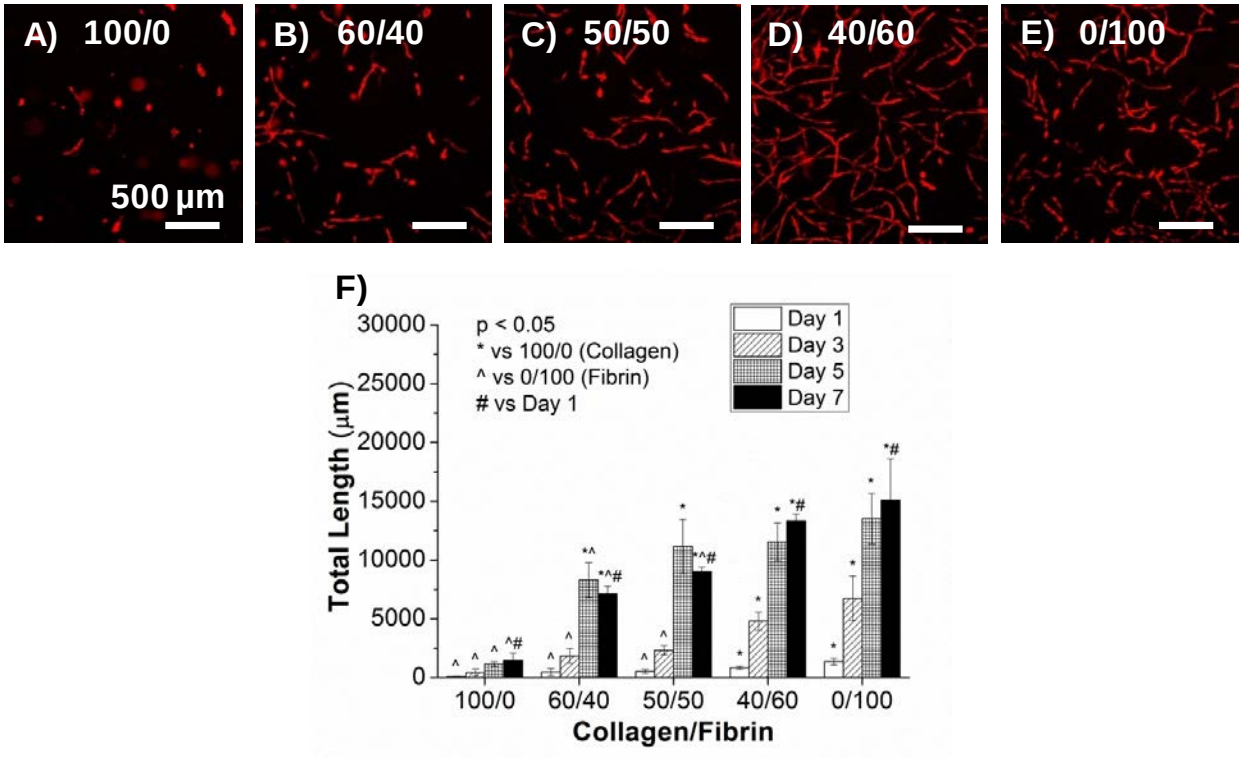

Figure 4.2 - Images of vessel-like structures in COL/FIB matrices of indicated composition at an HUVEC:bmMSC ratio of 1:5. Vessel-like structure formation showed a positive correlation with increasing fibrin content. (A-E) Representative images of vessel-like structures in COL/FIB matrices of indicated composition at an HUVEC:bmMSC ratio of 1:5. (F) Quantification of total network length in each of the matrix compositions over time in culture

Figure 4.2G shows quantification of the number of network segments in each of the matrix compositions over time. These data closely mirror the total network length data, indicating that the vessel-like networks grew through branching and joining, as opposed to simple elongation of existing vessel segments. This trend of network growth via branching and joining of segments was evident in all of the samples analyzed (see Supplementary Data Figures 4.1-4.4).

Effect of Cell Ratio

Figure 4.3A shows vasculogenesis data at day 7 for all five matrix compositions and all five HUVEC:bmMSC ratios investigated.

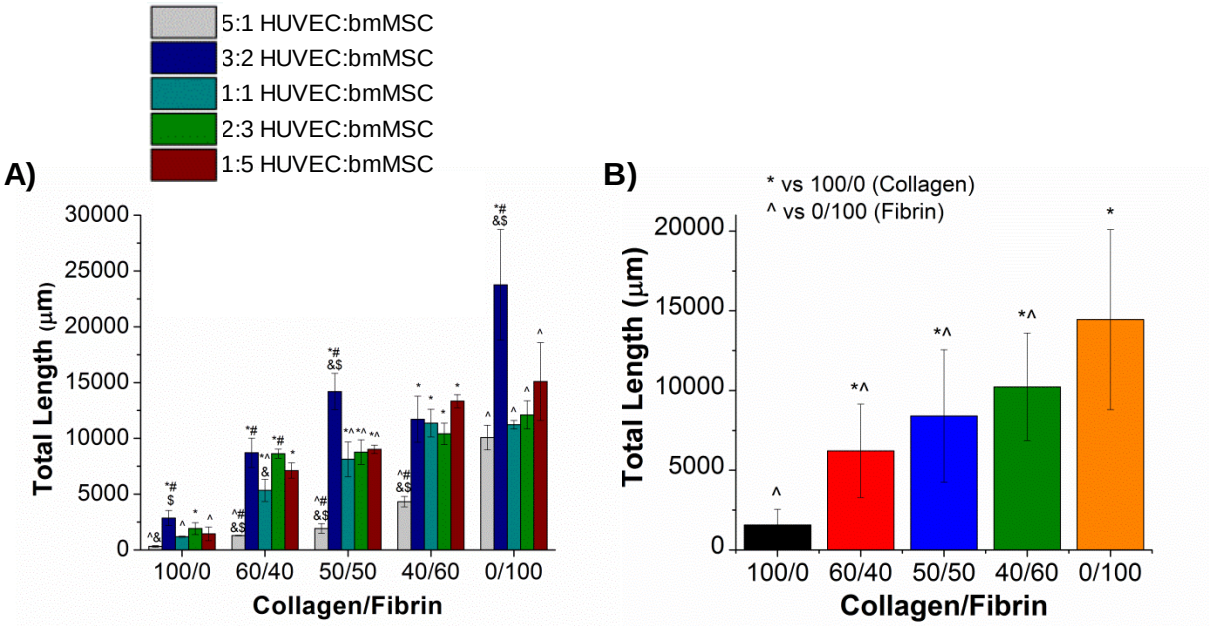

Figure 4.3 – Network length of all cell ratios and all matrix compositions. Total length measurements positively correlated with increasing fibrin content. (A) Total network length as a function of matrix composition at all five cell rations investigated at day 7 in culture. (B) Average network length, using data from all cell ratios, as a function of matrix composition

The trend of increasing network formation with increasing fibrin content is evident in these data as well. Within each matrix composition, the 5:1 HUVEC:bmMSC ratio resulted in the lowest values for total network length relative to all other cell ratios. In the 100/0, 50/50, and 0/100 compositions, the 3:2 HUVEC:bmMSC ratio resulted in significantly greater values of total network length, compared to the other cell ratios. In general, there was no marked difference in vessel-like structure formation between the 1:1, 2:3, and 1:5 HUVEC:bmMSC ratios. Figure 4.3B shows the total network length as a function of matrix composition, using data pooled across all cell ratios, and indicates significant differences caused by altered protein content.

A full panel of experiments was performed, which included each of the five matrix compositions seeded with each of the five cell ratios, and analyzed at each of the four time points. Figures 4.2 and 4.3 summarize the trends that were observed across all samples, and the

remainder of the full data set is presented in Supplemental Figures 4.1-4.4. In the 2:3, 1:1, and 3:2 HUVEC-bmMSC samples, the trends of increasing vessel formation with time and with increasing fibrin content were maintained. However, in the 5:1 HUVEC-bmMSC samples the degree of vasculogenesis was markedly lower across all matrix compositions. Although vessel-like structures formed rapidly at this cell ratio, the network did not continue to expand, but instead retracted over time. In general, the pure fibrin (0/100) matrices resulted in significantly more ($p<0.05$) vessel-like structure formation compared to the 100/0, 60/40, and 50/50 matrix compositions. However, the 0/100 and 40/60 were similar in their behavior. Overall, it was clear that time and matrix composition had a greater effect on vasculogenesis than HUVEC:bmMSC ratio.

These findings allowed us to narrow the set of matrix and cell formulations to be used in subsequent experiments. A COL/FIB composition of 40/60 was selected because it supported vasculogenesis to the same degree as pure fibrin, and both of these materials had the most robust response of the compositions tested. Similarly, an HUVEC:bmMSC ratio of 1:1 was selected because this cell ratio behaved similar to the other ratios in the 40/60 matrix. The selection of a single construct formulation facilitated the extension of our studies without requiring all formulations to be examined.

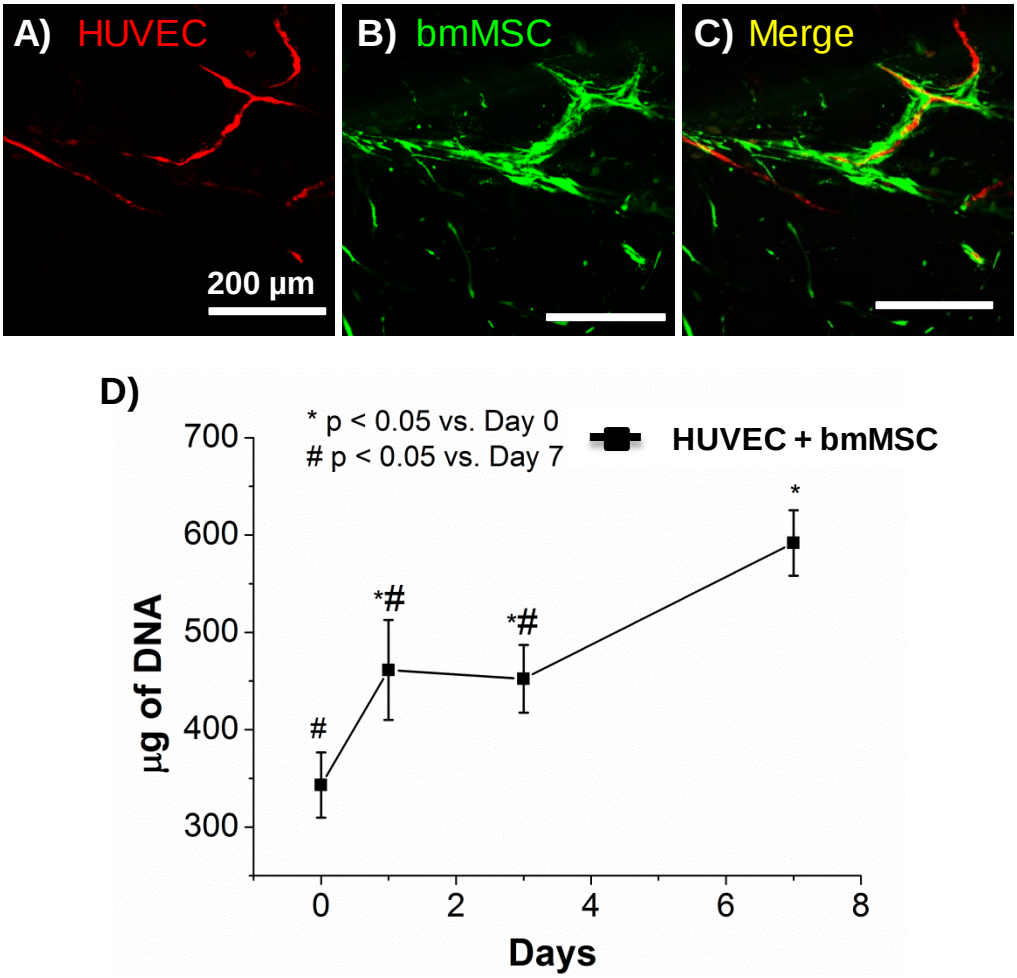

Figure 4.4 - Characterization of cell-seeded 40/60 COL/FIB constructs with 1:1 HUVEC-bmMSC ratio. Both cell types were co-localized after 7 days in culture indicating a peri-endothelial interactions. Embedded cells proliferated during the 7 day culture period. (A-C) Co-localization of bmMSC and HUVEC. (D) Cell proliferation of HUVEC and bmMSC

Distinct labeling of HUVEC and bmMSC using different fluorescent labels allowed the examination of the spatial relationships between the cell types in 3D COL/FIB materials, as shown in Figure 4.4. Panel A shows extended HUVEC and panel b shows bmMSC clustering at day 7 in culture. Overlay of these images (panel C) shows very clear association of bmMSC with HUVEC that suggests their role as pericytes in stabilizing vessels.

Figure 4.4D shows the total DNA extracted from cell-seeded composite matrices, which was used as a measure of cell number and proliferation over the 7 day culture period. The number of cells increased significantly day 0 (post-gelation) to day 1, and then plateaued from day 1 to 3. Significant cell proliferation was again evident between day 3 and day 6, and overall the cell content of the gels increased by about 70% over the 7 day period.

Mechanical Properties of COL/FIB Materials

To evaluate the effect of material properties on vasculogenesis, the shear moduli (storage and loss modulus) of the COL/FIB composite gels were evaluated at all five matrix compositions. Representative time sweeps are shown in Figure 4.5A and revealed distinct gelation curves for the pure and composite materials. Pure collagen (100/0) gelled rapidly and the modulus rose sharply, followed by a gradual decrease in modulus over time until it plateaued. Pure fibrin (0/100) had a delayed gelation response and then gelled to reach a plateau modulus. The mixed composites had intermediate behavior, which depended on their composition. The average moduli of gelled materials are presented in Figure 4.5B, which shows that gel stiffness as represented by the storage modulus (G') decreased with increasing fibrin content. The 100/0 composition was significantly stiffer than the other materials. The 40/60 and the 100/0 compositions exhibited very similar mechanical properties. Figures 4.5C shows the correlation between total network length and matrix stiffness, and suggests an inverse linear relationship between these parameters ($R^2 = 0.92$).

The loss modulus (G") was also calculated from the dynamic testing data, and generally followed the same trends as the storage modulus. This parameter provides a measure of the viscoelastic nature of the hydrogels, and reflects the amount of viscous energy dissipation under

dynamic conditions. We did not include this parameter in our interpretation of network formation in different materials, since the 3D gels were cultured under static conditions, in which viscous effects are unlikely to play a major role.

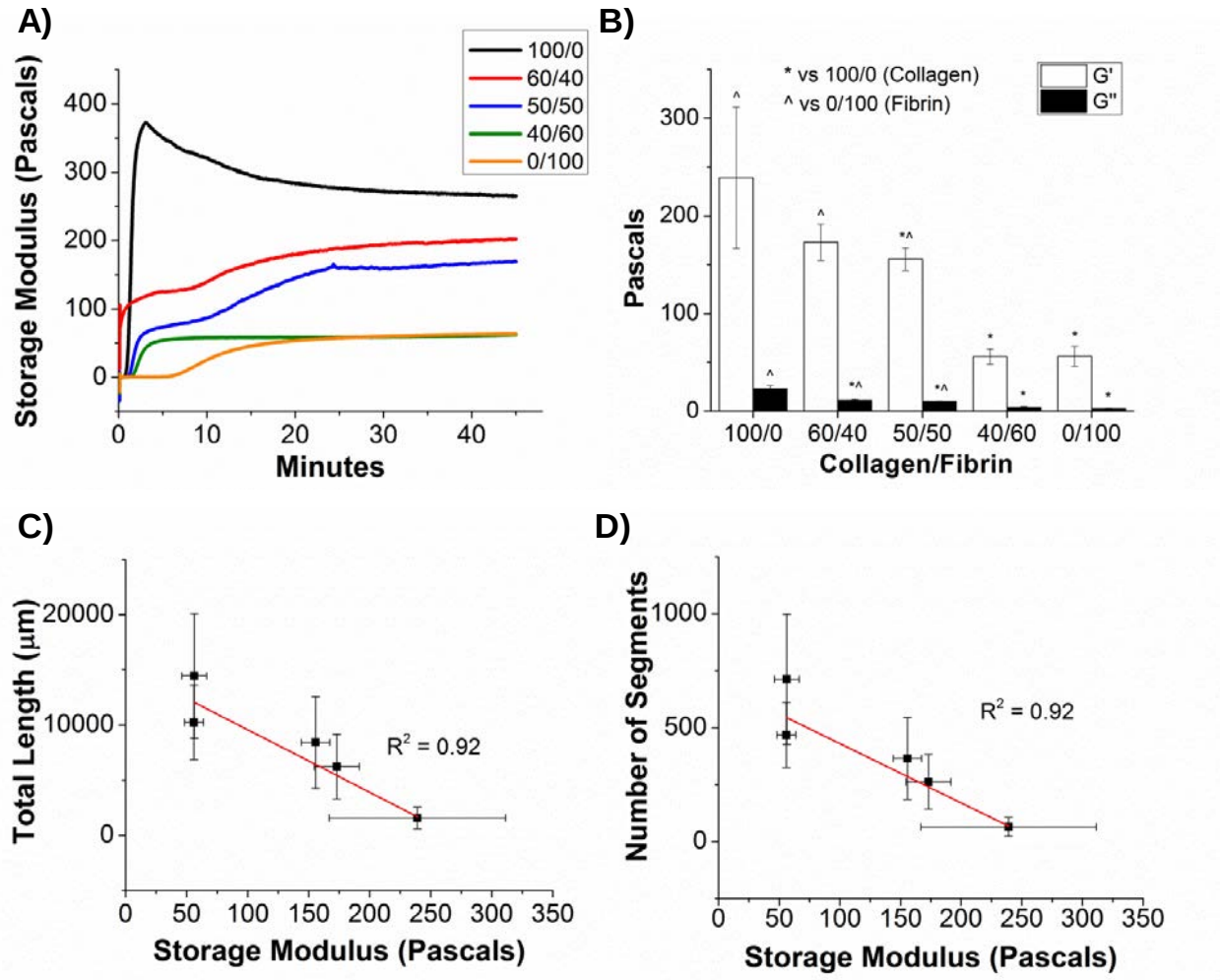

Figure 4.5 - Gel rheometry for COL/FIB matrices. Storage modulus measurements decreased with increasing fibrin content. (A) Representative gel rheometry time sweeps for COL/FIB matrices. (B) Average storage (G') and loss (G') moduli for COL/FIB matrices. (C, D) Correlations between formation of vessel-like structures and material stiffness

Effect of Protein Concentration

The observed relationship between matrix stiffness and extent of vessel-like structure formation led us to further investigate this effect. To this end 40/60 COL/FIB gels were created at total protein concentrations of 1.25 mg/ml, 2.50 mg/mL and 5.00 mg/ml, to alter overall matrix stiffness while keeping the COL/FIB ratio constant. The rheological properties and associated vasculogenesis data at 1:1 HUVEC:bmMSC for these materials are shown in Figure 4.6. The gelling curves in panel a show that protein concentration affects the mechanical properties of these composites. The 1.25 mg/ml gels had a storage modulus of 11±4 Pa, which increased to 56±8 Pa ($p<0.03$) at 2.50 mg/ml, and to 222±37 Pa ($p<0.001$) at 5.00 mg/ml, and the loss moduli followed a similar trend. Representative images of vasculogenesis in these materials at day 7 are shown in Figures 4.6C-E and network length is quantified in Figures 4.6f. There was no statistical difference between the 1.25 mg/ml and the 2.50 mg/ml materials at any time point. However, the 5.00 mg/ml materials exhibited dramatically decreased formation of vessel-like structures, relative to the lower concentration matrices at all time points ($p<0.05$). We observed a significant increase in cell proliferation at day 7 in the 5.00 mg/ml COL/FIB group compared to the 1.25 and 2.5 mg/ml COL/FIB hydrogels (Supplemental Figure 4.6A).

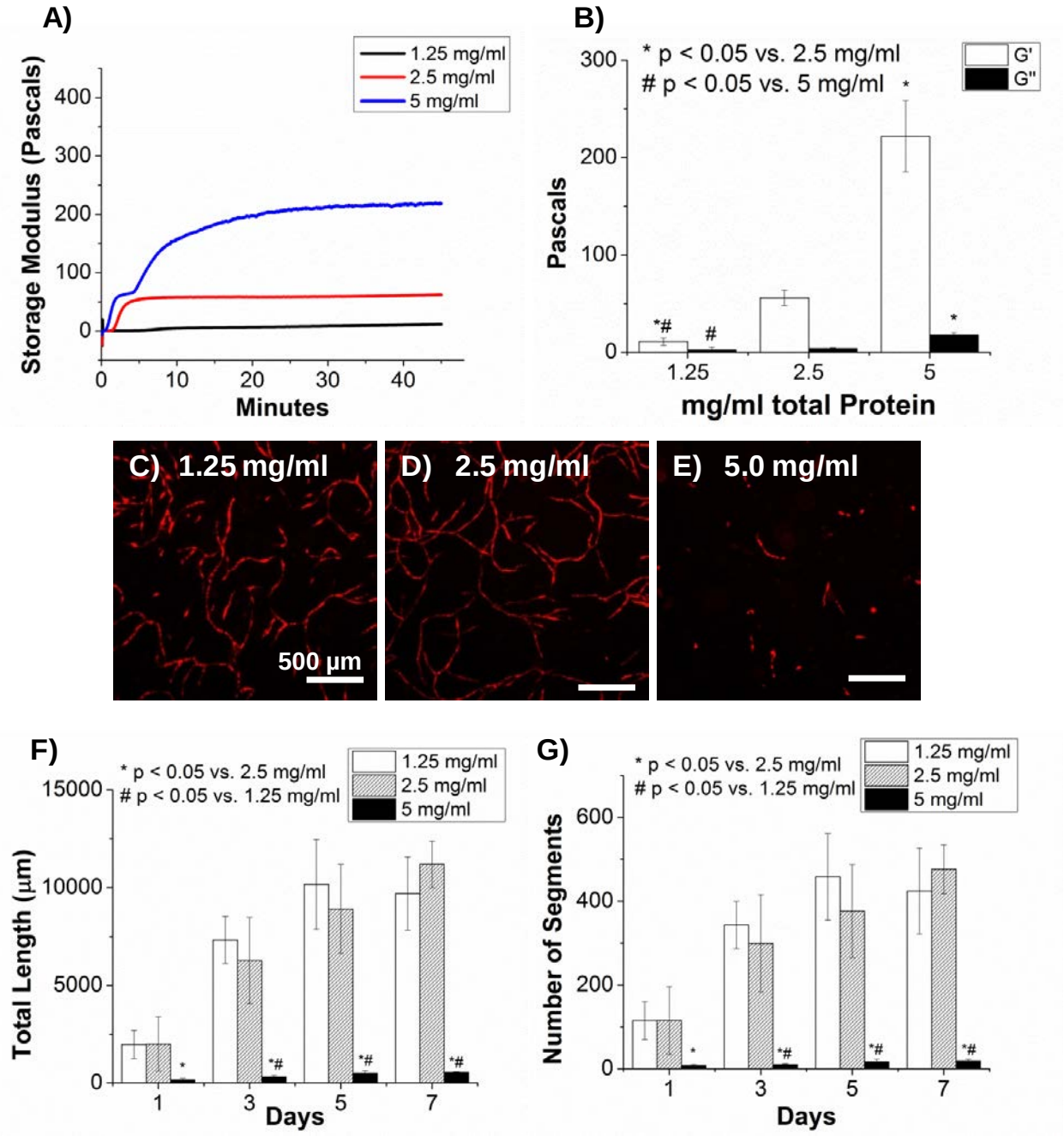

Figure 4.6 - Effect of total protein concentration on vasculogenesis in 40/60 COL/FIB matrices. Increasing total protein content from 2.5 mg/ml to 5 mg/ml significantly decreased network formation during the 7 day culture period. (A) Representative gel rheometry time sweeps. (B) Storage and loss moduli. (C-E) Representative images on day 7 of culture. (F,G) Quantification of vessel-like structures

Effect of Glyoxal Crosslinking

Another approach to changing the mechanical properties of protein gels without altering the overall composition is to crosslink the matrix. To this end we used glyoxal, a small dialdehyde that crosslinks free amine groups, to stiffen 40/60 COL/FIB composite gels. The rheological properties and associated vasculogenesis data for these materials seeded with 1:1 HUVEC:bmMSC are shown in Figure 4.7.

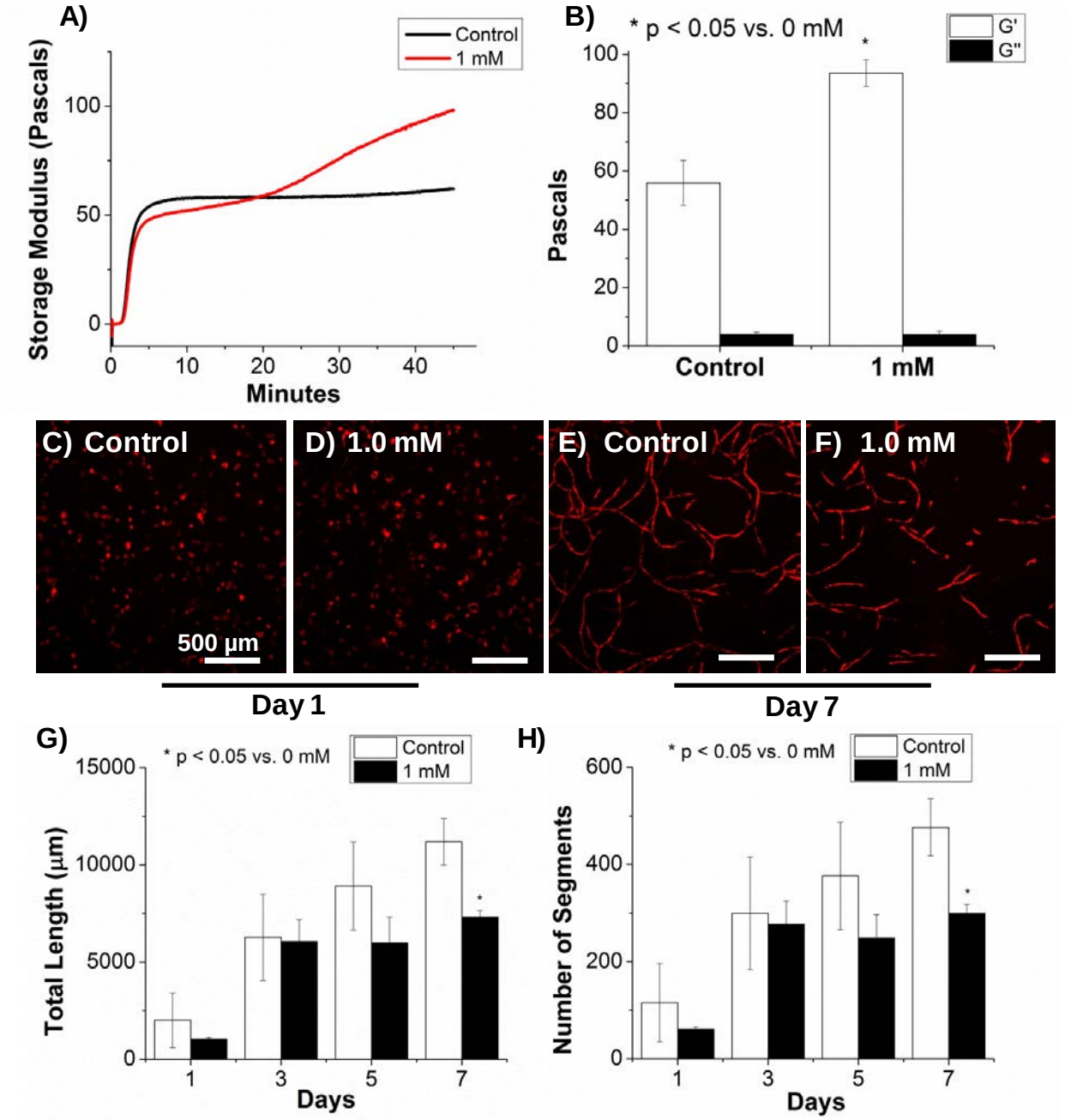

Figure 4.7 Effect of glyoxal crosslinking on vasculogenesis in 40/60 COL/FIB matrices. Crosslinking 40/60 COL/FIB matrices with 1 mM glyoxal led to a decrease in network formation after 7 days in culture. (A) Representative gel rheometry time sweeps. (B) Storage and loss moduli. (C-F) Representative images on day 7 of culture. (G,H) Quantification of vessel-like structures

Treatment with glyoxal altered the gelation dynamics (panel 4.7A) and resulted in an approximately 2-fold increase in the storage moduli (panel 4.7B) of gels with otherwise identical composition. Vessel-like structures formed in both untreated control and crosslinked gels (panels

4.7C-4.7F), but crosslinked materials exhibited significantly lower values of both total network length by day 7 (panels 4.7G). Cell viability was assessed in both control and crosslinked gels, as shown in Figure 4.8.

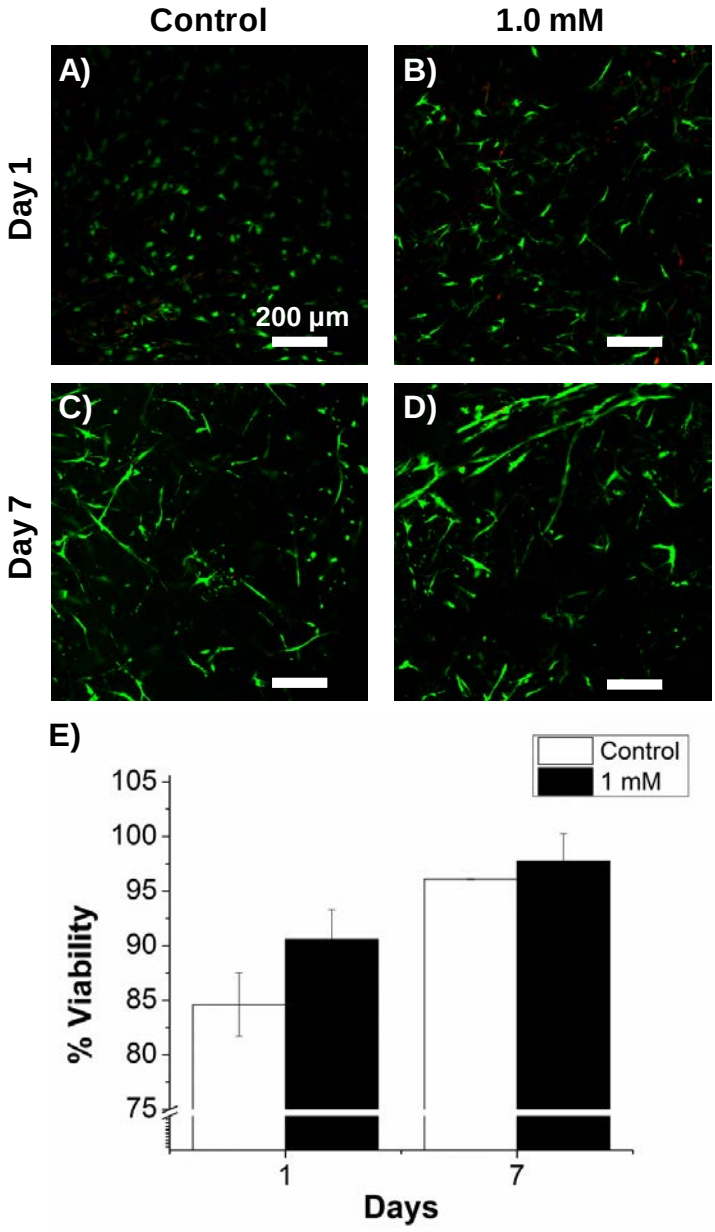

Figure 4.8 - Cell viability in 3D constructs after glyoxal treatment. The addition of 1 mM glyoxal to the COL/FIB hydrogels did not alter cell viability after 1 or 7 days in culture. (A-D) Representative images on days 1 and 7 of culture. (E) Quantification of cell viability

Viability was high in all samples at both day 1 and day 7 (panels 4.8A-4.8D), and there was no significant difference in viability between treatments at either time point (panel 4.8E). There was a significant decrease in cell number of HUVEC and bmMSC co-cultures at day 1 between control and glyoxal-crosslinked gels, but there were not a significant difference in cell number at day 7 (Supplemental Figure 4.6B). HUVEC alone COL/FIB composite gels were investigated to further evaluate the effect of glyoxal crosslinking on HUVEC. There was a significant decrease in DNA content from day 0 in both the control and glyoxal conditions, but there were no differences between the two conditions at days 1,3, or 7 (Supplemental Figure 4.7C). Vessel-like structures were not formed in either the control or glyoxal condition indicating the importance of the stromal cell the co-culture system (Supplemental Figure 4.7A,B).

4.4 - Discussion

This series of studies examined the effects of material composition, HUVEC:bmMSC ratio, and matrix stiffness on vasculogenesis in a well-defined, three-dimensional in vitro model. The relative amounts of collagen and fibrin in the matrices were shown to have a marked effect on the formation of vessel-like networks in COL/FIB materials. In particular, the degree of vasculogenesis clearly increased in a dose-dependent manner with increasing fibrin content. While it is well established that both the extracellular matrix and the presence of stromal cells can modulate vasculogenesis, the interaction between these factors and in particular the effects of matrix type and density on the vasculogenic response are not fully understood. Earlier studies that used collagen and fibrin in vasculogenesis assays showed that these proteins can affect neovessel formation [30, 15, 37], however the properties of the matrix that produce these effects are still being elucidated. The present study used compositionally defined 3D composite

materials to further contribute to our understanding of how these biologically active and structurally important wound healing proteins can regulate neovessel formation.

The communication between HUVEC and stromal cells is an area of increasing importance in a variety of fields [20, 24], and therefore we examined the effect of varying the HUVEC:bmMSC ratio on the degree of vasculogenesis. The chosen HUVEC:bmMSC fractions were varied from 1:5 to 5:1 to cover a relatively wide range of ratios, while the total cell concentration was kept constant. Interestingly, the group with the highest relative fraction of HUVEC (5:1) exhibited the lowest vasculogenic response over a week in culture in all five of the tested matrix compositions. Although this cell ratio supported rapid formation of vessel-like structures initially, the total length and number of vessel-like structures decreased over time in culture. This behavior contrasts with the other (lower) HUVEC:bmMSC ratios examined, which exhibited steadily increasing network length over time. These results highlight the importance of pericyte-like cells in promoting and stabilizing nascent structures. In addition, clear co-localization of HUVEC and bmMSC was observed when both cell types were labeled and imaged, further suggesting peri-endothelial interaction between the two cell types. These associations between endothelial and stromal cells have been shown to be important for stable neovessel formation in other recent studies [14, 17].

The 40/60 COL/FIB material seeded with 1:1 HUVEC:bmMSC was selected for further study because it exhibited the highest degree of vasculogenesis. This composition was statistically the same as pure fibrin in this regard, however in some applications a composite matrix may have advantages over a pure material. For example, the use of composite matrices has become more common in tissue engineering applications in order to harness both the mechanical and biochemical properties of such materials [30, 38]. The 1:1 HUVEC:bmMSC

ratio was statistically similar to the other ratios that showed robust vasculogenesis. Assessment of DNA content in the composite materials over time showed that cell number increased initially, followed by a plateau phase, and a subsequent second phase of cell growth. Cell proliferation is important to the vascular extension and maturation process. In this study, we were not able to distinguish between DNA contributed by HUVEC and that contributed by bmMSC. However, the initial growth phase may reflect proliferation of HUVEC, which have been shown to be capable of rapid division in response to mitogen stimulation [39]. The later growth phase may reflect either continued HUVEC division to extend vessels or may be due to proliferation of bmMSC, which may grow more slowly as they establish pericyte function [40].

Rheological analysis showed that the mechanical properties of the COL/FIB composite materials varied with composition. In particular, the pure collagen materials were the stiffest and the pure fibrin materials were the least stiff, with the stiffness of composite materials falling in between the pure materials. A clear inverse relationship existed between matrix stiffness and degree of vessel-like structure formation. These findings agree with those of other recent studies that have examined the role of matrix compliance in the formation of neovasculature *in vitro* and *in vivo* [33, 34], which have suggested that vasculogenesis is inhibited in stiffer matrices. In the present study, we further investigated the role of matrix stiffness in modulating vasculogenesis by performing studies on 40/60 COL/FIB materials fabricated at a range of total protein concentrations. The resulting materials varied in stiffness in direct relation to the total protein content. The stiffest materials (5.00 mg/ml) exhibited about a 4-fold increase in storage modulus relative to the standard 2.50 mg/ml materials, and showed a correspondingly decreased vasculogenic response. In contrast, the least stiff materials (1.25 mg/mL) exhibited a storage modulus only about one fifth of the standard 2.5 mg/ml materials, but showed no statistical

difference in the formation of vessel-like structures. These results provide further evidence that matrix stiffness may be involved in modulating vasculogenesis, but also suggest that there may be a minimum stiffness below which the effect is no longer evident.

Increasing the total protein concentration in gel matrices does not alter the stiffness independently of all other factors that may affect cell function, since increased protein content can also lead to changes in adhesive ligand density and porosity of the matrices. Analysis of matrix architecture using confocal reflectance microscopy verified that the matrix architecture varied with both changing matrix composition and concentration (see Supplemental Figure 4.5). In an attempt to further isolate the effects of stiffness the protein matrices were crosslinked with glyoxal, a small dialdehyde that we have used previously to increase the mechanical properties of protein matrices without adversely affecting the viability of embedded cells [35]. Glyoxal crosslinking induced a two-fold increase in storage modulus in the 40/60 COL/FIB matrix composition with a resulting decrease in total network length at day 7. However confocal reflectance imaging showed that the matrix structure was also changed by crosslinking, though the effect was relatively modest. Viability staining confirmed that the decrease in vasculogenic response was not due to cell death. Cell proliferation quantification also confirmed that the decrease in vasculogenic response was not due to cell death. These data further support the idea that increased matrix stiffness results in decreased vessel-like structure formation, though the effect of crosslinking on stiffness may not have been completely independent of matrix architecture.

This study has demonstrated that matrix composition is a potent modulator of vasculogenic activity in 3D matrices containing embedded HUVEC and bmMSC. In particular, fibrin-containing matrices were permissive of a robust vasculogenic response, whereas matrices

with a high collagen Type I content resulted in decreased vessel-like structure formation. Importantly, composites could be created that maintained strong vasculogenic activity while also containing both collagen and fibrin, which may be beneficial in some applications. The ratio of HUVEC:bmMSC was not a strong modulator of the vasculogenic response, although high HUVEC:bmMSC ratios (5:1) resulted in unstable vessel formation. The clear correlation between matrix stiffness and the vasculogenic response suggested that mechanical properties may be important in modulating vessel formation, and follow-up experiments in which stiffness was varied provided supporting evidence for this idea. However, the experimental treatments used in this study also altered the matrix architecture, which may have lead to changes in mass transport, ligand density, or other parameters that could modulate vasculogenesis. Taken together, these results are relevant to the variety of in vitro systems that have been developed to study angiogenesis and vasculogenesis, and in particular those that rely on 3D protein matrices to simulate the tissue environment. In addition, these data are relevant to efforts to understand and promote vasculogenesis in engineered tissues, which is a key challenge in the transplantation of larger structures.

4.5 – Supplemental Figures

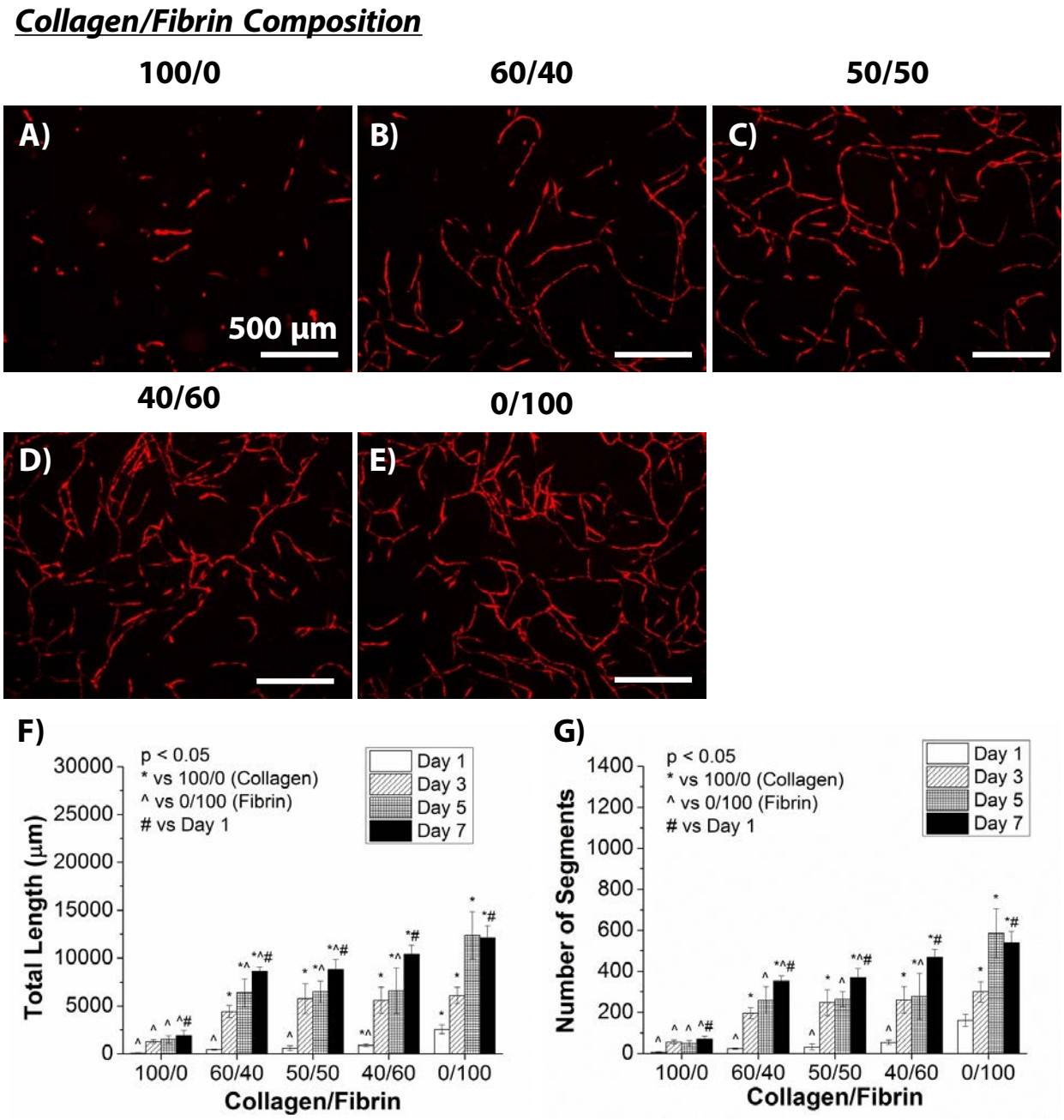

Supplemental Figure 4.1 - 2:3 HUVEC:bmMSC ratio. Vessel-like structure formation showed a positive correlation with increasing fibrin content. (A-E) Representative images of formed vessel-like structures on the five matrix compositions. (F,G) Quantification of the total length and number of segments on the five matrix compositions

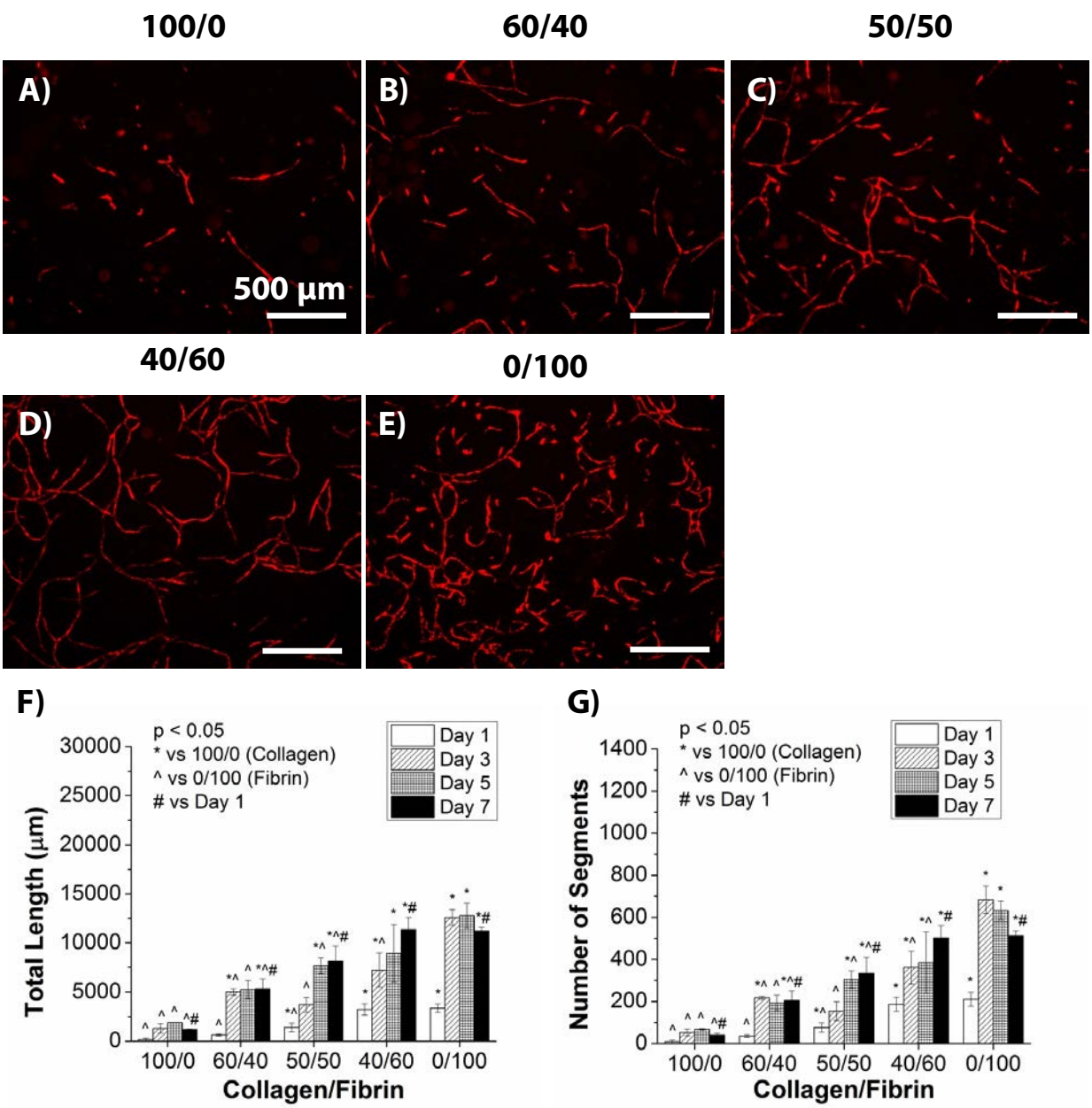

Supplemental Figure 4.2 - 1:1 HUVEC:bmMSC ratio. Vessel-like structure formation showed a positive correlation with increasing fibrin content. (A-E) Representative images of formed vessel-like structures on the five matrix compositions. (F,G) Quantification of the total length and number of segments on the five matrix compositions

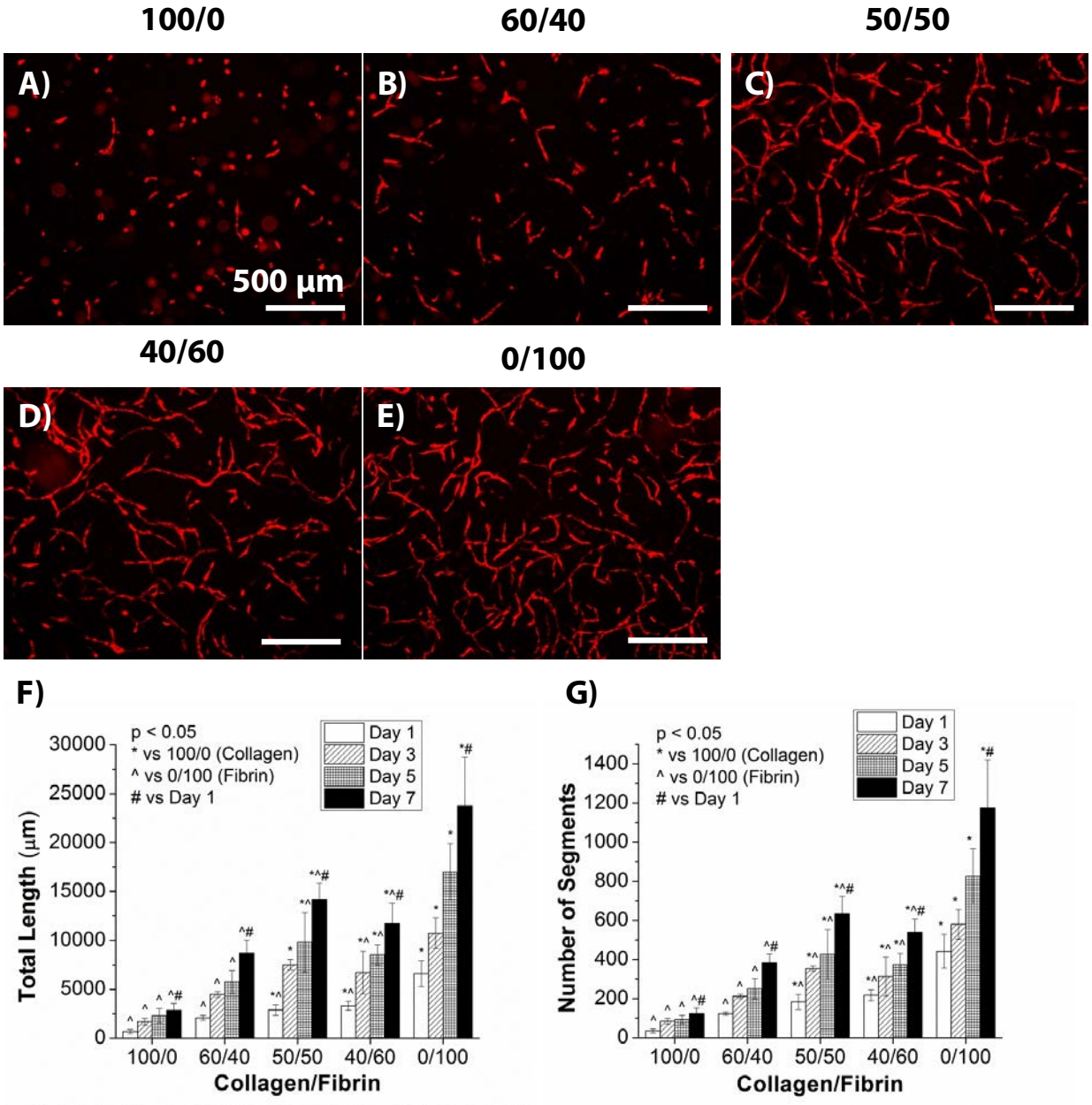

Supplemental Figure 4.3 - 3:2 HUVEC:bmMSC ratio. Vessel-like structure formation showed a positive correlation with increasing fibrin content. (A-E) Representative images of formed vessel-like structures on the five matrix compositions. (F,G) Quantification of the total length and number of segments on the five matrix compositions

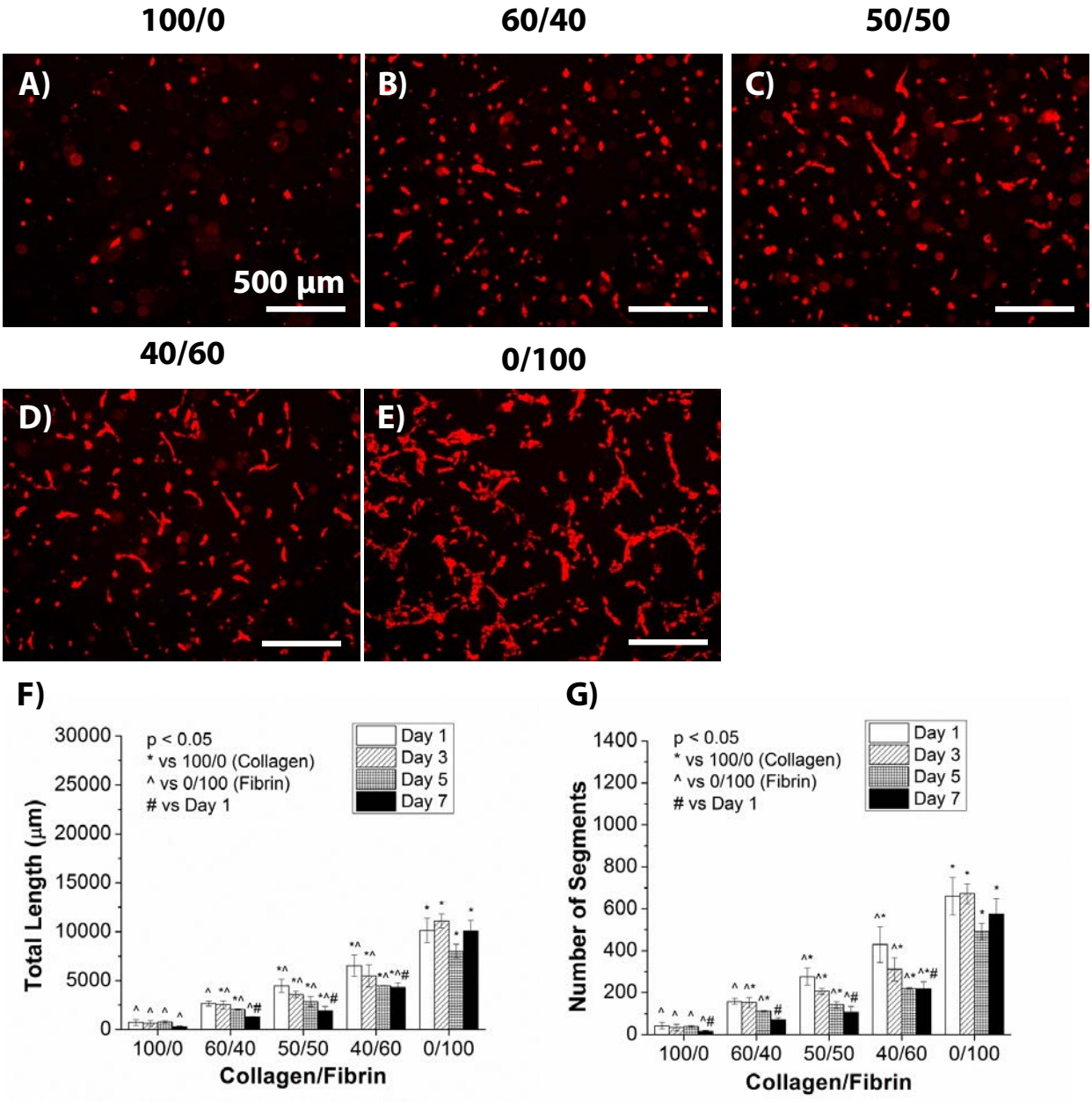

Supplemental Figure 4.4 - 5:1 HUVEC:bmMSC ratio. Vessel-like structure formation showed a positive correlation with increasing fibrin content. (A-E) Representative images of formed vessel-like structures on the five matrix compositions. (F,G) Quantification of the total length and number of segments on the five matrix compositions

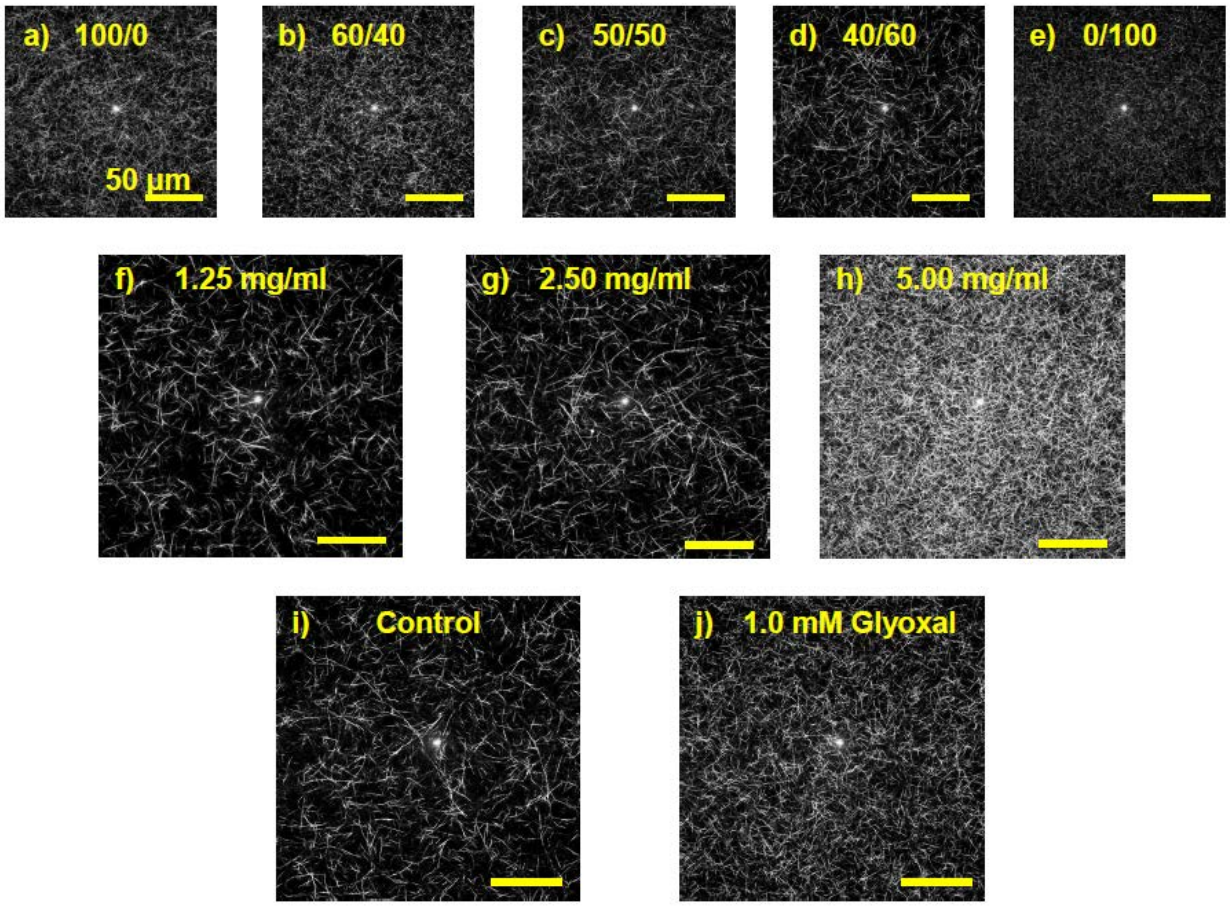

Supplemental Figure 4.5 – Confocal reflectance images of COL/FIB matrices. Qualitative analysis showed alterations in the matrix architecture when the matrix composition, total protein content, and crosslinking density were modulated. Representative confocal reflectance images of COL/FIB matrices (A-E), the effect of total protein concentration (F-H), and the effect of glyoxal crosslinking.

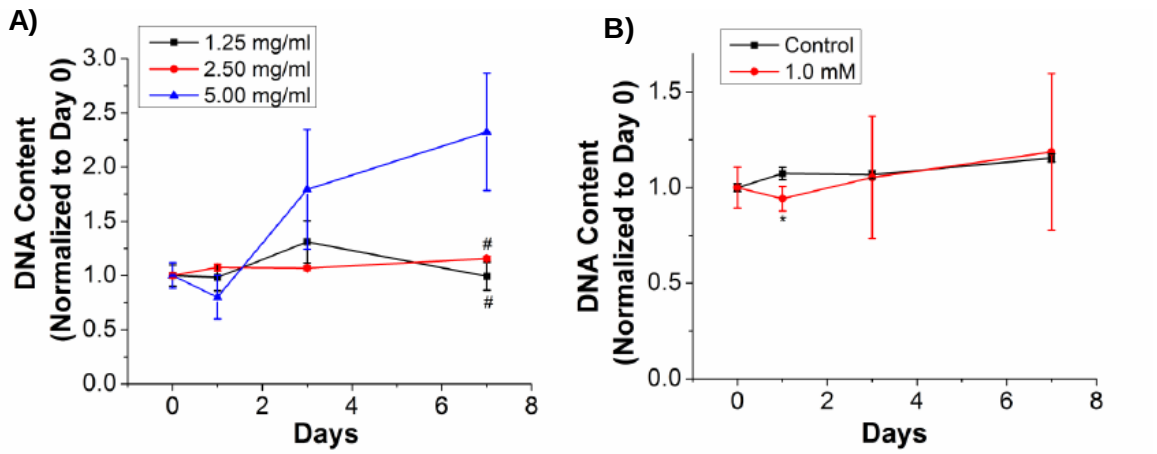

Supplemental Figure 4.6 – Cell proliferation of HUVEC and bmMSC co-cultures in 40/60 COL/FIB matrices. Increasing the total protein content of the hydrogels to 5.00 mg/ml led to a significant increase in total DNA. Crosslinking matrices with glyoxal did not alter DNA content. (A) Effect of total protein concentration. (#) denotes statistical significance against 5.00 mg/ml. (B) Effect of glyoxal crosslinking. (*) denotes statistical significance against control.

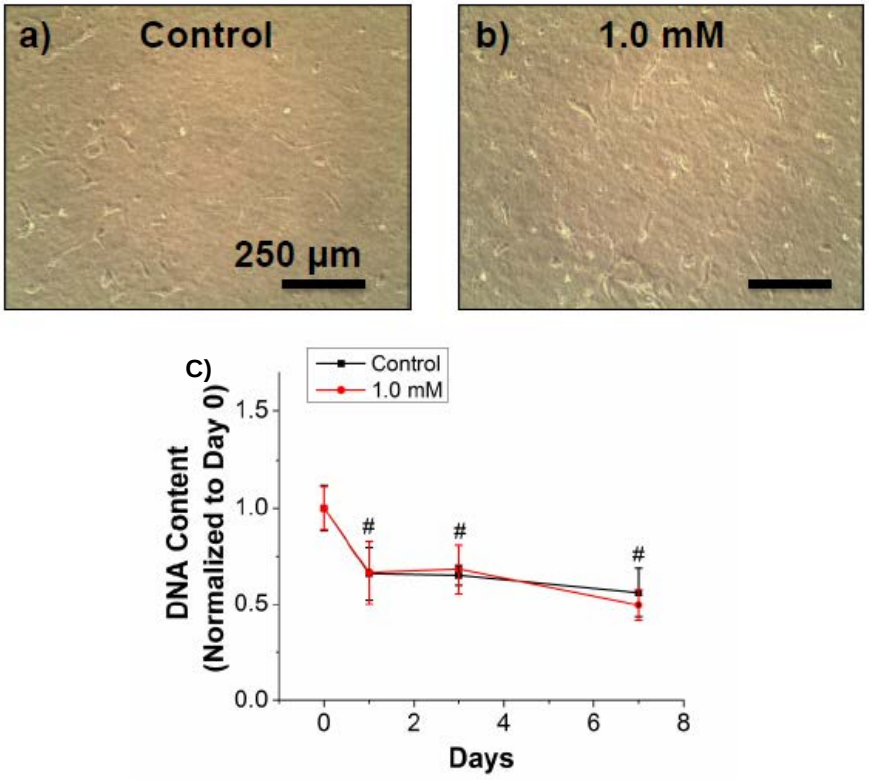

Supplemental Figure 4.7 – Effect of glyoxal crosslinking on cell proliferation of EC alone in 40/60 COL/FIB matrices. Cellular DNA decreased from day 0 and there were no significant changes between the control of glyoxal conditions any time points. (A,B) Representative images on day 7 of culture. (C) DNA quantification. (#) denotes statistical significance against day 0.

4.6 – References

1. Jain RK. Molecular regulation of vessel maturation. Nature Medicine 9, 685, 2003.

2. Langer R, Vacanti JP. Tissue Engineering. Science 260, 920, 1993.

3. Mikos AG, Herring SW, Ochareon P, Elisseeff J, Lu HH, Kandel R, Schoen FJ, Toner M, Mooney D, Atala A, Van Dyke ME, Kaplan DL, Vunjak-Novakovic G. Engineering Complex Tissues. Tissue Engineering 12, 3307, 2006.

4. Novosel HUVEC, Kleinhans C, Kluger PJ. Vascularization is the key challenge in tissue engineering. Advanced Drug Delivery Reviews 63, 300, 2011.

5. Santos MI, Reis RL. Vascularization in Bone Tissue Engineering: Physiology, Current Strategies, Major Hurdles and Future Challenges. Macromolecular Bioscience 10, 12, 2010.

6. Lovett M, Lee K, Edwards A, Kaplan DL. Vascularization Strategies for Tissue Engineering. Tissue Engineering: Part B 15, 353, 2009.
7. Vailhe B, Vittet D, Feige JJ. In vitro models of vasculogenesis and angiogenesis. Laboratory Investigation 81, 439, 2001.

8. Davis GE, Stratman AN, Sacharidou A, Koh W. Molecular basis for endothelial lumen formation and tubulogenesis during vasculogenesis and angiogenic sprouting. International Review of Cell and Molecular Biology 288, 101, 2011.

9. Koh W, Stratman AN, Sacharidou A, Davis GE. In vitro three dimensional collagen matrix models of endothelial lumen formation during vasculogenesis and angiogenesis. Methods in Enzymology 443, 83, 2008.

10. Shepherd B, Jay S, Saltzman W, Tellides G, Pober J. Human aortic smooth muscle cells promote arteriole formation by coengrafted endothelial cells. Tissue Engineering Part A 15, 165, 2009.

11. Au P, Tam J, Fukumura D, Jain RK. Bone marrow derived mesenchymal stem cells facilitate engineering of long-lasting functional vasculature. Blood 111, 4551, 2008.

12. Ghanaati S, Fuchs S, Webber MJ, Orth C, Barbeck M, Gomes ME, Reis RL, Kirkpatrick CJ. Rapid vascularization of starch-poly(caprolactone) in vivo by outgrowth of endothelial cells in co-culture with primary osteoblasts. Journal of Tissue Engineering and Regenerative Medicine 5, e136, 2011.

13. Merfeld-Clauss S, Gollahalli N, March K, Traktuev D. Adipose tissue progenitor cells directly interact with endothelial cells to induce vascular network formation. Tissue Engineering Part A 16, 2953, 2010.

14. Stratman AN, Malotte KM, Mahan RD, Davis MJ, Davis GE. Pericyte recruitment during vasculogenic tube assembly stimulates endothelial basement membrane matrix formation. Blood 114, 5091, 2009.

15. Hellstrom M, Gerhardt H, Kalen M, Li X, Eriksson U, Wolburg H, Betsholtz C. Lack of Pericytes Lead to Endothelial Hyperplasia and Abnormal Vascular Morphogenesis. The Journal of Cell Biology 153, 543, 2001.

16. Baluk P, Hashizume H, McDonald DM. Cellular abnormalities of blood vessels as targets in cancer. Current Opinion in Genetics and Development 15, 102, 2005.

17. Ghajar CM, Kachgal S, Kniazeva E, Mori H, Costes SV, George SC, Putnam AJ. Mesenchymal cells stimulate capillary morphogenesis via distinct proteolytic mechanisms. Experimental Cell Research 316, 813, 2010.

18. Sorrell JM, Baber MA, Caplan AI. Influence of adult mesenchymal stem cells on in vitro vascular formation. Tissue Engineering Part A 15, 1751, 2009.

19. Duffy GP, Ahsan T, O'Brien T, Barry F, Nerem RM. Bone marrow-derived mesenchymal stem cells promote angiogenic processes in a time- and dose-dependent manner in vitro. 15, 2459, 2009.

20. Ghajar CM, Blevins KS, Hughes CCW, George SC, Putnam AJ. Mesenchymal Stem Cells Enhance Angiogenesis in Mechanically Viable Prevascularized Tissues via Early Matrix Metalloproteinase Upregulation. Tissue Engineering 12, 2875, 2006.

21. Gruber R, Kandler B, Holzmann P, Vogele-Kadletz M, Losert U, Fischer MB, Watzek G. Bone Marrow Stromal Cells Provide a Local Environment That Favors Migration and Formation of Tubular Structures of Endothelial Cells. Tissue Engineering 11, 896, 2005.

22. Pati S, Khakoo AY, Zhao J, Jimenez F, Gerber MH, Harting M, Redell JB, Grill R, Matsuo Y, Guha S, Cox CS Retz MS, Holcomb JB, Dash PK. Human mesenchymal stem cells inhibit vascular permeability by modulating vascular endothelial cadherin/β-catenin signaling. Stem Cells and Development 20, 89, 2011.

23. Caplan AI. All bmMSCs are pericytes? Cell Stem Cell 3, 229, 2008.

24. Ma J, van den Beucken JJJP, Yang F, Both SK, Cui F-Z, Pan J, Jansen JA. Coculture of Osteoblasts and Endothelial Cells: Optimization of Culture Medium and Cell Ratio. Tissue Engineering Part C: Methods 17, 349, 2011.

25. Melero-Martin JM, De Obaldia ME, Kang S-Y, Khan ZA, Yuan L, Oettgen P, Bischoff J. Engineering Robust and Functional Vascular Networks In Vivo With Human Adult and Cord Blood–Derived Progenitor Cells. Circulation Research 103, 194, 2008.

26. Rouwkema J, De Boer J, Van Blitterswijk CA. Endothelial Cells Assemble into a 3-Dimensional Prevascular Network in a Bone Tissue Engineering Construct. Tissue Engineering 12, 2685, 2006.

27. Dietrich F, Lelkes PI. Fine-tuning of a three-dimensional microcarrier-based angiogenesis assay for the analysis of endothelial-mesenchymal cell co-cultures in fibrin and collagen gels. Angiogenesis 9, 111, 2006.

28. Martineau L, Doillon CJ. Angiogenic response of endothelial cells seeded dispersed versus on beads in fibrin gels. Angiogenesis 10, 269, 2007.

29. Kroon ME, van Schie MLJ, van der Vecht B, van Hinsbergh VWM, Koolwijk P. Collagen type I retards tube formation by human microvascular endothelial cells in a fibrin matrix. Angiogenesis 5, 257, 2002.

30. Rowe SL, Stegemann J. Interpenetrating Collagen-Fibrin Composite Matrices with Varying Protein Contents and Ratios. Biomacromolecules 7, 2942, 2006.

31. Rowe SL, Stegemann JP. Microstructure and Mechanics of Collagen-Fibrin Matrices Polymerized Using Ancrod Snake Venom Enzyme. Journal of Biomechanical Engineering 131, 061012, 2009.

32. Critser PJ, Kreger ST, Voytik-Harbin SL, Yoder MC. Collagen matrix physical properties modulate endothelial colony forming cell-derived vessels in vivo. Microvascular Research 80, 23, 2010.

33. Kniazeva E, Kachgal S, Putnam AJ. Effects of Extracellular Matrix Density and Mesenchymal Stem Cells on Neovascularization In Vivo. Tissue Engineering Part A 17, 905, 2011.

34. Allen P, Melero-Martin J, Bischoff J. Type I collagen, fibrin and PuraMatrix matrices provide permissive environments for human endothelial and mesenchymal progenitor cells to form neovascular networks. Journal of Tissue Engineering and Regenerative Medicine 5, e74, 2011.

35. Wang L, Stegemann JP. Glyoxal crosslinking of cell-seeded chitosan/collagen hydrogels for bone regeneration. Acta Biomaterialia 7, 2410, 2011.

36. Kotlarchyk MA, Shreim SG, Alvarez-Elizondo MB, Estrada LC, Singh R, Valdevit L, Kniazeva E, Gratton E, Putnam AJ, Botvinick EL. Concentration Independent Modulation of Local Micromechanics in a Fibrin Gel. PLOS One 6, e20201, 2011.

37. Collen A, Koolwijk P, Kroon ME, Van Hinsbergh VWM. Influence of fibrin structure on the formation and maintenance of capillary-like tubules by human microvascular endothelial cells. Angiogenesis 2, 153, 1998.

38. Seidlits SK, Drinnan CT, Petersen RR, Shear JB, Suggs LJ, Schmidt CE. Fibronectin-hyaluronic acid composite hydrogels for three-dimensional endothelial cell culture. Acta Biomaterialia 7, 2401, 2011.

39. Bala K, Ambwani K, Gohil NK. Effect of different mitogens and serum concentration on HUVHUVEC morphology and characteristics: Implication on use of higher passage cells. Tissue and Cell 43, 216, 2011.

40. Rao RR, He J, Leach JK. Biomineralized composite substrates increase gene expression with nonviral delivery. Journal of Biomedical Materials Research Part A 94, 344, 2010.

CHAPTER 5

Effects of Hydroxyapatite on Endothelial Network Formation in Collagen/Fibrin Composite Hydrogels In Vitro and In Vivo

5.1 Introduction

Transplantation and engraftment of engineered tissues requires creation of a vascular supply, either through vasculogenesis, the *de novo* formation of blood vessels, or through angiogenesis, the creation of new vessels via sprouting from existing vasculature [1]. The diffusive limit for nutrient transport in most tissues has been suggested to be only a few hundred microns, and therefore a new vascular supply to implanted tissue must be created to provide convective transport to the region [2]. A variety of model systems have been created to study the process of vasculogenesis, including 3D systems using extracellular matrix proteins such as collagen, fibrin, and Matrigel® [3-6]. Previous work in our lab has shown composite collagen/fibrin (COL/FIB) matrices to be permissive to endothelial network formation *in vitro* when human umbilical vein endothelial cells (HUVEC) are co-cultured with bone marrow-derived mesenchymal stem cells (bmMSC) [7]. The degree of vasculogenesis was shown to be dependent on HUVEC:bmMSC ratio and the composition of the matrix.

In most studies of vasculogenesis in 3D hydrogels *in vitro*, volume reduction of the matrix is prevented by constraining the sample at its boundaries. This technique prevents remodeling and compaction of the matrix by the contractile forces exerted by embedded cells. Unconstrained gel compaction leads to increased matrix density and a concomitant increase in matrix stiffness [8, 9]. It is has been suggested that matrix mechanics play an important role in

regulating endothelial network formation. Increased stiffness has been shown to promote angiogenesis in some studies [10, 11], while other studies have shown an inverse relationship between increased matrix stiffness and neovessel growth, both *in vitro* and *in vivo* [3, 7, 12-15]. In addition, unconstrained gel compaction has been shown to result in the regression of endothelial networks *in vitro* [16, 17].

Bioceramics have been included in vasculogenesis and angiogenesis models to promote neovessel growth both *in vitro* and *in vivo* for bone tissue engineering applications. Bioactive glasses are ceramics containing oxidized mineral that have been shown to be proangiogenic at low concentrations, presumably by increasing endothelial cell proliferation via dissolution into ionic components [18-22]. Similarly, hydroxyapatite (HA) is the mineral component of bone, and also has been examined for its ability to promote both vasculogenesis and angiogenesis. Low concentrations of HA have been shown to be compatible with HUVEC, and to maintain the prototypical morphology and biochemical markers associated with normal HUVEC function [23, 24]. HA has also been incorporated into 3D silk scaffolds designed to promote angiogenesis [25], and it has been observed that production of vascular endothelial growth factor (VEGF) from bmMSC is increased on poly (lactide-*co*-glycolide)-HA composite scaffolds [26]. In addition to its proangiogenic biochemical effects, it has been suggested that HA can inhibit cell-mediated compaction of protein hydrogels by providing structural integrity to the extracellular matrix [27].

In the current study, we examined the addition of HA to COL/FIB composite hydrogels, as a means to modulate the degree of vasculogenesis by seeded HUVEC and bmMSC in both constrained and unconstrained model systems. Our motivation was the observation that vasculogenesis is inhibited in unconstrained 3D hydrogels due to matrix compaction, but that HA can have both proangiogenic effects and can reduce gel remodeling. We systematically added

HA to 3D composite hydrogels and examined vascular network formation *in vitro*. We also measured matrix compaction and the mechanical properties of the hydrogels in an effort to understand the relationship between construct morphology and vasculogenic response. Cell-seeded COL/FIB/HA constructs were then implanted subcutaneously into mice to determine whether the effects of HA translated to changes in neovascularization in vivo. These studies demonstrate the use of HA in protein-based composite matrices, and contribute to our understanding of how vasculogenesis can be modulated in bone tissue engineering applications.

5.2 Materials and Methods

Cell Culture

Human umbilical vein endothelial cells (HUVEC) were harvested from umbilical cords as previously described [7]. Briefly, umbilical veins were irrigated with sterile phosphate buffered saline (PBS) and then incubated with 0.1% collagenase (Type I, Worthington Biochemical, Lakewood, NJ) at 37°C for 20 min. The digestion product was collected, the vein was washed with PBS, and the resulting suspension was centrifuged. The cell pellet was re-suspended in Endothelial Growth Medium-2 (EGM-2, Lonza) and plated into flasks. After 24 hours, the cells were washed with PBS to remove residual erythrocytes. HUVEC were cultured in Endothelial Growth Medium-2 (EGM-2; Lonza Inc., Walkersville, MD, USA) and used at passage 4. Human bone marrow-derived mesenchymal stem cells (bmMSC; Lonza) were cultured in Dulbecco's modified Eagles medium – low glucose (DMEM; Thermo Scientific; Logan, UT, USA) with 10% fetal bovine serum (FBS; Invitrogen, Carlsbad, CA, USA) and 1% penicillin and streptomyocin (Invitrogen) and used at passage 7. Media was changed every other day for both cells types.

Formation of Three-Dimensional Collagen/Fibrin/Hydroxyapatite Hydrogels

Collagen/fibrin (COL/FIB) composite hydrogels were created as previously described [7]. Briefly, bovine skin COL Type I (4.0 mg/ml; MP Biomedicals, Solon, OH, USA) was dissolved in 0.02 N acetic acid and bovine fibrinogen (4.0 mg/ml; Sigma Aldrich, St. Louis, MO, USA) was dissolved in EGM-2. Stock solutions of hydroxyapatite (HA; Sigma) were prepared at concentrations of 0, 12.5, 25, 50, 100, and 200 mg/ml HA in DMEM and sonicated for 1 hour prior to use to facilitate homogenous dispersion in hydrogels [28]. Hydrogels were formed by adding COL and FIB at a mass ratio of 40/60 (total protein concentration 2.5 mg/ml) to a mixture of 10% FBS, 10% 5X-concentrated DMEM, 5% 0.1 N NaOH, 2% thrombin (0.1 UT/ml; Sigma), and 10% HA in DMEM at 4ºC. The resulting final concentrations of HA in the hydrogels were 0, 1.25, 2.5, 5, 10, and 20 mg/ml. Matrix mixtures were placed into a 24-well plate and gelled at 37ºC for 45 minutes. Both HUVEC and bmMSC were added directly into the gel mixture at a ratio of 1:1 HUVEC:bmMSC and a total cell concentration of (2.4×10^5 cells/ml). For constrained culture studies, hydrogels were kept in the original 24-well plates and adhered to the walls of the wells. For unconstrained studies, constructs were freed from the well walls and were transferred to non-tissue culture treated 6-well plates. All hydrogels were cultured in EGM-2 for 7 days at 37ºC and 5% CO_2.

Endothelial Network Formation Assay

Vessel-like structure formation was quantified as previously described [7]. Briefly, HUVEC were labeled through a retroviral expression system (Orbigen Inc., San Diego, CA, USA) to enable stable expression of a fluorescent protein (mCherry; Clontech, Mountain View,

CA, USA). Cell-seeded hydrogels were imaged at day 7 with a fluorescent microscope (Olympus America Inc., Center Valley, PA, USA). For both constrained and unconstrained hydrogels, five representative images were taken of each gel and analyzed using the Angiogenesis Tube Module in Metamorph Premier Software (Molecular Devices Inc., Sunnyvale, CA, USA). Total network length of vessel-like structures formed *in vitro* was calculated by setting a minimum width, maximum width, and intensity over background.

Mechanical Properties Testing

Gel rheology was performed on acellular COL/FIB/HA hydrogels as previously described [7]. Briefly, pre-formed COL/FIB/HA solutions were loaded into a gel rheometer (AR-G2, TA Instruments, New Castle, DE, USA) and a time sweep was conducted for 45 minutes at 37ºC. The storage (G') and loss (G'') moduli were calculated from the final 5 minutes of the time sweep.

Compressive testing was performed by placing hydrogels under uniaxial compression using a 1.5 mm hemispherical indenter mounted on a 50 g load cell in a Test Resources frame (Test Resources Inc., Shakopee, MN, USA). Samples were removed from buffer and mounted on a dry rubber block to prevent slipping. Each was compressed at a rate of 0.33 cm/s and force-displacement curves were generated at a sample rate of 200 Hz. Force-displacement curves were truncated to less than 25% compression and the Young's Modulus (E) was determined from the equation below [29] using a non-linear least squares algorithm implemented in MATLAB.

$$E = \frac{3F}{4r^{\frac{1}{2}}} \frac{(1-\nu^2)}{d^{\frac{3}{2}}}$$

E is the compressive Young's modulus

F is the load measured by the load cell

r is the radius of the indenter

ν is the Poisson's ratio (assumed to be 0.5)

d is the depth of penetration measured by the linear encoder

Measurement of Gel Compaction and 3-D Ultrasound Imaging

Representative images of unconstrained hydrogels were taken using a standard CCD camera in manual mode with a constant exposure setting at days 0, 1, 3, 5, and 7 to qualitatively demonstrate gel compaction throughout the time course. Ultrasound imaging of the constructs was performed with a Vevo 770 (VisualSonics Inc., Toronto, Canada) using an RMV 707B imaging probe with a nominal 30 MHz center frequency, 15-45 MHz bandwidth (−6 dB), 12.7 mm focal distance, and 2.2 mm depth of focus (−6 dB), as described previously [28]. For each gel, a 3D ultrasound image data containing a series of consecutive B-mode images with a spatial interval of 100 μm was collected. The interval between adjacent A-lines in a B-mode cross-sectional image was 50 μm. Volumes of these gels were measured from the ultrasound images using a semi-automated segmentation procedure, in which an edge detection algorithm identified the contour of the gel in an ultrasound B-mode image. Subsequent contours in adjacent frames or images were drawn semi-automatically until the contours in all frames were drawn, thus providing the volume of the gel within the contoured region.

Subcutaneous Implants

All animal studies were conducted in accordance with the National Institutes of Health Guidelines following a protocol approved by the University of Michigan Committee on Use and Care of Animals. Seven-week old male C.B.-17/SCID mice (Taconic Labs, Hudson, NY, USA)

were administered an anesthetic analgesic drug cocktail containing ketamine (95 mg/kg, Fort Dodge Animal Health, Fort Dodge, IA), xylazine (9.5 mg/kg, Lloyd Laboratories, Shenandoah, IA), and buprenorphine (0.059 mg/kg, Bedford Laboratories, Bedford, OH) via intraperitoneal injection. Each mouse was shaved and sterilized with Betadine® (Thermo Fisher Scientific, Fremont, CA) on its dorsal surface and wiped with alcohol prior to injection. COL/FIB/HA constructs containing 0, 2.5, or 20 mg/ml HA and a total cell concentration of 10.0×10^6 cells/ml were used for the *in vivo* studies. Acellular constructs served as controls. Two implants per animal were created with gel solutions of 300 µl. After injection, animals were kept stationary for 5 minutes and then placed in fresh cages.

Laser Doppler Perfusion Imaging

Mice were anesthetized as previously described and blood flow through the implant was imaged using laser Doppler Perfusion Imaging (LDPI; Perimed AB, Sweden) [30]. Mice were imaged in triplicate and a region of interest (ROI) was overlayed over the implant area to calculate mean perfusion through each implant. Results were calculated as fold change from perfusion values over the baseline (before implantation).

Histology and Immunohistochemistry

Explants were retrieved at day 7 and then fixed in zinc-buffered formalin (Z-Fix; Anatech Ltd., Battle Creek, MI) overnight. Samples were sent to AML Laboratories (Baltimore, MD) for embedding in paraffin and sectioned into 5 µm sections. Sections were then demineralized in a solution of 10% ethylenediamine tetraacetic acid (EDTA; Sigma) and Z-Fix for 3 hours at 4ºC. Tissue sections were rehydrated, steamed in a vegetable steamer for 25 minutes in antigen

retrieval solution (Dako, Carpinteria, CA), and then equilibrated in Tris-buffered saline with Tween 20 (TBS-T; Sigma). Sections were then incubated at 4 ºC in human anti-mouse CD31 (Dako) diluted 1:50 in TBS-T overnight and then treated with horse radish peroxidase-conjugated anti-mouse secondary antibody. Hematoxylin and eosin (H&E) was used as a counterstain.

Quantification of In Vivo Vessel Formation

Blood vessels found within the implants were quantified manually by three blinded observers. Ten random images per sample at 20X magnification were used to quantify the number of human CD-31 stained vessels (i.e. those that arose from implanted cells) as well as the total number of vessels within the implant region. All vessels were quantified if they displayed a lumen containing erythrocytes and human vessels were identified if they displayed a positive CD31 stain around the lumen.

Statistical Analysis

All quantitative analyses were performed using a one-way analysis of variance test (ANOVA) with a protected Fisher's Least Significant Difference *post hoc* test. Statistical significance was set at $p < 0.05$. Numerical values and bare charts are presented as mean ± standard error.

5.3 Results

Vasculogenesis in Constrained and Unconstrained COL/FIB/HA Hydrogels

Figure 5.1 shows representative images and quantification of endothelial network formation in constrained COL/FIB/HA materials after 7 days of culture. At low concentrations of HA (1.25 and 2.5 mg/ml), formation of vessel-like structures was similar to control constructs (0 mg/ml HA). However, higher concentrations of HA (5, 10, 20 mg/mL) inhibited vascular network formation. Quantification of total network length in these samples showed no significant differences between the 0, 1.25, and 2.5 mg/ml conditions, but a statistically significant decrease in total network length between the control group and the 5, 10, and 20 mg/ml HA groups.

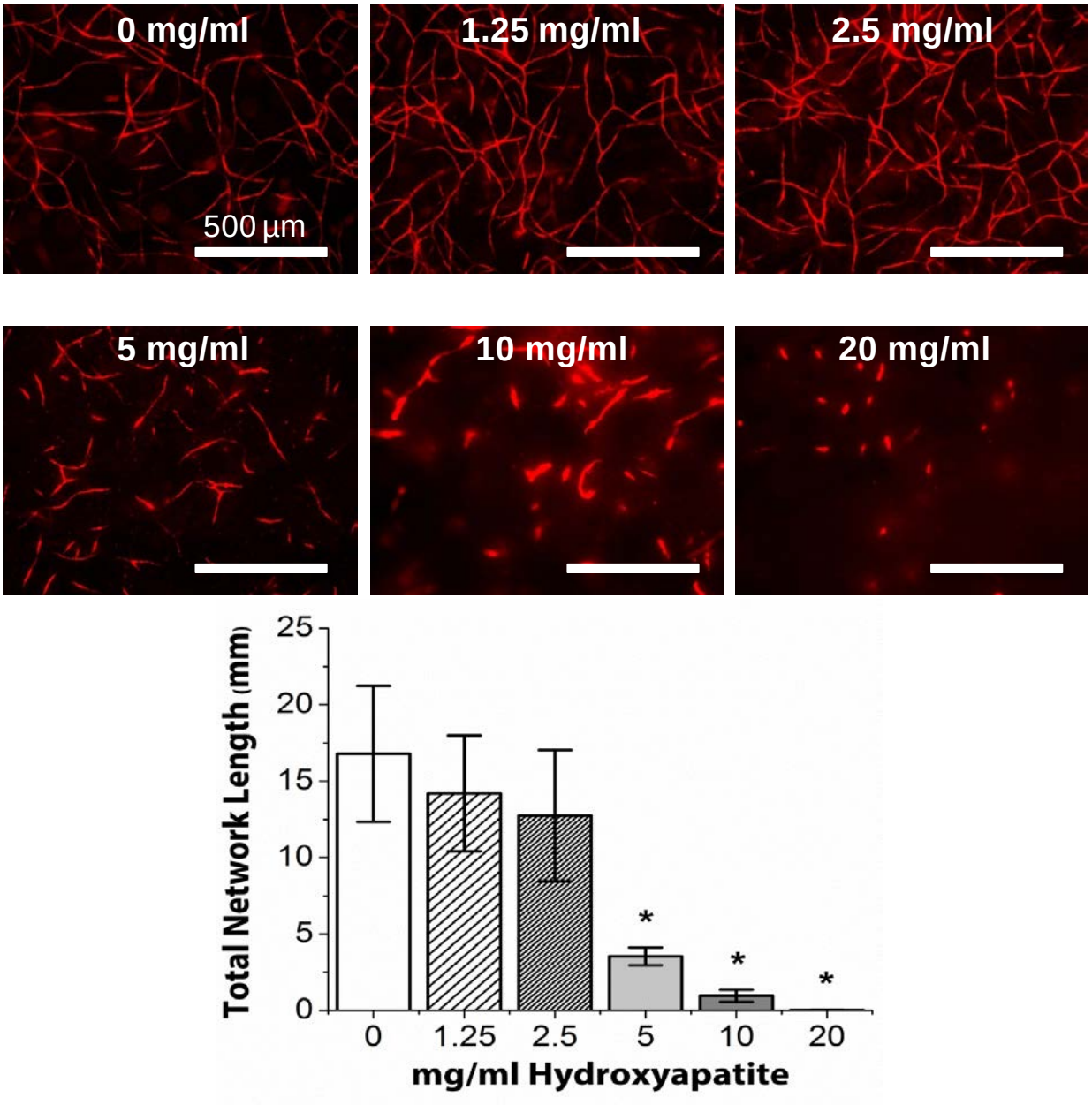

Figure 5.1: Endothelial network formation in constrained COL/FIB/HA composite hydrogels at day 7. Network formation was similar in COL/FIB/HA hydrogels containing 1.25 and 2.5 mg/ml HA compared to COL/FIB hydrogels. Upper panels show representative images of network structures in COL/FIB matrices at indicated HA concentrations. Graph shows quantification of total network length at each HA concentration. *Statistical significance ($p<0.05$) against 0 mg/ml (pure collagen/fibrin).

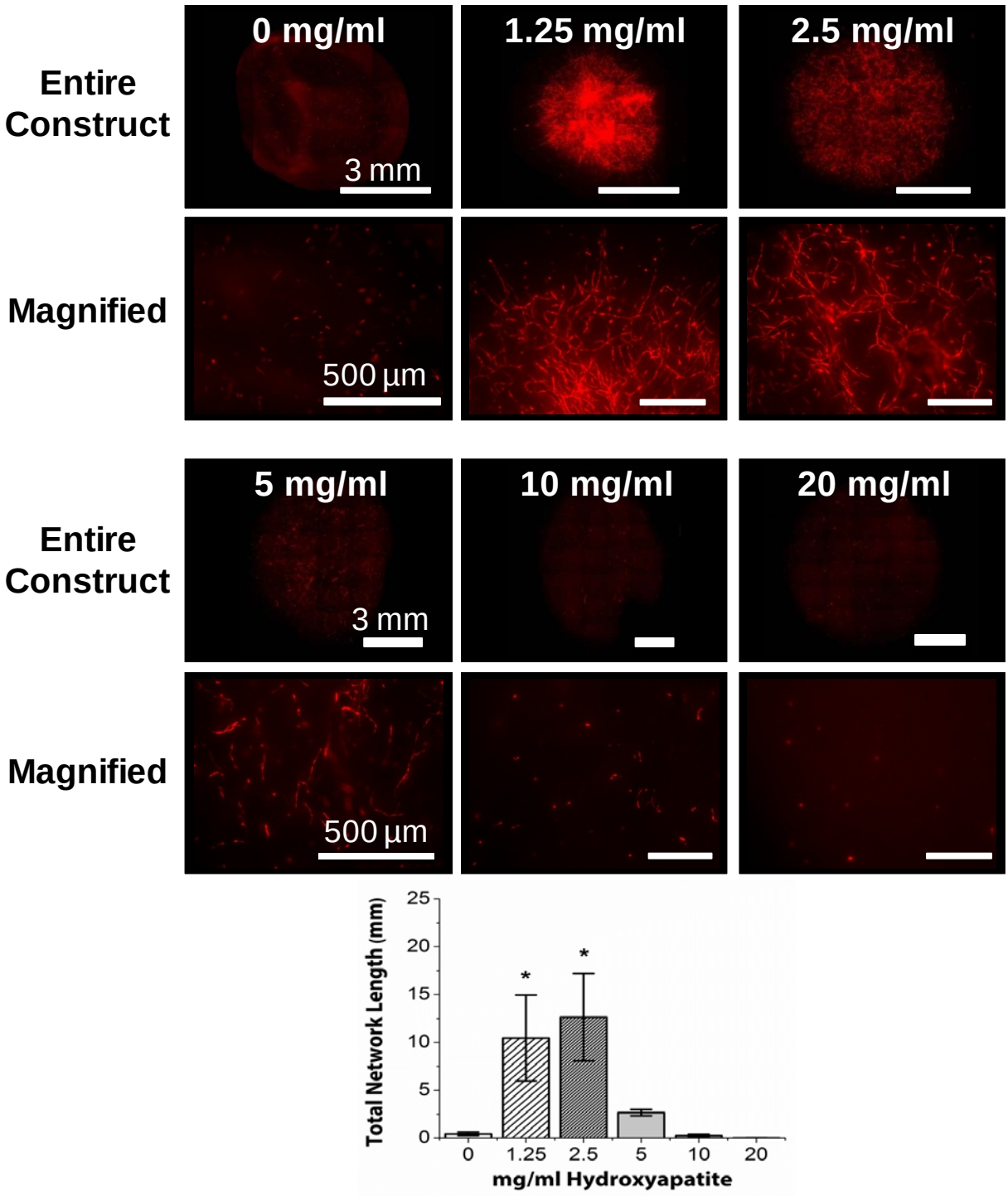

Figure 5.2: Endothelial network formation in unconstrained COL/FIB/HA composite hydrogels at day 7. Network formation was recovered in COL/FIB/HA hydrogels containing 1.25 and 2.5 mg/ml HA. Upper panels show representative images of network structures in COL/FIB matrices at indicated HA concentrations (both entire construct and magnified subsections are presented). Graph shows quantification of total network length at each HA concentration. *Statistical significance ($p<0.05$) against 0 mg/ml (pure collagen/fibrin).

Endothelial network formation in unconstrained COL/FIB/HA hydrogels after 7 days in culture is presented in Figure 5.2. Images of entire constructs, as well as magnified regions of each construct type are shown in order to clearly show the extent of vasculogenesis in these compacted gels. Endothelial network formation was dramatically reduced in constructs without HA (0 mg/ml), but addition of low concentrations of HA (1.25 and 2.5 mg/ml) lead to a recovery of vascular networks. Similar to the constrained hydrogels, there was a marked decrease in endothelial network formation in the hydrogels containing high concentrations of HA (5, 10 and 20 mg/ml). Quantification of total network length in these samples confirmed that the 1.25, and 2.5 mg/ml conditions were statistically greater than controls, whereas the 5, 10, and 20 mg/ml HA groups were not statistically different from controls. Notably, the degree of vessel formation in the 1.25, and 2.5 mg/ml groups was also statistically the same as in the constrained constructs without HA.

Hydrogel Compaction

Representative images of COL/FIB/HA hydrogels at day 0 (immediately after gelation) and at day 7 in unconstrained culture are shown in Figure 5.3. At the initial time point (day 0) all constructs are essentially the same size because cell-mediated compaction has not yet occurred. However, by day 7 the constructs have reduced their volume to varying degrees, depending on the HA content.

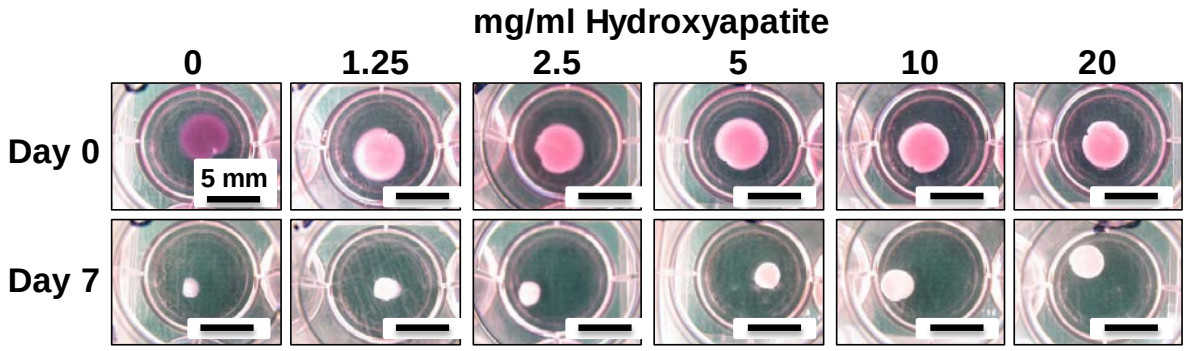

Figure 5.3: Compaction of COL/FIB/HA hydrogels after 7 days of culture. Images of COL/FIB/HA constructs in culture wells immediately after fabrication at day 0 (upper panels) and after 7 days of compaction (lower panels).

Figure 5.4 shows high resolution three-dimensional volume renderings and two-dimensional sections of constructs at day 7, obtained through non-invasive ultrasound imaging. Control constructs without HA (0 mg/ml) compacted strongly, and the degree of compaction generally decreased with increasing HA content. Quantification of construct volume from rendered ultrasound images showed that compaction in the 1.25, and 2.5 mg/ml conditions was not statistically different than controls, whereas the 5, 10, and 20 mg/ml HA groups compacted statistically significantly less than controls.

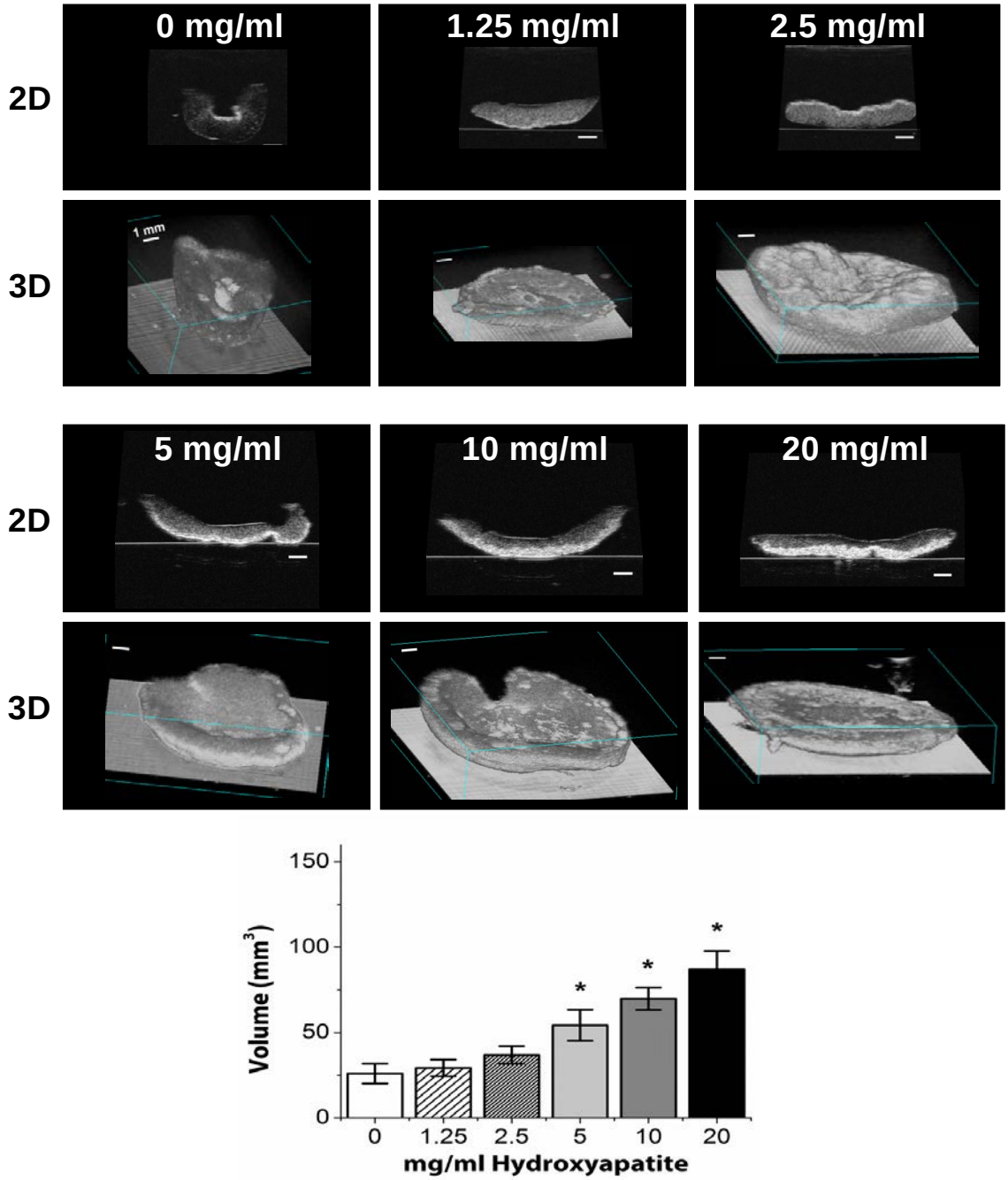

Figure 5.4: Ultrasound imaging and volumetric analysis of compacted COL/FIB/HA matrices. Images showing 2D sections (upper panels) and 3D volume renderings (lower panels) of COL/FIB/HA constructs after 7 days of unconstrained culture. Graph shows quantification of construct volume at each HA concentration. *Statistical significance ($p<0.05$) against 0 mg/ml (pure collagen/fibrin). Scale bar = 1 mm.

Mechanical Properties of COL/FIB/HA Hydrogels

Figure 5.5 shows mechanical properties data for COL/FIB/HA hydrogels, including the storage moduli at day 0 as determined by gel rheology, and the elastic moduli at day 7 as

determined by compressive testing. At the day 0 timepoint before the gels could compact, there was a statistically significant decrease in the storage modulus of the hydrogels when low concentrations of HA (1.25 and 2.5 mg/ml) were added, compared to the control 0 mg/ml condition. However, at higher HA concentrations (5, 10, 20 mg/ml), the mechanical properties at day 0 were statistically the same as control constructs. After gel compaction had occurred (day 7), compressive testing revealed that hydrogels containing 5 and 10 mg/ml hydroxyapatite were significantly stiffer than the 0 mg/ml condition, though the other conditions were not statistically different from controls without HA.

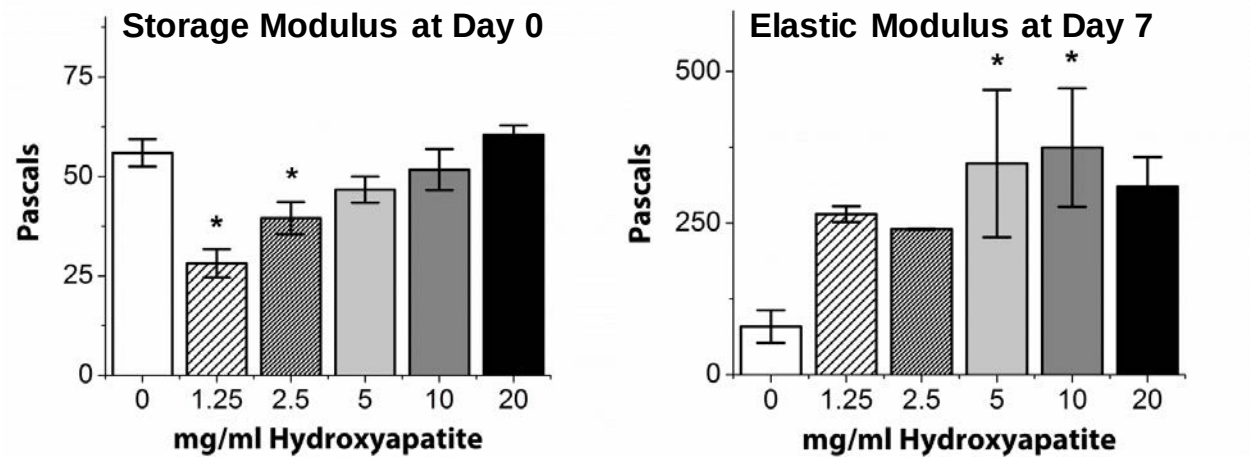

Figure 5.5: Mechanical property measurements of COL/FIB/HA matrices. Left graph shows average storage (G') moduli measured at the time of gelation. Right graph shows average elastic moduli of compacted gels measured after 7 days of unconstrained culture. *Statistical significance against 0 mg/ml HA (pure collagen/fibrin).

In Vivo Implantation of COL/FIB/HA Materials

Three HA concentrations, 0, 2.5, and 20 mg/ml, were chosen for implantation experiments to evaluate the effect of HA incorporation on vascularization *in vivo*. Laser Doppler perfusion imaging (LDPI) allowed for non-invasive quantification of blood perfusion throughout each implant at days 0 (immediately after implantation), 3, and 7, as shown in Figure 5.6. Perfusion to implants was increased significantly compared to baseline values in all conditions at

both days 3 and 7. However, there were no significant differences between the implants containing HA and those without.

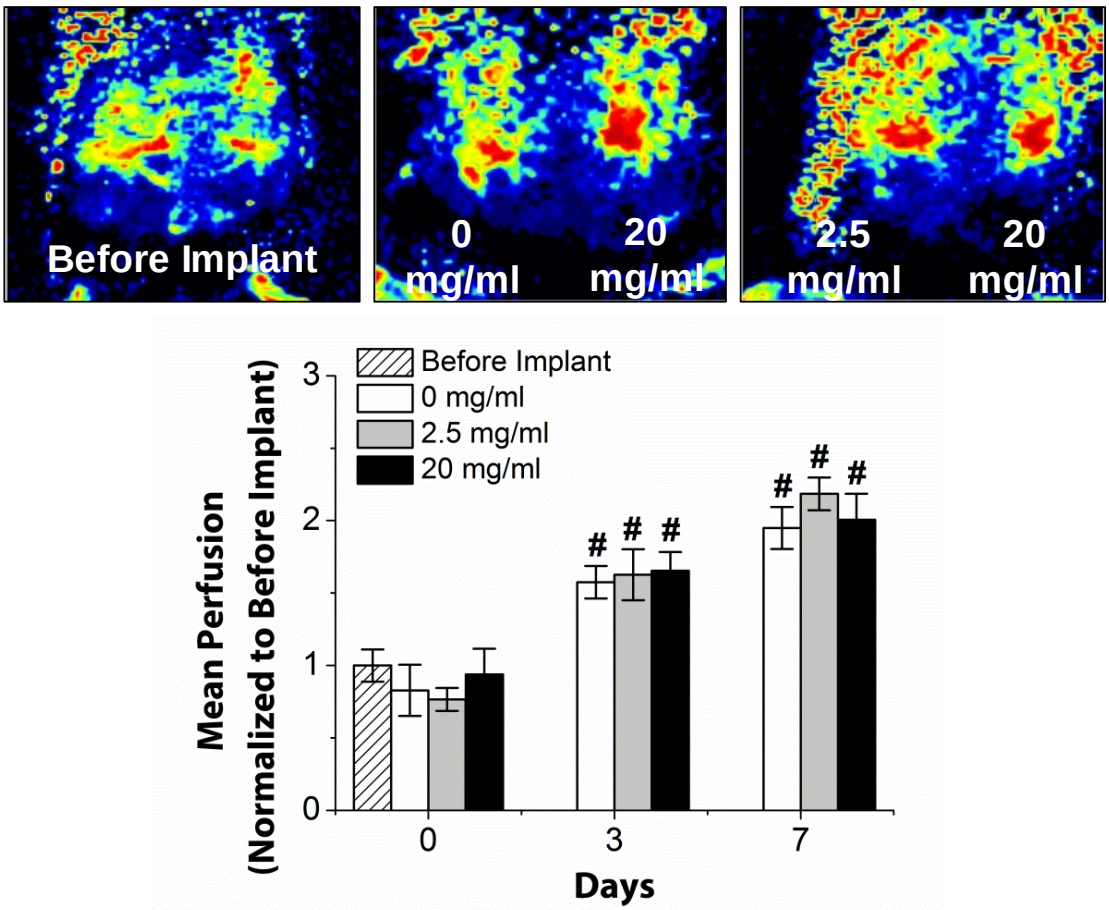

Figure 5.6: Laser Doppler perfusion imaging (LDPI) of implanted COL/FIB/HA materials. Blood perfusion was above baseline and similar in all conditions at all time points.Images show LDPI heat maps indicating degree of perfusion at day 7. Graph shows quantification of mean perfusion at indicated HA concentrations. *Statistical significance against 0 mg/ml (pure collagen/fibrin); #Statistical significance against baseline (Before Implantation).

Representative human CD31 and H&E stained sections from cellular implants are shown in Figure 5.7. In all samples, numerous capillaries containing erythrocytes were evident throughout the implant site. Mononuclear inflammatory cells were present in all three conditions suggesting a potential inflammatory reaction to the implanted materials. Further, free erythrocytes were located throughout the implant region, particularly in the lower HA containing hydrogels. There was also a rich supply of small, positively-stained human capillaries within all

of the HA conditions. Quantification of both the number of human vessels and the total number of vessels within the implant area yielded no significant differences between the three implanted conditions (0, 2.5, and 20 mg/ml). In contrast, acellular control constructs with the same amounts of HA demonstrated no capillary formation and therefore vessel number was not quantified (Supplemental Figure 5.1).

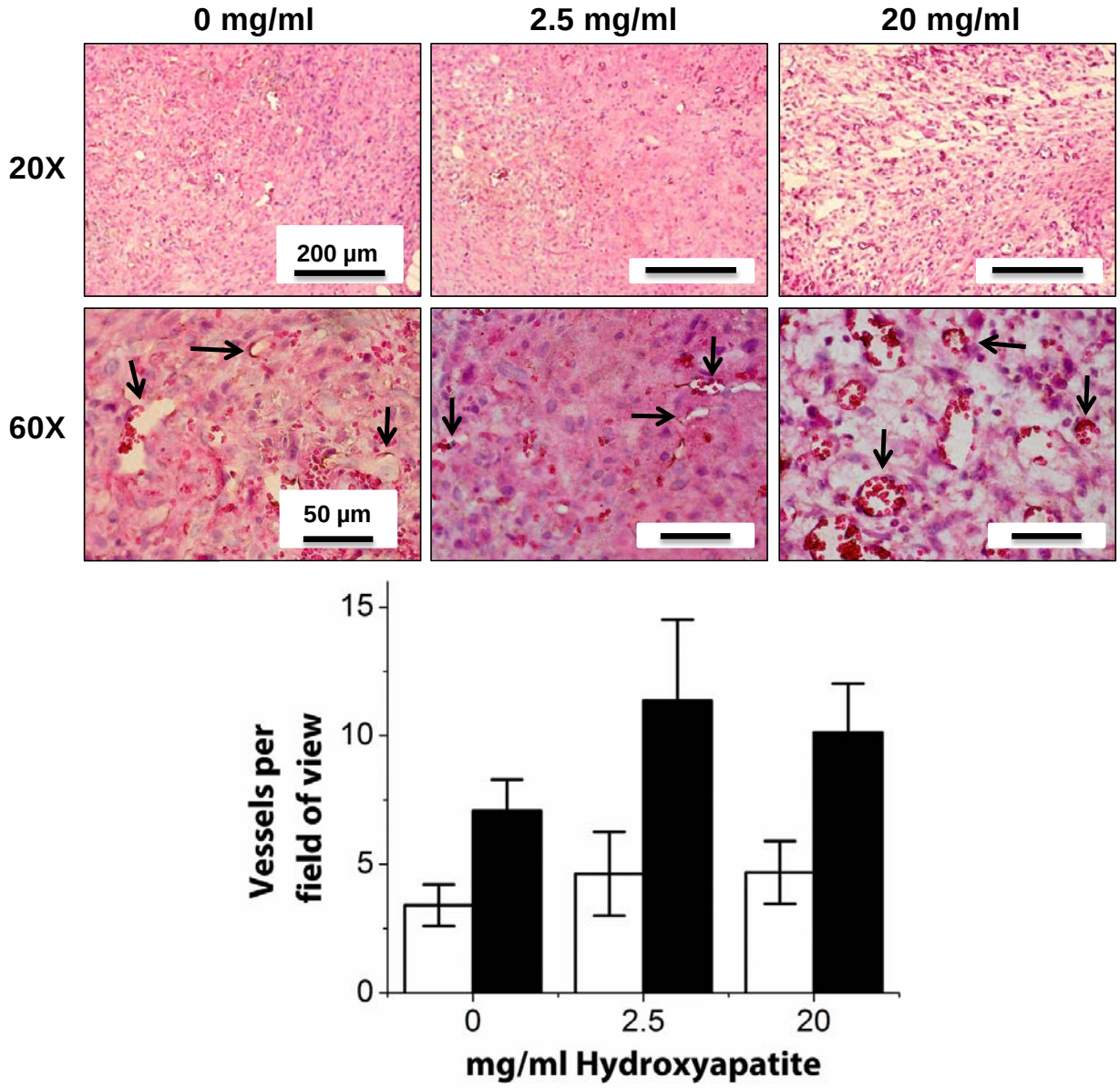

Figure 5.7: Histological analysis of COL/FIB/HA materials after 7 days of subcutaneous implantation in the mouse. There were no significant differences between the conditions after 7 days post-implantation. Image panels show human CD31 and H&E staining at two magnifications. Arrows point to new vessels. Graph shows quantification of number of human-derived vessels and total number of vessels.

5.4 Discussion

COL/FIB materials are known to support vasculogenesis, and in this study we examined the effect of incorporating HA into the matrix on endothelial network formation. *In vitro*, we studied both constrained and unconstrained hydrogels. In constrained constructs, addition of less than 2.5 mg/ml HA resulted in similar levels of vasculogenesis as in COL/FIB hydrogels containing no HA. However, amounts of HA above 5 mg/ml were shown to be detrimental to vasculogenesis in constrained constructs. In unconstrained hydrogels containing no HA, vascular network formation was essentially abolished. Addition of low levels of HA was successful in rescuing the vasculogenic response, even though these hydrogels compacted to a similar degree. However higher HA levels were again detrimental to network formation in unconstrained hydrogels, in spite of diminished gel compaction. The beneficial effect of low levels of HA did not translate to *in vivo* implants, as all conditions resulted in similar degrees of both xenogeneic and host vasculature within the implant region.

The compaction of protein hydrogels is a well characterized phenomenon caused by cell contractile forces that result in remodeling of the extracellular matrix. This process has been shown to cause regression of endothelial tube assembly [16] and we observed similar anti-vasculogenic effects in our unconstrained hydrogel studies. The addition of low concentrations of HA to unconstrained COL/FIB hydrogels rescued endothelial network formation to the point where it was statistically indistinguishable from control constrained gels without HA. The mechanism of action of this effect is not clear, but may be related to increased secretion of VEGF from bmMSC in response to the HA, increased adsorption of proangiogenic growth factors and cytokines to the HA, or modulation of matrix metalloproteinase activity.

The relationship between the degree of vasculogenesis and the bulk mechanical properties of COL/FIB matrices has been previously investigated [7]. In the present study, matrix stiffness at day 0 was slightly reduced by the addition of low levels of HA, but these differences were abolished as the gel compacted. By day 7, the 5 and 10 mg/ml loading levels were more stiff than the control, but the other conditions were statistically the same as the control. In addition, quantitative assessment of construct volume using ultrasound imaging showed that low concentrations of HA yielded a similar degree of compaction as hydrogels without HA. Therefore the effect of HA does not seem to be mediated by mechanical properties or by changes in gel compaction, though it may have affected related factors such as matrix architecture, ligand binding density, mass transport, and matrix porosity.

In vivo implantation of COL/FIB/HA composite gels showed no beneficial effect of the HA component on perfusion. Perfusion values measured through LDPI increased over time in all implants, indicating increased blood flow relative to the pre-implant level. By day 7, human-derived vasculature was evident in the implant site in all conditions, as indicated by vessels that stained positive for human CD31. Host vasculature also infiltrated the implants, suggesting possible pro-angiogenic properties of composite COL/FIB/HA matrices. It is interesting to note that while HA was not clearly beneficial to vascular network formation *in vivo*, neither was it detrimental. Even the relatively high 20 mg/ml HA level, which strongly inhibited vasculogenesis *in vitro*, showed good perfusion and neovascularization *in vivo*. The differences between *in vitro* and *in vivo* results may be due to the richer and more complex environment in native tissue. Resident and recruited cells such as monocytes, leukocytes, and macrophages may secrete cytokines and other factors that mask or overcome the effects of transplanted HA.

This study has demonstrated that formation of endothelial networks in COL/FIB hydrogels is affected by the culture method, and in particular that unconstrained compaction of these matrices results in a loss of vasculogenesis. This response could be recovered in unconstrained matrices *in vitro* by the addition of relatively low concentrations of HA. However, the effect of HA did not translate to *in vivo* subcutaneous implants, which were unaffected by the presence of HA. While the mechanism of HA-enhanced network formation *in vitro* is not clear, these findings have relevance to the development of biomaterials for bone tissue engineering. HA is used widely as an additive and as a scaffold for promoting bone regeneration. As larger bone defects are targeted, the concomitant creation of a vasculature as the bone heals has become a main goal of orthopaedic tissue engineers. Understanding the effect of HA in protein-based and other biomaterial systems will facilitate design of scaffolds that are effective in generating the desired physiological response.

5.5 Supplemental Figures

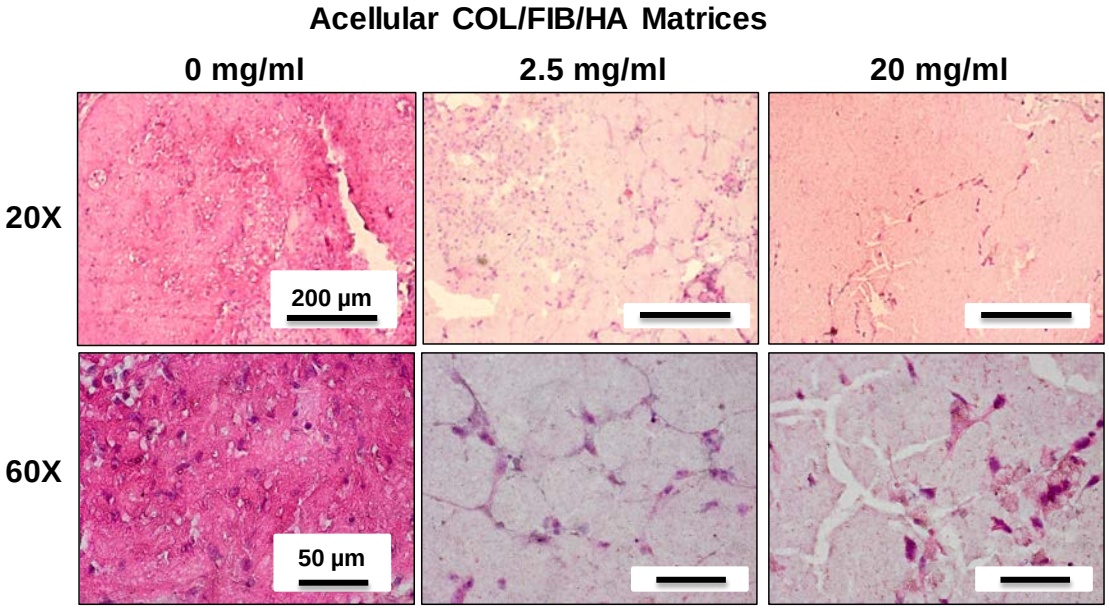

Supplemental Figure 5.1: Histological analysis of acellular COL/FIB/HA matrices after 7 days of subcutaneous implantation in the mouse. No vessels were observed after 7 days post-implantation. Image panels show human CD31 and H&E staining at two magnifications.

5.5 References

1. Jain RK. Molecular regulation of vessel maturation. Nat Med 9, 685, 2003.

2. Novosel HUVEC, Kleinhans C, Kluger PJ. Vascularization is the key challenge in tissue engineering. Adv Drug Deliv Rev 63, 300, 2011.

3. Allen P, Melero-Martin J, Bischoff J. Type I collagen, fibrin and PuraMatrix matrices provide permissive environments for human endothelial and mesenchymal progenitor cells to form neovascular networks. J Tissue Eng Regen Med 5, e74, 2011.

4. Dietrich F, Lelkes PI. Fine-tuning of a three-dimensional microcarrier-based angiogenesis assay for the analysis of endothelial-mesenchymal cell co-cultures in fibrin and collagen gels. Angiogenesis 9, 111, 2006

5. Martineau L, Doillon CJ. Angiogenic response of endothelial cells seeded dispersed versus on beads in fibrin gels. Angiogenesis 10, 269, 2007.

6. Melero-Martin JM, De Obaldia ME, Kang SY, Khan ZA, Yuan L, Oettgen P, Bischoff J. Engineering robust and functional vascular networks in vivo with human adult and cord blood-derived progenitor cells. Circ Res 103, 194, 2008.

7. Rao RR, Peterson AW, Ceccarelli J, Putnam AJ, Stegemann JP. Matrix composition regulates three-dimensional network formation by endothelial cells and mesenchymal stem cells in collagen/fibrin materials. Angiogenesis 15, 253, 2012.

8. Fernandez P, Bausch AR. The compaction of gels by cells: a case of collective mechanical activity. Integr Biol (Camb) 1, 252, 2009.

9. Lund AW, Bilgin CC, Hasan MA, McKeen LM, Stegemann JP, Yener B, Zaki MJ, Plopper GE. Quantification of spatial parameters in 3D cellular constructs using graph theory. J Biomed Biotechnol 2009, 928286, 2009.

10. Mason BN, Starchenko A, Williams RM, Bonassar LJ, Reinhart-King CA. Tuning three-dimensional collagen matrix stiffness independently of collagen concentration modulates endothelial cell behavior. Acta Biomater 9, 4635, 2013.

11. Lee PF, Bai Y, Smith RL, Bayless KJ, Yeh AT. Angiogenic responses are enhanced in mechanically and microscopically characterized, microbial transglutaminase crosslinked collagen matrices with increased stiffness. Acta Biomater 9, 7178, 2013.

12. Critser PJ, Kreger ST, Voytik-Harbin SL, Yoder MC. Collagen matrix physical properties modulate endothelial colony forming cell-derived vessels in vivo. Microvasc Res 80, 23, 2010.

13. Ghajar CM, Blevins KS, Hughes CC, George SC, Putnam AJ. Mesenchymal stem cells enhance angiogenesis in mechanically viable prevascularized tissues via early matrix metalloproteinase upregulation. Tissue Eng 12, 2875, 2006.

14. Ghajar CM, Chen X, Harris JW, Suresh V, Hughes CC, Jeon NL, Putnam AJ, George SC. The effect of matrix density on the regulation of 3-D capillary morphogenesis. Biophys J 94, 1930, 2008.

15. Kniazeva E, Kachgal S, Putnam AJ. Effects of extracellular matrix density and mesenchymal stem cells on neovascularization in vivo. Tissue Eng Part A 17, 905, 2011.

16. Davis GE, Pintar Allen KA, Salazar R, Maxwell SA. Matrix metalloproteinase-1 and -9 activation by plasmin regulates a novel endothelial cell-mediated mechanism of collagen gel contraction and capillary tube regression in three-dimensional collagen matrices. J Cell Sci 114, 917, 2001.

17. Saunders WB, Bayless KJ, Davis GE. MMP-1 activation by serine proteases and MMP-10 induces human capillary tubular network collapse and regression in 3D collagen matrices. J Cell Sci 118, 2325, 2005.

18. Bi L, Jung S, Day D, Neidig K, Dusevich V, Eick D, Bonewald L. Evaluation of bone regeneration, angiogenesis, and hydroxyapatite conversion in critical-sized rat calvarial defects implanted with bioactive glass scaffolds. J Biomed Mater Res A 100, 3267, 2012.

19. Gorustovich AA, Roether JA, Boccaccini AR. Effect of bioactive glasses on angiogenesis: a review of in vitro and in vivo evidences. Tissue Eng Part B Rev 16, 199, 2010.

20. Leach JK, Kaigler D, Wang Z, Krebsbach PH, Mooney DJ. Coating of VEGF-releasing scaffolds with bioactive glass for angiogenesis and bone regeneration. Biomaterials 27, 3249, 2006.
21. Leu A, Leach JK. Proangiogenic potential of a collagen/bioactive glass substrate. Pharm Res 25, 1222, 2008.

22. Leu A, Stieger SM, Dayton P, Ferrara KW, Leach JK. Angiogenic response to bioactive glass promotes bone healing in an irradiated calvarial defect. Tissue Eng Part A 15, 877, 2009.

23. Pezzatini S, Solito R, Morbidelli L, Lamponi S, Boanini E, Bigi A, Ziche M. The effect of hydroxyapatite nanocrystals on microvascular endothelial cell viability and functions. J Biomed Mater Res A 76, 656, 2006.

24. Rücker M, Laschke MW, Junker D, Carvalho C, Tavassol F, Mülhaupt R, Gellrich NC, Menger MD. Vascularization and biocompatibility of scaffolds consisting of different calcium phosphate compounds. J Biomed Mater Res A 86, 1002, 2008.

25. Sun L, Parker ST, Syoji D, Wang X, Lewis JA, Kaplan DL. Direct-write assembly of 3D silk/hydroxyapatite scaffolds for bone co-cultures. Adv Healthc Mater 1, 729, 2012.

26. He J, Decaris ML, Leach JK. Bioceramic-mediated trophic factor secretion by mesenchymal stem cells enhances in vitro endothelial cell persistence and in vivo angiogenesis. Tissue Eng Part A 18, 1520, 2012.

27. Liu Y, Williams DJ. Incorporation of hydroxyapatite sol into collagen gel to regulate the contraction mediated by human bone marrow-derived stromal cells. IEEE Trans Nanobioscience 9, 1, 2010.

28. Gudur M, Rao RR, Hsiao YS, Peterson AW, Deng CX, Stegemann JP. Noninvasive, Quantitative, Spatiotemporal Characterization of Mineralization in Three-Dimensional Collagen Hydrogels Using High-Resolution Spectral Ultrasound Imaging. Tissue Eng Part C Methods 18, 935, 2012.

29. Gent AN. On the relation between indentation hardness and Young's modulus. IRI Trans 34, 46, 1958.

30. Grainger SJ, Carrion B, Ceccarelli J, Putnam AJ. Stromal cell identity influences the in vivo functionality of engineered capillary networks formed by co-delivery of endothelial cells and stromal cells. Tissue Eng Part A 19, 1209, 2013.

CHAPTER 6

Dual-Phase Osteogenic and Vasculogenic Engineered Tissue for Bone Formation

6.1 Introduction

A main goal in orthopaedic tissue engineering is the regeneration of bone, and in particular to develop methods for improved healing of recalcitrant bone fractures and large defects. Many bone tissue engineering strategies aim to recapitulate the native structure of bone by combining cells, materials, and signaling molecules in defined architectures. The primary structural matrix of bone consists of a collagenous extracellular matrix mineralized by the hydroxyapatite (HA) [1]. Bone also contains a rich vascular supply within its structure, which is vital to maintaining its high metabolic demand [2]. Therefore both the osseous and the vascular components of bone are critical to forming functional tissue, and bone healing requires concomitant development of both components. This need for a blood supply to nourish newly forming bone has motivated a variety of approaches to engineering vascularized bone tissue.

Controlled delivery of multiple growth factors is one strategy to achieve regeneration of vascularized bone tissue, though the results have been mixed. Patel and coworkers co-delivered bone morphogenetic protein-2 (BMP-2) and vascular endothelial growth factor (VEGF) in an orthotopic rat critical size defect [3]. The dual (BMP-2 + VEGF) group exhibited significantly higher bone volume percentage as measured by micro-computed tomography at 4 weeks compared to the other conditions, but was not statistically different from the other groups at 12 weeks. In later work by the same group, the doses of each of the growth factors were varied in an

attempt to reduce BMP-2 concentration while achieving comparable bone formation, however the co-delivery of BMP-2 and VEGF did not result in an increase in bone formation compared to BMP-2 alone [4]. In another study, Shah and coworkers evaluated the use of polyelectrolyte films to control delivery rates of BMP-2 and VEGF and demonstrated enhanced bone formation measured by micro-computed tomography in the dual delivery group, compared to BMP-2 alone at 9 weeks [5]. Similarly, genetic modification of bone marrow-derived mesenchymal stem cells (bmMSC) for the constitutive delivery of both BMP-2 and VEGF demonstrated enhanced healing in the dual group compared to either growth factor alone [6]. These studies have demonstrated the potential promise of dual growth factor release, but the approach is hampered by the complexity of controlling dosing and obtaining the needed temporal release profile [7-10].

Cell-based approaches to vascularized bone tissue engineering also are being pursued [11, 12]. Numerous studies have shown that co-culture of endothelial cells and osteogenic cells allows for the formation of both vascular networks and mineralized tissue post-implantation. Kaigler and coworkers implanted poly(lactide-co-glycolide) (PLGA) scaffolds containing a co-culture of human microvascular endothelial cells (HMVEC) and bone-marrow derived mesenchymal stem cells (bmMSC) into immunodeficient mice and monitored ectopic bone formation over 8 weeks [13]. Total vasculature was similar in the implants containing both cell types (bmMSC+HMVEC) compared to the bmMSC alone, but bone formation was significantly higher in the dual cell condition compared to bmMSC alone. Usami and coworkers also demonstrated ectopic bone formation through the co-transplantation of endothelial progenitor cells (EPC) and bmMSC on collagen fiber meshes [14]. Both neovasculature and bone formation were significantly higher in the bmMSC+EPC group at 12 weeks post-implantation.

Orthotopic models have also been used to demonstrate osteogenesis induced by transplant of multiple cell types. Grellier and coworkers delivered alginate microspheres seeded with human umbilical vein endothelial cells (HUVEC) and bmMSC into a femoral defect model in immunocompromised mice [15]. Enhanced bone regeneration was observed in the dual condition (bmMSC+HUVEC) compared to the bmMSC group alone. In an attempt to look at the effects of pre-differentiation, Tsigkou and coworkers first seeded bmMSC on PLGA scaffolds and then cultured the cell-seeded scaffolds for one week in osteogenic supplemented medium to induce differentiation [16]. The scaffold was then coated with a collagen/fibronectin hydrogel containing bmMSC and HUVEC and implanted subcutaneously into immunodeficient mice. Both perfused human vasculature and bone formation were observed after 8 weeks post-implantation, suggesting an added benefit to pre-differentiating bmMSC prior to implantation in forming vascularized bone tissue.

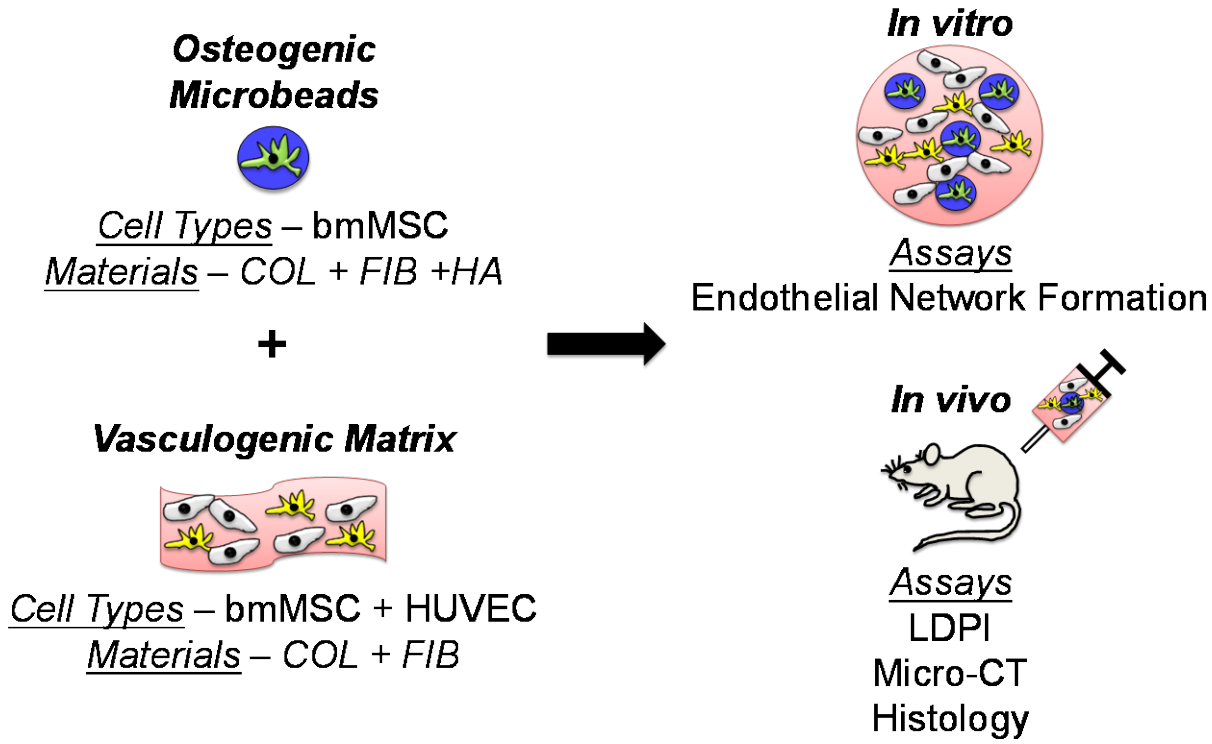

Figure 6.1 – Schematic of the design and fabrication of the dual-phase engineered tissue. Modular bone marrow-derived mesenchymal stem cell (bmMSC) seeded within collagen/fibrin/hydroxyapatite (COL/FIB/HA) microbeads were generated and cultured in osteogenic media for 14 days. These microbeads were then combined within a COL/FIB matrix containing a co-culture of human umbilical vein endothelial cells (HUVEC) and undifferentiated bmMSC. In vitro studies were performed to investigate endothelial network formation around the osteogenic microbeads. In vivo work was performed to monitor neovascularization and ectopic bone formation in a mouse subcutaneous model. Green cells - osteogenically differentiated bmMSC, yellow cells - undifferentiated bmMSC, gray cells - HUVEC.

The goal of the present study was to evaluate the effectiveness of a minimally invasive, injectable, dual-phase tissue engineering approach to the regeneration of vascularized bone, as shown schematically in Figure 6.1. Our laboratory has previously employed modular tissue engineering techniques to fabricate three-dimensional (3D) cell-seeded hydrogel "microbeads" comprised of physiologically relevant proteins and polysaccharides, and has shown that they can be used as microenvironments to support osteogenic differentiation of embedded bmMSC [17, 18]. We have also shown that composite matrices formed from collagen and fibrin (COL/FIB) support the formation of vessel-like structures when seeded with a defined co-culture of bmMSC

and HUVEC [19]. In the present work, we have combined osteogenically differentiated bmMSC-seeded COL/FIB microbeads with a COL/FIB matrix containing both bmMSC and HUVEC. We performed *in vitro* studies to examine vessel network formation around the microbeads, and *in vivo* experiments to measure ectopic bone formation in a subcutaneous injection model in immunocompromised mice. The development of injectable methods to potentiate the formation of vascularized bone would be an important advance in tissue engineering, and would have an impact on a variety of clinical pathologies in which bone healing is delayed or incomplete.

6.2 Materials and Methods

Cell Culture

Human bone marrow-derived mesenchymal stem cells (bmMSC; Lonza Inc., Walkersville, MD) were cultured in Minimum Essential Media Alpha (α-MEM; Life Technologies, Grand Island, NY) supplemented with 10% bmMSC-qualified fetal bovine serum (FBS; Life Technologies) and 1% penicillin and streptomyocin (PS; Life Technologies). bmMSC were used between passages 6-8 with media changes every other day. Human umbilical vein endothelial cells (HUVEC) were isolated from umbilical cords as previously described [19]. HUVEC were cultured in Endothelial Growth Media-2 (EGM-2; Lonza) and used between passages 4-5. Culture medium was changed every other day.

Formation of Osteogenic Microbeads

Collagen/fibrin/hydroxyapatite (COL/FIB/HA) composite microbeads were fabricated as previously described [18]. Briefly, bovine type I COL (MP Biomedicals, Solon, OH) was dissolved at a concentration of 4.0 mg/ml in 0.02 N acetic acid. Bovine fibrinogen (FIB; Sigma

Aldrich, St. Louis, MO) was dissolved in serum-free Dulbecco's modified Eagle's medium (DMEM; Thermo Scientific, Logan, UT) at 4.0 mg/ml clottable protein. COL and FIB were combined to yield a total protein concentration of 2.5 mg/ml (mass ratio 50/50) and added to a mixture containing 2% bovine thrombin (1 UT/ml; Sigma), 1 mM glyoxal (Sigma), 5% 0.1 N NaOH, 10% 5X-concentrated DMEM, 10% FBS, and 2.5 mg/ml of nano-hydroxyapatite (HA; Sigma) at 4°C. HA was sonicated for 1 hour prior to use to maintain homogenous distribution of the particles after microbead encapsulation [20]. Cells were added directly into the gel mixture to guarantee their uniform distribution within the microbeads. The mixture was then injected into a bath of 100 cSt polydimethylsiloxane (PDMS; Xiameter, Dow Corning) that was cooled to 0°C and stirred at 600 RPM for 5 minutes with a double-bladed impeller. The temperature was then increased to 37°C, inducing gelation of COL and FIB and formation of composite microbeads with embedded bmMSC. Collection of microbeads from the oil phase was performed by centrifuging the mixture at 200X g for 5 minutes and washing with phosphate buffered saline (PBS; Life Technologies) supplemented with Pluronic L101 (BASF, Florham Park, NJ). Microbeads were cultured and maintained in α-MEM supplemented with 2 mg/ml ε-amino caproic acid (ACA; Sigma) to prevent fibrinolysis. Media was changed every other day. Acellular microbeads were stained with EZBlue Coomasie reagent and visualized with a light microscope (Olympus America, Center Valley, PA) [18]. Acellular microbeads were also labeled with 5 μg/ml FITC-Fibrinogen (Life Technologies) at the time of microbead fabrication to visualize dispersion within COL/FIB hydrogels.

Osteogenic Differentiation of Microbeads

Cell-seeded microbeads were induced to differentiate toward the osteogenic lineage by culturing the microbeads for 14 days in α-MEM supplemented with 2.0 mg/ml ACA, 50 µg/ml ascorbic acid 2-phosphate (Sigma), 10 mM β-glycerophosphate (Sigma), and 100 nM dexamethasone (Sigma). Microbeads were collected by centrifugation at 200X g for 5 minutes prior to the media change.

Fabrication of Vasculogenic Matrix

Composite collagen/fibrin hydrogels were fabricated as previously described to serve as a vasculogenic surrounding matrix for the microbeads [19]. Both cell-seeded and acellular microbeads were encapsulated directly into the vasculogenic gel mixture at a ratio of 1:1 bead mixture:gel mixture by centrifuging the microbeads for 5 min at 200 x g and then removing the excess media. COL and FIB (total protein concentration of 2.5 mg/ml and a mass ratio of 40/60) were then added at 4°C to 2% bovine thrombin (1 UT/ml), 5% 0.1 N NaOH, 10% 5X-concentrated DMEM, 10% FBS, and serum-free EGM-2 to bring the final volume to 100%. The mixture was then transferred into a 24-well plate and allowed to gel for 30 min. Four conditions were used throughout the study as listed in Table 6.1. For bmMSC-HUVEC co-culture conditions, both cell types were added into the gel mixture at 300,000 cells/ml (600,000 total cells/ml) at a 1:1 cell ratio. EGM-2 was added on top of the gels and cell-seeded gels were cultured at 37°C and 5% CO_2. Media was changed every other day. A summary of the *in vitro* cell concentrations and conditions is shown in Table 6.1.

Table 6.1. *In Vitro* Conditions and Cell Concentrations		
	COL/FIB/HA Microbeads	**COL/FIB Hydrogel**
Blank	Acellular	Acellular
Vasculo	Acellular	3×10^5 bmMSC/ml + 3×10^5 HUVEC/ml
Osteo	1×10^6 bmMSC/ml	Acellular
Osteo + Vasculo	1×10^6 bmMSC/ml	3×10^5 bmMSC/ml + 3×10^5 HUVEC/ml

Table 6.1 – *In Vitro* Conditions and Cell Concentrations. bmMSC – bone marrow-derived mesenchymal stem cells, HUVEC – human umbilical vein endothelial cells.

Immunofluorescent Staining

At days 7 and 14, cell-seeded microbeads and hydrogels were washed twice in PBS for 5 min/wash and then fixed in zinc-buffered formalin (Z-Fix; Anatech, Battle Creek, MI) for 10 min at 4°C. After two subsequent washes in PBS, embedded cells were permeabilized with 0.5% Triton X-100 (Sigma) in PBS for 20 min at room temperature. Gels were then washed again twice in PBS for 5 min/wash, and the appropriate stain was added at room temperature. Stains were added to 1% bovine serum albumin (BSA; Sigma) in PBS at the appropriate concentration: 165 nM AlexaFluor 488 phalloidin (Life Technologies), 20 µg/ml rhodamine labeled Ulex Europaeus Agglutinin I (UEA-1; Vector Laboratories, Burlingame, CA), and 10 nM fluorescent DAPI (Life Technologies). Gels were then washed twice in PBS prior to imaging on a confocal microscope (Nikon Instruments Inc., Melville, NY).

Implantation into Ectopic Model in the Mouse

All animal experiments were performed in accordance with the National Institutes of Health Guidelines and by following a protocol approved by the University of Michigan's Committee on Use and Care of Animals. Male C.B.-17/SCID mice (Taconic Labs, Hudson, NY, USA) were anesthetized via intraperitoneal injection of a drug cocktail containing ketamine (95 mg/kg, Fort Dodge Animal Health, Fort Dodge, IA), buprenorphine (0.059 mg/kg, Bedford Laboratories, Bedford, OH), and xylazine (9.5 mg/kg, Lloyd Laboratories, Shenandoah, IA). The injection site

on the dorsal surface of the mouse was then shaved and sterilized with betadine (Thermo Fisher Scientific, Fremont, CA) and alcohol prior to injection. Microbeads were added into the gel mixture at a ratio of 1:1 bead mixture:gel mixture and the total cell concentration was increased relative to the *in vitro* studies to 10.0×10^6 cells/ml for the bmMSC-HUVEC co-culture conditions (Osteo + Vasculo and Vasculo). A higher cell concentration was used in this phase of the study in order to be comparable to previous *in vivo* studies that have demonstrated the presence of transplanted perfused human vasculature [21, 22]. Table 6.2 shows a summary of the cell concentrations used with each condition. Two hydrogels were injected per animal with a final gel solution of 300 µl; mice were kept stationary for 2 minutes after injection and then placed in fresh cages.

Table 6.2. *In Vivo* Conditions and Cell Concentrations

	COL/FIB/HA Microbeads	**COL/FIB Hydrogel**
Blank	Acellular	Acellular
Vasculo	Acellular	5×10^6 bmMSC/ml + 5×10^6 HUVEC/ml
Osteo	1×10^6 bmMSC/ml	Acellular
Osteo + Vasculo	1×10^6 bmMSC/ml	5×10^6 bmMSC/ml + 5×10^6 HUVEC/ml

Table 6.2 – *In Vivo* Conditions and Cell Concentrations. bmMSC – bone marrow-derived mesenchymal stem cells, HUVEC – human umbilical vein endothelial cells.

Laser Doppler Perfusion Imaging

Blood flow through the implant was imaged non-invasively using laser Doppler perfusion imaging (LDPI; Perimed AB, Sweden) [21]. After sedation as previously described, mice were imaged in triplicate. A region of interest (ROI) was drawn over the implant area and the mean perfusion through each implant was calculated. Results are represented as fold change from perfusion values before implantation (baseline).

Micro-Computed Tomography (µCT) Imaging

Ectopic bone formation was measured using Micro-Computed Tomography imaging (µCT*;* µCT100 Scanco Medical, Bassersdorf, Switzerland). Explanted tissues were first embedded in 1% agarose and placed in a 34 mm diameter tube and scanned over the entire length of the specimen. Scan settings were set to voxel size 15 µm, 55 kVp, 109 µA, 0.5 mm AL filter, and integration time 500 ms. Analysis of the bone volume (BV) and tissue mineral density (TMD) of each sample was performed using the manufacturer's software, and a fixed global threshold of 16% (160 on a grayscale of 0–1000) was used to segment bone from non-bone.

Histology

Harvested samples were paraffin embedded, sectioned, and stained with hematoxylin and eosin (H&E) and Von Kossa at the Histology Core Facility at the University of Michigan Dental School. Human cell staining was performed using a human UEA-1 staining kit per manufacturer's instructions (Vector Laboratories). Total vessel density was quantified by manually quantifying representative images of each sample in five distinct areas of the implant. Vessels were defined as structures with lumens containing erythrocytes.

Statistical Analysis

All values are presented as mean +/- standard deviation. N = 5 samples for *in vivo* samples. Statistical significance was set to $p < 0.05$ and was determined by a one-way analysis of variance (ANOVA) test with a protected Fisher's Least Significant Difference test.

6.3 Results

Dispersion of Microbeads within COL/FIB Hydrogels

Figure 6.2 shows acellular COL/FIB/HA microbeads in suspension (Figure 6.2A) and fluorescently-labeled acellular COL/FIB/HA microbeads dispersed within COL/FIB hydrogels. A maximum projection reconstruction of sequential confocal images over 100 µm showed homogenous distribution of microbeads in the XY-plane without aggregation over the imaged area (Figure 6.2B). A 3D reconstruction of the corresponding Z-stack also showed distribution of microbeads in the Z-axis (Figure 6.2C).

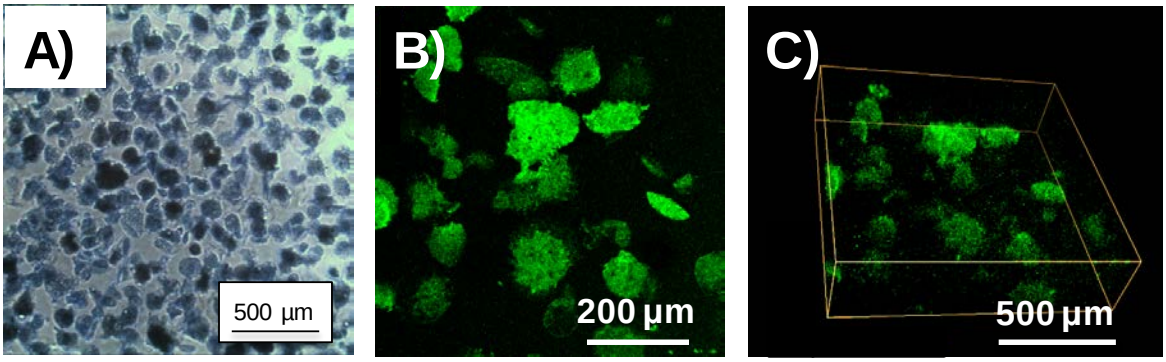

Figure 6.2 – Acellular COL/FIB/HA microbeads and COL/FIB/HA microbeads embedded within a COL/FIB hydrogel. Microbeads remained homogenously dispersed within the outer hydrogel after gelation. Light micrograph (A) and fluorescent images (B,C) of acellular COL/FIB/HA microbeads. (B) Max-intensity projection over 100 µm distance of FITC-labeled COL/FIB/HA microbeads. (C) 3D reconstruction.

Formation of Endothelial Networks around Microbeads In Vitro

The generation of vessel-like structures at Day 14 around COL/FIB/HA microbeads embedded in COL/FIB hydrogels is shown in Figure 6.3. The locations of microbeads are indicated by "MB" in the image. Ulex Europaeus Agglutinin I (UEA-1), a human endothelial cell marker, was used to stain vessel networks. Phalloidin served to label the actin cytoskeleton of both the bmMSC and HUVEC, and DAPI showed the nuclei of all cells. Both the Vasculo and Osteo + Vasculo conditions treatments showed clear evidence of the formation of vessel-like structures after two weeks in culture, as evidenced by positive UEA-1 staining. Co-localization

of bmMSC and HUVEC was observed in both of these conditions (positive staining for actin and UEA-1 indicates HUVEC, whereas positive actin stain not associated with UEA-1 indicates bmMSC). The co-localization of the two cell types *in vitro* suggests peri-endothelial interaction between the two cell types in the composite hydrogel. Neither the Blank (acellular) nor the Osteo condition exhibited positive UEA-1 staining or vessel-like structures.

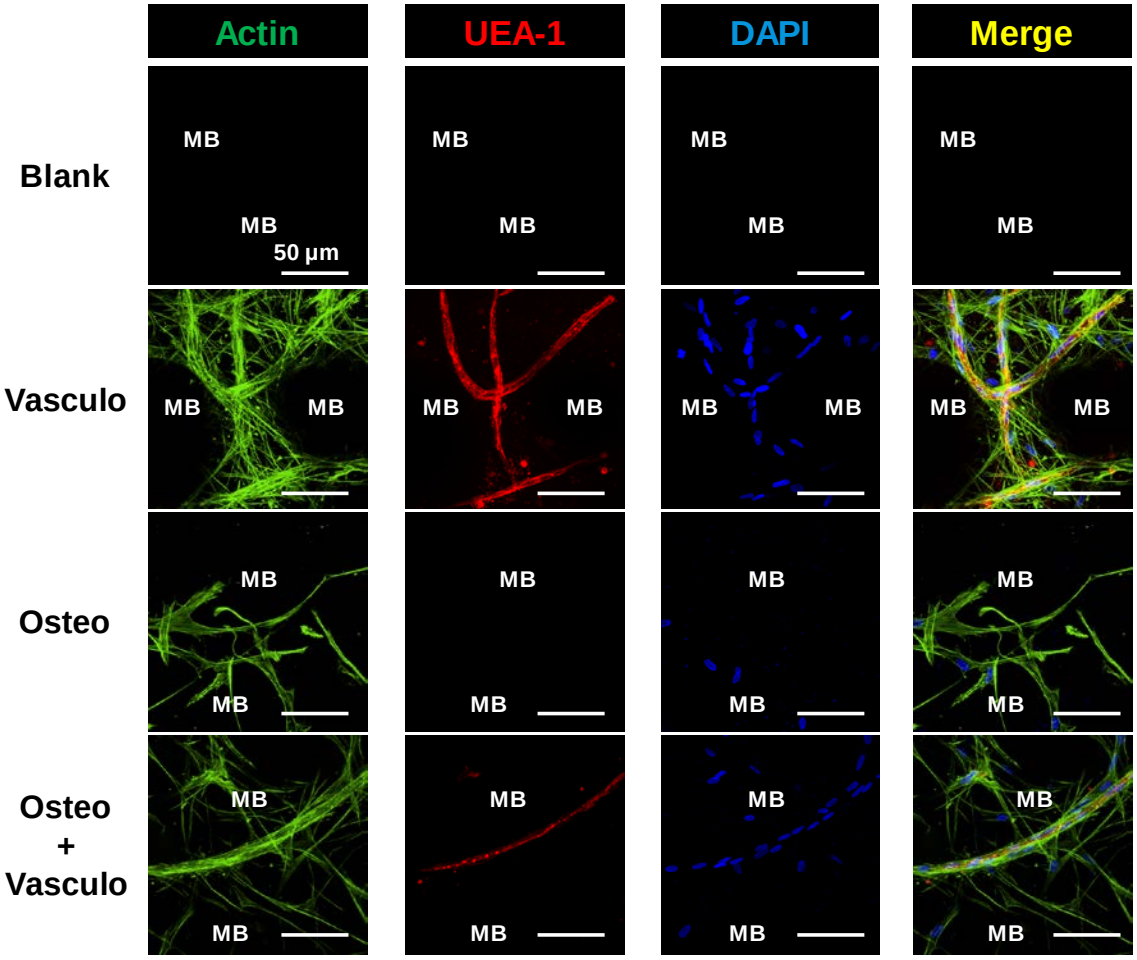

Figure 6.3 – Vessel-like structure formation around microbeads. Acellular (Blank, Vasculo) and osteogenically differentiated bmMSC-seeded microbeads (Osteo, Osteo + Vasculo) were embedded within acellular (Blank, Osteo) or bmMSC-HUVEC (Vasculo, Osteo + Vasculo) composite COL/FIB hydrogels and cultured for 14 days. Vessel-like structure formation was observed in the conditions containing HUVEC. The actin cytoskeleton of both cell types is labeled in green, human UEA-1, an endothelial cell marker, is labeled in red, and cell nuclei are labeled blue. The locations of microbeads are indicated by "MB." Scale bar = 50 µm.

Neovascularization of Osteogenic-Vasculogenic Constructs In Vivo

Subcutaneous injection of osteogenic microbeads suspended in vasculogenic matrix was used to evaluate the degree of both neovascularization and ectopic bone formation generated by implanted hydrogels. Laser Doppler perfusion imaging (LDPI) provided non-invasive measurements of blood flow throughout the implant over the 8 week time course (Figure 6.4). A baseline of vascular perfusion was taken before implantation and used to normalize all values at all time points. Perfusion was significantly higher ($p < 0.05$) in all conditions at both 1 and 4 weeks post-implantation, compared to the pre-implant baseline. At 8 weeks post-implantation, perfusion values in all conditions except the Vasculo samples remained significantly higher than the baseline, indicating constant perfusion through the implant site. There were no significant differences in perfusion between any of the conditions at any of the time points except between the Vasculo and Osteo conditions at 8 weeks.

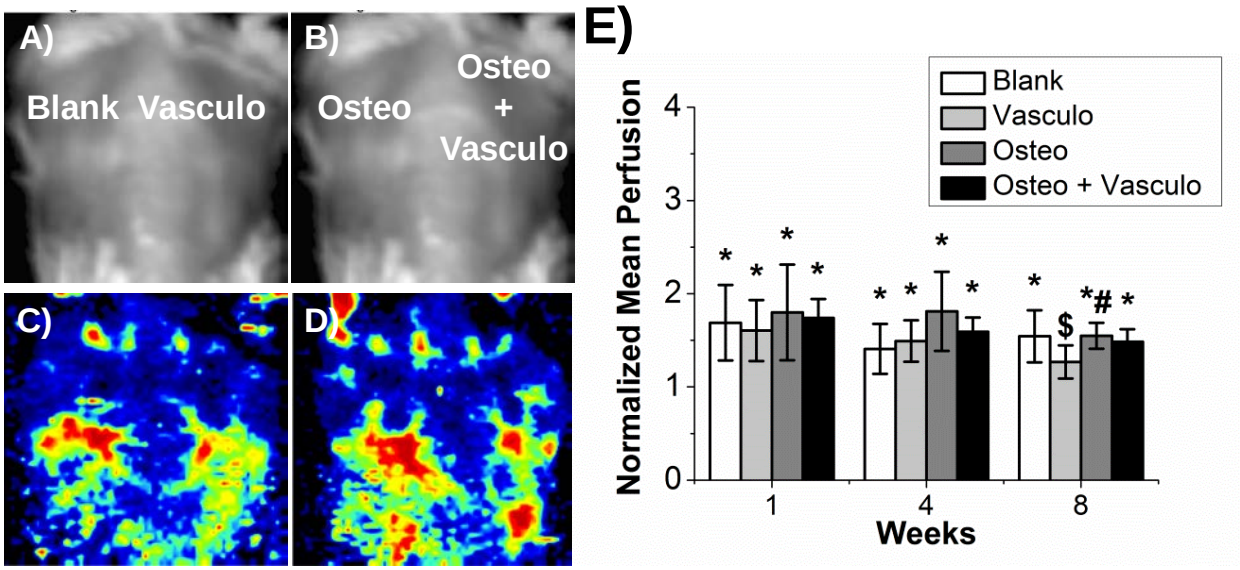

Figure 6.4 – Laser Doppler Perfusion Imaging. There were no significant differences between any of the conditions at 1 or 4 weeks. At 8 weeks, the Vasculo only group was not significantly different than the baseline. Representative photographs of mice (A,B) and heat maps (C,D) corresponding to perfusion through the implants at 8 weeks. (E) Quantification of mean perfusion normalized to before implant. *Statistically significant ($p<0.05$) vs. perfusion before implantation. #Statistically significant ($p<0.05$) vs Vasculo. $Statistically significant ($p<0.05$) vs Osteo.

Histological analysis of explanted tissues was also used to examine the degree of vascularization and neovessel formation. Vessel density was quantified at both 4 and 8 weeks and showed no significant differences between any of the conditions at either time point (Figure 6.5). The transplantation of bmMSC-HUVEC co-cultures did not enhance the degree of vascularization compared to the control Blank (acellular) condition or to the Osteo alone group. Further, there was little evidence of positive staining for human UEA-1 in the Osteo + Vasculo and the Vasculo conditions at 4 weeks (Figure 6.6).

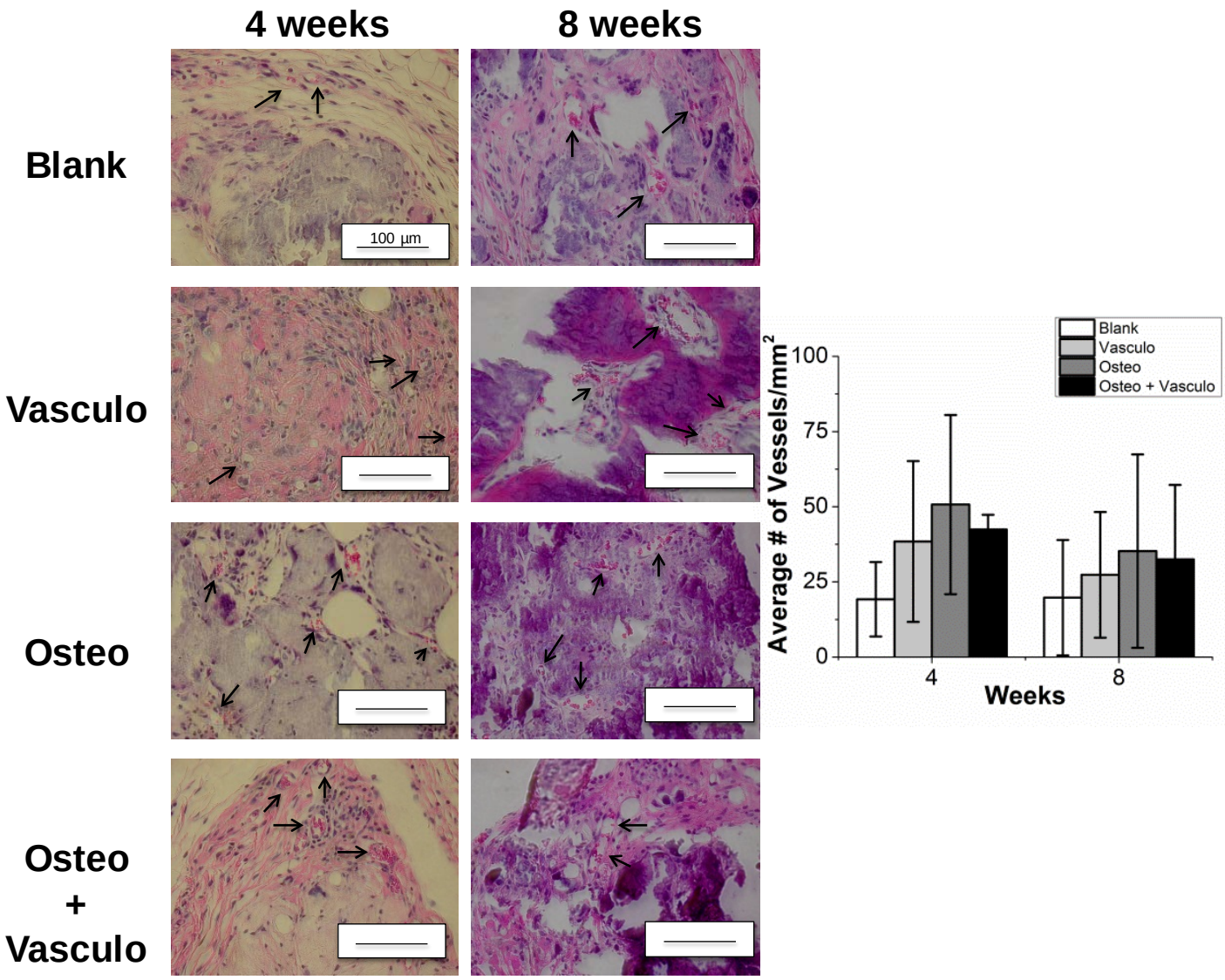

Figure 6.5 – Total vessel density quantification at 4 and 8 weeks post-implantation. Quantification of erythrocyte containing vessels yielded no significant differences between any of the conditions at either time point. Arrows indicate perfused vessels. Scale bar = 100 µm.

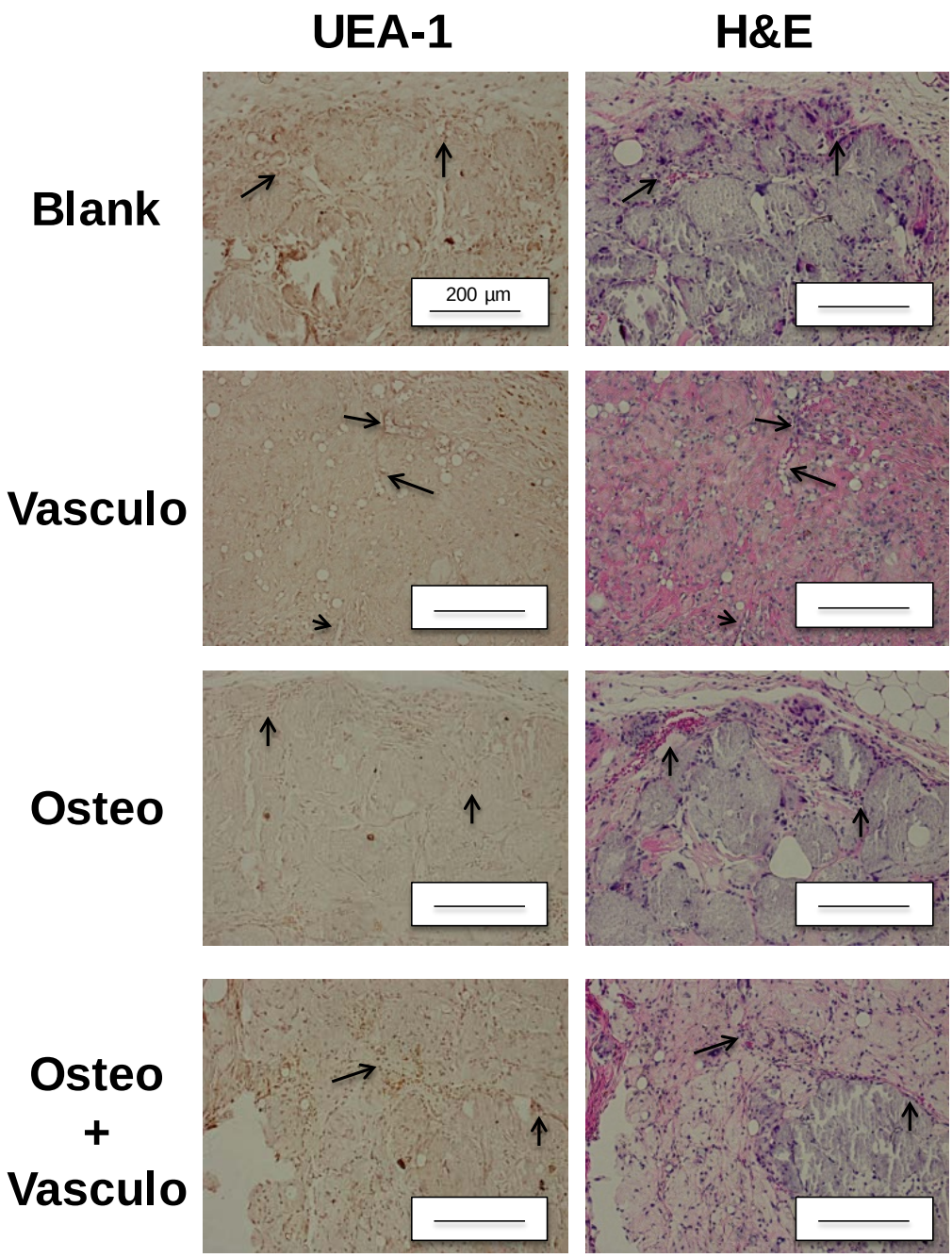

Figure 6.6 – Human UEA-1 Staining with serial H&E staining at 4 weeks. There was no clear indication of positive UEA-1 staining suggesting a lack of human endothelial cells after 4 weeks of implantation. Arrows indicate corresponding vasculature in the UEA-1 and H&E stained slides. Scale bar = 200 µm.

Ectopic Bone Formation

Micro-Computed Tomography was used as a method to non-destructively image and quantify bone volume and tissue mineral density of explanted tissues (Figure 6.7). At 4 weeks, there were no significant differences between the bone volumes (BV) of the Blank, Vasculo, or Osteo + Vasculo conditions. However, the BV of the Osteo alone group was significantly higher compared to all other groups. At 8 weeks, both the Blank and Osteo conditions had significantly higher BV compared to the Vasculo and Osteo + Vasculo groups. Evaluation of tissue mineral density (TMD) showed no differences across treatments at the 4 week time point. At the 8 week time point the Blank treatment showed significantly higher TMD compared to the Vasculo or Osteo conditions. Histological analysis and Von Kossa staining confirmed the μCT data (Figure 6.8), and showed the same trends. Positive mineral staining was evenly distributed throughout the implanted structures in amounts that correlated with the BV calculations.

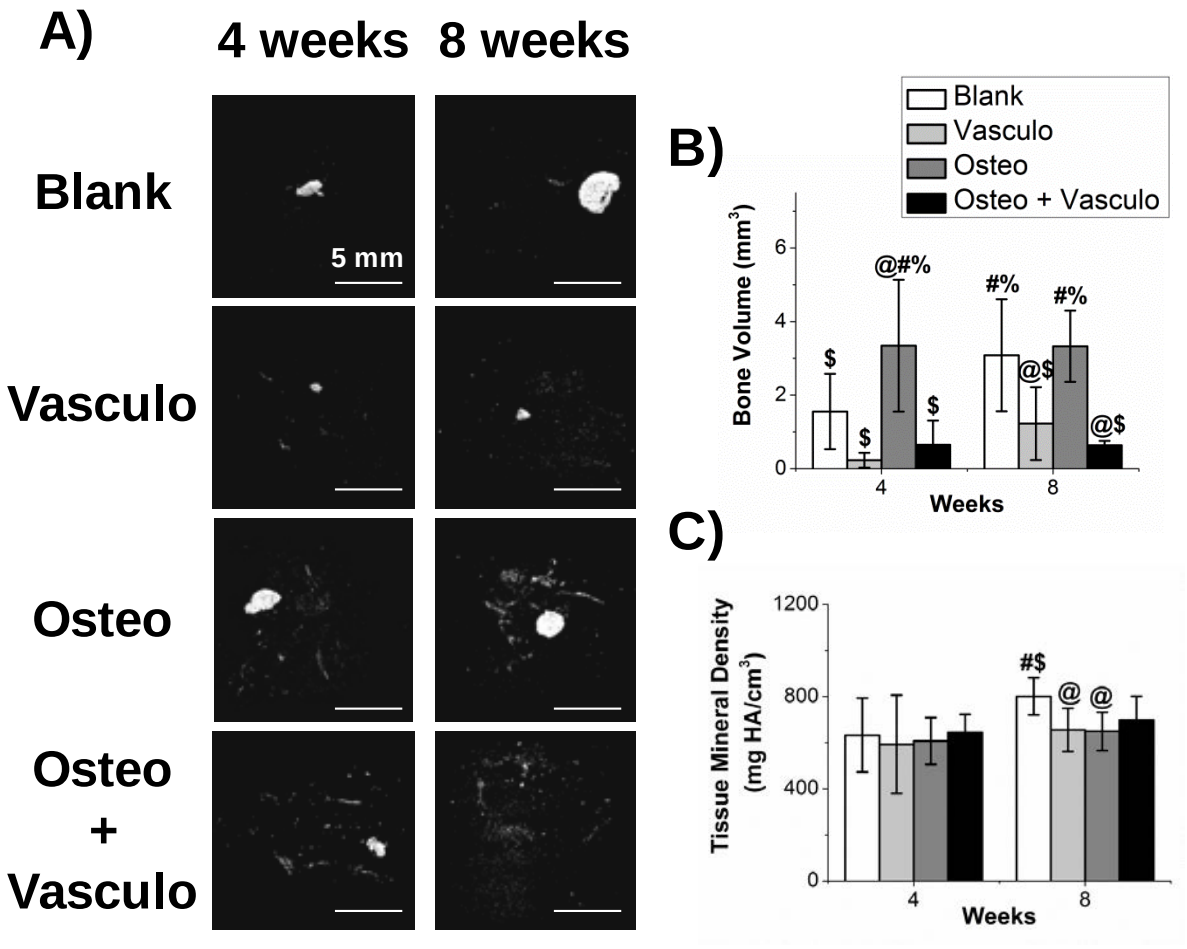

Figure 6.7– Micro-computed tomography analysis of ectopic bone formation. The Osteo only group demonstrated the highest bone volume at 4 weeks and both the Osteo and Blank groups had the highest bone volume at 8 weeks. (A) Representative 3D volumetric images of newly formed bone. (B) Bone volume. (C) Tissue mineral density. @Statistically significant ($p<0.05$) vs Blank. #Statistically significant ($p<0.05$) vs Vasculo. $Statistically significant ($p<0.05$) vs Osteo. %Statistically significant ($p<0.05$) vs Osteo+Vasculo.

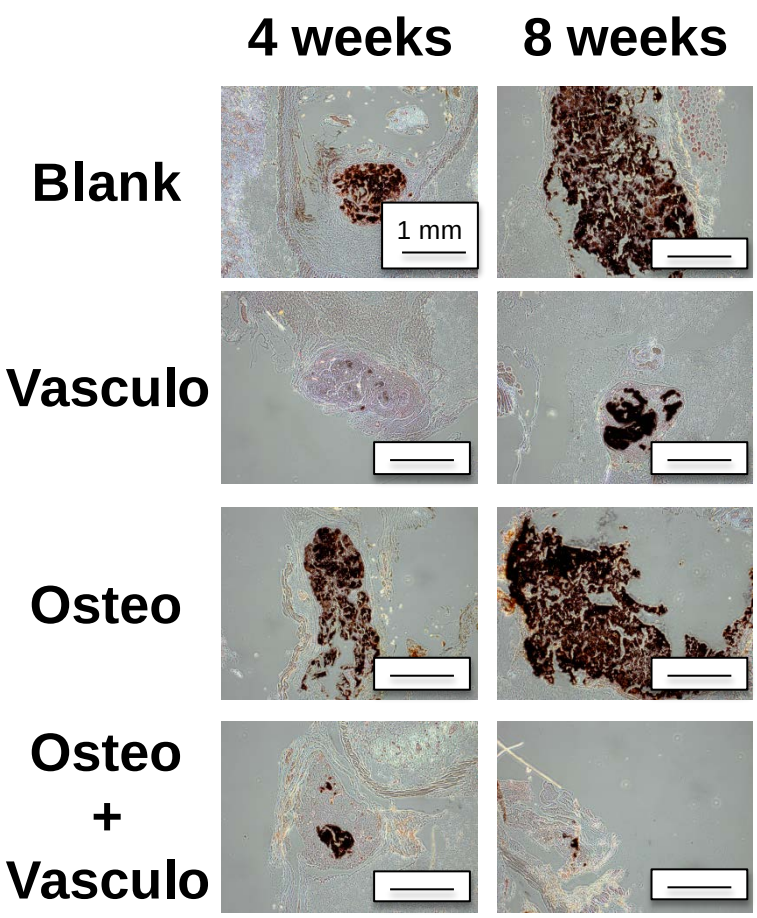

Figure 6.8 – Von Kossa Staining of distributed mineral within the implant site at 4 and 8 weeks. Positive black staining indicating mineralization mirrored the MicroCT results. Scale bar = 1 mm.

6.4 Discussion

The goal of this study was to evaluate a dual-phase microbead-hydrogel system for promoting bone formation. The osteogenic microbead phase consisted of pre-differentiated bmMSC that were embedded in microscale (50-250 µm diameter) COL/FIB/HA modules. The microbeads in turn were distributed within a 3D vasculogenic matrix consisting of a COL/FIB hydrogel containing a bmMSC-HUVEC co-culture. Our previous work has demonstrated that microbeads support osteogenic differentiation of bmMSC [18], and that populations of microbeads can be collected and injected through a needle without the loss of cell viability [17].

Therefore microbeads can be maintained in culture and exposed to desired differentiation conditions, and can subsequently be collected and implanted without the need to disrupt the cellular microenvironment. Microbeads also can be combined with other types of biomaterials to create multiphase constructs [23]. In the present work, we homogeneously dispersed osteogenically pre-differentiated microbeads within a collagen/fibrin composite hydrogel containing a co-culture of bmMSC-HUVEC that we have previously shown to support vasculogenesis *in vitro* [19]. The rationale for combining these phases was to promote simultaneous cellular osteogenesis and neovascularization to enhance the formation of new bone. The overall objective of this work is to develop a minimally-invasive therapy for treating large and recalcitrant bone defects.

We first investigated vasculogenesis in 3D hydrogel constructs that contained either acellular or osteogenically-differentiated cell-seeded microbeads *in vitro*. Robust endothelial cell networks formed in the hydrogel in both conditions containing HUVEC (Osteo + Vasculo, Vasculo). Interestingly, we did not observe an inhibitory effect of including osteogenically differentiated cells into our system on *in vitro* vessel formation. Although there are contradictory reports in the literature [24], some studies have observed that the differentiated state of co-cultured bmMSC can influence vascular network formation by HUVEC [25]. In addition, we did not observe positive staining for endothelial cell markers in osteogenic microbeads when cultured alone, in contrast to reports that have suggested that mesenchymal stem cells can differentiate along both osteogenic and vasculogenic cell lineages [26-29]. Taken together, our *in vitro* data provided support that osteogenic microbeads could be used in combination with a vasculogenic outer matrix, without impeding vascular network formation.

We then progressed to a subcutaneous implant model in the mouse to examine bone and blood vessel formation by both mono- and dual-phase constructs. The bmMSC in the osteogenic microbead component were pre-differentiated for two weeks prior to being combined with an outer hydrogel containing a combination of undifferentiated bmMSC and HUVEC immediately prior to injection. Previous studies have shown that the co-transplantation of undifferentiated bmMSC and HUVEC lead to vasculogenesis containing human cells within this animal model at 1 and 2 weeks [21, 22]. The subcutaneous location of the implants also allows angiogenesis from surrounding fat and muscle tissue, allowing perfusion of the implant site. The animal model supported the implantation of two constructs per animal, and therefore facilitated contralateral comparisons in this proof-of-concept study.

Non-invasive Doppler imaging showed consistent, above-baseline levels of construct perfusion regardless of the treatment condition, with the exception the purely vasculogenic condition at 8 weeks, which showed a significant decline in perfusion. In addition, quantification of neovasculature using histology showed no significant differences between the conditions at either time point. These data suggest that while the constructs were well perfused, the inclusion of endothelial cells did not improve vascularization of the implant site. Although human endothelial cells were originally implanted in constructs and previous studies have shown they contribute to vasculature at earlier time points [21, 22], we observed little evidence of human UEA-1 staining in these explanted tissues at 4 weeks. The microbeads used in this study contained exogenous HA, the primary mineral component of bone, which has been shown to have an osteoinductive effect on bmMSC [30]. However, HA has also shown the ability to promote sprouting of HUVEC [31, 32], and induces the secretion of the angiogenic growth factor VEGF when presented to bmMSC [30, 33]. The HA contained within the microbeads may have

provided an angiogenic signal for the host vasculature to infiltrate the implant and support bone formation. Therefore, the exogenously supplied HUVEC may not have been needed to achieve perfusion of the implants.

The benefits of combining endothelial cells with mesenchymal stem cells to potentiate bone formation have been shown in a variety of ways. *In vitro* studies have confirmed that co-culture of these cell types can achieve reciprocal beneficial effects: endothelial cells can secrete BMP-2 to serve as osteogenic signal for mesenchymal stem cells [13], which conversely can release VEGF to provide an angiogenic signal for endothelial cells [34]. Several studies have shown comparable [35] or increased bone formation [36, 37] with the transplantation of both cell types in orthotopic bone regeneration models. Ectopic models have yielded either increased [13, 16] or equivalent [38, 39] bone formation in the dual cell condition, compared to the osteogenic cell condition alone. In the present study, addition of undifferentiated bmMSC in combination with HUVEC exhibited a clear inhibitory effect on ectopic bone formation by osteogenically differentiated microbeads *in vivo*. The presence of undifferentiated bmMSC in dual-phase condition may have resulted in signals that inhibited bone formation.

We elected to use a subcutaneous ectopic model to examine proof-of-concept of our dual-phase approach. However, in this model it is possible that exogenous cells are not required to achieve neovascularization of the implant. An orthotopic model, in which angiogenesis from surrounding tissue is reduced, may be more appropriate for demonstrating the potential of the dual-phase tissue approach. In particular, a dual-phase engineered tissue may be of most value in ischemic bone wounds, in which the host tissue does not have the ability to regenerate the vasculature needed to support bone regeneration. While there are no reliable small animal

models of ischemic bone repair, our approach may show benefit in large segmental defects, which typically result in non-union unless a therapeutic intervention is applied.

This study has demonstrated the use of an injectable, modular approach that applies COL/FIB/HA microbeads for orthopaedic applications. The microbead phase generated robust bone formation in an ectopic model. Contrary to our expectation, the addition of undifferentiated bmMSC and HUVEC as part of the vasculogenic phase had an inhibitory effect on bone formation in this model. The mechanism of inhibition is unclear, but may be related to the presence of undifferentiated bmMSC in proximity to the osteogenic phase. Testing of this approach in a non-union or ischemic model may illuminate whether endothelial cells and/or bmMSC can potentiate bone healing in recalcitrant wounds. This works provides insight into bone formation by implanted bmMSC, and may lead to improved methods for engineering vascularized bone tissue. Such injectable therapies would aid in the treatment of a variety of orthopaedic pathologies in which bone regeneration is delayed or prevented.

6.5 References

1. Clarke B. Normal bone anatomy and physiology. Clin J Am Soc Nephrol 3, S131, 2008.

2. Buck DW 2nd, Dumanian GA. Bone biology and physiology: Part I. The fundamentals. Plast Reconstr Surg 129, 1314, 2012.

3. Patel ZS, Young S, Tabata Y, Jansen JA, Wong ME, Mikos AG. Dual delivery of an angiogenic and an osteogenic growth factor for bone regeneration in a critical size defect model. Bone 43, 931, 2008.

4. Young S, Patel ZS, Kretlow JD, Murphy MB, Mountziaris PM, Baggett LS, Ueda H, Tabata Y, Jansen JA, Wong M, Mikos AG. Dose effect of dual delivery of vascular endothelial growth factor and bone morphogenetic protein-2 on bone regeneration in a rat critical-size defect model. Tissue Eng Part A 15, 2347, 2009.

5. Shah NJ, Macdonald ML, Beben YM, Padera RF, Samuel RE, Hammond PT. Tunable dual growth factor delivery from polyelectrolyte multilayer films. Biomaterials 32, 6183, 2011.

6. Kumar S., Wan C., Ramaswamy G., Clemens T.L., Ponnazhagan S. Mesenchymal stem cells expressing osteogenic and angiogenic factors synergistically enhance bone formation in a mouse model of segmental bone defect. Mol Ther 18, 1026, 2010.

7. McKay WF, Peckham SM, Badura JM. A comprehensive clinical review of recombinant human bone morphogenetic protein-2 (INFUSE Bone Graft). Int Orthop 31, 729, 2007.

8. Carreon LY, Glassman SD, Brock DC, Dimar JR, Puno RM, Campbell MJ. Adverse events in patients re-exposed to bone morphogenetic protein for spine surgery. Spine 33, 391, 2008.

9. Shahlaie K, Kim KD. Occipitocervical fusion using recombinant human bone morphogenetic protein-2: adverse effects due to tissue swelling and seroma. Spine 33, 2361, 2008.

10. Epstein NE. Pros, cons, and costs of INFUSE in spinal surgery. Surg Neurol Int 2, 10, 2011.

11. Nguyen LH, Annabi N, Nikkhah M, Bae H, Binan L, Park S, Kang Y, Yang Y, Khademhosseini A. Vascularized bone tissue engineering: approaches for potential improvement. Tissue Eng Part B Rev 18, 363, 2012.

12. Liu Y, Chan JK, Teoh SH. Review of vascularised bone tissue-engineering strategies with a focus on co-culture systems. J Tissue Eng Regen Med. 2012 [Epub ahead of print]

13. Kaigler D, Krebsbach PH, West ER, Horger K, Huang YC, Mooney DJ. Endothelial cell modulation of bone marrow stromal cell osteogenic potential. FASEB J 19, 665, 2005.

14. Usami K, Mizuno H, Okada K, Narita Y, Aoki M, Kondo T, Mizuno D, Mase J, Nishiguchi H, Kagami H, Ueda M. Composite implantation of mesenchymal stem cells with endothelial

progenitor cells enhances tissue-engineered bone formation. J Biomed Mater Res A 90, 730, 2009.

15. Grellier M, Granja PL, Fricain JC, Bidarra SJ, Renard M, Bareille R, Bourget C, Amédée J, Barbosa MA. The effect of the co-immobilization of human osteoprogenitors and endothelial cells within alginate microspheres on mineralization in a bone defect. Biomaterials 30, 3271, 2009.

16. Tsigkou O, Pomerantseva I, Spencer JA, Redondo PA, Hart AR, O'Doherty E, Lin Y, Friedrich CC, Daheron L, Lin CP, Sundback CA, Vacanti JP, Neville C. Engineered vascularized bone grafts. Proc Natl Acad Sci U S A 107, 3311, 2010.

17. Wang L, Rao RR, Stegemann JP. Delivery of mesenchymal stem cells in chitosan/collagen microbeads for orthopedic tissue repair. Cells Tissues Organs 197, 333, 2013.

18. Rao RR, Peterson AW, Stegemann JP. Osteogenic differentiation of adipose-derived and marrow-derived mesenchymal stem cells in modular protein/ceramic microbeads. J Biomed Mater Res A 101, 1531, 2013.

19. Rao RR, Peterson AW, Ceccarelli J, Putnam AJ, Stegemann JP. Matrix composition regulates three-dimensional network formation by endothelial cells and mesenchymal stem cells in collagen/fibrin materials. Angiogenesis 15, 253, 2012.

20. Gudur M, Rao RR, Hsiao YS, Peterson AW, Deng CX, Stegemann JP. Noninvasive, quantitative, spatiotemporal characterization of mineralization in three-dimensional collagen hydrogels using high-resolution spectral ultrasound imaging. Tissue Eng Part C Methods 18, 935, 2012.

21. Grainger SJ, Carrion B, Ceccarelli J, Putnam AJ. Stromal cell identity influences the in vivo functionality of engineered capillary networks formed by co-delivery of endothelial cells and stromal cells. Tissue Eng Part A 19, 1209, 2013.

22. Kniazeva E, Kachgal S, Putnam AJ. Effects of extracellular matrix density and mesenchymal stem cells on neovascularization in vivo. Tissue Eng Part A 17, 905, 2011.

23. Caldwell DJ, Rao RR, Stegemann JP. Assembly of discrete collagen-chitosan microenvironments into multiphase tissue constructs. Adv Healthc Mater 2, 673, 2013.

24. Thébaud NB, Siadous R, Bareille R, Remy M, Daculsi R, Amédée J, Bordenave L. Whatever their differentiation status, human progenitor derived - or mature - endothelial cells induce osteoblastic differentiation of bone marrow stromal cells. J Tissue Eng Regen Med 6, e51, 2012.

25. Hoch AI, Binder BY, Genetos DC, Leach JK. Differentiation-dependent secretion of proangiogenic factors by mesenchymal stem cells. PLoS One **7**, e35579, 2012.

26. Janeczek Portalska K, Leferink A, Groen N, Fernandes H, Moroni L, van Blitterswijk C, de Boer J. Endothelial differentiation of mesenchymal stromal cells. PLoS One 7, e46842, 2012.

27. Zhang R, Gao Z, Geng W, Yan X, Chen F, Liu Y. Engineering vascularized bone graft with osteogenic and angiogenic lineage differentiated bone marrow mesenchymal stem cells. Artif Organs 36, 1036, 2012.

28. Mihaila SM, Frias AM, Pirraco RP, Rada T, Reis RL, Gomes ME, Marques AP. Human adipose tissue-derived SSEA-4 subpopulation multi-differentiation potential towards the endothelial and osteogenic lineages. Tissue Eng Part A 19, 235, 2013.

29. Correia C, Grayson W, Eton R, Gimble JM, Sousa RA, Reis RL, Vunjak-Novakovic G. Human adipose-derived cells can serve as a single-cell source for the in vitro cultivation of vascularized bone grafts. J Tissue Eng Regen Med 2012 [Epub ahead of print]

30. He J, Genetos DC, Leach JK. Osteogenesis and trophic factor secretion are influenced by the composition of hydroxyapatite/poly(lactide-co-glycolide) composite scaffolds. Tissue Eng Part A 16, 127, 2010.

31. Rücker M., Laschke MW, Junker D, Carvalho C, Tavassol F, Mülhaupt R, Gellrich NC, Menger MD. Vascularization and biocompatibility of scaffolds consisting of different calcium phosphate compounds. J Biomed Mater Res A 86, 1002, 2008.

32. Pezzatini S, Solito R, Morbidelli L, Lamponi S, Boanini E, Bigi A, Ziche M. The effect of hydroxyapatite nanocrystals on microvascular endothelial cell viability and functions. J Biomed Mater Res A 76, 656, 2006.

33. He J, Decaris ML, Leach JK. Bioceramic-mediated trophic factor secretion by mesenchymal stem cells enhances in vitro endothelial cell persistence and in vivo angiogenesis. Tissue Eng Part A 18, 1520, 2012.

34. Kaigler D, Krebsbach PH, Polverini PJ, Mooney DJ. Role of vascular endothelial growth factor in bone marrow stromal cell modulation of endothelial cells. Tissue Eng 9, 95, 2003.

35. Koob S, Torio-Padron N, Stark GB, Hannig C, Stankovic Z, Finkenzeller G. Bone formation and neovascularization mediated by mesenchymal stem cells and endothelial cells in critical-sized calvarial defects. Tissue Eng Part A 17, 311, 2011.

36. Seebach C, Henrich D, Kähling C, Wilhelm K, Tami AE, Alini M, Marzi I. Endothelial progenitor cells and mesenchymal stem cells seeded onto beta-TCP granules enhance early vascularization and bone healing in a critical-sized bone defect in rats. Tissue Eng Part A 16, 1961, 2010.

37. Kim JY, Jin GZ, Park IS, Kim JN, Chun SY, Park EK, Kim SY, Yoo J, Kim SH, Rhie JW, Cho DW. Evaluation of solid free-form fabrication-based scaffolds seeded with osteoblasts and

human umbilical vein endothelial cells for use in vivo osteogenesis. Tissue Eng Part A 16, 2229, 2010.

38. Fedorovich NE, Haverslag RT, Dhert WJ, Alblas J. The role of endothelial progenitor cells in prevascularized bone tissue engineering: development of heterogeneous constructs. Tissue Eng Part A 16, 2355, 2010.

39. Geuze RE, Wegman F, Oner FC, Dhert WJ, Alblas J. Influence of endothelial progenitor cells and platelet gel on tissue-engineered bone ectopically in goats. Tissue Eng Part A 15, 3669, 2009.

CHAPTER 7

Summary, Discussion, Conclusions and Future Directions

7.1 Summary

In the first aim (Chapter 3), we explored whether collagen/fibrin (COL/FIB) and collagen/fibrin hydroxyapatite (COL/FIB/HA) microbeads could support the osteogenic differentiation of bone marrow-derived mesenchymal stem cells (bmMSC) and adipose-derived stem cells (AdSC) [1]. These cell types were chosen because both are commonly used in osteogenic studies and can be used as autologous cell sources. The inclusion of HA into these matrices produced an osteoinductive effect on the encapsulated bmMSC as alkaline phosphatase (ALP) activity significantly increased in both the growth (control) and osteogenic conditions compared to cells seeded within microbeads not containing HA. Further, these cells mineralized COL/FIB microbeads (without HA) after culture in osteogenic media for two weeks indicating that the cells were adopting the osteogenic phenotype. COL/FIB/HA microbeads containing bmMSC did not show an increase in mineral content, likely due to the presence of mineral within the microbeads. AdSC also mineralized their respective microbeads, however, they did not demonstrate the same response to HA in terms of ALP activity. COL/FIB/HA microbeads were chosen as the support material for the osteogenic microbeads. We elected to continue subsequent aims using bmMSC as they satisfied both of our markers of osteogenesis in these studies.

In the first part of the second aim (Chapter 4), both cell ratio and matrix composition were varied in HUVEC and bmMSC co-cultures seeded within 3D COL/FIB composite hydrogels [2]. The bmMSC served as pericytes in this model and provided paracrine signals that

stimulated HUVEC to form vessel-like structures. Endothelial network formation increased with increasing fibrin content in the composite matrices although the 40/60 COL/FIB exhibited the same degree of vessel-like structure formation compared to pure fibrin. Mechanical property measurements showed an inverse correlation between matrix stiffness and network formation. We further investigated this by modulating both the total protein concentration and crosslinking the 40/60 COL/FIB matrices using glyoxal and again, network formation demonstrated a negative correlation with matrix stiffness. However, qualitative assessment of the matrix microarchitecture indicated that our alterations in mechanical properties also led to changes in the matrix structure. Although the mechanical properties could not be altered independently from other properties, the results from this sub-aim suggest that COL/FIB matrices are permissive to network formation by bmMSC-HUVEC co-cultures and that vessel-like structure generation can be modulated by matrix mechanics. From this sub-aim, we chose the 40/60 COL/FIB composite hydrogels with a 1:1 HUVEC:bmMSC cell ratio for our continued vasculogenic studies.

Hydroxyapatite was then systematically added to the 40/60 COL/FIB hydrogels in a dose-dependent manner to evaluate its effect of network formation in unconstrained hydrogels (Chapter 5). In an unconstrained environment, cell contractile forces induce compaction of COL/FIB composite hydrogels thereby leading to a loss of vessel-like structure generation. Network formation in unconstrained hydrogels was recovered *in vitro* using low concentrations of HA, while network formation remained reduced using high concentrations of HA compared to constrained hydrogels without particulate mineral. This phenomenon was then assessed *in vivo* in a SCID mouse subcutaneous model. After one week, histological analysis of implanted hydrogels demonstrated successful transplantation of human endothelial cells and the creation of erythrocyte-filled vessels. However, there were no significant differences in the number of

capillaries generated in the conditions containing the low concentration HA compared to those without mineral. Although this result did not match our *in vitro* findings that HA enhanced network formation in unconstrained hydrogels, it did indicate that any HA present within implanted matrices would not induce detrimental effects towards vasculogenesis. This is particularly relevant to the results provided from the first aim in which COL/FIB/HA microbeads were selected as support structures for the osteogenic differentiation of bmMSC.

In the final aim (Chapter 6), osteogenic microbeads were combined within the surrounding vasculogenic matrix. Endothelial networks were formed around the embedded microbeads in the conditions containing HUVEC in the outer COL/FIB hydrogel. A subcutaneous bone formation model was then utilized to measure both vasculogenesis and osteogenesis within implants at 4 and 8 weeks. Blood flow was not significantly different between any of the conditions at any time point, except at 8 weeks where the vasculogenic matrix alone was lower than all other groups. Ectopic bone formation measured by micro-computed tomography demonstrated significantly higher bone volume in the osteogenic microbead condition at 4 weeks and the blank and osteogenic microbead conditions at 8 weeks, compared to the dual Osteo + Vasculo condition. Histological analysis of total vessel density within the implants showed no significant differences between the conditions at any time point. At 4 weeks, there was no clear indication of human endothelial cells by UEA-1 staining in either the dual osteogenic/vasculogenic or the vasculogenic alone conditions, suggesting transplanted cells/vasculature could have regressed and or have been remodeled within a month. Von Kossa staining confirmed the micro-computed tomography data, as mineralized tissue was present within the implants. These data suggest an inhibitory effect of the vasculogenic component on bone formation in the non-ischemic model. However, this work suggests the potential use of

microbeads in bone regeneration applications. Dual-phase implants may be more effective in ischemic orthotopic bone regeneration models, and these results demonstrate that such constructs can be designed, fabricated, and delivered for therapeutic use.

7.2 Discussion

This work presents an incremental step in the engineering of vascularized bone and has touched upon the fields of modular tissue engineering, biomaterial synthesis, *in vitro* endothelial network formation, matrix mechanics, and *in vivo* vasculogenesis and osteogenesis. Previous work from our lab has fabricated microbeads from protein/polysaccharide composite matrices such as collagen/agarose [3, 4], chitosan/fibrin [5], and collagen/chitosan [6, 7]. Pure protein microbeads have been difficult to fabricate through the water-in-oil emulsion process used to create these microbeads as they are difficult to harvest from the oil phase and are fragile. We were able to generate composite collagen/fibrin microbeads by controlling the rate of gelation of the fibrin through increasing the thrombin concentration. Supplementation of these microbeads with hydroxyapatite increased the density of the modular structures which provided structural integrity and prevented the aggregation of microbeads when cultured over two weeks. The addition of HA also presented embedded mesenchymal stem cells with an osteoinductive signal [8]. The first Aim provided data that both confirmed findings within the current literature pertaining to stem cell differentiation [9-13] but also presented a novel approach that could be used to design and fabricate the next generation of modular tissue engineered constructs.

In vitro endothelial network formation has been a well-studied phenomenon within the literature through both angiogenesis and vasculogenesis models. Previous studies have shown beneficial effects on network formation when endothelial cells are co-cultured with a stromal cell

type such as bmMSC [14-16]. Others have also demonstrated a negative effect on *in vitro* vasculogenesis when fibrin matrices supplemented with collagen [17-19]. We performed a systematic set of studies and varied both cell ratio and matrix composition in an attempt to create an optimized model for *in vitro* endothelial network formation in collagen/fibrin matrices. We were able to identify a composite collagen/fibrin matrix that was comparable to pure fibrin in terms of vessel-like structure formation. Also, in accordance with other studies, we observed a negative correlation between network formation and matrix stiffness. We elected to further pursue this observation by modulating both total protein concentration and by crosslinking the collagen/fibrin matrices. Qualitative assessment of matrix architecture indicated that we could not alter matrix stiffness without affecting matrix microarchitecture. This finding is an important addition to the field in which many have attempted to change matrix mechanics without considering their effects on porosity, mass transport, ligand density, and other parameters. We were able to contribute data and suggest a method towards the design of biomaterials that are permissive to vasculogenesis. This strategy could extend beyond orthopedic applications.

In the next study, we attempted to provide a solution to one particular issue within the angiogenesis/vasculogenesis tissue engineering literature. In an unconstrained environment, cells are able to exert contractile forces on their surrounding microenvironments which can then lead to an inhibition of vessel-like structure formation [20-23]. We approached this problem by adding hydroxyapatite in a dose-dependent manner to the COL/FIB hydrogels containing a co-culture of bmMSC and HUVEC examined in the previous study. We observed a recovery of endothelial network formation in unconstrained hydrogels containing low concentrations of hydroxyapatite. This finding corroborated current work that has shown increased vessel ingrowth in materials containing low concentrations of bioceramics such as Bioglass [24-28]. Investigation

of these COL/FIB/HA hydrogels in a mouse subcutaneous model showed that this beneficial effect did not occur in an *in vivo* environment. However, there was not an inhibitory effect by the hydroxyapatite on *in vivo* vasculogenesis. The inclusion of HA into these matrices was chosen due to its relation to this thesis as a whole, but it allowed us to attempt a different approach to the problem than currently used in the vasculogenesis field. Mineral within vasculature is usually observed in pathological conditions and is therefore viewed as a detrimental factor in the field [29]. We were able to provide insight towards the design of unconstrained biomaterials that could support *in vitro* vasculogenesis by utilizing a different methodology than typically used in the field. This approach could benefit the vascular tissue engineering field by offering a method to create pre-vascularized structures *in vitro* which can then be implanted for rapid inosculation with host vasculature.

In the final Aim, we combined the results from the previous study to create a dual-phase osteogenic and vasculogenic tissue. Current work in vascularized bone tissue engineering has probed whether the co-implantation of endothelial cells and mesenchymal stem cells can form vascularized bone *in vivo* [30, 31]. Typically these studies used undifferentiated cells, but the microbead technology developed in the first Aim allowed for pre-differentiation of embedded stem cells prior to implantation. In a related study, a combinatorial osteogenic and vasulogenic tissue was created by first osteogenically differentiated bmMSC on a solid scaffold prior to combination with a hydrogel containing a bmMSC-HUVEC co-culture [32]. Although we employ a similar method to generate a dual-phase tissue, our construct was purely hydrogel-based and can therefore be injected into the defect site in a minimally invasive manner. Our system was able to form ectopic bone in both the acellular control and Osteo conditions indicating that the material combination chosen for microbeads throughout the thesis might be

sufficient to generate vascularized bone *in vivo*. The study as a whole demonstrated the further need to understand the interplay between bmMSC and HUVEC as well as the implications of transplanting both undifferentiated and osteogenically differentiated bmMSC.

In the first chapter, we identified bone fractures that led to non-unions as one clinical problem that could be addressed by the findings of this thesis. We initially chose biomaterials that have been approved for both bone and vascular indications in an attempt to expedite clinical use. The combinatorial approach developed throughout this dissertation could be delivered into non-load bearing fractures or those that have been fixated with metal rods and plates. Moreover, our biomaterial could be used in other bone-related diseases such as avascular necrosis in which vascularized bone grafts have been commonly used [33]. In this condition, necrosis, or cell death, of bone tissue is caused due to an interruption of the blood supply. The necrotic tissue is removed by both macrophages and osteoclasts and this remodeling can lead to a collapse of the subchondral bone layer in joints such as the hip. In patients with these complications, our dual-phase tissue could serve as a space-filling material and provide the necessary osteogenic and angiogenic signals to regenerate bone tissue potentially delaying or completely avoiding total hip replacement. Taken together, this thesis has provided a potential minimally-invasive injectable strategy for vascularized bone tissue engineering applications.

7.3 Conclusions

Aim 1: Formation of osteogenic microbeads

Collagen/fibrin/hydroxyapatite composite microbeads could be utilized as materials to direct human bone marrow-derived mesenchymal stem cells differentiation towards the osteogenic lineage.

Aim 2: Generation of a vasculogenic matrix

COL/FIB composite hydrogels were found to be permissive to endothelial network formation of human umbilical vein endothelial cells when co-cultured with bmMSC and the obtained results demonstrated a negative correlation with the mechanical properties of the COL/FIB composite matrices. The addition of hydroxyapatite to these constructs enhanced network formation in unconstrained hydrogels *in vitro*, but did not increase vasculogenesis *in vivo*.

Aim 3: Dual-Phase Engineered Tissue for Enhanced Bone Formation

Our dual phase engineered tissue consisting of osteogenic microbeads embedded within a vasculogenic matrix did not demonstrate enhanced bone formation compared to the acellular control at either 4 or 8 weeks post-implantation. Osteogenic microbeads alone demonstrated the highest amount of ectopic bone at 4 weeks. At 8 weeks, both the acellular control and the Osteo groups formed increased bone volume compared to the Vaculo conditions indicating an inhibitory effect on ectopic bone formation with the inclusion of a bmMSC and HUVEC co-culture.

7.4 Future Directions

The results of this work demonstrate the feasibility of delivering cell-seeded hydrogel microenvironments *in vivo* within a vasculogenic matrix towards the goal of the forming ectopic bone. Clinical translation of this work will require continued studies to develop a dual-phase tissue for enhanced bone regeneration. Future work includes

1. Optimizing the dual-phase tissue *in vitro* and performing subsequent *in vivo* studies to validate improvement in bone formation with the addition of a co-culture of bmMSC and HUVEC
2. Studying the osteogenic/vasculogenic construct in an orthotopic bone regeneration model
3. Generating pre-vascularized microbeads that could inosculate with host vasculature immediately after implantation
4. Investigating alternate cell sources to facilitate clinical translation

In the final study, we combined the results from the Aim 1 and 2 to form a dual-phase osteogenic-vasculogenic system. However, we did not validate this tissue's potential to induce both a vasculogenic and osteogenic response *in vitro* nor optimize parameters within this tissue for the most robust response. Future work using the current system could include varying the microbead to matrix ratio and total cell concentration as well as investigating whether pre-differentiation of bmMSC in the microbeads or in the vasculogenic matrix will enhance the final tissue properties. *In vitro* studies could be conducted to improve the system and assays such as quantification of endothelial network formation around embedded microbeads, cell proliferation, gene expression of both osteogenic (ALP, BMP-2, osteopontin, osterix, bone sialoprotein, collagen I) and vasculogenic (VEGF, VE-Cadherin, CD31) markers, calcium deposition in the tissue, as well as protein secretion of late osteogenic markers (osteopontin and osteocalcin) could serve to direct the final dual-phase tissue parameters. After these have been sufficiently studied, another ectopic bone formation experiment could be performed to validate the potential benefits of the dual-phase tissue *in vivo.* In the next ectopic study, earlier time points should be included in order to fully understand the system's development in the *in vivo* environment. We did not

observe human endothelial cells in our current study but those cells presumably aid in vascular tissue formation at early (1-2 week) time points. The future study could include these samples as well as a 12 week time point to fully understand the dual-phase tissue's development and progression.

Further *in vivo* studies using orthotopic pre-clinical models are necessary to demonstrate bone regeneration induced by our dual-phase tissue. The subcutaneous mouse model employed in these studies provided proof-of-concept results that show promise in the use of pre-differentiated cell-seeded microbeads as a cell-based therapy, but validation in orthotopic animal models such as cranial or femoral defect models are needed to demonstrate *in vivo* bone regeneration. Longer time points (up to 12 weeks), biomechanical testing, micro-computed tomography analysis, and histological confirmation of newly formed bone would all be required to indicate the tissue's potential to generate vascularized bone prior to use in clinical practice.

Another potential avenue of this work would be to create vasculogenic microbeads with pre-formed vessel-like structures *in vitro* that would later be combined with osteogenic microbeads prior to implantation. Current work has shown promise in creating sub-millimeter-sized collagen gel cylinders, or modules, and coating the outer surface of these structures with endothelial cells to enhance vascularization *in vivo* [34-36]. In a similar vein to the work discussed in this thesis, collagen/fibrin composite materials can potentially be used to generate vessel-like structures *in vitro* by co-culturing bmMSC and HUVEC. Future work would focus on the fabrication of robust vasculogenic microbeads and validating their ability to inosculate with host tissue *in vivo*. These pre-formed vessels could presumably connect with host vasculature immediately after injection and transport blood throughout the transplanted area.

Next, vasculogenic and osteogenic microbeads could be combined *in vitro* to study the tissue development and progression of this next-generation dual-phase tissue. As mentioned earlier, gene expression, protein expression, and calcium deposition could all be monitored in order to optimize vasculogenic to osteogenic microbead ratio. *In vivo* delivery of this system could be achieved by concentrating or patterning the microbeads into a paste and injecting them into both ectopic and orthotopic models. These studies would provide insight towards the goal of engineering pre-vascularized osteogenic structures for enhanced bone healing.

One major hurdle in the translation of cell therapy strategies is in the use of the appropriate cell type that will be able to regenerate tissue while maintaining a proper immunological reaction. In this study, we used commercially available bmMSC and AdSC, yet, if autologous cell types were to be used, each donor cell type would need to be optimized and examined *in vitro* prior to use in order to overcome patient-to-patient variations. The use of stem cells from allogeneic sources is being explored, particularly due to their immunomodulatory properties. Different endothelial cell sources other than the ones used in work would need to be employed for translational purposes. HUVEC provide an excellent model cell type as they can be easily isolated from fresh umbilical cords yet they are limited in their clinical use. Other endothelial cell types such as microvascular endothelial cells or endothelial progenitor cells should be explored as potential candidates for cell therapy approaches to engineering vascularized bone tissue.

The fields of cell therapy and tissue engineering all provide cues towards the regeneration of long bone fractures. Designing combinatorial approaches to the concomitant formation of vasculature and bone tissue will aid in providing therapies for patients that suffer from non-unions that prevent them from participating in normal activities. The results demonstrated

through the present work provide a step towards this goal and offer advances in stem cell differentiation, biomaterial synthesis, capillary morphogenesis, and ectopic bone generation, all of which will lead towards the goal of engineering vascularized bone tissue.

7.5 References

1. Rao RR, Peterson AW, Stegemann JP. Osteogenic differentiation of adipose-derived and marrow-derived mesenchymal stem cells in modular protein/ceramic microbeads. J Biomed Mater Res A. 101, 1531, 2013.

2. Rao RR, Peterson AW, Ceccarelli J, Putnam AJ, Stegemann JP. Matrix composition regulates three-dimensional network formation by endothelial cells and mesenchymal stem cells in collagen/fibrin materials. Angiogenesis 15, 253, 2012.

3. Lund AW, Bush JA, Plopper GE, Stegemann JP. Osteogenic differentiation of mesenchymal stem cells in defined protein beads. J Biomed Mater Res B Appl Biomater 87, 213, 2008.

4. Batorsky A, Liao J, Lund AW, Plopper GE, Stegemann JP. Encapsulation of adult human mesenchymal stem cells within collagen-agarose microenvironments. Biotechnol Bioeng 92, 492, 2005.

5. Chen Z, Wang L, Stegemann JP. Phase-separated chitosan-fibrin microbeads for cell delivery. J Microencapsul 28, 344, 2011.

6. Wang L, Rao RR, Stegemann JP. Delivery of mesenchymal stem cells in chitosan/collagen microbeads for orthopedic tissue repair. Cells Tissues Organs 197, 333, 2013.

7. Caldwell DJ, Rao RR, Stegemann JP. Assembly of discrete collagen-chitosan microenvironments into multiphase tissue constructs. Adv Healthc Mater 2, 673, 2013.

8. He J, Genetos DC, Leach JK. Osteogenesis and trophic factor secretion are influenced by the composition of hydroxyapatite/poly(lactide-co-glycolide) composite scaffolds. Tissue Eng Part A 16, 127, 2010.

9. Strioga M, Viswanathan S, Darinskas A, Slaby O, Michalek J. Same or not the same? Comparison of adipose tissue-derived versus bone marrow-derived mesenchymal stem and stromal cells. Stem Cells Dev 21, 2724, 2012.

10. Shafiee A, Seyedjafari E, Soleimani M, Ahmadbeigi N, Dinarvand P, Ghaemi N. A comparison between osteogenic differentiation of human unrestricted somatic stem cells and mesenchymal stem cells from bone marrow and adipose tissue. Biotechnol Lett 33, 1257, 2011.

11. Miyazaki M, Zuk PA, Zou J, Yoon SH, Wei F, Morishita Y, Sintuu C, Wang JC. Comparison of human mesenchymal stem cells derived from adipose tissue and bone marrow for ex vivo gene therapy in rat spinal fusion model. Spine 33, 863, 2008.

12. Noel D, Caton D, Roche S, Bony C, Lehmann S, Casteilla L, Jorgensen C, Cousin B. Cell specific differences between human adipose-derived and mesenchymal-stromal cells despite similar differentiation potentials. Exp Cell Res 314, 1575, 2008.

13. De Ugarte DA, Morizono K, Elbarbary A, Alfonso Z, Zuk PA, Zhu M, Dragoo JL, Ashjian P, Thomas B, Benhaim P, Chen I, Fraser J, Hedrick MH. Comparison of multi-lineage cells from human adipose tissue and bone marrow. Cells Tissues Organs 174, 101, 2003.

14. Shepherd B, Jay S, Saltzman W, Tellides G, Pober J. Human aortic smooth muscle cells promote arteriole formation by coengrafted endothelial cells. Tissue Engineering Part A 15, 165, 2009.

15. Au P, Tam J, Fukumura D, Jain RK. Bone marrow derived mesenchymal stem cells facilitate engineering of long-lasting functional vasculature. Blood 111, 4551, 2008.

16. Ghanaati S, Fuchs S, Webber MJ, Orth C, Barbeck M, Gomes ME, Reis RL, Kirkpatrick CJ. Rapid vascularization of starch-poly(caprolactone) in vivo by outgrowth of endothelial cells in co-culture with primary osteoblasts. Journal of Tissue Engineering and Regenerative Medicine 5, e136, 2011.

17. Critser PJ, Kreger ST, Voytik-Harbin SL, Yoder MC. Collagen matrix physical properties modulate endothelial colony forming cell-derived vessels in vivo. Microvascular Research 80, 23, 2010.

18. Kniazeva E, Kachgal S, Putnam AJ. Effects of Extracellular Matrix Density and Mesenchymal Stem Cells on Neovascularization In Vivo. Tissue Engineering Part A 17, 905, 2011.

19. Allen P, Melero-Martin J, Bischoff J. Type I collagen, fibrin and PuraMatrix matrices provide permissive environments for human endothelial and mesenchymal progenitor cells to form neovascular networks. Journal of Tissue Engineering and Regenerative Medicine 5, e74, 2011.
20. Fernandez P, Bausch AR. The compaction of gels by cells: a case of collective mechanical activity. Integr Biol (Camb) 1, 252, 2009.

21. Lund AW, Bilgin CC, Hasan MA, McKeen LM, Stegemann JP, Yener B, Zaki MJ, Plopper GE. Quantification of spatial parameters in 3D cellular constructs using graph theory. J Biomed Biotechnol 928286, 2009.

22. Davis GE, Pintar Allen KA, Salazar R, Maxwell SA. Matrix metalloproteinase-1 and -9 activation by plasmin regulates a novel endothelial cell-mediated mechanism of collagen gel contraction and capillary tube regression in three-dimensional collagen matrices. J Cell Sci 114, 917, 2001.

23. Saunders WB, Bayless KJ, Davis GE. MMP-1 activation by serine proteases and MMP-10 induces human capillary tubular network collapse and regression in 3D collagen matrices. J Cell Sci 118, 2325, 2005.

24. Gorustovich AA, Roether JA, Boccaccini AR. Effect of bioactive glasses on angiogenesis: a review of in vitro and in vivo evidences. Tissue Eng Part B Rev 16, 199, 2010.

25. Bi L, Jung S, Day D, Neidig K, Dusevich V, Eick D, Bonewald L. Evaluation of bone regeneration, angiogenesis, and hydroxyapatite conversion in critical-sized rat calvarial defects implanted with bioactive glass scaffolds. J Biomed Mater Res A 2012.

26. Leach JK, Kaigler D, Wang Z, Krebsbach PH, Mooney DJ. Coating of VEGF-releasing scaffolds with bioactive glass for angiogenesis and bone regeneration. Biomaterials 27, 3249, 2006.

27. Leu A, Leach JK. Proangiogenic potential of a collagen/bioactive glass substrate. Pharm Res 25, 1222, 2008.

28. Leu A, Stieger SM, Dayton P, Ferrara KW, Leach JK. Angiogenic response to bioactive glass promotes bone healing in an irradiated calvarial defect. Tissue Eng Part A 15, 877, 2009.

29. Hofmann Bowman MA, McNally EM. Genetic pathways of vascular calcification. Trends Cardiovasc Med 22, 93, 2012.

30. He J, Decaris ML, Leach JK. Bioceramic-mediated trophic factor secretion by mesenchymal stem cells enhances in vitro endothelial cell persistence and in vivo angiogenesis. Tissue Eng Part A 18, 1520, 2012.

31. Kaigler D, Krebsbach PH, West ER, Horger K, Huang YC, Mooney DJ. Endothelial cell modulation of bone marrow stromal cell osteogenic potential. FASEB J 19, 665, 2005.

32. Tsigkou O, Pomerantseva I, Spencer JA, Redondo PA, Hart AR, O'Doherty E, Lin Y, Friedrich CC, Daheron L, Lin CP, Sundback CA, Vacanti JP, Neville C. Engineered vascularized bone grafts. Proc Natl Acad Sci U S A 107, 3311, 2010.

33. Fang T, Zhang EW, Sailes FC, McGuire RA, Lineaweaver WC, Zhang F. Vascularized fibular grafts in patients with avascular necrosis of femoral head: a systematic review and meta-analysis. Arch Orthop Trauma Surg 133, 1, 2013.

34. Chamberlain MD, Gupta R, Sefton MV. Bone marrow-derived mesenchymal stromal cells enhance chimeric vessel development driven by endothelial cell-coated microtissues. Tissue Eng Part A 18, 285, 2012.

35. Gupta R, Van Rooijen N, Sefton MV. Fate of endothelialized modular constructs implanted in an omental pouch in nude rats. Tissue Eng Part A 15, 2875, 2009.

36. Khan OF, Sefton MV. Endothelialized biomaterials for tissue engineering applications in vivo. Trends Biotechnol 29, 379, 2011.

APPENDIX A

Selected Protocols

A.1 Collagen/Fibrin Composite Microbead Fabrication

Materials

- Collagen – Calf Skin Type I
  - MP Biomedicals, Product # 150026
- Fibrinogen – Bovine Plasma
  - Sigma-Aldrich, Product # F8630
- Thrombin – Bovine Plasma
  - Sigma-Aldrich, Product # T4648 or T6200
- Sodium Hydroxide (NaOH)
  - Sigma-Aldrich, Product # S2770
- Glyoxal
  - Sigma-Aldrich , Product # 128465
- Fetal Bovine Serum (FBS)
  - Life Technologies, Product # 12662029 or 10437028
- 1X and 5X Dulbecco's Modified Eagle's Medium (DMEM)
  - Fisher Scientific, Product # 50-003-PB
- Phosphate buffered saline (PBS)
  - Life Technologies, Product # 21300-025
- ε-amino caproic acid (ACA)
  - Sigma-Aldrich, Product # A7824
- Pluronic L101 Surfactant
  - BASF
- Polydimethyl siloxane (PDMS)
  - Dow Corning
- 100 ml beaker
- Double-bladed impeller
- Impeller controller system
- Water bath heater

Cell Preparation

- Trypsinize cells, count, and re-suspend in desired cell concentration
- Centrifuge cells at 200 x g, aspirate media
- Resuspend cells in media components → FBS, 5X DMEM, 1X DMEM
- Place sample on ice until ready to add other components

Impeller and Oil Set-Up

- Heat water bath to 37ºC
    - Make sure thermometer is placed into the water bath
- Add 75 ml of PDMS into a 100 ml beaker
    - Place beaker in ice container and surround with ice
- Connect impeller to system
- Move beaker surrounded ice up to impeller

Microbead Fabrication

- Add components in the following order while mixing with a micropipette
    - Media Components
        - FBS, 5X DMEM, 1X DMEM
    - Glyoxal
    - NaOH
    - Collagen
    - Fibrinogen
    - Thrombin
- Collect gel mix into a 5 ml serological pipette
- Start mixing impeller in PDMS bath at desired speed
- Slowly add mixture into of PDMS pre-cooled to 0ºC (on ice)
    - Add at approximately 5 ml of gel mixture in 30 seconds
- Turn vortexer on/off to break big clumps of mixture
- Mix for 5 mins at 0ºC (on ice)
- Transfer beaker (oil + microbeads) to a water bath pre-heated to 37ºC
- Mix for 25 mins at 37ºC (water bath)

Microbead Collection

- Collect oil + microbeads into two 50 ml centrifuge tubes
- Add 3 ml of PBS + L101
- Invert tube slowly for 5 mins
- Centrifuge at 200 x g for 5 mins
- Remove oil, combine samples into one 15 ml centrifuge, fill with PBS + L101
- Centrifuge at 200 x g for 5 mins
- Wash samples in PBS + L101 for 5 mins/wash
    - Centrifuge at 200 x g between each wash

Microbead Cell Culture

- Culture microbeads with cells in 15 ml centrifuge tubes
- Add 3-5 ml of media
- Place on its side in the incubator
    - Use the top of a well-plate to keep tube angled
- Loosen cap to allow for gas exchange
- Change media every 2-3 days
    - Centrifuge at 200 x g
    - Aspirate media

- Re-suspend microbeads with a serological pipette

Notes

- Autoclave impeller, beakers and water bath container prior to use with cells
- Changing oil viscosity changes bead size
  - Lower viscosity = bigger microbeads
  - Higher viscosity = smaller microbeads
- Changing impeller speed changes bead size
  - Lower speed = bigger microbeads
  - Higher speed = smaller microbeads
- Concentrations of components that have been used
  - Collagen/fibrin mass ratio 40/60 and 50/50
  - Collagen → 1 – 1.25 mg/ml
  - Fibrin → 1.25 – 1.5 mg/ml
  - Thrombin → 1 UT/ml
    - Do NOT use 0.1 UT/ml, microbeads will not form
  - Glyoxal → 0.5 – 1 mM
  - NaOH → 0.1 N
- Culture microbeads in media supplemented with 2 mg/ml ε-amino caproic acid (ACA) to prevent fibrinolysis and degradation of microbeads

A.2 Live/Dead Staining and Quantification

Materials

- LIVE/DEAD® Viability/Cytotoxicity Kit, for mammalian cells
    - Life Technologies, Product # L3224
    - Can buy Calcein AM separately
        - Fisher Scientific (Calbiochem), Product # 206700
- Phosphate buffered saline (PBS)
    - Life Technologies, Product # 21300-025

Protocol

- Culture gels or cells until time point
- Perform assay 2-3 hours before imaging
- Transfer gels to a bigger plate
- Wash gels 3x in PBS for 10 mins/wash
- Add Live/Dead stain for 30-45 minutes at 37°C [1 ml/gel]
    - To prepare 5 ml
        - Calcein AM – 5 µl
        - Ethidium Homodimer – 10 µl
    - NOTE – all subsequent steps must be done in the dark!
- Wash gels 3x in PBS for 10 mins/wash
- Image using Confocal Microscope

Cell Viability Calculations

- Open "Merge" file in ImageJ
- Image → Color → Split Channels
- Image → Adjust → Threshold
    - Green (0, 112)
    - Red (0, 125)
- Process → Binary → Watershed
- Analyze → Analyze Particles → OK
- Calculate Viability

$$\% \text{ Viability} = \frac{\text{Green}}{(\text{Green} + \text{Red})} \times 100\%$$

A.3 Actin Cytoskeletal Staining

Materials

- Alexa Fluor® 488 Phalloidin
  - Life Technologies, Product # A12379
- 4',6-Diamidino-2-Phenylindole, Dihydrochloride (DAPI)
  - Life Technologies, Product # D1306
- Zinc-buffered formalin (Z-Fix)
  - Anatech Ltd., Product # 174
- Triton X-100
  - Sigma-Aldrich, Product # T9284
- Bovine Serum Albumin (BSA)
  - Sigma-Aldrich, Product # A1933
- Phosphate buffered saline (PBS)
  - Life Technologies, Product # 21300-025

Procedure

- Wash cells 2x with PBS for 5 minutes
- Fix cells in Z-fix at 4ºC for 10 minutes
- Wash cells 2x for 5 minutes/wash in PBS
- Permeabilize cells with 0.5% Triton X-100 in PBS for 20 minutes at RT
  - 50 µl Triton X-100 in 10 ml of PBS
- Wash cells 2x for 5 mins/wash minutes in PBS
- Add Stain, incubate for 45 mins at RT [Cover in foil]
  - 1% BSA in PBS
    - 100 mg in 10 mls of PBS
  - Phalloidin → 1:40 dilution in PBS
  - DAPI → 1:1,000 dilution in PBS
  - For 1 ml of Stain
    - 10 mg of BSA
    - 975 µl of PBS
    - 25 µl Phalloidin dye
    - 1 µl of DAPI
- Wash cells 2x for 5 mins/wash minutes in PBS [Cover in foil]
- Store at 4ºC until imaging

A.4 Osteogenic Supplements

Beta-Glycerophosphate (β-GP) → Final concentration 10 mM

- β-GP Catalog # G9422
- Make stock β-GP at 1 M
- Add 1.08 grams of β-GP to 5 ml of serum-free media
- Add 10 µl/ml of osteogenic media

Ascorbic 2-Phosphate (A2P) → Final concentration 50 µg/ml

- Make stock A2P at 5 mg/ml
- Add 25 mg of A2P to 5 ml of serum-free media
- Add 10 µl/ml of osteogenic media

Dexamethasone (DEX) → Final concentration 100 nM

- Make stock DEX at 100 µM
    - Not soluble in 10 mM stock
- Add 1.9 mg of DEX to 50 ml of serum-free media
- Add 1 µl/ml of osteogenic media

NOTES

- Store all osteogenic supplements in -80ºC freezer
- Aliquots in 250 µl for β-GP and A2P
    - 25 µl for DEX
- Add to media at every media change
- A2P is light sensitive – prepare osteogenic media in the dark

CELL TYPES

Mesenchymal Stem Cells (MSC) → DMEM – Low Glucose or α-MEM (with ascorbic acid)

- 10 mM β-GP
- 50 µg/ml A2P
- 100 nM DEX

Adipose-Derived Stem Cells (ASC) → DMEM – Low Glucose or α-MEM (with ascorbic acid)

- 10 mM β-GP
- 50 µg/ml A2P
- 100 nM DEX

MC3T3 – Mouse Preosteoblasts → α-MEM

- 10 mM β-GP
- 50 µg/ml A2P
    - ENSURE MEDIA DOES NOT ALREADY HAVE ASCORBIC ACID

A.5 Alkaline Phosphatase Activity (ALP) Assay

Materials

- P-Nitrophenol
  - Sigma-Aldrich, Product # N7660
- 2-Amino-2-methyl-1-propanol
  - Sigma-Aldrich, Product # A65182
- Phosphatase substrate
  - Sigma-Aldrich, Product # P4744
- Collagenase Type I
  - Fisher Scientific (MP Biomedicals), Product # ICN1951091
- Tris-HCl
  - Sigma-Aldrich, Product # T5941
- IGEPAL
  - Sigma-Aldrich, Product # I8896
- Phenylmethanesulfonyl fluoride
  - Sigma-Aldrich, Product # 78830
- Sodium hydroxide (NaOH)
  - Sigma-Aldrich, Product # 221465

Sample Collection and Lysis

- Flash-freeze samples in liquid N_2 and freeze in -80°C freezer until all samples are collected
- Digest samples in Lysis Buffer for 1.5 hours at 37°C
  - Use tissue homogenizer to break up samples if not digested in 1 hour
- Lysis Buffer (5 ml)
  - 10 mM Tris Buffer – pH 7.4
  - 0.6 mg/ml of Collagenase Type I
    - 3 mg of Collagenase Type I
  - 0.2% IGEPAL
    - 10 µl IGEPAL
  - 2 mM PMSF in Ethanol
    - 200 mM Stock → Dissolve 348.4 mg in 10 ml Ethanol
      - Aliquot and freeze in -20ºC
    - Add 50 µl of stock PMSF
- Freeze-Thaw samples 2X at room temperature and in -80°C freezer

Prepare AMP Buffer (125 ml)

- Solution A (62.5 ml)
  - 50 ml of MilliQ H_2O
  - 6.25 ml of AMP
  - Adjust pH to 10
  - Add water to bring final volume to 62.5 ml
- Solution B (62.5 ml)
  - 0.263 Phosphate substrate
  - 62.5 ml of MilliQ H_2O

- 1 M $MgCl_2$
    - 1.9 g $MgCl_2$
    - 20 ml of MilliQ H_2O
- Combine Solution A and Solution B and add 1.25 ml of 1 M $MgCl_2$
- Prepare aliquots of 12 ml, store in -80°C freezer

Standard Curve

- Dilute p-nitrophenol stock solution 1:10 in water
    - 100 µl of p-nitrophenol
    - 900 µl of MilliQ H_2O

	nmol/well	µl p-nitrophenol (1 mM)	Lysis Buffer
A	0	0	100
B	2.5	12.5	87.5
C	5	25	75
D	7.5	37.5	62.5
E	10	50	50
F	12.5	62.5	37.5
G	15	75	25
H	20	100	0

Assay

- Add 5-20 µl of standard or sample in duplicate or triplicate
- Add AMP buffer to bring the volume up to 100 µl
- Incubate plates at 37°C for 5 – 20 mins
    - Reaction will cause wells to become yellow
    - Monitor and stop the reaction before the samples become darker than the highest standard
    - Record the time
- Stop the reaction by adding 100 µl of 0.5 M NaOH
- Read absorbance at 405 nm
- Report values as nM/mg DNA/min

Notes

- Perform DNA assay or protein assay to normalize values
- Cover aliquots of AMP buffer in foil
- Do not use AMP buffer aliquots if they become yellow in the freezer
- Prepare new aliquots of AMP buffer every 6 months

A.6 Quant-iT™ PicoGreen® Assay for DNA Quantification

Materials

- Quant-iT™ PicoGreen® dsDNA Assay Kit
  - Life Technologies, Product # P7589
- Collagenase Type I
  - Fisher Scientific (MP Biomedicals), Product # ICN1951091
- Tris-HCl
  - Sigma-Aldrich, Product # T5941
- IGEPAL
  - Sigma-Aldrich, Product # I8896
- Phenylmethanesulfonyl fluoride
  - Sigma-Aldrich, Product # 78830

Sample Collection and Lysis

- Flash-freeze samples in liquid N_2 and freeze in -80°C freezer until all samples are collected
- Digest samples in Lysis Buffer for 1.5 hours at 37°C
  - Use tissue homogenizer to break up samples if not digested in 1 hour
- Lysis Buffer (5 ml)
  - 10 mM Tris Buffer – pH 7.4
  - 0.6 mg/ml of Collagenase Type I
    - 3 mg of Collagenase Type I
  - 0.2% IGEPAL
    - 10 µl IGEPAL
  - 2 mM PMSF in Ethanol
    - 200 mM Stock → Dissolve 348.4 mg in 10 ml Ethanol
      - Aliquot and freeze in -20ºC
    - Add 50 µl of stock PMSF
- Freeze-Thaw samples 2X at room temperature and in -80°C freezer

TE Buffer, DNA Stock Solution, and PicoGreen Dye

- Dilute 20X TE buffer (in kit) to 1X
  - 1 ml of TE buffer, 19 ml of MilliQ H_2O
- DNA stock →100 µg/ml; diluted to 2 µg/ml in either TE or Tris Buffer
  - 10 µl stock + 490 µl buffer
- Dilute PicoGreen Dye according to pico_procedure.xls file
  - 0.75 µl Pico Dye
  - 149.25 µl TE Buffer

Standards

	Concentrations (ng/ml)	DNA (µl)	Buffer (µl)
A	0	0	600
B	50	15	585
C	100	30	570
D	166.67	50	550
E	250	75	525
F	333.33	100	500
G	666.66	200	400

Samples

- Dilute samples to ensure they are in linear range
- 1:12.5 dilution
    - 40 µl sample + 460 µl TE Buffer
- 1:25 dilution
    - 20 µl + 480 µl TE Buffer
- 1:50 dilution
    - 10 µl + 490 µl TE Buffer
- 1:10 dilution
    - 10 µl + 990 µl TE Buffer

Assay

- Add 50 µl standard/samples to each well in duplicates
- Add 100 µl buffer into each well
- Add 150 µl PicoGreen buffer into each well
    - Cover well plates with foil to avoid light exposure
    - Incubate for 2-3 mins
- Read plates using fluorescent reader (498/518 nm)

Notes

- Collagen and fibrin have limited effects on PicoGreen fluorescence.

A.7 OCPC Calcium Assay

Materials

- 1 N Acetic Acid
  - Sigma-Aldrich, Product # 318590
- Calcium Chloride Dihydride ($CaCl_2 \bullet 2\ H_2O$)
  - Fisher Scientific, Product # C69-500
- Ethanolamine
  - Sigma-Aldrich, Product # 398136
- Boric Acid
  - Sigma-Aldrich, Product # B6768
- Potassium Hydroxide (KOH)
- o-Cresolphthalein Complexone
  - Sigma-Aldrich, Product # P5631
- Hydroxyquinoline
  - Sigma-Aldrich, Product # H6878
- 95% Ethanol
- MilliQ H_2O

Sample preparation

- Flash-freeze samples in liquid N_2 and freeze in -80°C freezer until all samples are collected
- Add 0.5 ml – 1 ml 1 N acetic acid to each sample
- Shake overnight at room temperature

Solutions

- Calcium Standard
  91.75 mg $CaCl_2 \bullet 2\ H_2O$ in 25 ml MilliQ (Stock: 1 mg/ml)
- Solution A: 14.8 M ethanolamine/boric acid buffer, pH = 11 (natural)
  0.5 ml ethanolamine
  1.0 ml MilliQ
  0.36 g boric acid – mix
  0.5 ml ethanolamine – mix til boric acid is dissolved
  8 ml ethanolamine
- Solution B: OCPC (natural)
  166.7 µl 1 N KOH (2.81 g KOH in 50 ml MilliQ)
  25 ml MilliQ
  26.7 mg OCPC – mix and dissolve
  166.7 µl 1 N Acetic Acid
- Solution C: hydroxyquinoline (orange)
  0.5 g 8-hydroxyquinoline
  10 ml 95% ethanol
- Worksolution: 5 parts A + 5 parts B + 2 parts C + 88 parts MilliQ

Standard Curve

A	100 µg/ml	100 µl Calcium Standard	900 µl acetic acid
B	50 µg/ml	500 µl from A	500 µl acetic acid
C	25 µg/ml	500 µl from B	500 µl acetic acid
D	12.5 µg/ml	500 µl from C	500 µl acetic acid
E	6.25 µg/ml	500 µl from D	500 µl acetic acid
F	3.125 µg/ml	500 µl from E	500 µl acetic acid
G	1.5625 µg/ml	500 µl from F	500 µl acetic acid
H	0 µg/ml		1000 µl acetic acid

Assay

- 10 µl sample/standard into each well
- 300 µl work solution to each well
- Incubate 10 minutes at room temperature
- Read plate at 575 nm

A.8 BCA Protein Assay

Materials

- Bicinchoninic acid (BCA) Protein Assay
  - Thermo Scientific, Product # PI-23227
- Tris-HCl
  - Sigma-Aldrich, Product # T5941
- IGEPAL
  - Sigma-Aldrich, Product # I8896
- Phenylmethanesulfonyl fluoride
  - Sigma-Aldrich, Product # 78830

Sample Collection and Lysis

- Flash-freeze samples in liquid N_2 and freeze in -80°C freezer until all samples are collected
- Digest samples in Lysis Buffer for 1.5 hours at 37°C
  - Use tissue homogenizer to break up samples if not digested in 1 hour
- Lysis Buffer (5 ml)
  - 10 mM Tris Buffer – pH 7.4
  - 0.2% IGEPAL
    - 10 µl IGEPAL
  - 2 mM PMSF in Ethanol
    - 200 mM Stock → Dissolve 348.4 mg in 10 ml Ethanol
      - Aliquot and freeze in -20ºC
    - Add 50 µl of stock PMSF
- Freeze-Thaw samples 2X at room temperature and in -80°C freezer

Standard Curve

- Transfer 1 ampule of standard solution to a microcentrifuge tube
  - Stock solution → 2.0 mg/ml

A	2000 ng/µl	300 µl of Stock	
B	1500 ng/µl	375 µl of Stock	125 µl 0.2% Triton-X 100
C	1000 ng/µl	325 µl of Stock	325 µl 0.2% Triton-X 100
D	750 ng/µl	175 µl from B	175 µl 0.2% Triton-X 100
E	500 ng/µl	325 µl from C	325 µl 0.2% Triton-X 100
F	250 ng/µl	325 µl from E	325 µl 0.2% Triton-X 100
G	125 ng/µl	325 µl from F	325 µl 0.2% Triton-X 100
H	0 µg/ml		400 µl 0.2% Triton-X 100

Work Solution

- Add 25 ml Solution A to 0.5 ml of Solution B
  - Solutions in kit
  - Prepares enough work solution for 1 full plate

Assay

- 25 µl sample/standard into each well
- 200 µl work solution to each well
- Place on shaker for 30 seconds
- Incubate 30 minutes at 37°C
- Read the plate at 562 nm

A.9 UEA-1 Human Endothelial Cell Staining

Materials

- Rhodamine labeled Ulex Europaeus Agglutinin I (UEA-I)
  - Vector Laboratories, Product # RL-1062
- Zinc-buffered formalin (Z-Fix)
  - Anatech Ltd., Product # 174
- Triton X-100
  - Sigma-Aldrich, Product # T9284
- Bovine Serum Albumin (BSA)
  - Sigma-Aldrich, Product # A1933
- Phosphate buffered saline (PBS)
  - Life Technologies, Product # 21300-025

Procedure

- Wash cells 2x with PBS for 5 minutes
- Fix cells in Z-fix at 4ºC for 10 minutes
- Wash cells 2x for 5 minutes/wash in PBS
- Permeabilize cells with 0.5% Triton X-100 in PBS for 20 minutes at RT
  - 50 µl Triton X-100 in 10 ml of PBS
- Wash cells 2x for 5 mins/wash minutes in PBS
- Add Stain, incubate for 45 mins at RT [Cover in foil]
  - 1% BSA in PBS
  - Rhodamine UEA-1 →1:100 dilution in PBS
  - For 1 ml of Stain
    - 10 mg of BSA
    - 10 µl of PBS
- Wash cells 2x for 5 mins/wash minutes in PBS [Cover in foil]
- Store at 4ºC until imaging

A.10 Enzyme-Linked Immunoabsorbant Assay - BMP-2

Materials

- Human/Mouse/Rat BMP-2 Quantikine ELISA kit
  - R&D Systems, Product # DBP200
  - Included in the kit
    - BMP-2 Microplate
    - BMP-2 Standard
    - BMP-2 Conjugate
    - Assay Diluent RD1-9
    - Calibrator Diluent RD5P Concentrate
    - Wash Buffer Concentrate
    - Color Reagent A
    - Color Reagent B
    - Stop Solution
    - Plate Sealers

Sample Collection and Lysis

- Collect media at time points and flash-freeze in liquid N_2
- Freeze in -80°C freezer until all samples are collected

Reagent Preparation

- Wash buffer
  - Dilute 20 ml of Wash Buffer Concentrate into 480 ml diH_2O
- Substrate Solution
  - Add Color Reagents A and B together in equal volumes 15 minutes prior to use
- Calibrator Diluent RD5P (1X)
  - Dilute 20 ml of Calibrator RD5P into 180 ml of diH_2O, let sit for 15 mins prior to use
- BMP-2 Standard
  - Reconstitute BMP-2 Standard in 1.0 ml of diH_2O, let sit for 15 mins prior to use

BMP-2 Standard Values			
A	4000 pg/ml	200 µl of OPN Standard	800 µl Calibrator Diluent RD5P
B	2000 pg/ml	500 µl of A	500 µl Calibrator Diluent RD5P
C	1000 pg/ml	500 µl of B	500 µl Calibrator Diluent RD5P
D	500 pg/ml	500 µl of C	500 µl Calibrator Diluent RD5P
E	250 pg/ml	500 µl of D	500 µl Calibrator Diluent RD5P
F	125 pg/ml	500 µl of E	500 µl Calibrator Diluent RD5P
G	62.5 pg/ml	500 µl of F	500 µl Calibrator Diluent RD5P
H	0 pg/ml		500 µl Calibrator Diluent RD5P

Procedure

- Add 100 µl of Assay Diluent RD1-19 to each well
- Add 50 µl of standard/sample to well. Add in duplicate

- Cover with adhesive strip and incubate at room temperature for 2 hours
- Aspirate each well and wash 4X in Wash Buffer
- Blot against clean paper towels after washing to remove excess liquid
- Add 200 µl of BMP-2 Conjugate to each well
- Cover with new adhesive strip and incubate at room temperature for 2 hours
- Aspirate each well and wash 4X in Wash Buffer
- Blot against clean paper towels after washing to remove excess liquid
- Add 200 µl of Substrate Solution to each well (make solution 15 mins prior to use)
- Cover with adhesive strip and incubate at room temperature for 30 mins. Cover from light.
- Add 50 µl of Stop Solution to each well
- Read plate at 450 nm

A.11 Enzyme-Linked Immunoabsorbant Assay - Osteopontin

Materials

- Human Osteopontin (OPN) Quantikine ELISA kit
  - R&D Systems, Product # DOST00
  - Included in the kit
    - OPN Microplate
    - OPN Standard
    - OPN Conjugate
    - Assay Diluent RD1-9
    - Calibrator Diluent RD5-24 Concentrate
    - Wash Buffer Concentrate
    - Color Reagent A
    - Color Reagent B
    - Stop Solution
    - Plate Sealers

Sample Collection and Lysis

- Collect media at time points and flash-freeze in liquid N_2
- Freeze in -80°C freezer until all samples are collected

Reagent Preparation

- Wash buffer
  - Dilute 20 ml of Wash Buffer Concentrate into 480 ml diH_2O
- Substrate Solution
  - Add Color Reagents A and B together in equal volumes 15 minutes prior to use
- OPN Standard
  - Reconstitute OPN Standard in 1.0 ml of diH_2O, let sit for 15 mins prior to use

OPN Standard Values			
A	20 ng/ml	60 µl of OPN Standard	540 µl Calibrator Diluent RD5-24
B	10 ng/ml	300 µl of A	300 µl Calibrator Diluent RD5-24
C	5 ng/ml	300 µl of B	300 µl Calibrator Diluent RD5-24
D	2.5 ng/ml	300 µl of C	300 µl Calibrator Diluent RD5-24
E	1.25 ng/ml	300 µl of D	300 µl Calibrator Diluent RD5-24
F	0.625 ng/ml	300 µl of E	300 µl Calibrator Diluent RD5-24
G	0.312 ng/ml	300 µl of F	300 µl Calibrator Diluent RD5-24
H	0 ng/ml		300 µl Calibrator Diluent RD5-24

Procedure

- Add 100 µl of Assay Diluent RD1-6 to each well
- Add 50 µl of standard/sample to well. Add in duplicate
- Cover with adhesive strip and incubate at room temperature for 2 hours
- Aspirate each well and wash 4X in Wash Buffer
- Blot against clean paper towels after washing to remove excess liquid
- Add 200 µl of OPN Conjugate to each well
- Cover with new adhesive strip and incubate at room temperature for 2 hours
- Aspirate each well and wash 4X in Wash Buffer
- Blot against clean paper towels after washing to remove excess liquid
- Add 200 µl of Substrate Solution to each well (make solution 15 mins prior to use)
- Cover with adhesive strip and incubate at room temperature for 30 mins. Cover from light.
- Add 50 µl of Stop Solution to each well
- Read plate at 450 nm

A.12 Hematoxylin and Eosin (H&E) Staining [Histology]

Materials

- Toluene
  - Fisher Scientific, Product # T324
- 100% Ethanol (EtOH)
  - Sigma-Aldrich, Product #459844
- Scientific Device Laboratory Aqua Hold Pap Pen
  - Fisher Scientific, Product # 23-769-300
- Thermo Scientific *Lab Vision* Mayer's Hematoxylin
  - Fisher Scientific, Product # TA-125-MH
- Ammonium hydroxide
  - Sigma-Aldrich, Product # 320145
- Eosin Y Stain
  - Fisher Scientific, Product # 2845-32
- Fisher HealthCare *Xylene* Mounting Media
  - Fisher Scientific, Product # 23-245-691

Rehydration of Slides

- Place slides in toluene for 5 mins
- Repeat in new toluene for 5 mins
- Place slides in 100% EtOH for 3 mins
- Repeat in 100% EtOH for 3 mins
- Place slides in 95% EtOH for 3 mins
- Repeat in 95% EtOH for 3 mins
- Place in ddH_2O for > 30 secs

H&E Staining

- Use PAP pen to mark around tissue section (make a box around each section, don't have to get that close to each tissue)
- Place slides in hematoxylin bath for 10 mins at room temperature
- Rinse gently in ddH_2O bath
- Dip slides 10X in 0.037 M ammonium
- Rinse slides in ddH_2O bath for 5 mins
- Place slides in 95% EtOH for 30 secs
- Place slides in eosin for 30-60 secs

Dehydration of Slides

- Place slides 95% EtOH for 1 min
- Repeat in new 95% EtOH for 1 min
- Place slides in 100% EtOH for 2 mins
- Repeat in new 100% EtOH for 2 mins
- Place slides in toluene for 2 mins
- Repeat in new toluene for 2 mins
- Apply mounting medium (Xylene-based) and place coverglass over samples
- Remove bubbles with edge of forceps and allow to dry before imaging

A.13 Von Kossa (VK) Staining [Histology]

Materials

- Toluene
  - Fisher Scientific, Product # T324
- 100% Ethanol (EtOH)
  - Sigma-Aldrich, Product #459844
- Scientific Device Laboratory Aqua Hold Pap Pen
  - Fisher Scientific, Product # 23-769-300
- Silver Nitrate
  - Sigma-Aldrich, Product #S6506
- Sodium Thiosulfate
  - Sigma-Aldrich, Product #217263
- Eosin Y Stain
  - Fisher Scientific, Product # 2845-32
- Fisher HealthCare *Xylene* Mounting Media
  - Fisher Scientific, Product # 23-245-691

Rehydration of Slides

- Place slides in toluene for 5 mins
- Repeat in new toluene for 5 mins
- Place slides in 100% EtOH for 3 mins
- Repeat in 100% EtOH for 3 mins
- Place slides in 95% EtOH for 3 mins
- Repeat in 95% EtOH for 3 mins
- Place in ddH_2O for > 30 secs

VK Staining (Eosin Counterstain)

- Use PAP pen to mark around tissue section (make a box around each section, don't have to get that close to each tissue)
- Place slides in 1% silver nitrate for 1 hour under UV
  - 1 gram of silver nitrate in 100 mls of ddH_2O
- Rinse gently in ddH_2O bath
- Place slides in 5% sodium thiosulfate for 5 mins
  - 5 grams of sodium thiosulfate in 100 mls of ddH_2O
- Rinse slides in ddH_2O bath for 5 mins
- Place slides in 95% EtOH for 30 secs
- Place slides in eosin for 30-60 secs

Dehydration of Slides

- Place slides 95% EtOH for 1 min
- Repeat in new 95% EtOH for 1 min
- Place slides in 100% EtOH for 2 mins
- Repeat in new 100% EtOH for 2 mins
- Place slides in toluene for 2 mins

- Repeat in new toluene for 2 mins
- Apply mounting medium (Xylene-based) and place coverglass over samples
- Remove bubbles with edge of forceps and allow to dry before imaging

A.14 CD31 Staining [Histology]

Materials

- Toluene
  - Fisher Scientific, Product # T324
- 100% Ethanol (EtOH)
  - Sigma-Aldrich, Product #459844
- HRP Mouse (DAB+) EnVision Kit
  - Dako, Product #K4006
  - Kit includes
    - DAKO antigen retrieval solution
    - Peroxidase block
    - DAB+ Substrate Chromagen
- Tris-Base
  - Fisher Scientific, Product #BP152-1
- Sodium chloride (NaCl)
  - Fisher Scientific, Product #S640
- Triton X-100
  - Sigma-Aldrich, Product # T9284
- Scientific Device Laboratory Aqua Hold Pap Pen
  - Fisher Scientific, Product # 23-769-300
- Monoclonal Mouse Anti-Human CD31, Endothelial Cell Antibody
  - Dako, Product #M0823
- Thermo Scientific *Lab Vision* Mayer's Hematoxylin
  - Fisher Scientific, Product # TA-125-MH
- Ammonium hydroxide
  - Sigma-Aldrich, Product # 320145
- Eosin Y Stain
  - Fisher Scientific, Product # 2845-32
- Fisher HealthCare *Xylene* Mounting Media
  - Fisher Scientific, Product # 23-245-691

Day 1

Prepare stock solutions

- Make 10X Tris-Buffered Saline (500 mls)
  - 44 g NaCl
  - 15.75 g Tris
  - 500 ml of ddH_2O
- Make 1X Tris-Buffered Saline + 0.1% Triton-X 100 (100 mls)
  - 10 mls 10X TBS
  - 1 ml Triton-X 100
  - Bring volume up to 100 mls with ddH2O

Rehydration of Slides

- Place slides in toluene for 5 mins
- Repeat in new toluene for 5 mins
- Place slides in 100% EtOH for 3 mins
- Repeat in 100% EtOH for 3 mins
- Place slides in 95% EtOH for 3 mins
- Repeat in 95% EtOH for 3 mins
- Place in ddH_2O for > 30 secs

CD31 Staining (H&E Counterstain)

- Add ddH_2O to heating compartment of food steamer
- Add DAKO antigen retrieval solution to slide cassette and insert slides
- Place cassette in steamer and steam for 25 mins
- Wash slides in TBST and remove moisture from around tissues
- Use PAP pen to mark around tissue section (make a box around each section, don't have to get that close to each tissue)
- Apply peroxidase block (enough to cover the specimen) and incubate at RT for 5 mins
- Wash gently with ddH_2O wash bottle without focusing stream on sample
- Place in TBST bath and remove moisture from around tissues
- Add primary antibody and incubate overnight at 4ºC (cover samples in plastic trays with parafilm)
    - Anti-CD31 → 1:50 dilution in TBST

<u>Day 2</u>

CD31/UEA-1 Staining (H&E Counterstain)

- Wash in TBST and remove excess moisture
- Apply secondary antibody and incubate at RT for 30 mins
- Apply liquid DAB+ substrate-chromagen and incubate for 10 mins at RT
- Rinse gently with ddH_2O wash bottle without focusing flow on the sample
- Place slides in hematoxylin bath for 10 mins at RT
- Rinse gently in ddH_2O bath
- Dip slides 10X in 0.037 M ammonium
- Rinse slides in ddH_2O bath for 5 mins
- Place slides in 95% EtOH for 30 secs
- Place slides in eosin for 30-60 secs

Dehydration of Slides

- Place slides 95% EtOH for 1 min
- Repeat in new 95% EtOH for 1 min
- Place slides in 100% EtOH for 2 mins
- Repeat in new 100% EtOH for 2 mins
- Place slides in toluene for 2 mins

- Repeat in new toluene for 2 mins
- Apply mounting medium (Xylene-based) and place coverglass over samples
- Remove bubbles with edge of forceps and allow to dry before imaging

A.15 UEA-1 Staining [Histology]

Materials

- Toluene
  - Fisher Scientific, Product # T324
- 100% Ethanol (EtOH)
  - Sigma-Aldrich, Product #459844
- Tris-Base
  - Fisher Scientific, Product #BP152-1
- Sodium chloride (NaCl)
  - Fisher Scientific, Product #S640
- Triton X-100
  - Sigma-Aldrich, Product # T9284
- Scientific Device Laboratory Aqua Hold Pap Pen
  - Fisher Scientific, Product # 23-769-300
- Antigen Unmasking Solution, Citric Acid Based
  - Vector Laboratories, Product # H-3300
- Streptavidin/Biotin Blocking Kit
  - Vector Laboratories, Product # SP-2002
- Carbo-Free Blocking Solution (10X Concentrate)
  - Vector Laboratories, Product # SP-5040
- Biotinylated Ulex Europaeus Agglutinin I (UEA-1) Antibody
  - Vector Laboratories, Product # B-1065
- ImmPACT DAB Peroxidase Substrate
  - Vector Laboratories, Product # SK-4105
- Thermo Scientific *Lab Vision* Mayer's Hematoxylin
  - Fisher Scientific, Product # TA-125-MH
- Ammonium hydroxide
  - Sigma-Aldrich, Product # 320145
- Eosin Y Stain
  - Fisher Scientific, Product # 2845-32
- Fisher HealthCare *Xylene* Mounting Media
  - Fisher Scientific, Product # 23-245-691

Prepare stock solutions

- Make 10X Tris-Buffered Saline (500 mls)
  - 44 g NaCl
  - 15.75 g Tris
  - 500 ml of ddH_2O
- Make 1X Tris-Buffered Saline + 0.1% Triton-X 100 (100 mls)
  - 10 mls 10X TBS
  - 1 ml Triton-X 100
  - Bring volume up to 100 mls with ddH2O
- Make 1X Carbo-Free Blocking Solution
  - 1 ml of 10X Carbo-Free Blocking Solution (stock)

    - 9 ml of ddH_2O
- Make VECTASTAIN Elite ABC Reagent
    - 5 mls of TBST
    - 2 drops of Reagent A (gray label)
    - 2 drops of Reagent B (gray label)
    - Allow to stand for 30 minutes prior to use
- Make ImmPACT DAB Peroxidase Substrate
    - 1 ml of ImmPACT DAB Diluent
    - 1 drop of ImmPACT DAB Chromogen concentrate

Rehydration of Slides

- Place slides in toluene for 5 mins
- Repeat in new toluene for 5 mins
- Place slides in 100% EtOH for 3 mins
- Repeat in 100% EtOH for 3 mins
- Place slides in 95% EtOH for 3 mins
- Repeat in 95% EtOH for 3 mins
- Place in ddH_2O for 5 minuites

UEA-1 Staining (H&E Counterstain)

- Add ddH_2O to heating compartment of food steamer
- Add Antigen Unmasking Solution to slide cassette and insert slides
- Place cassette in steamer and steam for 25 mins
- Wash slides in TBST and remove moisture from around tissues
- Use PAP pen to mark around tissue section (make a box around each section, don't have to get that close to each tissue)
- Incubate sections with streptavidin solution for 15 mins
- Rinse gently with ddH_2O wash bottle without focusing flow on the sample
- Incubate sections with biotin solution for 15 mins
- Rinse gently with ddH_2O wash bottle without focusing flow on the sample
- Block non-specific binding by incubating sections in Carbo-Free Blocking Solution for 30 mins at RT
- Wash gently in TBST for 5 mins
- Add UEA-1 primary antibody (2-20 µg/ml final concentration) and incubate for 30 minutes at room temperature
    - Biotinylated Anti-UEA-1 → 1:100 dilution in PBS

        ****Prepare VectaSTAIN Elite ABC Reagent****
- Wash in TBST for 5 mins at RT and remove excess moisture
- Incubate sections in VECTASTAIN Elite ABC Reagent for 30 mins at RT
- Wash in TBST for 5 mins at RT and remove excess moisture
- Add ImmPACT DAB for 2-10 mins (until it develops) at RT
- Wash in ddH_2O for 5 mins at RT
- Place slides in hematoxylin bath for 10 mins at RT
- Rinse gently in ddH_2O bath
- Dip slides 10X in 0.037 M ammonium

- Rinse slides in ddH_2O bath for 5 mins
- Place slides in 95% EtOH for 30 secs
- Place slides in eosin for 30-60 secs

Dehydration of Slides

- Place slides 95% EtOH for 1 min
- Repeat in new 95% EtOH for 1 min
- Place slides in 100% EtOH for 2 mins
- Repeat in new 100% EtOH for 2 mins
- Place slides in toluene for 2 mins
- Repeat in new toluene for 2 mins
- Apply mounting medium (Xylene-based) and place coverglass over samples
- Remove bubbles with edge of forceps and allow to dry before imaging

A.16 AR-G2 Rheometer

Set up

- Turn on Air
- Close the valve – push latch up to unlock
- Turn on switch for the rheometer
    - WAIT until starts spinning before doing anything else
- Unscrew black cover gently from the top – NEVER pull off screw from bottom
- Change the stage by hitting the left most button on machine
    - Reconnect each component until it clicks
    - Order does not matter
- Switch screws if necessary
    - Pull up slowly, do not touch sides
    - Do NOT add geometry until after configure inertia

Calibration

- Open AR Instrument Control Program
- Options → Instrument → Inertia → Calibrate
- Add geometry
    - Hand tighten from screw on top, NEVER from the bottom
- Select plate (8 mm or 20 mm) in Plate Settings
- Plate → Settings → Calibrate (sets geometry inertia)
- Options →Instrument → Miscellaneous → Calibrate → Apply
- Lower stage by pushing down arrow on program, get close to bottom
- Instrument → Gap → Zero gap → Continue
- Instrument → Rotational Mapping → Set to 1 iteration → Perform Mapping
    - Takes about 5 minutes to complete
- Load oscillatory procedure
    - Sets parameters to measure
    - If new, Instrument → Oscillatory Mapping → Perform New Mapping
- Add sample
- Set gap to 1000 microns
    - Make sure touches sample
- Run Experiment

Turning off

- Close program
- Switch back screw to 20 mm screw
- Place foil over stage
- Turn off rheometer
- Turn off gas

A.17 Compressive Testing Machine

Set up → Do 2 hours before testing

- Screw adaptor into base
- Turn on (in this order)
    - Computer
    - Control Module → black
    - Power Module → white
        - Switch to "ON"
        - Pull out emergency stop
            - Will max out piston to the top
- Screw in platens
    - Bigger platen to bottom
    - Smaller platen to top
- Double click "Start 1st 1220 800LM"
    - Opens Machine Calibration
        - Do NOT mess with
- Double click "V2 Script Program"
- File → Open → DMA Control
- Machine Offline → Go online

Machine Offset

- Utilities → Offset Readout
- 1 actuator
- 3 channels
    - Encoder1 → tells machine where to go
    - Load → cell, gives reliable value
    - LVDT → sensor that measures the position of the piston, gives a reliable value
- Offset all values to 0
    - Encoder1, Load, LVDT

Run Sample

- Click "Switch On"
    - Green light on White Power Module turns on
- Negative values in system move piston down
- Values are in mm
- Target point – where piston will move
- Time – duration for movement
- Click "DAQ"
    - Set to Manual
    - Need unique name for every sample
        - Only 8 characters, avoid spaces
- Log Rate → 200 Hz
    - 200 data points per second

Static Testing

- Test → Monotomic
- Target point – where to move to while testing
- Time – how long during ramp to point
    - Ramp – Linear
    - Sine – Sine wave performed
- Left Panel → triggers to make stop
    - Max displacement set to 5 mm
- Notes
    - Rate at which compression occurs affects values → pick 1 number for settings and keep constant
        - Time to ramp – 0.5 to 2 seconds
- Move start point to right above gel
- DAQ → Set name → Close
- Start Recording → Start Test → Stop Recording

Dynamic Testing

- Test → Dynamic
- Mean – absolute position
- End cycle count – absolute value
- Start Recording → Start Test → Stop Recording

Exporting Data

- DAQ → Export → All Data → Export
    - Outputs Excel File
    - Do NOT touch anything until "Done"
    - Sheet 1 – first set of data
- Excel File contains
    - LVDT – position where it is
    - Load – force in grams
- Convert to stress and strain to calculate Apparent Young's Modulus
- Force = (Load/1000) x (9.8 m/s^2)
- Area = cross sectional area of top of gel
    - Measure with micrometer or from picture in ImageJ
- Strain = calculate from LVDT values
- Plot stress vs. strain curve
    - Take slop of linear region as Apparent Young's Modulus

Turning Off

- Turn DAQ system to “Switch Off”
- Machine → “Go Offline”
- File → Quit (Do not hit X Button)
- Close the Machine Control Application
- Take out platens
    - MAKE SURE THESE ARE REMOVED
- Push Emergency Stop Button
    - Cuts Power from system
    - MAKE SURE PLATENS ARE REMOVED OR THEY WILL GET CRUSHED
- Turn off Power Module – white
- Turn off Control Module – black
- Turn off computer

APPENDIX B

Fabrication and Delivery of 3D Cell-Seeded Hydrogel Microenvironments

B.1 Introduction

In contrast to traditional tissue engineering techniques in which cells are seeded onto a scaffold, modular tissue engineering aims to fabricate engineered tissues through the assembly of cell-seeded biomimetic structures [1]. Tissue subunits, or "modules," are utilized to generate larger tissue structures that have been employed for orthopedic, vascular, and numerous other applications. Methods such as micro-fabrication of cell-laden hydrogels [2, 3], cell printing [4, 5], or the creation of cell sheets [6, 7] have been employed in modular tissue engineering applications. Current work in the formation of cell-seeded hydrogels includes creating collagen microspheres in small droplets and through water-in-oil emulsion techniques [8, 9]. Cheng et. al utilized two different types of microspheres fabricated in this method to assemble larger tissue structures with compartmentalized cell phenotypes [10].

Our lab has previously generated cellular microenvironments, or "microbeads," by encapsulating stem cells directly within hydrogels composed of natural ECM proteins and polysaccharides such as collagen, fibrin, agarose and chitosan [11-16]. Multiple factors including soluble cues, cell-to-cell contacts, and mechanical cues can be modulated in these cellular niches as an attempt to control cell adhesion, proliferation, phenotype and differentiation. These robust cellular microenvironments have potential in matrix-enhanced cell delivery applications that can be applied numerous tissue engineering applications.

In the present work, we describe the methodology behind fabricating protein and polysaccharide-based microbeads. Numerous bead formulations are described as well as the effect on microbead size and size distribution by varying oil viscosity and impeller speed. Cell viability after microbead fabrication and in long-term culture is assessed and delivery methods of microbeads are evaluated to demonstrate feasibility of using these microbeads in modular tissue engineering applications.

B.2 Materials and Methods

General Microbead Fabrication

The general process of microbead fabrication using a water-in-oil emulsion technique is summarized in Figure B.1. Extracellular matrix (ECM) proteins and polysaccharides were reconstituted from a lyophilized form into a liquid and then mixed with chemicals, enzymes, growth factors, and cross-linking agents to form 3D hydrogels microbeads. Cells were added directly into the pre-gelled mixture to allow for homogenous distribution of the cells upon gelation. The solution was then injected into a polydimethylsiloxane (PDMS; Xiameter, Dow Corning, Midland, MI) bath and stirred with a double-bladed impeller. The pH of the gel solution and/or the temperature of the PDMS bath were then changed to allow for gelation and formation of stable microbeads. The microbeads formed in the oil phase were collected by centrifuging the mixture at 200 x g and were washed in PBS containing a surfactant, Pluronic L101 (BASF, Florham Park, NJ), to reduce surface tension between the water and oil phase.

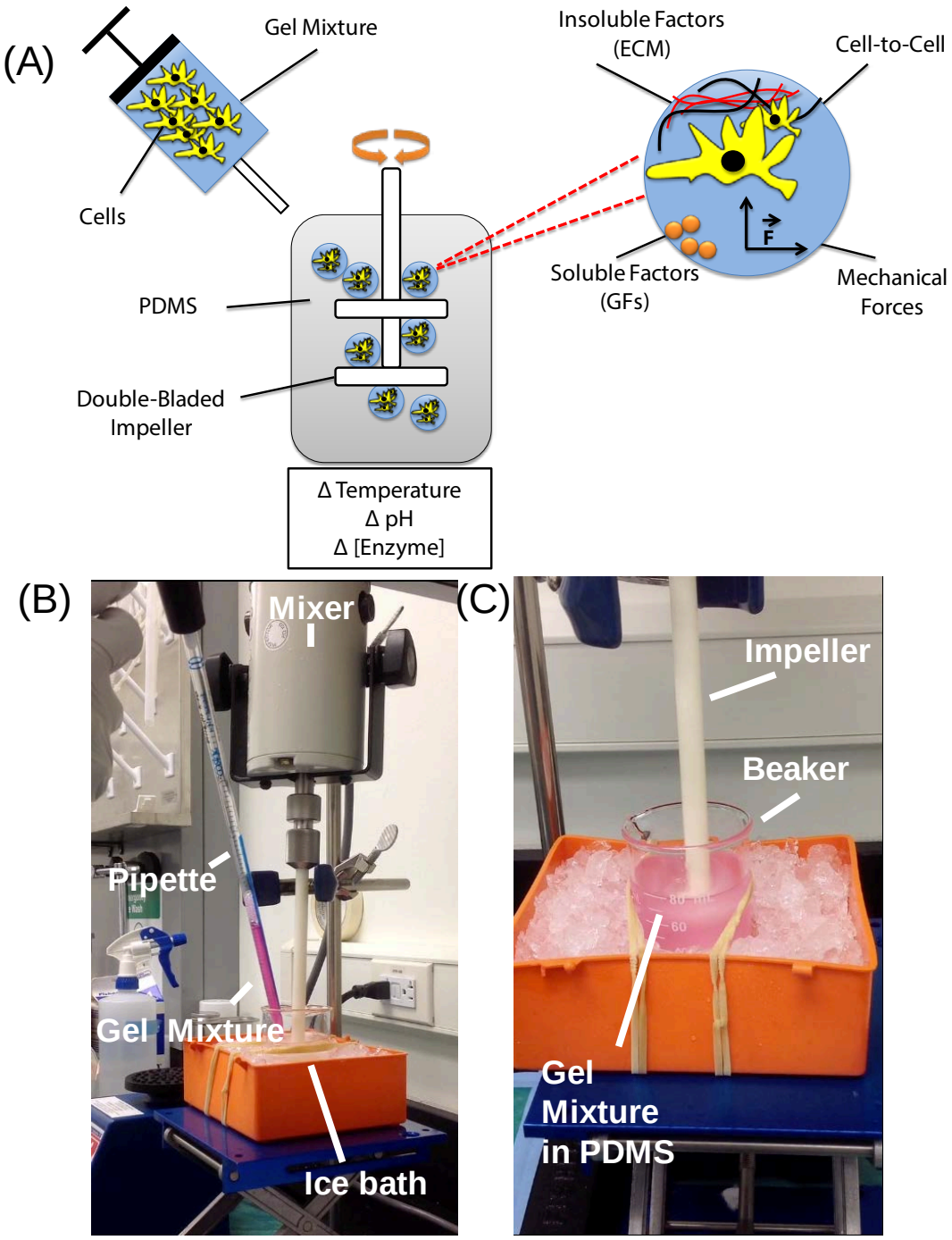

Figure B.1 – Microbead preparation process. (A) Schematic of microbead fabrication process. (B, C) – Photographs of microbead preparation

Microbead Formulations

Numerous microbead compositions have been fabricated using different biomaterials and gelation initiators. Each formulation provides a matrix for a tissue-specific application.

Collagen microbeads were generated by mixing 5x concentrated Dulbecco's Modified Eagle's Medium (DMEM; Life Technologies, Carlsbad, CA), Fetal Bovine Serum (FBS; Life Technologies), 0.1 N sodium hydroxide (NaOH; Sigma Aldrich, St. Louis, MO), 6.0 mg/ml bovine type I collagen (MP Biomedicals, Solon, OH), and 1 mM glyoxal (Sigma) for a final concentration of 3.0 mg/ml collagen in the microbeads. The mixture was emulsified in PDMS and collagen polymerization was initiated by raising the temperature of the mixture to 37°C. After mixing for 25 minutes, microbeads were collected from the oil phase by centrifugation at 200 x g.

Collagen/agarose composite microbeads were fabricated by mixing 5x concentrated DMEM, FBS, 0.1 N NaOH, 4.0 mg/ml bovine type I collagen and 2.0% agarose (Fisher Scientific, Pittsburgh, PA) in varying ratios [11, 12]. Collagen polymerization is both temperature (37°C) and pH (7) sensitive; therefore, maintaining a cold acidic state prevents premature gelation. Agarose, on the other hand, polymerizes in a cold state. Therefore, collagen was precooled to 4°C and the agarose was preheated to 60°C. All components were then injected into an emulsification bath containing PDMS kept at 37°C and mixed with an impeller for 6 minutes to allow for even formation of ECM droplets. The mixture was then cooled on ice for 30 minutes to form spherical beads. Collagen/agarose microbeads have beneficial properties for osteogenic applications.

Chitosan/fibrin microbeads were prepared by adding chitosan (2% wt/vol) and fibrin (stock solution 60 mg/ml) in a pre-cooled solution containing β-GP and 0.1 UT/ml thrombin

(Sigma) at various chitosan-fibrin ratios [13]. During the emulsification step, the solution was injected into a PDMS bath kept at 4°C. Thermal and enzymatic gelation occurred by raising the temperature to 37°C and mixing for 20 minutes. The emulsion temperature was then reduced to 4°C to stabilize the microbeads. Microbeads were centrifuged out of the oil phase at 200 x g.

Collagen/chitosan microbeads have been prepared in two methods. In the first method, 5 mg/ml of high molecular weight chitosan (Sigma) was dissolved in 0.02 N acetic acid and was crosslinked with 7.5% genipin (Wako Chemicals USA, Richmond, VA) for 15 mins at 37°C. The solution was then cooled for 5 mins at 25°C. Type I collagen (4 mg/ml) and 15% gelatin Type A at 50°C and 4°C, respectively, were then added to the chitosan solution. A 0.1 N NaOH solution at 4°C was quickly added to the matrix mixture to neutralize the pH.

In the second method, 2% wt/vol chitosan (FMC BioPolymer, Philadelphia, PA) dissolved in 0.1 N acetic acid and collagen (stock solution 4 mg/ml) were added together with physical and chemical crosslinkers, beta-glycerophosphate (β-GP; Sigma) and 1 mM glyoxal, respectively [14, 15]. The mixture was injected into a PDMS bath kept on ice and co-polymerization was conducted by increasing the temperature of the bath to 37°C. Microbeads were then collected from the oil phase by centrifuging the mixture at 200 x g.

Collagen/hydroxyapatite (HA) microbeads have been formulated through the addition of particulate nano-HA (<200 nm; Sigma) to the pre-gelled mixture. A cold mixture of collagen (final concentration 3 mg/ml), nano-HA (final concentration 10 mg/ml), 1x DMEM, 5x DMEM, FBS, and 0.1 M NaOH then injected into the PDMS phase kept on ice. After 5 minutes of emulsification, the temperature was raised to 37°C and rotated for another 25 minutes to allow for collagen gelation. Collagen-HA beads were collected through centrifugation at 200 x g. The

addition of HA particles increased the density of the microbeads and facilitated separation from the oil phase.

Collagen/fibrin composite microbeads have been fabricated by mixing collagen (final concentration 1.25 mg/ml) and fibrin (final concentration 1.25 mg/ml) with 5x DMEM, 1x DMEM, FBS, 0.1 M NaOH, and thrombin (final concentration 1 UT/ml). The gel mixture was injected into PDMS and kept on ice for 5 minutes [16]. The temperature was then raised to 37°C and mixed for 25 minutes to allow for gelation of collagen and fibrin. Microbeads were collected through centrifugation at 200 x g.

All of the microbead formulations listed above were stained with EZBlue reagent (Sigma) to allow for visualization of the protein content within microbeads.

Effect of Viscosity and Impeller Speed on Microbead Diameter and Size Distribution

The effect of oil viscosity was examined on collagen/chitosan microbeads. The dynamic viscosity of the PDMS oil was varied from 20 centistokes (CS), 50 CS, and 100 CS to determine its effect on microbead size and size distribution. Microbeads were collected and visualized under a light microscope and microbead diameter was analyzed using ImageJ software (National Institute of Health, Bethesda, MD).

The effect of impeller speed was investigated on collagen/HA microbeads. The impeller speed was varied from 600 to 1200 revolutions per minute (RPM) in increments of 200 RPM. Size and size distribution were analyzed as described above.

Cell Viability Assessment

MC3T3-E1 Subclone 14 (generously provided by Dr. R.T. Franchesci, University of Michigan) [17] were cultured in Minimum Essential Medium (αMEM) alpha (Life Technologies) supplemented with 10% mesenchymal stem cell-qualified FBS and 1% PS. At passage 8, MC3T3 (1.0 X 10^6 cells/ml) were added directly in to the gel mix at to allow for homogenous distribution within microbeads. Collagen/fibrin (mass ratio 50/50) composite microbeads were fabricated in 100 CS PDMS using an impeller speed of 600 RPM. Microbeads were cultured statically in 15 ml centrifuge tubes. Cell viability and cell morphology were assessed at days 1 and 7 using a vital stain kit (Live/Dead®, Life Technologies). Microbeads were washed three times in sterile PBS for 5 mins/wash and then incubated at 37°C for 45 min in a solution containing 4.0 µm calcein-AM and 4.0 µm ethidium homodimer-1 in PBS. After three subsequent PBS washes, microbeads were imaged using a laser scanning confocal microscope (Olympus America Inc., Center Valley, PA).

Cell Morphology (Actin, Nucleus)

To assess cell morphology, the actin cytoskeleton was stained with either Texas-red phalloidin or FITC phalloidin (Life Technologies). The cell nucleus was visualized using a DAPI stain (Life Technologies). Cells, gels, and microbeads to be stained and imaged were first washed twice in PBS for five minutes at room temperature. They were then subsequently fixed using Z-fix (buffered zinc formalin fixative, Anatech Ltd, Battle Creek, MI) for ten minutes at 4°C. After fixation, the samples were washed twice in PBS at room temperature. To permeabilize the cell membranes and allow for infiltration of staining, the samples were permeabilized with 0.5% Triton X-100 (Sigma) for twenty minutes at room temperature. The

samples were then washed twice in PBS for five minutes and stored in PBS until staining was performed. The stain was created by mixing Bovine Serum Albumin (Sigma) at 10 mg/mL of stain, labeled phalloidin at 25 µL/mL, DAPI at 1 µL/mL, and 974 µL/mL of PBS. Stain was added to the samples for 45 minutes at room temperature in the dark. The samples were then washed in PBS for 5 minutes, and stored in PBS at 4°C in the dark until imaging. Imaging was performed using a laser scanning confocal microscope (Nikon A-1, Nikon Instruments, Melville, USA) at the MIL center in the NCRC.

Visualization of Microbeads

In order to visualize the structure of the microbeads, Collagen-Fibrin microbeads were created using FITC-fibrinogen (Life Technologies). FITC-fibrinogen was added at 9 µg/mL to the filtered fibrinogen mixture in the dark. Collagen-Fibrin microbeads were then created as previously described, in the dark, using human mesenchymal stem cells at 250,000 cells/mL of bead mixture. The microbeads were cultured for seven days, and then subsequently imaged in fibrin gels.

Microbead construct creation and visualization

A potential delivery method for microbeads is the creation of constructs for implant. Using a previously described method [14], centrifuged constructs were created using collagen-chitosan beads with embedded human dermal fibroblasts and human mesenchymal stem cells at a concentration of 1,000,000 cells/mL of bead mixture. Disk constructs were created on top of filter paper, removed, and placed into culture dishes for seven days. At the one and seven day mark, the samples were fixed, permeabilized, and stained with FITC-phalloidin and DAPI for

morphological visualization. Live/Dead staining was also performed at the day one and day seven mark to observe cell viability.

Injectable Delivery of Microbeads

Microbeads were delivered two ways. The first method involved the delivery of FITC collagen fibrin microbeads cultured for 7 days through a 25 ½ gauge needle in a fibrin gel. 500 µL of beads, at a concentration of 1 mL of bead preparation/ mL of media, were centrifuged in a microcentrifuge tube at 200 g for five minutes. The media was then aspirated off the beads. In order to create the fibrin gel for delivery, bmMSC FBS (Gibco, Grand Island, NY) at 10%, 1x DMEM at 22.5%, fibrinogen at a final concentration of 2.5 mg/mL, and thrombin at a final concentration of 1 UT/mL were sequentially added to the bead mixture, and then aspirated using a syringe with attached needle. This mixture was then injected into a microscope imaging plate and allowed to set for 40 minutes, after which the samples were stained for their actin cytoskeleton and nuclei.

The second method of delivery involved the delivery of a microbead paste into a cartilage defect in a bovine knee. A bovine knee was acquired from Dunbar Meats (Milan, MI), and a layer of cartilage was removed from the knee joint. A plug of microbeads was prepared using centrifugation as previously described by Caldwell et al [14] with blue particles for visualization, and placed into the defect. Using a microspatula, the microbeads were fit to the defect. The joint underwent articulation manually, and the results were recorded by standard photography.

B.3 Results

Microbead Size and Morphology

Microbeads collected from the oil phase are shown in Figures B.2, B.3, and B.4. Microbead size varied inversely with both oil viscosity (Figure B.2) and impeller speed (Figure B.3). Average microbead size decreased from 505.6 µm at 20 CS to 247.5 µm at 100 CS. Furthermore, the size distribution became less variable with increasing oil viscosity as indicated by the decrease in standard deviation values. Similarly, microbead size decreased from 195.8 µm at 600 RPM to 51.3 µm at 1200 RPM. Size distribution also became narrower with increasing speed.

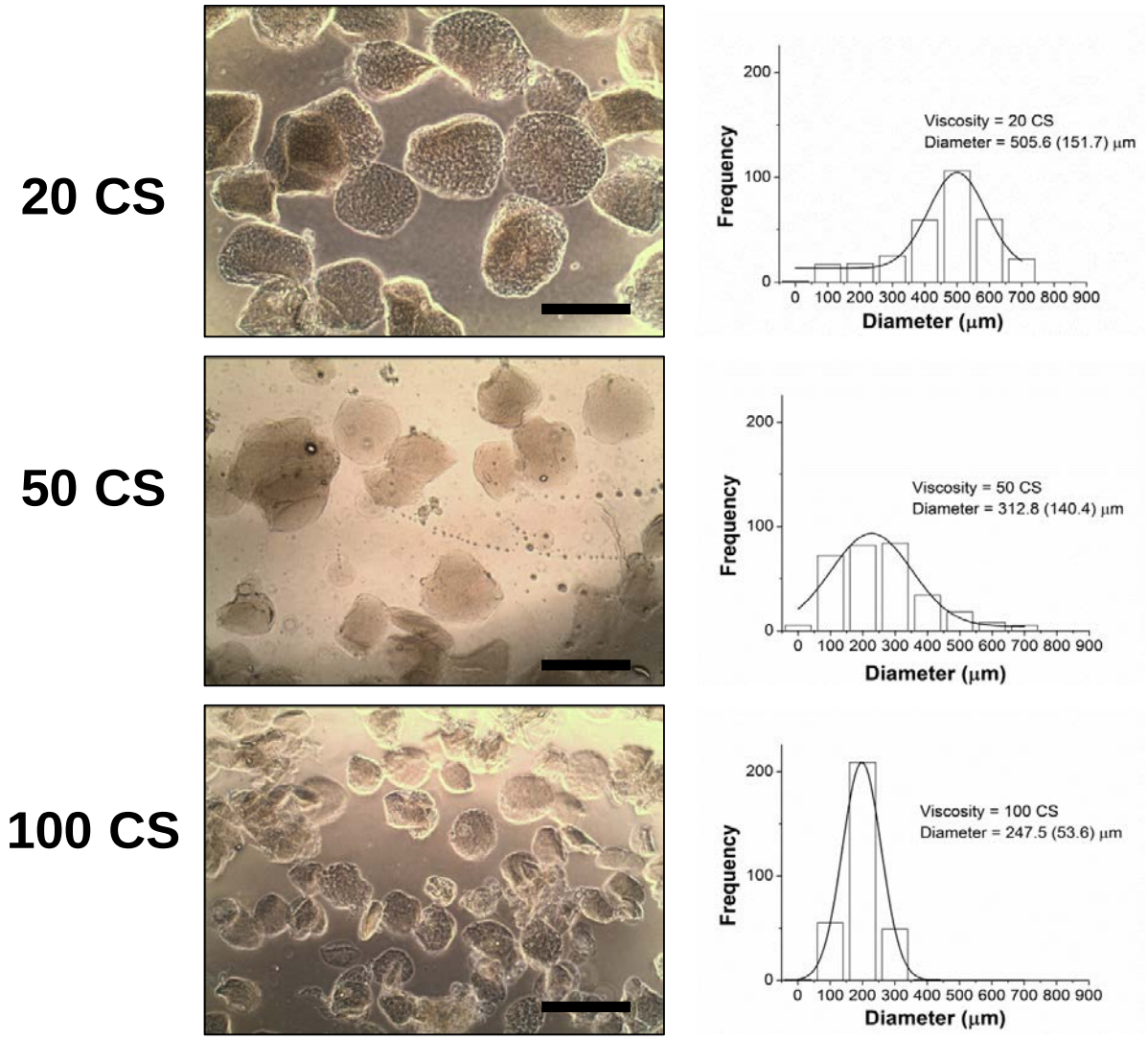

Figure B.2 – Effect of viscosity on microbead size and size distribution. Microbead size decreased with increasing oil viscosity. Scale bar = 500 µm

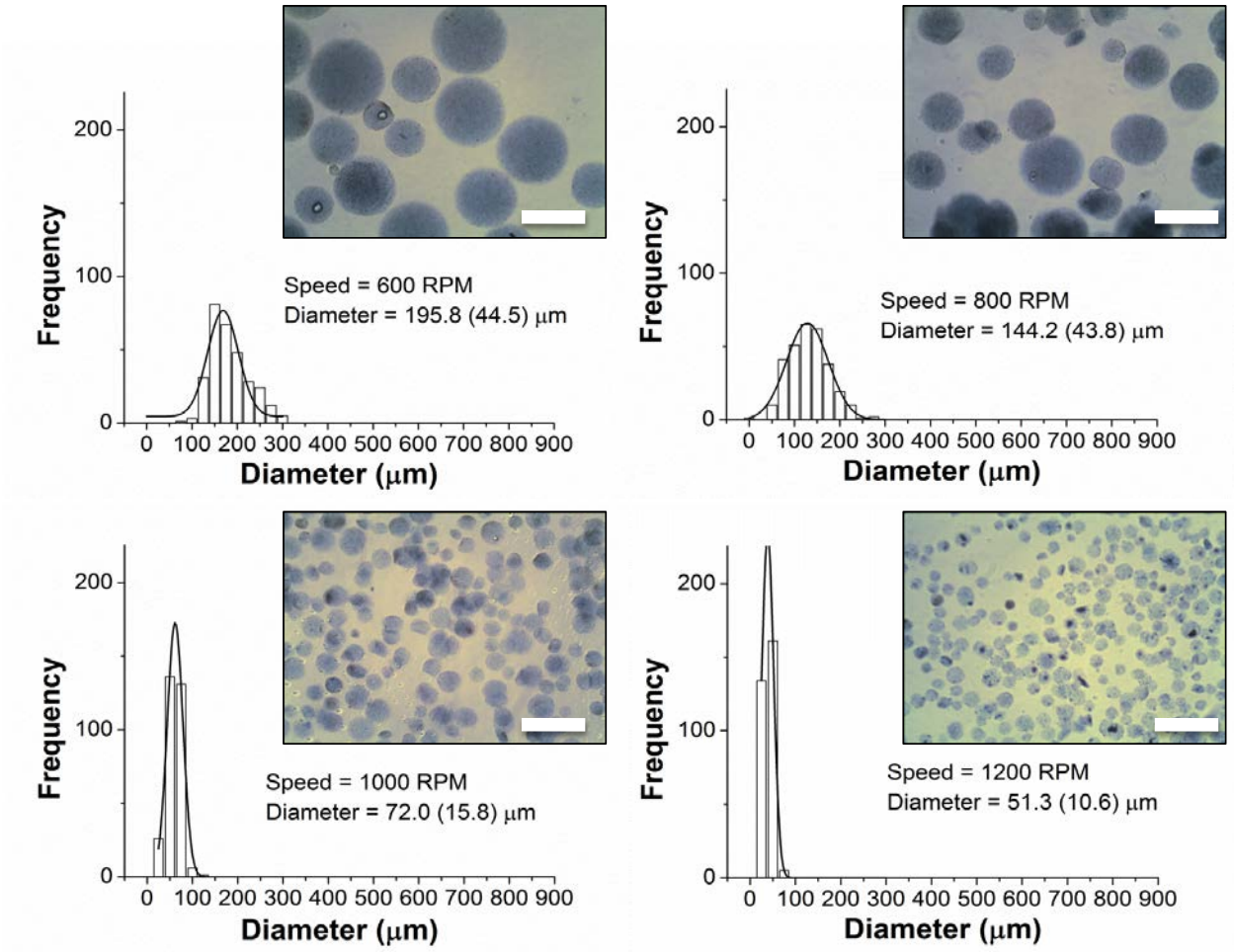

Figure B.3 – Effect of impeller speed on microbead size and size distribution. Microbead size decreased with increasing impeller speed. Scale bar = 250 μm.

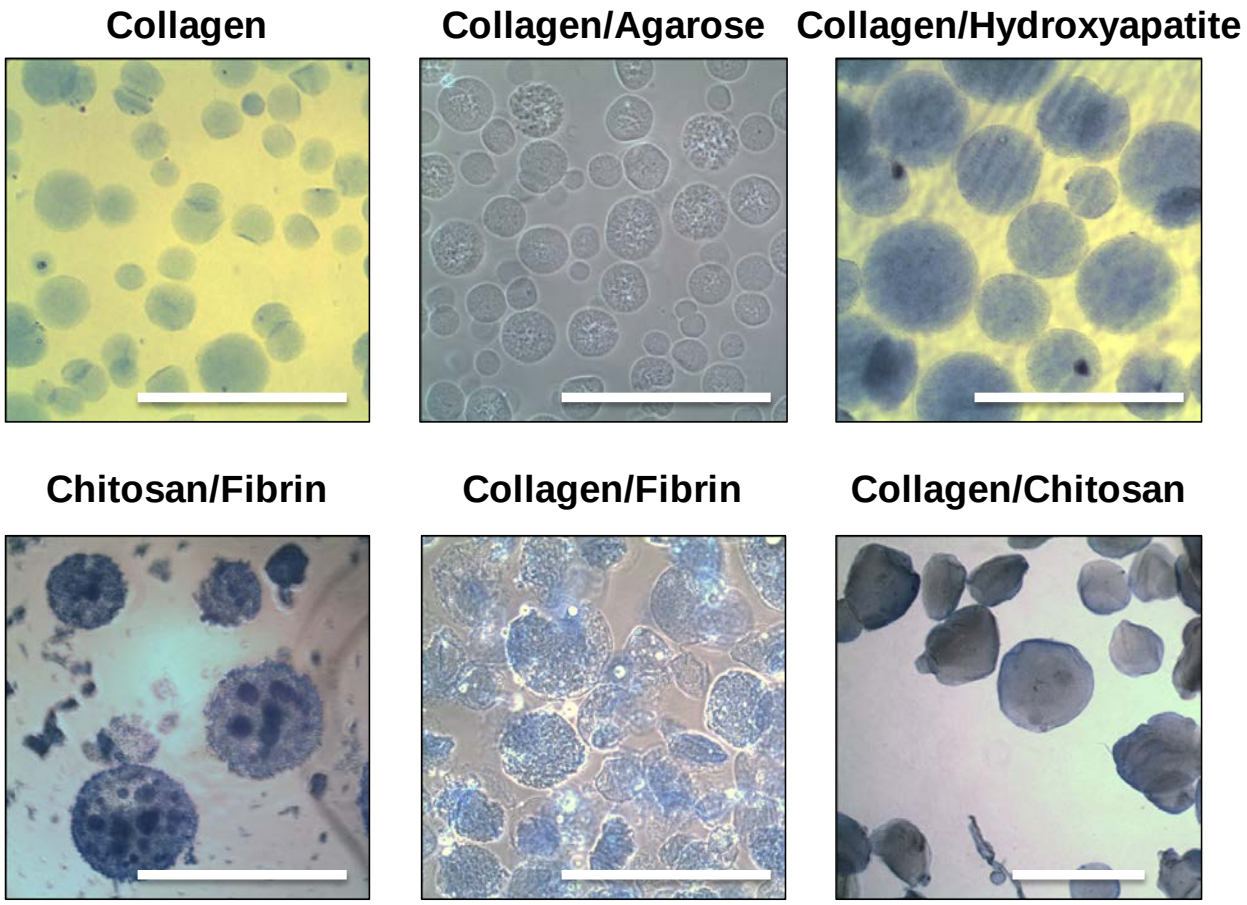

Figure B.4 –Microbead formulations. Scale bar = 500 μm

All composite microbead formulations depicted spherical morphology (Figure B.4). Homogenous blue staining in chitosan/collagen and collagen/HA microbeads implied an even distribution of the protein component within these microbead formulations. However, chitosan/fibrin microbeads exhibited a phase separation in their morphology with the chitosan forming a shell around the inner fibrin core. Collagen/HA microbeads exhibited homogenous dispersion of the nano-HA crystals throughout the microbeads as indicated by the darker images obtained through light microscopy.

Cell Viability and Matrix Architecture within Microbeads

MC3T3 cells embedded within 50/50 collagen/fibrin microbeads demonstrated high viability (approximately 75% on day 1, and 90% on day 7) over seven days in culture, as shown in Figure B.5. Cells spread and proliferated over this time period within the microbeads. The collagen/fibrin fibrillar structure within microbeads was observed in the confocal reflectance images in Figure B.5. After seven days in culture, the microbeads with seeded MC3T3 cells maintained their spherical shape as shown by the confocal reflectance images.

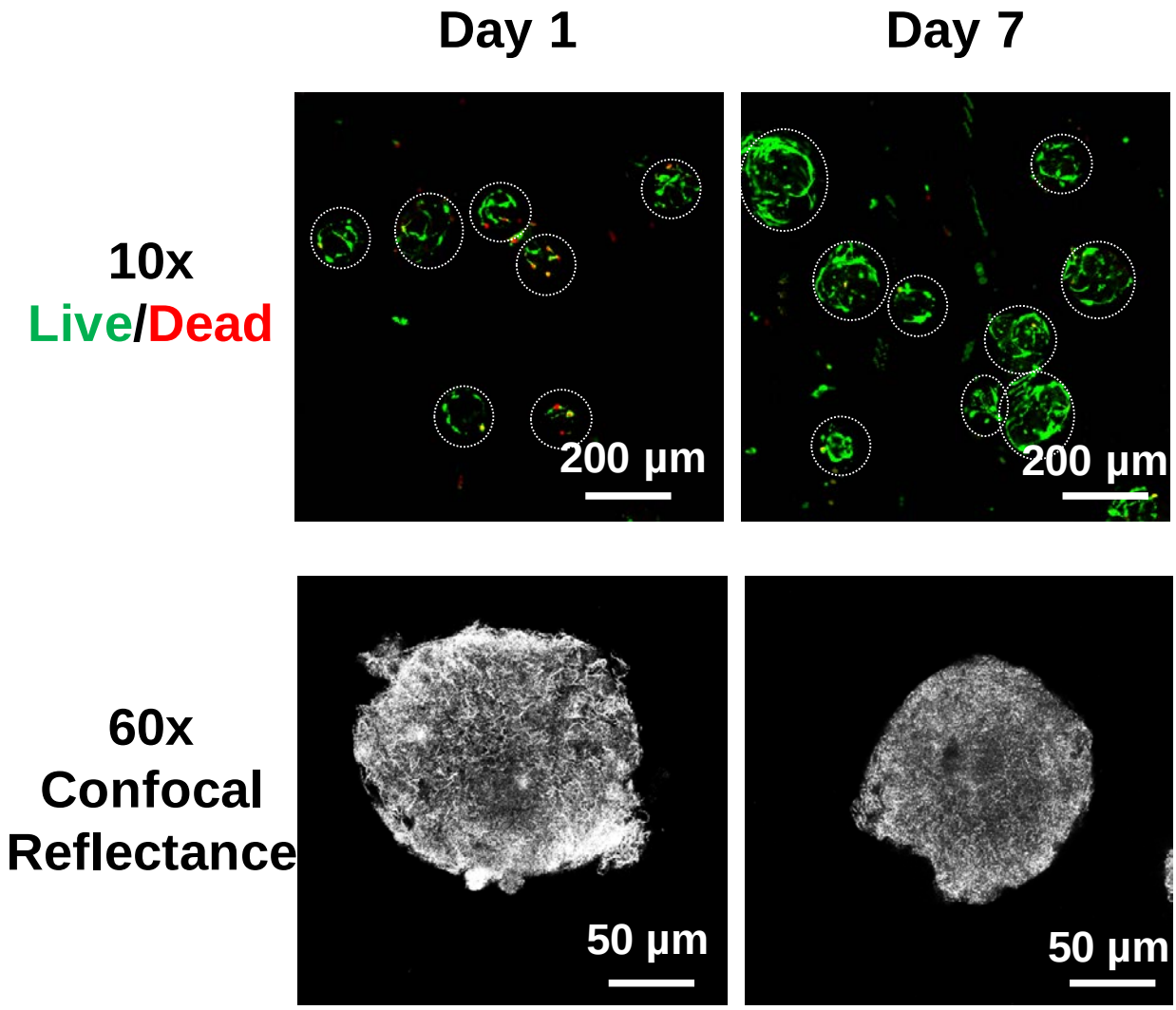

Figure B.5 – Cell viability of MC3T3 cells seeded within 50/50 collagen/fibrin composite microbeads. Embedded cells remained viable after 1 and 7 days post-microbead fabrication. Green staining indicates live cells, red staining indicates dead cells. Dashed areas depict areas of microbeads. Scale bar = 200 µm. Confocal reflectance images of collagen/fibrin composite microbeads demonstrated the matrix architecture throughout the culture period.

Cell Morphology

50/50 collagen/fibrin microbeads with bmMSC cultured for seven days and embedded in a fibrin gel demonstrated spreading and proliferation within and on the surface of the microbead (Figure B.6). A maximum intensity projection of a population of microbeads demonstrated that

microbeads could be visualized using FITC-fibrinogen, along with the actin cytoskeleton and nucleus of the human mesenchymal stem cells. A 3D reconstruction of a Z-Stack (Figure B.6) obtained of a singular microbead with embedded cells illustrated that the cytoskeleton spread throughout the entire volume of the microbead in all dimensions.

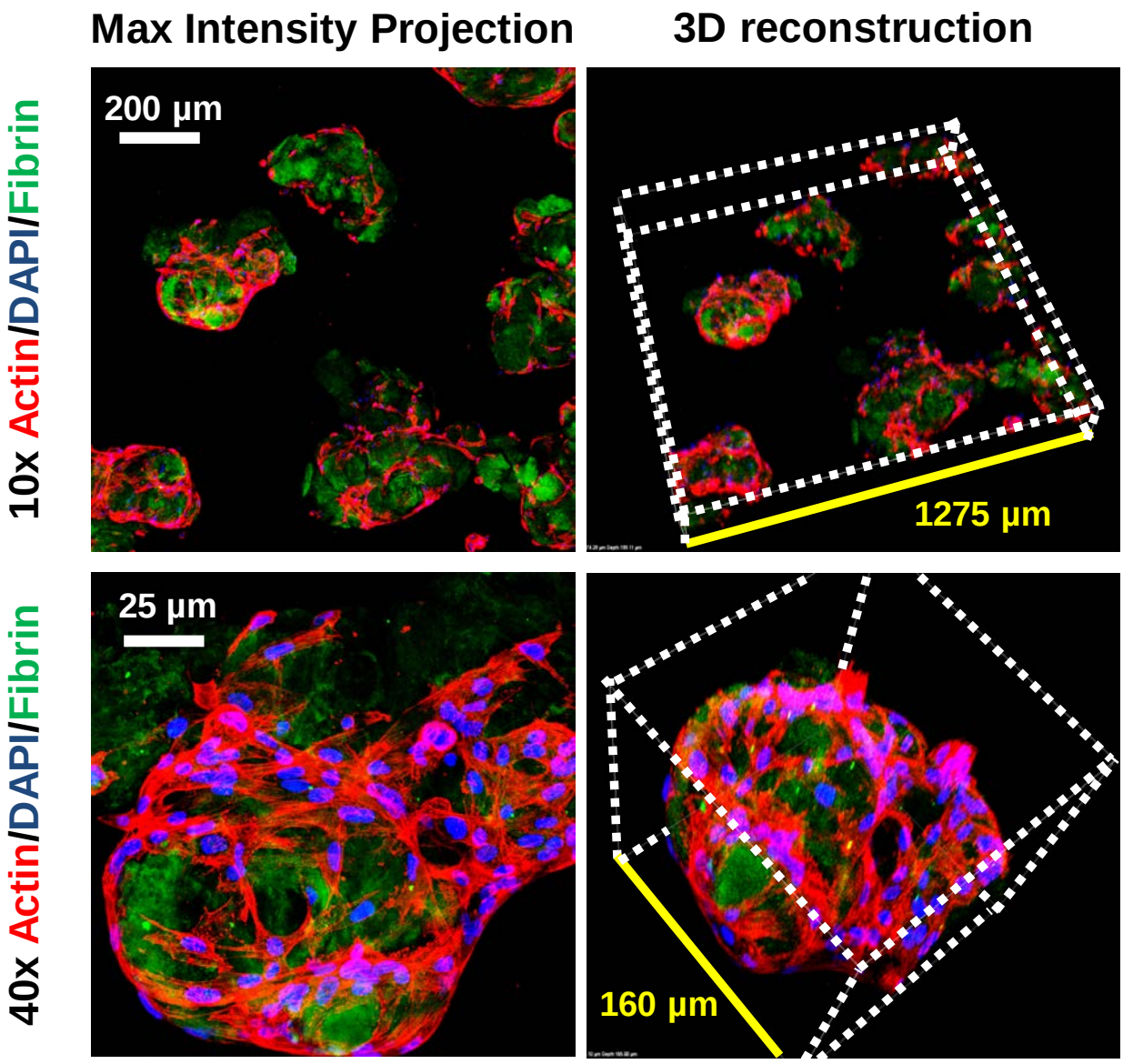

Figure B.6 – Cell spreading within COL/FIB microbeads. Actin (red) /DAPI (blue) Staining in FITC (green) COL/FIB Microbeads after 7 days in microbead culture. Maximum intensity projections and 3D reconstructions

Needle Injection

Collagen/fibrin microbeads were placed into a fibrin gel mixture and injected into a microscope well plate through a 25 ½ gauge needle, as shown in Figure B.7. The microbead and gel mixture was loaded through the needle into the syringe before gelation occurred, and a bubble-free gel was produced after needle injection. Collagen/fibrin microbeads with embedded bmMSC cultured for 7 days were able to be injected through a 25 ½ gauge needle in a fibrin gel with no apparent microbead or cell deformation, as seen by the microbead structure and cytoskeleton of the bmMSC (Figure B.7).

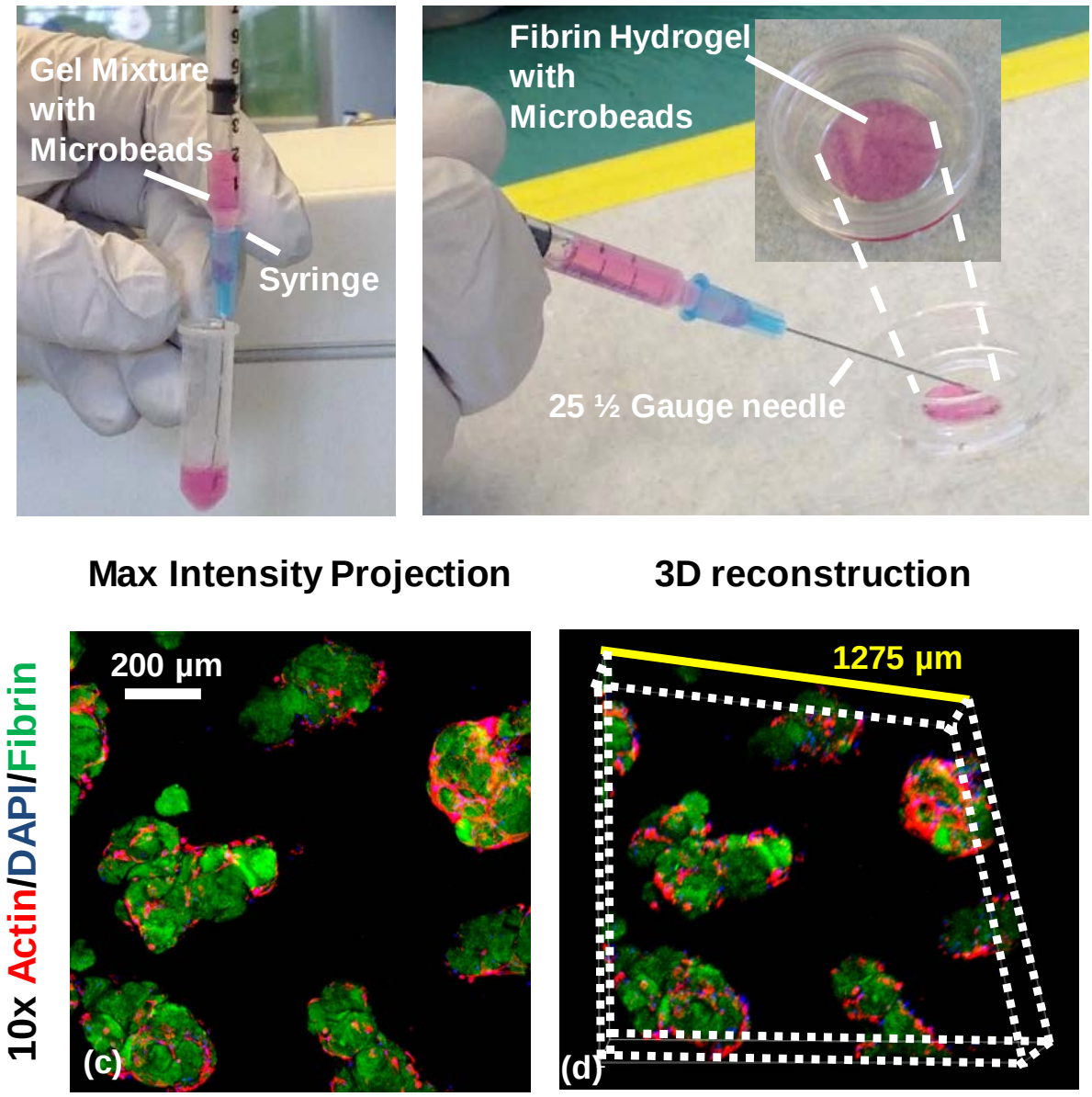

Figure B.7 – Delivery of Fibrin Gel with embedded Microbeads. Neither microbead shape or cell morphology were altered after injection of microbeads through a needle. Actin Staining (red) in FITC COL/FIB Microbeads after 7 days in microbead culture.

Vacuum Molding

Collagen/chitosan microbeads with embedded bmMSC were successfully vacuumed into cohesive constructs that were removed from filter paper, transferred to a 24 well plate, and cultured in media over 7 days (Figure B.8). bmMSC in constructs demonstrated high viability

over 7 days in culture. Additionally, confocal imaging of constructs indicated cell proliferation, alignment, and cell spreading as visualized through their actin cytoskeleton (Figure B.8).

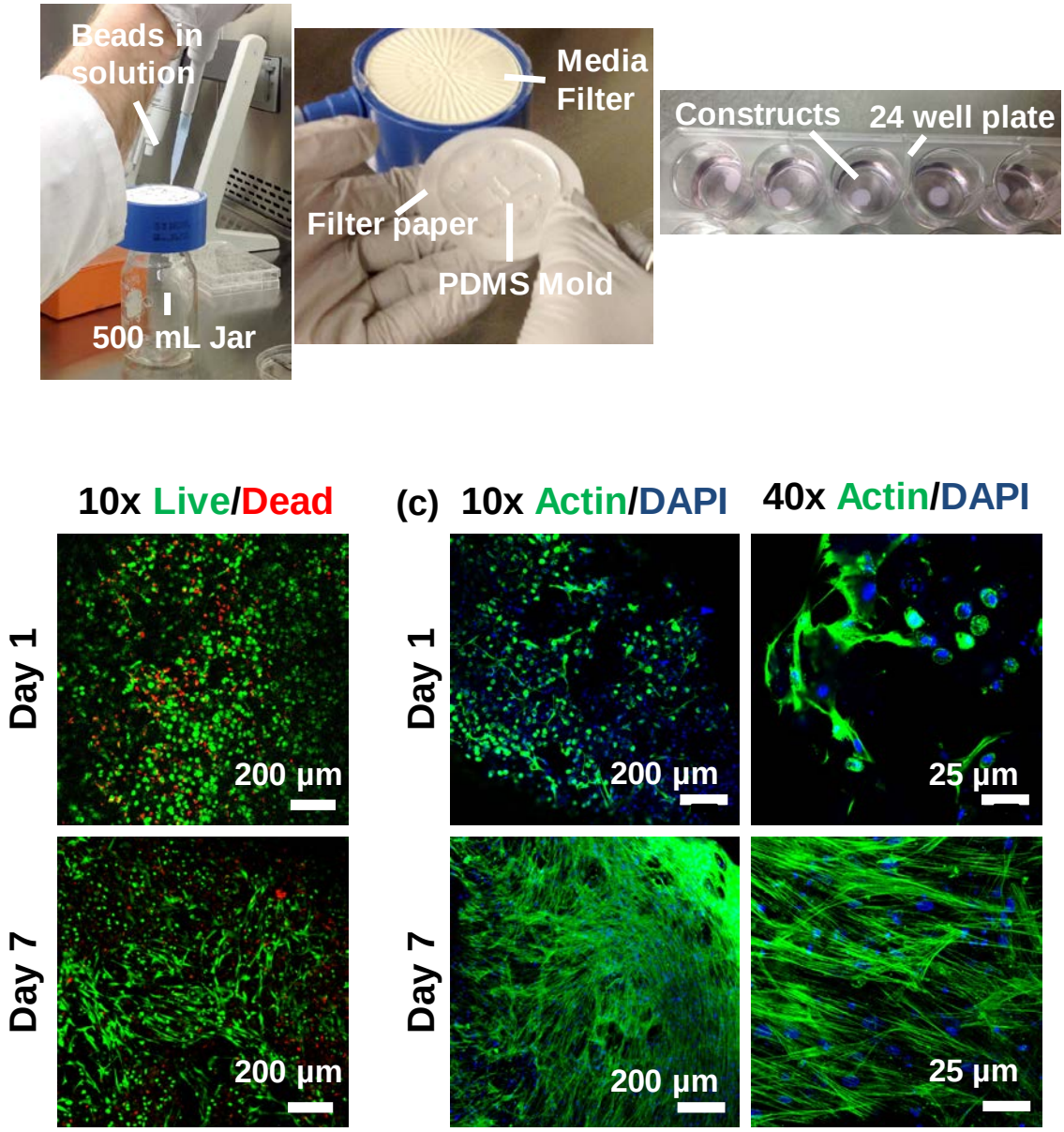

Figure B.8 – Vacuum molding of Constructs. Day 1 and Day 7 Live/Dead images of MSC collagen seeded constructs. Green staining indicates live cells, red straining indicates dead cells. Day 1 and Day 7 Actin/DAPI maximum intensity projection Images of MSC seeded constructs. Green staining indicates actin cytoskeleton, blue staining indicates cell nuclei.

Delivery into Cow Knee

Centrifuged collagen/fibrin microbeads were successfully delivered into an osteochondral defect in a bovine knee through a plastic tube and push rod (Figure B.9). The deposited microbeads were formed to fit the defect through the use of a spatula, subsequently producing an adhered microbead paste. This microbead paste demonstrated the ability to resist shear and compressive stresses through articulation of the bovine joint, even after repeated cycles.

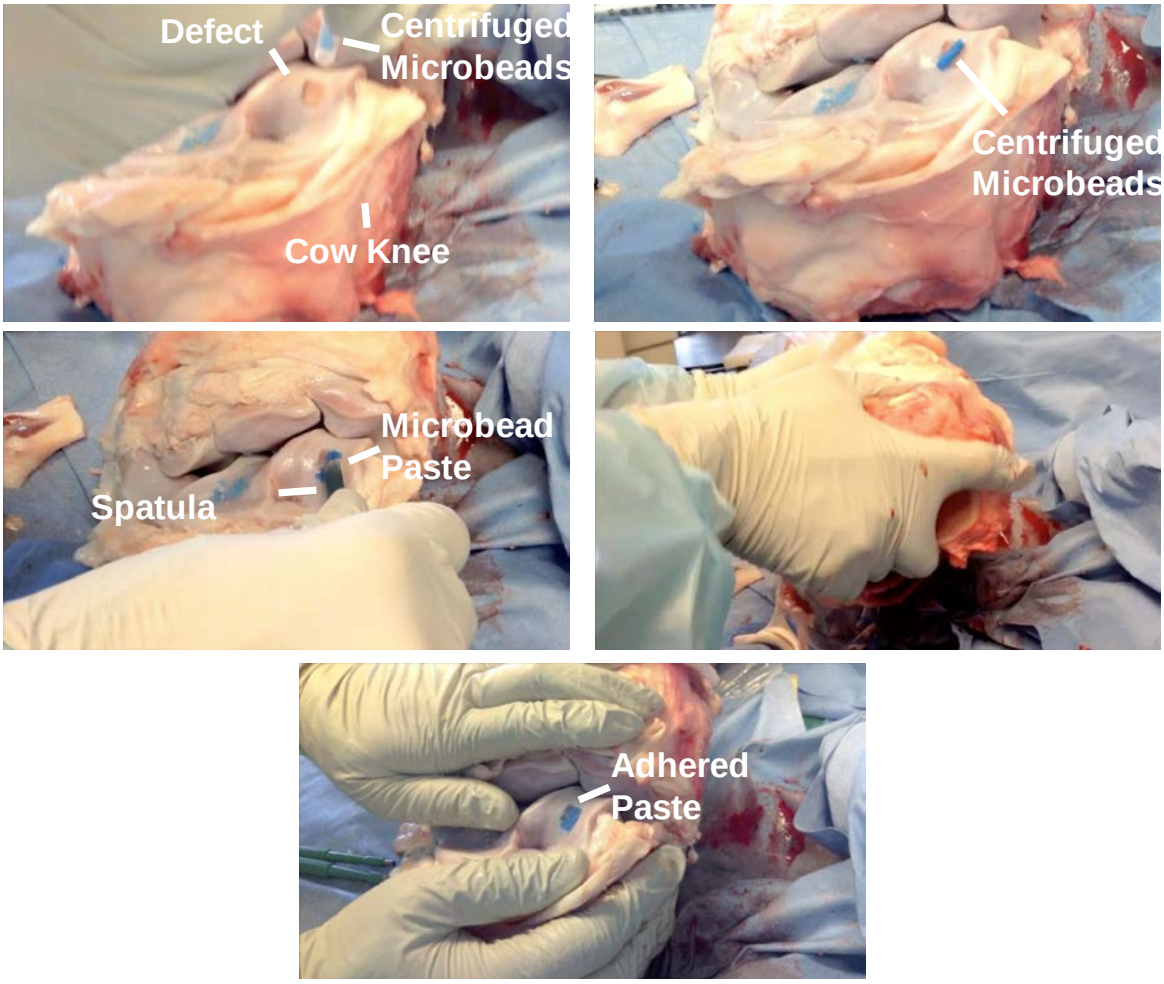

Figure B.9 – Delivery of microbeads into Cow Knee. Left to right, top to bottom - Delivery of centrifuged microbeads, Microbeads in defect, Spreading of microbead paste, Mechanical articulation of joint, Microbead adherence in defect after rubbing.

B.4 Discussion

In the current work, we have described methods to generate 3D cell-seeded hydrogel microenvironments, or "microbeads," through a water-in-oil emulsion process. We have described two parameters, oil viscosity and impeller speed, which have a significant effect on the control of both the size and size distribution of the microbeads. These microbeads can be created in a batch fabrication process which allow for large volumes of cell-seeded microenvironments to be generated at once. Direct encapsulation of MC3T3 inside these 3D hydrogel microenvironments can be achieved at the time of fabrication and cell viability remained high for a week in culture. This format is advantageous in that cells can be cultured in small volumes of physiologically relevant matrices, and then injected into a wound site.

Cell-seeded hydrogel microenvironments demonstrate the ability to support cell spreading after a week in culture with the use of human mesenchymal stem cells embedded within collagen/chitosan microbeads. The spreading of cells within and on beads demonstrates the potential for these microenvironments as cell culture and delivery vehicles. The microbeads are amenable to delivery as a construct, through a needle in a fibrin gel, or as an adhesive paste to a wound site. The microbeads formed into a construct support cell spreading, indicating that the microbeads are able to successfully maintain cell viability despite dehydration via vacuuming, packing of the microbeads within the constructs, and shear stress due to fluid flow during vacuuming. Vacuumed constructs indicate potential for implantation of precultured and predifferentiated cell combinations, cell co-culture studies, and cell patterning. The ability of the microbeads to maintain cell morphology after needle injection demonstrates the robustness and potential for the use of microbeads as a deliverable carrier for cell based therapies. An adhesive

microbead paste attached to a mock defect site created within a cow joint and demonstration of resistance to deformation under mechanical articulation of the joint.

Cell-seeded hydrogel microenvironments have been previously utilized as cell delivery vehicles for orthopedic applications. There is a need for better bone repair strategies for healing of complex fractures, non-unions, tumor resected sites, and periodontal defects, which together constitute over 4 million procedures per year worldwide [18]. Kim et. al developed biomimetic collagen-apatite microspheres through a water-in-oil emulsion technique that served as microcarriers for rat bone marrow derived stem cells [19]. Although these structures did not encapsulate cells directly, they demonstrated favorable adhesion properties for cells and upregulation of alkaline phosphatase activity, an osteogenic marker, as well as gene expression for osteogenic genes such as osteocalcin. Other work has utilized RGD-modified alginate microspheres to deliver a co-culture of human bone marrow stromal cells with endothelial cells into mouse femoral defect model [20]. The implantation of these hydrogel microspheres demonstrated bone regeneration and promoted mineralization of delivered cells. In our lab, we have generated collagen/agarose [12], collagen/chitosan [15], and collagen/fibrin microbeads [16] that have all demonstrated the ability to support osteogenic differentiation of embedded stem cells. Protein-based microbeads have supported osteogenic differentiation and remain viable post-injection. However, due to the relatively weak mechanical properties of the microbeads, they would not serve as favorable scaffolds for load bearing applications such as long bone defects. These systems could serve as cell delivery conduits for avascular necrosis, tumor resection areas, and oral-maxillofacial injuries and defects.

Hydrogel microenvironments could also be beneficial to deliver engineered vasculature into ischemic areas where blood supply to an organ is compromised. The lack of blood in

ischemic areas leads a decrease in oxygen, glucose, and nutrients as well as an increase in waste products. Extensive work has shown promise in creating sub-millimeter-sized collagen gel cylinders, or modules, and coating the outer surface of these structures with endothelial cells to enhance vascularization *in vivo* [21-23]. Collagen/fibrin composite materials are of particular interest for vasculogenic applications due to their roles in the wound healing response. Microbeads formed from these materials could be employed to generate vessel-like structures *in vitro* by co-culturing bmMSC and endothelial cells. The microbeads could be then concentrated into a paste and then injected into an ischemic site. These pre-formed vessels could presumably connect with host vasculature and transport blood throughout the transplanted area. Yet, these structures are difficult to form within microbeads due to the cell-generated forces which cause protein hydrogel structures to compact [24-26]. This dynamic process induces changes in the total protein density and cell cytoskeletal structure, thereby reducing the necessary cell tractional forces necessary to generate vessel-like structures [27]. Vascularization could also offer benefits in creating large tissue-engineered constructs by aiding in overcome to the diffusion limit 150-200 μm [28]. Delivering vasculogenic microbeads could serve as key regulators in maintaining tissue viability post-implantation [29].

Further studies are underway to augment cell-seeded microbeads in an attempt to direct cell phenotype and stem cell differentiation. Currently, we culture cell-seeded microbeads statically in suspension, yet the use of bioreactors and spinner flask culture methods can also be employed to allow for constant agitation of the microenvironments, potentially inducing changes in cell phenotype [30, 31]. Moreover, we have begun investigating the incorporation of polymeric microspheres (2-5 μm diameter) into microbeads for controlled drug and growth factor release. Gelatin microspheres have been fabricated in a similar emulsification process as

microbeads and have shown promise their ability to demonstrate controlled release of bone morphogenic protein-2 (BMP-2) [32]. Other alterations such as mineralizing microbeads through incubation in a modified culture media are underway in efforts to mechanically enhance the microbead structures.

Future work with cell-seeded microbeads involves the assembly of muti-phase constructs from different microbead formulations. One potential multi-phase construct, an osteochondral interface, has been manufactured with a continuous gradient between the bone-like and cartilage-like structures using collagen/chitosan and collagen/chitosan/HA microbeads, respectively. Our future goals are to develop dual-phase constructs consisting of both osteogenic and vasculogenic microbeads for bone regeneration applications. Bone is a highly metabolic tissue requiring a large vascular supply throughout its structure. By providing both endothelial cells and bmMSC to bone defect sites, we aim to develop a dual-phase cell therapy system that mimics that natural microenvironment within bone [33]. Although we have described specific applications for cell-seeded microbeads, these modules are amenable to any tissue/organ application such as islet transplantation, hepatic tissue engineering, and cardiac regeneration.

B.5 References

1. Nichol JW, Khademhosseini A. Modular tissue engineering: engineering biological tissues from the bottom up. Soft Matter 5, 1312, 2009.

2. Tejavibulya N, Youssef J, Bao B, Ferruccio T-M, Morgan JR. Directed self-assembly of large scaffold-free multi-cellular honeycomb structures. Biofabrication 3, 034110, 2011.

3. Tekin H, Tsinman T, Sanchez JG, Jones BJ, Camci-Unal G, Nichol JW, et al. Responsive Micromolds for Sequential Patterning of Hydrogel Microstructures. Journal of the American Chemical Society 133, 12944, 2011.

4. Jakab K, Norotte C, Marga F, Murphy K, Vunjak-Novakovic G, Forgacs G. Tissue engineering by self-assembly and bio-printing of living cells. Biofabrication 2, 022001, 2010.

5. Mironov V, Boland T, Trusk T, Forgacs G, Markwald RR. Organ printing: computer-aided jet-based 3D tissue engineering. Trends in Biotechnology 21, 157, 2003.

6. Elloumi-Hannachi I, Yamato M, Okano T. Cell sheet engineering: a unique nanotechnology for scaffold-free tissue reconstruction with clinical applications in regenerative medicine. Journal of Internal Medicine 267, 54, 2010.

7. Kelm JM, Fussenegger M. Scaffold-free cell delivery for use in regenerative medicine☆. Advanced Drug Delivery Reviews 62, 753, 2010.

8. Chan BP, Hui TY, Yeung CW, Li J, Mo I, Chan GCF. Self-assembled collagen–human mesenchymal stem cell microspheres for regenerative medicine. Biomaterials 28, 4652, 2007.

9. Kim HW, Gu HJ, Lee HH. Microspheres of Collagen-Apatite Nanocomposites with Osteogenic Potential for Tissue Engineering. Tissue Engineering 13, 965, 2007.

10. Cheng H-W, Luk KDK, Cheung KMC, Chan BP. In vitro generation of an osteochondral interface from mesenchymal stem cell–collagen microspheres. Biomaterials 32, 1526, 2011.

11. Batorsky A, Liao J, Lund AW, Plopper GE, Stegemann JP. Encapsulation of adult human mesenchymal stem cells within collagen-agarose microenvironments. Biotechnology and Bioengineering 92, 492, 2005.

12. Lund AW, Bush JA, Plopper GE, Stegemann JP. Osteogenic differentiation of mesenchymal stem cells in defined protein beads. Journal of Biomedical Materials Research Part B: Applied Biomaterials 87B, 213, 2008.

13. Chen Z, Wang L, Stegemann JP. Phase-separated chitosan–fibrin microbeads for cell delivery. Journal of Microencapsulation 28, 344, 2011.

14. Caldwell DJ, Rao RR, Stegemann JP. Assembly of discrete collagen-chitosan microenvironments into multiphase tissue constructs. Adv Healthc Mater 673, 2013.

15. Wang L, Rao RR, Stegemann JP. Delivery of mesenchymal stem cells in chitosan/collagen microbeads for orthopedic tissue repair. Cells Tissues Organs 197, 333, 2013.

16. Rao RR, Peterson AW, Stegemann JP. Osteogenic differentiation of adipose-derived and marrow-derived mesenchymal stem cells in modular protein/ceramic microbeads. J Biomed Mater Res A 101, 1531, 2013.

17. Wang D, Christensen K, Chawla K, Xiao G, Krebsbach PH, Franceschi RT. Isolation and characterization of MC3T3-E1 preosteoblast subclones with distinct in vitro and in vivo differentiation/mineralization potential. J Bone Miner Res 14, 893, 1999.

18. Al-Munajjed AA, Plunkett NA, Gleeson JP, Weber T, Jungreuthmayer C, Levingstone T, et al. Development of a biomimetic collagen-hydroxyapatite scaffold for bone tissue engineering using a SBF immersion technique. Journal of Biomedical Materials Research Part B: Applied Biomaterials 90B, 584, 2009.

19. Kim HW, Gu HJ, Lee HH. Microspheres of collagen-apatite nanocomposites with osteogenic potential for tissue engineering. Tissue Eng 13, 965, 2007.

20. Grellier M, Granja PL, Fricain J-C, Bidarra SJ, Renard M, Bareille R, et al. The effect of the co-immobilization of human osteoprogenitors and endothelial cells within alginate microspheres on mineralization in a bone defect. Biomaterials 30, 3271, 2009.

21. Chamberlain MD, Gupta R, Sefton MV. Bone Marrow-Derived Mesenchymal Stromal Cells Enhance Chimeric Vessel Development Driven by Endothelial Cell-Coated Microtissues. Tissue Engineering Part A, 2011.

22. Gupta R, Rooijen NV, Sefton MV. Fate of Endothelialized Modular Constructs Implanted in an Omental Pouch in Nude Rats. Tissue Engineering: Part A 15, 2875, 2009.

23. Khan OF, Sefton MV. Endothelialized biomaterials for tissue engineering applications in vivo. Trends in Biotechnology 29, 379, 2011.

24. Lund AW, Bilgin CC, Hasan MA, McKeen LM, Stegemann JP, Yener B, et al. Quantification of Spatial Parameters in 3D Cellular Constructs Using Graph Theory. Journal of Biomedicine and Biotechnology 2009, 1, 2009.

25. Saunders WB, Bayless KJ, Davis GE. 2005; MMP-1 activation by serine proteases and MMP-10 induces human capillary tubular network collapse and regression in 3D collagen matrices. J Cell Sci 118: 2325-2340.

26. Davis GE, Pintar Allen KA, Salazar R, Maxwell SA. Matrix metalloproteinase-1 and -9 activation by plasmin regulates a novel endothelial cell-mediated mechanism of collagen gel contraction and capillary tube regression in three-dimensional collagen matrices. J Cell Sci 114, 917, 2001.

27. Kniazeva E, Putnam AJ. Endothelial cell traction and ECM density influence both capillary morphogenesis and maintenance in 3-D. The American Journal of Physiology - Cell Physiology 297, C179, 2009.

28. Novosel HUVEC, Kleinhans C, Kluger PJ. Vascularization is the key challenge in tissue engineering. Advanced Drug Delivery Reviews 63, 300, 2011.

29. Lovett M, Lee K, Edwards A, Kaplan DL. Vascularization Strategies for Tissue Engineering. Tissue Engineering: Part B 15, 353, 2009.

30. Abousleiman R, Sikavitsas V. Bioreactors for Tissues of the Musculoskeletal System. Advances in Experimental Medicine and Biology 585, 243, 2007.

31. Yeatts AB, Fisher JP. Bone tissue engineering bioreactors: Dynamic culture and the influence of shear stress. Bone 48, 171, 2011.

32. Solorio L, Zwolinski C, Lund AW, Farrell MJ, Stegemann JP. Gelatin microspheres crosslinked with genipin for local delivery of growth factors. Journal of Tissue Engineering and Regenerative Medicine 4, 514, 2010.

33. Tsigkou O, Pomerantseva I, Spencer JA, Redondo PA, Hart AR, O'Doherty E, et al. Engineered vascularized bone grafts. Proceedings of the National Academy of Sciences 107, 3311, 2010.

APPENDIX C

Exogenous Mineralization of Cell-Seeded and Unseeded Collagen-Chitosan Hydrogels using Modified Culture Medium

C.1 Introduction

There is a clear need for materials and methods to improve bone healing outcomes, particularly in cases of large defects and non-unions. The natural healing response is often not adequate to obtain full repair, and in such cases strategies to augment bone regeneration can be applied. Autografts and allografts are currently used clinically, but are hampered by issues of tissue availability and consistency [1]. The generic tissue engineering approach is to combine cells, biomaterials, and growth factors in a controlled fashion to create living materials that can replace damaged tissue and/or enhance regeneration. In the case of bone tissue, a wide range of strategies have been employed, using a variety of cell types, materials, and biochemical factors [2].

One strategy for potentiating the bone healing response is to use materials that have been exogenously mineralized using defined ionic solutions. Simulated body fluid (SBF) is a solution formulated with ion concentrations similar to blood plasma, which mineralizes the surfaces and pore walls of both natural [3-7] and synthetic [8-10] scaffolds if thermodynamic conditions are appropriate. Kokubo et. al [11] first described that soaking a biomaterial in SBF leads to the *ex vivo* formation of a bone-like apatite coating, and later studies showed that such coatings can be both osteoconductive [10] and osteoinductive [13], and can facilitate the regeneration of bone [12, 14]. SBF-induced mineralization has been further examined as a method for controlling

osteoconductivity [5, 9, 15], as well as for protein [13, 16] and gene delivery [17, 18]. Taken together, this body of work has shown that SBF can be a useful tool to modify biomaterials for bone tissue engineering applications.

Previous studies using SBF to modify material scaffolds have been performed in the absence of cells, since the high ionic concentrations and lack of nutrients in SBF are not conducive to the maintenance of cell growth. However, cell-seeded materials have been proposed for a number of orthopaedic applications. Natural biomaterial hydrogels are of interest in such cases due to their ability to mimic the natural extracellular matrix [19] and provide tissue-specific cues to enhance cell attachment and stem cell differentiation [20]. Direct encapsulation of cells during gel formation can be used to facilitate homogenous cell distribution in hydrogels. Numerous natural polymers including collagen [3], chitosan [21], and composite matrices [22-25] have been employed to engineer tissues and have shown promise in bone regeneration [26]. A drawback of natural hydrogel materials is that they often lack mechanical strength and represent only the protein component of the native bone tissue. Mineralization of such matrices has been pursued as a strategy to improve their mechanical properties and more closely mimic the native matrix [6], however the cellular component is typically not included during the mineralization process.

In the present study, we mineralized 3D hydrogels using a modified culture medium that combined the ionic constituents of SBF with the nutrients, vitamins, and amino acids needed to maintain cell viability. The model tissue constructs consisted of fibroblast cells embedded in collagen-chitosan hydrogel matrices developed previously in our laboratory [24, 26]. Fibroblasts were used as a model cell type to examine the feasibility of mineralization in the presence of cells, since this non-mineralizing cell type allowed us to isolate the effects of mineralization to the medium alone. Both unseeded and fibroblast-seeded hydrogels were exposed to mineralizing

solutions that were formulated to induce biomineralization while also supporting cell growth, and the effects of such treatment on mineral content, mechanical properties, and cellular viability were determined. Our primary goal was to demonstrate that mineralization of protein-based hydrogels is possible in the presence of cells. The ability to mineralize cell-seeded protein matrices could be useful in creating mechanically stable and osteogenic tissue constructs, as well as in studying the process of biomineralization.

C.2 Materials and Methods

Media formulations

The composition of the mineralization medium was based on previously studied simulated body fluid (SBF) formulations, with modifications to enhance both mineralization and the ability to support cell growth. The base medium was Dulbecco's modified Eagle medium (DMEM; high glucose, Invitrogen, Carlsbad, CA, Catalog No. 12100), which was supplemented with ionic salts. Table C.1 shows the ion concentrations of relevant biological fluids and mineralizing media. The main augmentation to the modified medium formulation was a 4-fold increase in calcium (Ca^{2+}) and phosphate (PO_4^{3-}) in order to promote biomineralization, and an increased carbonate (HCO_3^-) level to provide buffering capacity. These modifications are further discussed in the Results and Discussion section. Liquid high glucose DMEM (Invitrogen, Catalog No. 10313) was used as control media.

Table B.1. Media Formulation Ion Concentrations (mM)								
	Na^+	**K^+**	**Ca^{2+}**	**Mg^{2+}**	**HCO_3^-**	**SO_4^{2-}**	**HPO_4^{2-}**	**pH**
Blood Plasma	142	3.6-5.5	2.1-2.6	1.0	27	1.0	0.6-1.5	7.2-7.4
Simulated Body Fluid (SBF)	142	5.0	2.5	1.5	4.2	0.5	1.0	7.4
Dulbecco' modified Eagle's Medium (DMEM)	155	5.3	1.8	0.8	44.1	0.8	0.9	7.4
Modified DMEM (mDMEM)	150	7.8	8.0	1.8	8.4	0.8	3.4	7.4

Table C.1 – Ionic composition of biological fluids and media formulations.

The modified medium (mDMEM) formulation was prepared by adding salts directly to DMEM to achieve final concentrations of 141 mM NaCl, 5.3 mM KCl, 6.2 mM $CaCl_2 \cdot H_2O$, 1.0 mM $MgCl_2$, 8.4 mM $NaHCO_3$, 0.8 mM $MgSO_4$, and 2.5 mM KH_2PO_4. This resulted in final concentrations of 149 mM sodium (Na^+), 7.8 mM potassium (K^+), 8.0 mM calcium (Ca^{2+}), 1.8 mM magnesium (Mg^{2+}), 8.4 mM carbonate (HCO_3^-), 0.8 mM sulfate (SO_4^{2-}), and 3.45 mM phosphate (HPO_4^{2-}). The medium was prepared at 25°C and titrated to a pH of 7.4. In experiments examining the effect of serum, mDMEM and control DMEM were supplemented with varying concentrations of fetal bovine serum (FBS; Invitrogen) and 1% penicillin/streptomycin (P/S; Invitrogen). As per previous protocols, mDMEM was changed every 12 hours to avoid precipitation in the culture solution and DMEM was changed every 3 days. In subsequent mineralization experiments using cells, the mineralization medium (MM) used was mDMEM supplemented with 2% FBS. The control medium (DM) was DMEM supplemented with 10% FBS.

Collagen-chitosan Gel Fabrication

Collagen-chitosan gel composites were formed through a β-GP induced mechanism as previously described [24]. Briefly, 4.0 mg/ml bovine Type I collagen (MP Biomedicals, Solon, OH) was dissolved in 0.02 N acetic acid (Sigma) and was mixed with 2.0 wt% chitosan (93% DDA; Biosyntech, Quebec, Canada) dissolved in 0.1 N acetic acid at a mass ratio of 50/50 collagen/chitosan. Beta-glycerophosphate (β-GP) and glyoxal were added as physical and chemical cross-linkers, respectively, at concentrations of 7.0 wt% β-GP and 0.5 mM glyoxal. A 400 µl aliquot of the pre-gelled mixture was injected into a well of a 24-well plate to create a disk-shaped construct with diameter of 1.5 cm. Gelation was then initiated by incubation of the mixture at 37°C for 30 min. Gels were washed three times in phosphate buffered saline (PBS; Invitrogen) for 10 min to remove excess β-GP prior to use.

Calcium Quantification

Calcium deposition on acellular gels after 3 days incubation in either modified medium or DMEM containing 0, 2, 5, 10% FBS was quantified using an orthocresolphthalein complex-one (OCPC) method as previously described [27]. Briefly, collagen-chitosan gels were washed three times in PBS for 10 minutes and frozen at days 0, 1, and 3. Samples were then digested in 0.5 ml of 1.0 N acetic acid overnight. Ten microliters of the dissolved solution was then incubated at 10 min at 25°C with 300 µl of a working solution consisting of 0.05 mg/ml of OCPC solution and ethanolamine/boric acid/8-hydroxyquinoline buffer (Sigma). Samples were read spectrophotometrically at 575 nm. Calcium values were quantified via a standard curve prepared from 0.0 to 100 µg/ml.

Gel Morphology and Von Kossa staining

Acellular gel morphology was examined 3 days after incubation in mineralization medium (MM = mDMEM + 2% FBS) and in control medium (DM = DMEM + 10% FBS). Gels were washed three times in PBS for 10 min each and then transferred to a 12-well plate for imaging using a standard CCD camera in manual mode with a constant exposure setting.

For von Kossa staining, acellular gels were washed three times in PBS for 10 min and then placed in zinc-buffered formalin (Anatech LTD, Battle Creek, MI) for 30 minutes, followed by immersion in 70% ethanol (Fisher Scientific, Pittsburgh, PA). Samples were cryosectioned into the top, middle (300 μm from the top face), and bottom face at the Histology Core Facility at the University of Michigan Dental School. Gels were stained with von Kossa reagent, embedded in paraffin and then mounted on slides. Images were taken at 4X magnification using an Olympus IX15 Microscope system (Olympus America, Center Valley, PA) and stitched together using Metamorph Premier software (Molecular Devices, Sunnyvale, CA). Images were quantified using ImageJ software (National Institute of Health, Bethesda, MD) using thresholding and color discrimination to define positive staining. The ratio of the stained to unstained area was used to determine the fraction of the sample that was positively stained in each sample.

Gel Rheology

Acellular collagen-chitosan constructs incubated in MM or DM for 3 days were washed three times in PBS for 10 min each and then evaluated by gel rheometry using an AR-G2 rheometer (TA Instruments, New Castle, DE). Gels were loaded on to a Peltier stage preheated to 37°C. A 8 mm steel parallel plate was used with a gap height of 1500 microns. A strain sweep was

performed over the course of 45 minutes with strain rates from 0.1 to 100% and a constant frequency of 1 radian/second. Reported values were taken over the linear range of the samples.

Cell Culture and Assays

Prior to gel fabrication, human neonatal dermal fibroblasts (hFb; Lonza Inc., Walkersville, MD) were cultured in DMEM containing 10% FBS and 1% PS. For cell assays, hFb were used at passage 7-9 and placed directly into the solution of collagen and chitosan at a concentration of 1.0×10^6 cells/ml prior to gelation, to allow for homogenous encapsulation within formed gels. Previous studies have shown that cells survive the encapsulation process [24, 26], and hFB were used in this study as a model cell type to isolate the effects of mineralization to the modified media solution.

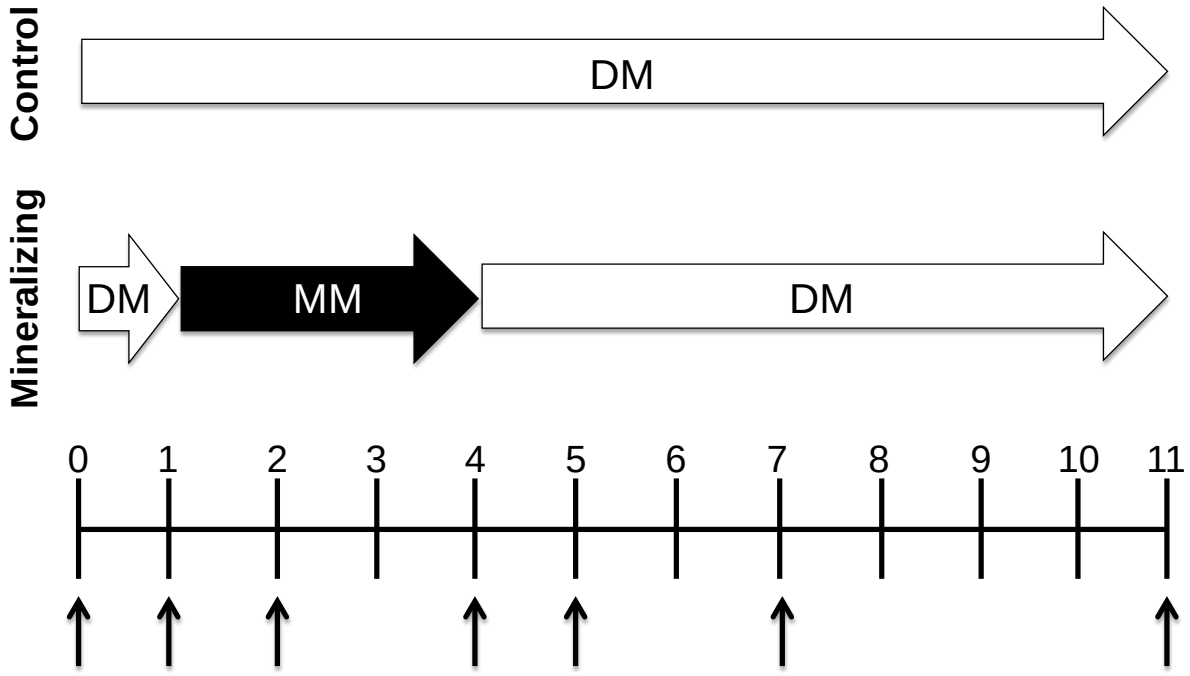

Figure C.1 – Experimental protocol showing timing of control cultures in standard DMEM (DM) and mineralizing cultures in modified DMEM (MM). All cell-seeded hydrogels were cultured in DM for 1 day. Mineralizing constructs were then incubated in MM for 3 days, followed by a 7 day recovery period in DM. Control constructs were incubated in DM for 11 days. Arrows on time scale indicate points at which constructs were sampled and analyzed.

Cell-seeded constructs in the MM condition were cultured for 1 day in DM, 3 days in MM, and then 7 days in DM for a recovery period. Samples were collected at days 0, 1, 2, 4, 5, 7, 11 corresponding to initial conditions, 1 day in DM, 1 day in MM, 3 days in MM, 1 day recovery in DM, 3 days recovery in DM, and 7 days recovery in DM (Figure C.1). Gels were washed three times in PBS for 10 min when switching between culture medium. Cell-seeded gels cultured in DM only were used as controls and samples were collected at corresponding time points.

To evaluate toxicity of the MM media, cell viability was examined using a vital stain kit (Live/Dead®, Molecular Probes, Eugene, OR). Constructs were washed three times in sterile PBS and incubated at 37°C for 45 min in a solution containing 4.0 µm calcein-AM and 4.0 µm

ethidium homodimer-1 in PBS. Gels were then washed again in PBS and imaged using a laser scanning confocal microscope (Olympus FluoView 500 Laser Scanning Confocal Microscope, Olympus). Image scans were captured at a horizontal plane 150 μm above the bottom surface of the gel and quantified using ImageJ software.

To quantify cell number during the mineralization period, DNA was extracted in 4.0 M guanidine hydrochloride solution and measured using a commercially available DNA assay (PicoGreen kit, Invitrogen). Calcium deposited on the constructs during the mineralization period was also measured using the OCPC assay described above.

Statistical Analysis

One-way ANOVA testing with Tukey's post hoc analysis was used to analyze the effect of FBS concentration over time on calcium deposition in acellular hydrogels. Student's T-test was used to assess the significance of the fractional area of von Kossa staining, rheological data, cell viability, DNA content, and calcium deposition in cell-seeded hydrogels treated with mineralizing medium, compared to control medium. One-way ANOVA with Tukey's post hoc analysis was used to analyze the effect of medium type over time on DNA content in cellular hydrogels. Statistical significance was set at $p < 0.05$. Numerical values are presented as mean +/- standard error of the mean (SEM). $N = 4$ for each assay, and error bars on graphs represent the standard error of the mean.

C.3 Results and Discussion

Rationale for media formulations

This work demonstrated the ability to mineralize protein biomaterials and change their properties both in the presence and absence of embedded cells. Mineralization techniques

typically employ simulated body fluid (SBF), however, the lack of nutrients, vitamins, amino acids, and glucose prevent these media from being used for cell culture. DMEM is a commonly used medium for cell culture that can lead to the precipitation of mineral nodules on hydroxyapatite and tricalcium phosphate scaffolds in normal cell culture environments [28]. Therefore we used DMEM as a base medium and supplemented it with the specific salts to enhance the mineralization process. Table B.1 shows the ion concentrations of SBF, DMEM, and mDMEM, as well as blood plasma for reference. The mineralizing DMEM (mDMEM) used in this study was formulated to have specific ionic concentrations aimed at maximizing mineral deposition [28]. mDMEM contained concentrations of sodium (Na^{+}), magnesium (Mg^{2+}), and sulfate (SO_4^{2-}) similar to conventional SBF. Calcium (Ca^{2+}) and phosphate (PO_4^{3-}) are the primary ions required for biomineralization, and were therefore added at concentrations approximately 4-fold higher than conventional SBF to promote rapid mineralization of substrates. The carbonate (HCO_3^{-}) level was maximized to serve as a pH buffer in the media to allow culture in a CO_2 incubator, though this anion may be associated with decreased mineralization. Each of these solutions was adjusted to physiological pH to provide an appropriate environment for cell culture.

Effect of serum on calcium deposition

Serum is a necessary supplement in cell culture medium because it contains growth factors that maintain cell viability and growth [28, 29]. However, in some systems serum proteins can detrimentally effect mineralization by delaying or inhibiting deposition [13, 30, 31]. To investigate the effect of serum on calcium deposition in collagen-chitosan materials, acellular hydrogel constructs were exposed to mineralizing DMEM supplemented with 0, 2, 5, and 10%

FBS. Gels incubated in control DMEM with 0, 2, 5, 10% FBS served as controls.

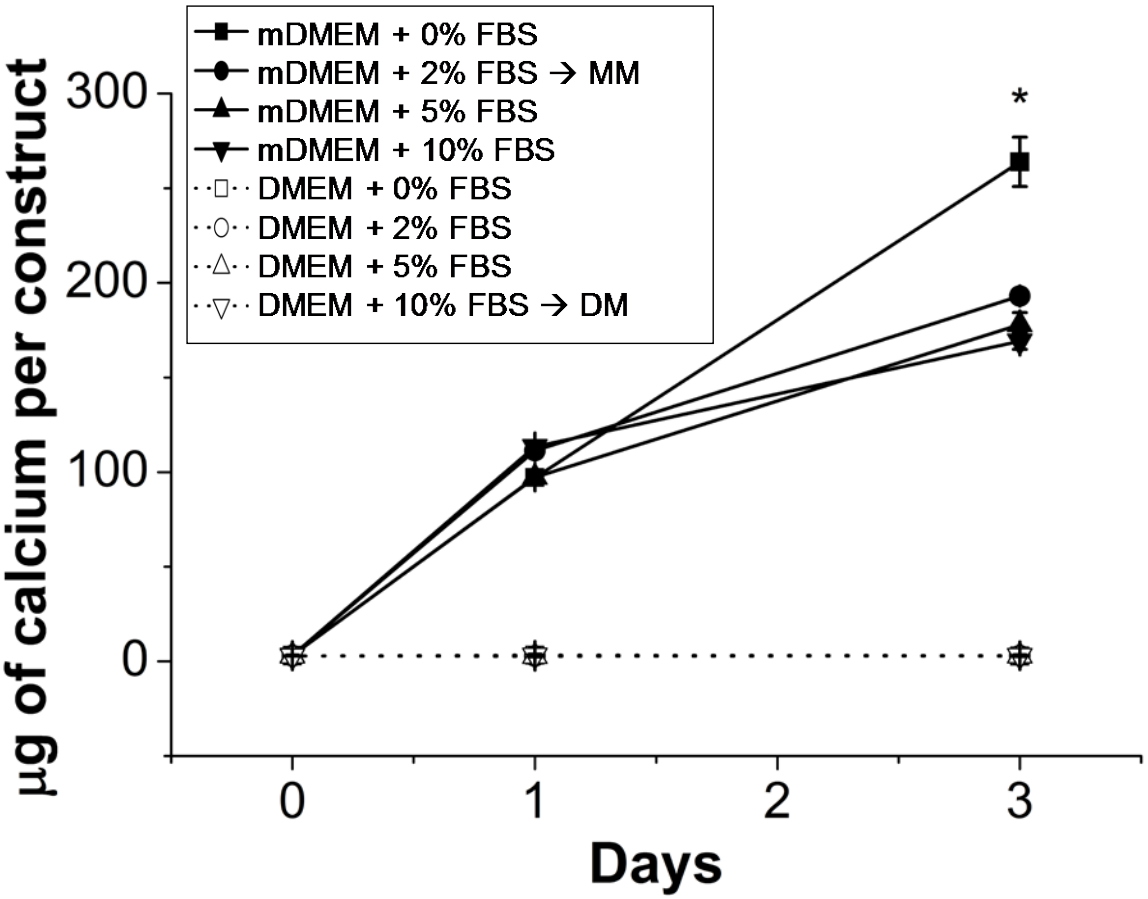

Figure C.2 – Calcium deposition in collagen-chitosan gels through incubation in mineralizing DMEM (mDMEM). Incubation in mineralizing media led to a significant increase in calcium content compared to control media (DMEM) after 3 days of culture. (*) denotes $p < 0.05$ from the groups containing FBS. Values are mean +/- standard error, n = 4.

Figure C.2 shows that calcium deposition increased significantly ($p<0.01$) from day 0 in all samples incubated in mineralizing DMEM by day 1, and that mineralization continued to increase to day 3 in culture. In contrast, samples exposed to control DMEM showed no evidence of calcium deposition regardless of serum content or time point. In mDMEM samples, the presence of serum had no effect on the degree of calcium deposition at the day 1 time point, but by day 3 serum-supplemented samples showed decreased mineral deposition, relative to the sample with no serum ($p<0.01$). There was no significant difference between 2, 5 and 10% serum. These data show that FBS had an inhibitory effect on calcium deposition, but that

mineralization did occur in the presence of serum proteins. Because of the need for at least a low level of serum for cell maintenance, mineralization studies conducted with cells were performed using mDMEM supplemented with 2% FBS as the mineralization medium (MM). The control medium (DM) was standard DMEM supplemented with 10% FBS, which is widely used for cell culture.

Mineralization of collagen-chitosan materials

Figure C.3 shows data on mineralization and mechanical properties of acellular collagen-chitosan matrices incubated in MM and DM for three days. Histological evaluation of Von Kossa stained sections taken at the top, middle, and bottom of the constructs showed clear differences in degree of phosphate deposition between mineralizing and control conditions (Fig. C.3A). After three days in incubation, constructs in DM remained translucent, whereas those in MM were opaque, and dark staining for calcium was more prominent in MM samples (Fig. C.3A inset). Quantification of relative phosphate staining showed that hydrogels in MM exhibited significantly higher phosphate levels at the top and middle of the constructs, though staining in the bottom section was not statistically different compared to constructs in DM. These results support the finding that MM induces mineralization, but show that mineral deposition was not

evenly distributed through the material.

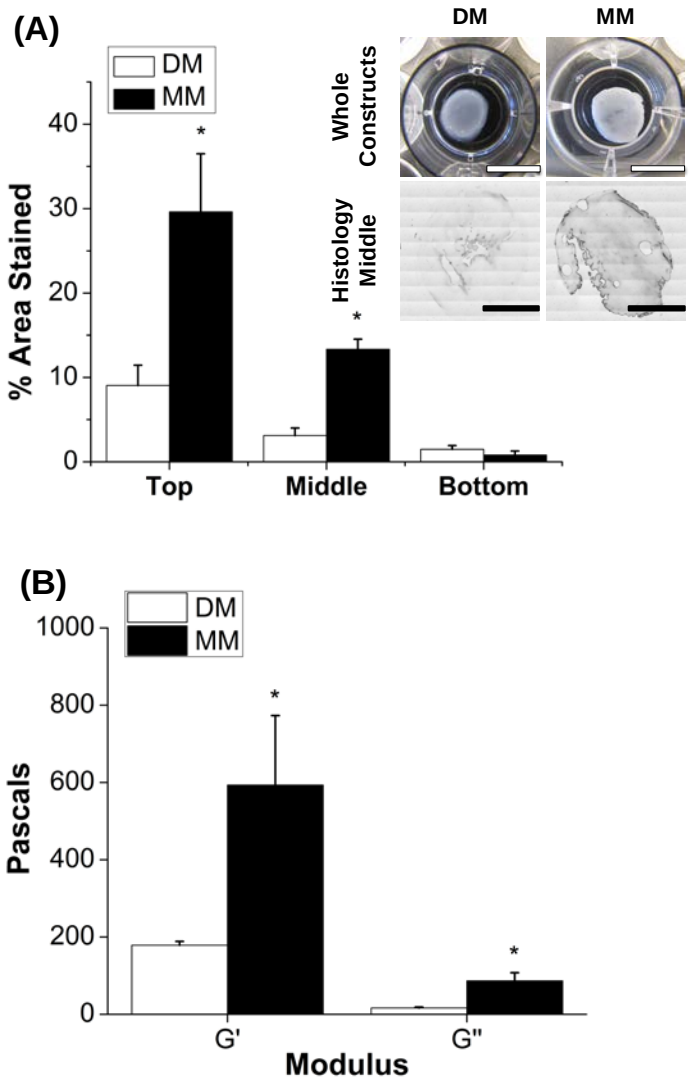

Figure C.3 – Regional calcium deposition, representative histological sections, and rheological characterization. Mineralization was distributed in the top and middle sections of constructs. Storage modulus measurements indicated a significant increase in mechanical properties after incubation in mDMEM. A) Quantification of calcium deposition in different regions of collagen-chitosan constructs using histological staining for calcium (n=4 at each location). Inset shows control and mineralized collagen-constructs (top row, scale bar = 1 mm) and representative histology sections (bottom row, scale bar = 500 μm). B) Storage (G') and loss (G") moduli for control and mineralized collagen-chitosan constructs after three days of culture (n=4, * denotes $p < 0.05$ from the control DM group).

Figure C.3B shows the storage (G') and loss (G'') modulus from acellular collagen-chitosan gels exposed to DM or MM for three days. Relative to control gels, mineralized gels exhibited a

3-fold increase in stiffness as reflected by the storage modulus ($p<0.05$). The loss modulus also increased significantly ($p<0.001$) in the MM condition, as compared to the DM condition. These data show that the mechanical properties of hydrogel constructs can be augmented by mineralization even over relatively short time periods. SBF treatment can affect the properties of scaffolds, though the effects can vary depending on the distribution of the mineral throughout the scaffolding material [8, 18]. Increasing the stiffness and toughness of protein hydrogel materials is desirable in order to allow implantation of constructs, particularly in load-bearing applications. A stiffer matrix may also attenuate the cell-mediated matrix remodeling that occurs in 3D protein hydrogels [32], and may direct the phenotype of progenitor cells toward an osteogenic phenotype [33].

Effect of mineralization on cell function

Viability data for hFb embedded in 3D collagen-chitosan materials are shown in Figure C.4 and Figure C.5A. Green staining indicates the cytoplasm of living cells, whereas red-stained nuclei identify dead cells. The culture protocol is shown schematically by the arrows in Figure C.4. Control constructs were cultured in DM for 11 days, whereas mineralized constructs were cultured in DM for one day, followed by three days of incubation in MM, and then 7 days of culture recovery in DM. All samples were imaged and assayed for cell function at days 1, 2, 4, 5, 7, and 11. After one day of culture in DM, cells began to spread through the collagen-chitosan matrix (Fig. C.4A, C.4B) and exhibited very high viability (>90%). Constructs subsequently exposed to MM showed significantly decreased viability ($p<0.05$) over the incubation period in MM (days 2 through 4, Fig. C.4D, C.4F), but viability was still high (~80%). The morphology of cells incubated in MM was more rounded than the control cells, which were highly stellate and

exhibited viability over 90% (Fig. C.4C, C.4E). Upon reintroduction into standard medium, cells in the mineralized constructs recovered a spread morphology (Fig. C.4H, C.4J, C.4L) and viability returned to the same level as in control constructs by day 11 (>90%).

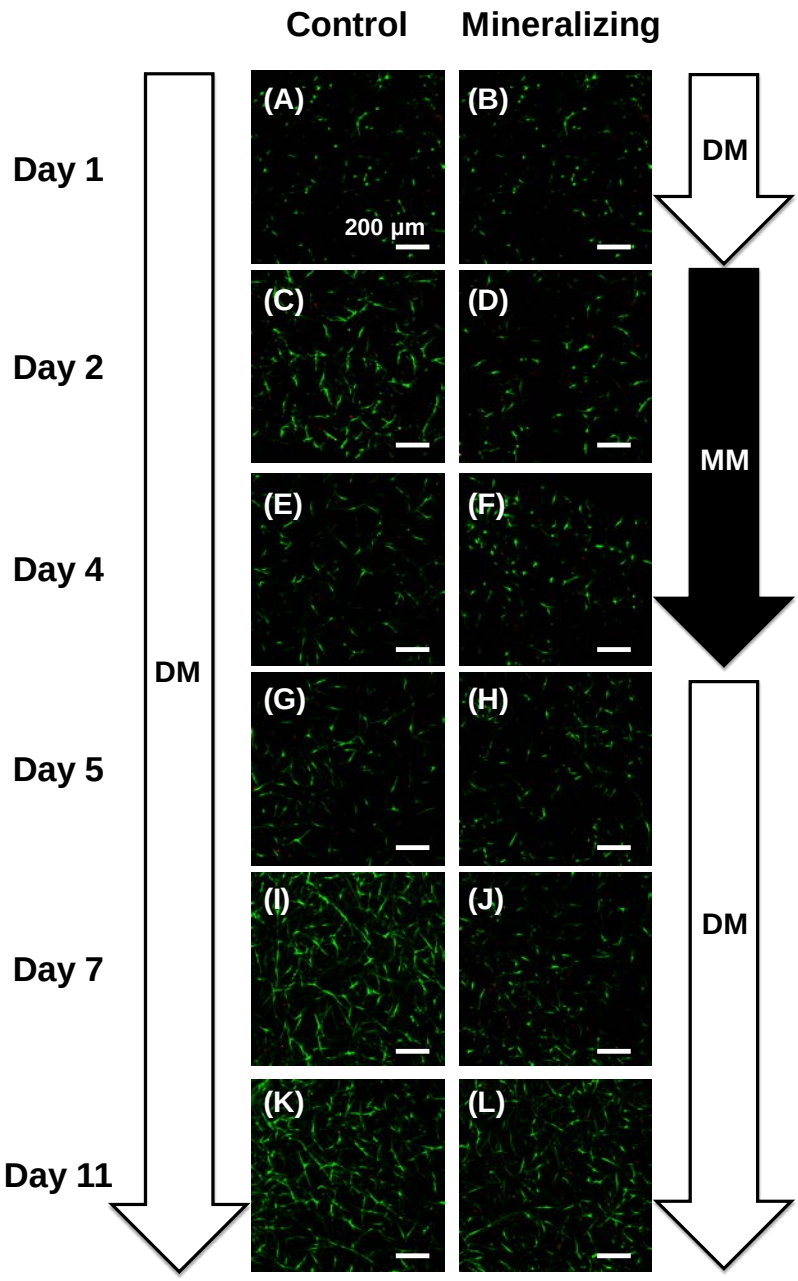

Figure C.4 – Live/Dead imaging of mineralized cell-seeded matrices. Cell viability remained high in control media, while viability decreased through culture in mineralizing media. Confocal micrographs of fibroblast-seeded collagen-chitosan gels cultured in control medium (A, C, E, G, I, K) or under mineralizing conditions (B, D, F, H, J, L). Cells are stained so that the cytoplasm of living cells is green and the nuclei of dead cells are red. Arrows at sides show culture protocol. Scale bar = 200 µm.

The DNA content of hydrogel constructs was used as a measure of cell number and is shown in Figure C.5B. Cell number increased steadily and significantly ($p<0.001$) over time in the DM

condition, resulting in an approximately 5-fold increase by day 11. Constructs in the mineralization group showed an initial rise in DNA content, which subsequently dropped significantly upon incubation in MM from days 2 through 4 ($p<0.0001$). Similar to cell viability, cell number in mineralized constructs recovered after transfer to DM, although the DNA content did not recover to the same levels as controls. The cell viability and cell number data provide different but complementary information on cell "health" in the constructs. A lack of cell proliferation would lead to a decrease in overall cell number over time, though viability observed as a snapshot at any given time can still be high, as observed in MM at the day 1 and 2 time points. Cell death is suggested by the data at the day 4 and 5 time points, since both viability and cell number were decreased. In contrast, when cells are proliferating then cell number will increase and viability can also be high. This corresponds to the trends observed in DM. Taken together these data suggest that incubation in mineralizing medium significantly reduces, and perhaps completely inhibits, the proliferation of the embedded cells while cell viability is also affected but remains high overall.

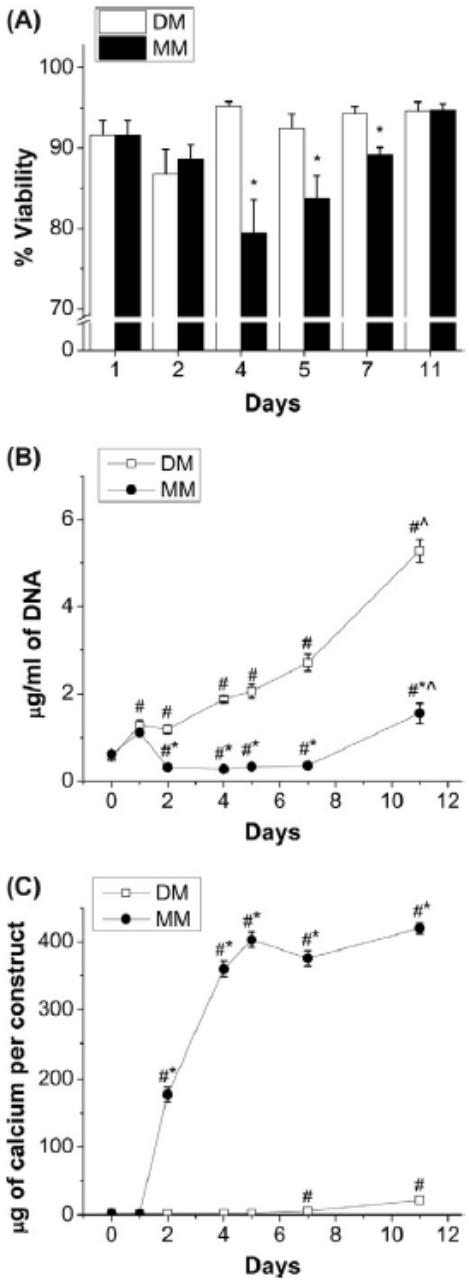

Figure C.5 – Quantification of cell viability, DNA content, and calcium deposition in cell-seeded mineralized constructs. Cell viability and DNA content both decreased while culturing cell-seeded hydrogels in mineralizing media, but could be recovered after switching to control media. Calcium content significantly increased in constructs cultured in mDMEM compared to control media. A) Cell viability (n=4), B) DNA content (n=4), and C) calcium content (n=4) of collagen-chitosan constructs cultured in control and mineralizing medium. (# denotes statistical significance from day 0 controls; * denotes statistical significance from DM controls; ^ denotes statistical significance from day 7).

Figure C.5C shows calcium deposition in cell-seeded constructs over the time course of the experiment. Upon transfer to MM at day 2, constructs in the mineralizing group showed a sharp and significant increase in calcium content and reached a level approximately 140-fold higher that controls after three days of incubation in MM ($p<0.001$). The calcium levels remained similarly high after transfer to recovery medium for the remainder of the experimental period. In contrast, constructs cultured in control medium (DM), showed very little calcium deposition, though a statistically significant increase over day 0 was observed at days 7 and 11 in DM ($p<0.001$).

Fibroblasts were used as a model cell type in this study in order to isolate the effects of the modified medium. Unlike bone marrow stromal cells and osteoblasts, fibroblasts are a non-mineralizing cell type and therefore increases in mineral content of the matrices can be attributed purely to the effect of the medium, and not cellular action. Preliminary studies showed that hFb could survive three days incubation in MM, though longer culture periods lead to increased cell death (data not shown). In 3D collagen-chitosan hydrogels, cell viability and proliferation rate decreased over three days of incubation in MM, but the cell population remained over 75% viable. These effects can be attributed to the hypertonic nature of MM, which is required to induce mineralization but can also modify cell function. Importantly, both the viability and proliferative capacity of fibroblasts recovered when collagen-chitosan constructs were cultured in standard DMEM after mineralization. These results suggest that the medium and protocol employed were sufficient to mineralize 3D protein constructs in the presence of living fibroblasts, and it is likely that similar results would be observed with other cell types.

A number of further questions remain to be answered in future studies. The specific structure and type of mineral being deposited is of interest because it has relevance to creating biomimetic

materials. In addition, it is known that the presence of mineral, either as a substrate or in solution, can affect differentiation of progenitor and stem cells. The influence of material stiffness on cell phenotype is of great interest in the field of tissue engineering, and mineralized matrices may provide a tool to examine such effects. While the biochemical and mechanical effects of matrix mineralization can be difficult to decouple, the ability to mineralize 3D protein-based materials may be another tool to study the effects of the tissue microenvironment on cell function. In addition, creating mineralized matrices in the presence of cells may be used to direct progenitor cell differentiation and/or to create more mechanically stable biomimetic constructs for orthopaedic and other applications.

C.4 Conclusions

This study represents an initial step in the development of techniques to mineralize 3D protein constructs in the presence of living cells. A modified culture medium and protocol were developed to achieve mineralization of collagen-chitosan matrices at physiological pH and temperature. Typically used SBF formulations do not support cell viability and growth and therefore are limited in their utility in the presence of cells. The modified medium used in this study contained a similar panel of mineralizing ions similar to SBF, though at modified concentrations, and also contained the nutrients and buffers needed to sustain cell function. It was shown that three day incubation of 3D collagen-chitosan materials resulted in mineral deposition and stiffening of the gels. Cell viability was reduced and cell number decreased during incubation in mineralizing medium, however a viable cell population was maintained and it was shown that viability and proliferation recovered after rescue in standard medium. These

results suggest that in vitro mineralization in defined media can be used to modulate the composition and properties of engineered tissues in the presence of living cells.

C.5 References

1. Mikos AG, Herring SW, Ochareon P, Elisseeff J, Lu HH, Kandel R, et al. Engineering Complex Tissues. Tissue Engineering 12, 3307, 2006.

2. Porter JR, Ruckh TT, Popat KC. Bone tissue engineering: A review in bone biomimetics and drug delivery strategies. Biotechnology Progress 25, 1539, 2009.

3. Al-Munajjed AA, et al. Development of a biomimetic collagen-hydroxyapatite scaffold for bone tissue engineering using a SBF immersion technique. Journal of Biomedical Materials Research Part B: Applied Biomaterials 90B, 584, 2009.

4. Suárez-González D, Barnhart K, Saito E, Vanderby R, Hollister SJ, Murphy WL. Controlled nucleation of hydroxyapatite on alginate scaffolds for stem cell-based bone tissue engineering. Journal of Biomedical Materials Research Part A 95A, 222, 2010.

5. Jayasuriya AC, Kibbe S. Rapid biomineralization of chitosan microparticles to apply in bone regeneration. Journal of Materials Science: Materials in Medicine 21, 393, 2009.

6. Gkioni K, Leeuwenburgh SCG, Douglas TEL, Mikos AG, Jansen JA. Mineralization of Hydrogels for Bone Regeneration. Tissue Engineering Part B: Reviews 16, 577, 2010.

7. Liu X, Smith LA, Hu J, Ma PX. Biomimetic nanofibrous gelatin/apatite composite scaffolds for bone tissue engineering. Biomaterials 30, 2252, 2009.

8. Davis HE, Rao RR, He J, Leach JK. Biomimetic scaffolds fabricated from apatite-coated polymer microspheres. Journal of Biomedical Materials Research Part A 90A, 1021, 2009.

9. Kretlow JD, Mikos AG. Review: Mineralization of Synthetic Polymer Scaffolds for Bone Tissue Engineering. Tissue Engineering 13, 927, 2007.

10. Murphy WL, Kohn DH, Mooney DJ. Growth of a continuous bonelike mineral within porous poly(lactide-co-glycolide) scaffolds in vitro. Journal of Biomedical Materials Research Part A 50, 50, 1999.

11. Kokubo T, Kushitani H, Sakka S, Kitsugi T, Yamamuro T. Solutions able to reproduce in vivo surface-structure changes in bioactive glass-ceramic A-W. Journal of Biomedical Materials Research 24, 721, 1990.

12. Kohn DH, Shin K, S.I. H, Jayasuriya AC, Leonova EV, Rosello RA, et al. Self-assembled mineral scaffolds as model systems for biomineralization and tissue engineering. Toronto: University of Toronto Press; 2005.

13. Luong LN, Hong SI, Patel RJ, Outslay ME, Kohn DH. Spatial control of protein within biomimetically nucleated mineral. Biomaterials 27, 1175, 2006.

14. Murphy W, Hsiong S, Richardson T, Simmons C, Mooney D. Effects of a bone-like mineral film on phenotype of adult human mesenchymal stem cells in vitro. Biomaterials 26, 303, 2005.

15. Ohtsuki C, Kamitakahara M, Miyazaki T. Coating bone-like apatite onto organic substrates using solutions mimicking body fluid. Journal of Tissue Engineering and Regenerative Medicine 1, 33, 2007.

16. Yang HS, La W-G, Bhang SH, Lee T-J, Lee M, Kim B-S. Apatite-Coated Collagen Scaffold for Bone Morphogenetic Protein-2 Delivery. Tissue Engineering Part A 17, 2153, 2011.

17. Luong LN, McFalls KM, Kohn DH. Gene delivery via DNA incorporation within a biomimetic apatite coating. Biomaterials 30, 6996, 2009.

18. Rao RR, He J, Leach JK. Biomineralized composite substrates increase gene expression with nonviral delivery. Journal of Biomedical Materials Research Part A 94, 344, 2010.

19. Ma PX. Biomimetic materials for tissue engineering. Advanced Drug Delivery Reviews 60, 184, 2008.

20. Lund AW, Yener B, Stegemann J, Plopper GE. The Natural and Engineered 3D Microenvironment as a Regulatory Cue During Stem Cell Fate Determination. Tissue Engineering: Part B 15, 371, 2009.

21. Bhat A, Dreifke MB, Kandimalla Y, Gomez C, Ebraheim NA, Jayasuriya AC. Evaluation of cross-linked chitosan microparticles for bone regeneration. Journal of Tissue Engineering and Regenerative Medicine 4, 532, 2010.

22. Batorsky A, Liao J, Lund AW, Plopper GE, Stegemann JP. Encapsulation of adult human mesenchymal stem cells within collagen-agarose microenvironments. Biotechnology and Bioengineering 92, 492, 2005.

23. Arpornmaeklong P, Pripatnanont P, Suwatwirote N. Properties of chitosan–collagen sponges and osteogenic differentiation of rat-bone-marrow stromal cells. International Journal of Oral and Maxillofacial Surgery 37, 357, 2008.

24. Wang L, Stegemann JP. Glyoxal crosslinking of cell-seeded chitosan/collagen hydrogels for bone regeneration. Acta Biomaterialia 7, 2410, 2011.

25. Cummings CL, Gawlitta D, Nerem RM, Stegemann JP. Properties of engineered vascular constructs made from collagen, fibrin, and collagen–fibrin mixtures. Biomaterials 25, 3699, 2004.

26. Wang L, Stegemann JP. Thermogelling chitosan and collagen composite hydrogels initiated with β-glycerophosphate for bone tissue engineering. Biomaterials 31, 3976, 2010.

27. Wang L, Singh M, Bonewald LF, Detamore MS. Signalling strategies for osteogenic differentiation of human umbilical cord mesenchymal stromal cells for 3D bone tissue engineering. Journal of Tissue Engineering and Regenerative Medicine 3, 398, 2009.

28. Lee JTY, et al. Cell culture medium as an alternative to conventional simulated body fluid. Acta Biomaterialia 7, 2615, 2011.

29. Tan EML, Uitto J, Bauer EA, Eisen AZ. Human Skin Fibroblasts in Culture: Procollagen Synthesis in the Presence of Sera from Normal Human Subjects and from Patients with Dermal Fibroses. The Journal of Investigative Dermatology 76, 462, 1981.

30. Combes C, Rey C, Freche M. In vitro crystallization of ostacalcium phosphate on type I collagen: influence of serum albumin. Journal of Materials Science: Materials in Medicine 10, 153, 1990.

31. Juhasz JA, Best SM, Auffret AD, Bonfield W. Biological control of apatite growth in simulated body fluid and human blood serum. Journal of Materials Science: Materials in Medicine 19, 1823, 2007.

32. Hong H, McCullough CM, Stegemann JP. The role of ERK signaling in protein hydrogel remodeling by vascular smooth muscle cells. Biomaterials 28, 3824, 2007.

33. Parekh SH, Chatterjee K, Lin-Gibson S, Moore NM, Cicerone MT, Young MF, Simon CG Jr. Modulus-driven differentiation of marrow stromal cells in 3D scaffolds that is independent of myosin-based cytoskeletal tension. Biomaterials 32, 2256, 2011.

APPENDIX D

Noninvasive, Quantitative, Spatiotemporal Characterization of Mineralization in 3D Collagen Hydrogels Using High Resolution Spectral Ultrasound Imaging

D.1 Introduction

Comprehensive and objective characterization of engineered tissues is a challenge in the development of new products that apply the tissue engineering approach of combining biomaterials, cells, and growth factors to generate living tissues [1]. Such engineered tissues are typically assessed using biochemical and histological assays that provide information about cell function and tissue development, but many of these assays require complex and destructive sample processing. In addition, relatively few assays provide true 3D spatial resolution of biochemical events and physical properties in developing tissues, and most are not suitable for longitudinal monitoring of the same constructs over time because of their invasive and often destructive nature. Nondestructive imaging and tissue characterization techniques are therefore highly attractive both for tissue engineering research and for translation of well-defined products to the clinic. Such techniques can help speed the development of tissue engineered technologies, reduce the cost of production, and improve the level of quality assurance.

Ultrasound imaging has shown promise for rapid and nondestructive imaging in tissue engineering. In particular, conventional ultrasound has been used to characterize the evolution of tissue components and corresponding changes in tissue properties in a variety of systems, as

summarized in Table D.1. For example, attenuation of gray scale (B-mode) ultrasound signals over time has been shown to correlate with matrix deposition and differentiation of adipose stem cells on synthetic scaffolds [2]. Similarly, gray scale signals have been used to assess collagen production by myofibroblasts in 3D fibrin matrices over time [3], as well as proliferation of bone marrow stromal cells in β-tricalcium phosphate scaffolds [4]. Acoustic parameters have also been correlated to the mechanical properties and cartilage matrix evolution by chondrocytes in polyethylene glycol hydrogels [5] and have been used characterize the mechanical properties of agarose hydrogels as they develop over time [6].

	Construct used	**Type of study**	**Parameter measured or estimated**	**Ultrasound parameter used**
Fite et al (ref. [2])	PLGA scaffold with adipose stem cells	Tissue development over 18 days	Ultrasound attenuation in chondrogenic constructs	Normalized intensity (in dB)
Kreitz et al (ref. [3])	Fibrin hydrogel with myofibroblasts	Tissue development over 35 days	Hydroxyproline content (collagen)	Mean grayscale
Oe et al (ref. [4])	Bone marrow stromal cell/β-tricalcium phosphate scaffold	Fresh gels	Number of cells	Amplitude
Rice et al (ref. [5])	PEG hydrogel with chondrocytes	Tissue development over 9.5 weeks	Mechanical properties (compressive modulus), matrix content	Speed of sound, slope of attenuation
Lizzi et al (ref. [6])	Agarose hydrogel	Fresh gels	Mechanical properties (Young's modulus)	Speed of sound
Ghudur et al (this study)	Collagen hydrogel doped with HA mineral or mineralized using SBF	Fresh gels; tissue development over 21 days	HA mineral; calcium mineral	Grayscale, spectral parameters (MBF, slope)

Table D.1 – Summary of reported studies using ultrasound to characterize engineered tissue constructs.

Conventional B-mode ultrasound imaging is based purely on gray scale values and is able to provide spatial and temporal information about sample morphology. However it provides little direct information about sample composition. A key drawback of purely gray scale analysis is that the image signal is dependent on a variety of factors including ultrasound transducer

response and image post-processing. The results are therefore operator- and system-dependent, and it is difficult to compare data taken on different imaging systems or at different times in an objective and meaningful fashion.

In contrast, spectral ultrasound imaging (SUSI) utilizes unprocessed, raw backscattered radiofrequency (RF) signals. In this approach, the power spectra of the RF signals from a region of interest are computed and calibrated to remove system input and output effects. Because the resulting spectra are often quasi-linear over the bandwidth used in typical ultrasound imaging, linear regression can be performed to obtain a relatively small set of parameters from the calibrated spectra. These parameters include the slope and intercept of the regression line, as well as the midband fit (MBF), which is the value of the linear function at the midpoint of the usable bandwidth. This analysis produces instrument-independent parameters that can greatly facilitate comparison of data between studies and time points, and which permit tissue characterization in an absolute and standardized manner [7]. It has been shown theoretically that these spectral parameters are related to tissue microstructural properties [8]. In particular, the slope provides information on the effective size of acoustic scatterers, and the MBF provides information on the concentration, size, and relative acoustic impedances of scattering particles in the sample. These parameters have also proven to be effective for identifying changes in tissue state for prostate, breast and other cancer tissues [9-12] as well as intravascular plaque [13,14]. In a similar manner, spectral analysis may therefore have utility in more fully characterizing the composition of engineered tissues.

In the present study, high resolution spectral ultrasound imaging was applied to a model engineered construct that mimics a mineralized tissue. We evaluated the ability of SUSI to determine the distribution of mineral in a 3D collagen gel that was loaded with hydroxyapatite

particles, to discriminate between different grades of hydroxyapatite, and to quantify particle distribution in the protein hydrogels. We also induced exogenous mineralization of pure collagen gels to assess the ability of SUSI to monitor changes in the constructs over time, and correlated spectral parameters with the concentration of mineral in the constructs. Our goal was to evaluate the utility of spectral ultrasound techniques for non-invasively imaging and characterizing mineral-containing protein materials, which may be relevant to orthopaedic and other tissue engineering applications.

D.2 Materials and Methods

3D Collagen Hydrogel Fabrication

3D collagen hydrogels were generated as previously described [15]. Briefly, collagen type I (MP Biomedicals, Solon OH) was dissolved at 4.0 mg/ml in cold 0.02 N acetic acid overnight. Constructs were created by mixing 10% fetal bovine serum (FBS; Invitrogen, Carlsbad CA), 10% Dulbecco's modified Eagle's medium (DMEM; Invitrogen), 20% 5X-concentrated DMEM, 10% 0.1 N NaOH (Sigma Aldrich, St. Louis MO) and 50% collagen stock solution at 4°C for a final collagen concentration of 2.0 mg/ml. The mixture (500 µl) was then injected into a 24 well plate and allowed to gel at 37°C for 45 min.

Addition of Hydroxyapatite to 3D Hydrogels

Composite collagen-hydroxyapatite (HA) hydrogels were fabricated by adding particulate HA directly to the gel mixture. Three types of hydroxyapatite were used, each with a different average particle size: reagent-grade (HA-R; Sigma) with a particle size of 590 µm, micro-grade (HA-M; Plasma Biotal Ltd., North Derbyshire, UK) with a particle size of 5 µm, and nano-grade

(HA-N; Sigma), with a particle size of <200 nm. A stock HA solution of 200 mg/ml HA in DMEM was prepared and autoclaved at 120°C for 20 minutes maintain to achieve sterility. Collagen-HA hydrogels were fabricated at 10.0 mg/ml by mixing cold 5% HA stock solution, 5% DMEM, 10% FBS, 20% 5X concentrated DMEM, 10% 0.1 N NaOH, and 50% collagen stock, and then initiating gelation by raising the temperature to 37°C. Constructs with higher and lower concentrations of HA (5.0 mg/mL and 20.0 mg/mL) were prepared by correspondingly changing the amount of HA stock solution used.

For dispersion studies, HA stock solution and DMEM (10% of final gel) were mixed at 4 °C and placed in a sonication water bath (Branson Ultrasonics, Danbury, CT) for 1 h to disrupt particle aggregates. The HA-DMEM mixture was then added immediately to the collagen pre-gel mixture and gelation was initiated as previously described.

Mineralization in Simulated Body Fluid

Simulated body fluid (SBF) was prepared as previously described [16]. The standard (1X) mineralizing solution has final ion concentrations of 141 mM NaCl, 4.0 mM KCl, 2.5 mM $CaCl_2 \bullet H_2O$, 1.0 mM $MgCl_2$, 4.2 mM $NaHCO_3$, 0.5 mM $MgSO_4$, and 1.0 mM KH_2PO_4 (Sigma). For this study, SBF solutions of higher-fold concentrations (2.5X and 5X) were prepared by increasing the concentrations of each reagent by the appropriate factor. Collagen hydrogels were fabricated as described above and were incubated at 37°C in 3.0 ml of either phosphate buffered saline (PBS), 2.5X SBF, or 5X SBF. The medium was replenished with fresh stock twice a day. Samples were imaged at days 3, 7, 10, 14, and 21.

Imaging and Data Acquisition

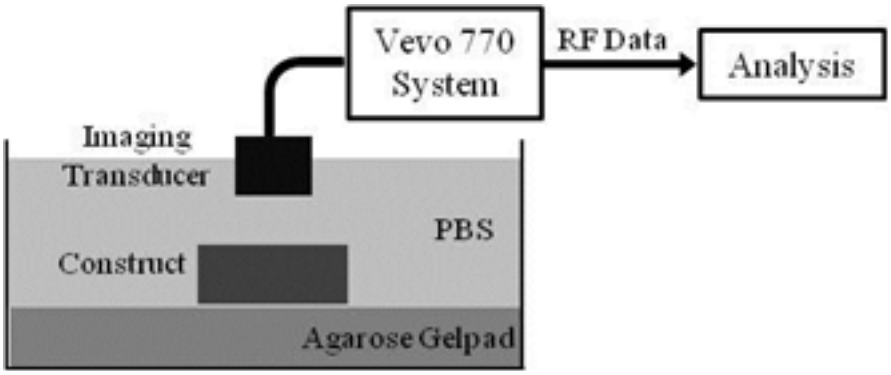

Figure D.1 – Schematic of experimental setup used for spectral ultrasound imaging of tissue construct.

Figure D.1 shows a schematic diagram of the imaging setup that included a 90 mm diameter Petri dish filled with PBS at room temperature. Collagen constructs were placed on top of an agar gel pad, which reduced signal reflection from the bottom of the dish. Ultrasound imaging was performed with a Vevo 770 instrument (VisualSonics Inc., Toronto, Canada) using an RMV 708 imaging probe with a nominal 55 MHz center frequency, 20-75 MHz bandwidth (−6 dB), 4.5 mm focal distance, and 1.5 mm depth of focus (−6 dB). 3D backscattered RF data from the tissue construct were collected at either 100% or 10% scanner power and 420 MS/s by performing multiple B-mode scans using an automatic 3D translational controller. The interval between adjacent A-lines and B-mode scans were 31 μm and 64 μm, respectively. After each RF acquisition of a construct, a reference RF acquisition of the setup without the construct was collected. This approach allowed the acquisition of operator-independent data and provided objective measures of each parameter.

Ultrasound Data Analysis

1) Grayscale (GS): Each A-line signal acquired as 3D RF data was Hilbert transformed to obtain the complex analytic signal $p(y,z)$. The conventional B-scan image is generally

constructed using the logarithmic amplitude envelope of this signal, $\log_{10}|p(y,z)|$. For quantitative analysis, the GS parameter (in mV) used in this study was the absolute value of the complex analytic signal, while the logarithm of the absolute value was used to create GS images:

$$GS(y,z) = \left|p(y,z)\right| \ \ or \ \ \log_{10}\left(\left|p(y,z)\right|\right) \tag{1}$$

The time of travel of the ultrasound pulse to the construct's top surface $\left(t_{top}\right)$, bottom surface $\left(t_{bottom}\right)$ and to the agar gel pad $\left(t_{pad}^{construct}\right)$ was determined based on grayscale thresholding using an automated algorithm. The time of travel to the agar gel pad without the construct $\left(t_{pad}^{ref}\right)$ was also determined as the reference. Using the known sound speed in the surrounding fluid medium $\left(C_f\right)$, the thickness of the construct was determined as:

$$Thickness = C_f\left[\left(t_{bottom} - t_{top}\right) + \left(t_{pad}^{ref} - t_{pad}^{construct}\right)\right] \tag{2}$$

2) Spectral parameters and parametric images: The power spectrum of each RF A-scan signal was calculated by taking the Fast Fourier Transform (FFT) of the data gated by a series of sliding Hamming windows of 0.2 μs, each offset by 0.1 μs. To remove artifacts associated with the transfer function of the ultrasound system, a calibrated power spectrum was generated by dividing the tissue power spectrum by the calibration spectrum, which was the power spectrum of the RF signal from the reflection of the imaging pulse from the interface of deionized water and phenylated silicone oil (Dow Corning 710, Midland MI) [17]. The calibrated power spectrum was processed by linear regression to find the spectral parameters, i.e. the slope and the MBF of the −15 dB bandwidth.

To better represent the spatial distribution of spectral features of the construct on the GS B-mode images, we constructed parametric images by marking each pixel with a color that

corresponded to the values of the spectral parameter. The density of each of the analysis parameters was calculated as:

$$X\ Density = \frac{\int_V X\ dV}{V}, \tag{3}$$

where *X* is either *GS* or spectral parameters evaluated for a selected volume (*V)* of the tissue construct. Ultrasound backscattering from pure collagen constructs (without mineral) was very low and its mean *GS* value within a 0.1 μs time window was very close to that of liquid medium alone, as expected. A threshold *GS* value based on pure collagen constructs was used to assist in identifying regions of the constructs that lacked mineral.

Calcium Quantification

The amount of calcium deposited in collagen hydrogels after incubation in PBS, 2.5X SBF, and 5X SBF was quantified at days 3, 7, 10, 14, and 21 using an orthocresolphthalein complex-one (OCPC) method [18]. Calcium content correlates to mineral deposition. Collagen gels were washed in PBS and digested in 0.5 ml of 1.0 N acetic acid overnight. 10.0 μl of the dissolved solution was then incubated for 10 minutes at room temperature with 300 μl of a working solution consisting of 0.05 mg/ml of OCPC solution and ethanolamine/boric acid/8-hydroxyquinoline buffer (Sigma). Samples were read spectrophotometrically at 575 nm. Calcium values were quantified by comparison to a standard curve prepared over a range of 0 – 100 μg/ml. Samples were diluted 100-fold or as necessary to obtain readings within the linear portion of the calibration curve.

Statistical Analysis

Four separate constructs were used for each biochemical and imaging assay. Aggregated SUSI data were collected from a 0.5 mm x 5.0 mm x thickness (~2 mm) volume of each construct and the data are presented as mean ± standard deviation. Statistical comparisons between parameters were made using Student's t-test for paired samples and the differences were considered significant at a level of $p<0.05$.

D.3 Results

Virtual Histology

The setup used in this study allowed rapid and noninvasive 3D imaging of collagen constructs while still in incubating culture medium. Image acquisition was completed in a few seconds at a frame rate of 45 Hz, and saving of the raw RF data required 2-3 minutes. In the present study, construct boundaries were determined manually based on GS thresholding, though this process could be automated and accelerated in the future. Overall, analysis of each construct using SUSI required about 5-10 minutes.

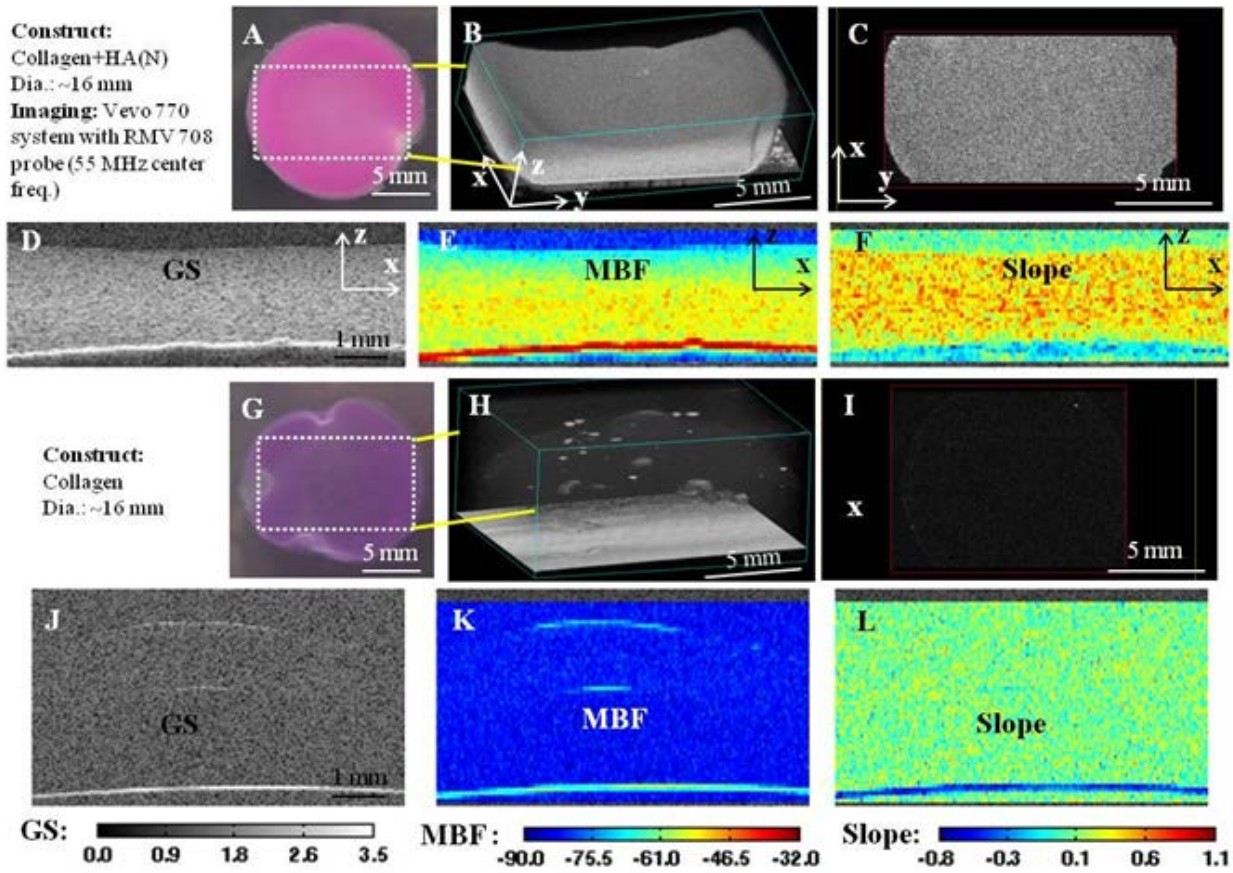

Figure D.2 – Virtual histology of 3D collagen constructs. Panels A-F show a collagen construct with added HA-N mineral, and panels G-L show corresponding images of a pure collagen control construct. (A, G) Color images of the top view of constructs. (B, H) 3D ultrasound rendered image of the section represented by white dotted box in A and G. (C, I) Ultrasound C-scans a transverse xy-plane. (D, J) Grayscale (GS), (E, K) mid-band fit (MBF) and (F, L) slope images of one section in the xz-plane.

Figure D.2 shows a representative example of ultrasound imaging and analysis output from a collagen hydrogel containing HA-N mineral (Fig D.2A-D.2F), as well as a "control" construct of pure collagen (Fig D.2G-D.2L). The photographs of the construct (Fig. D.2A, D.2G) show a top view (xy-plane) and the region that was imaged is indicated by the dotted rectangle. The 3D volume-rendered ultrasound images (Fig. D.2B, D.2H) show the overall dimension and morphology of the construct. This digital reconstruction can be rotated and/or sectioned to provide any desired viewing prospective. Figure D.2C is an image in the xy-plane at a defined depth (known as a C-scan) of the 3D of the HA-N construct, and shows homogeneous speckles

indicative of uniform spatial distribution of mineral in the construct. Similarly, a GS image in an xz-plane of the HA-N construct (Fig. D.2D) shows a mainly homogeneous distribution of mineral in the lateral (x) and depth (z) directions, as well as evidence of mineral settling at the bottom of the construct. The corresponding MBF image of the calibrated RF power spectrum (Fig. D.2E), which is related to scatterer radius and concentration in the construct, shows an increasing concentration of scatterer toward the bottom of the HA-N construct. In contrast, the slope parameter (Fig. C.2F), which varies inversely with scatterer radius, is relatively homogeneous in the bulk of the HA-N construct but decreases near the bottom of the construct, indicating settling of larger particles or cluster formation by the mineral. The corresponding rendered and RF spectrum images for the control construct (Fig D.2H-D.2L) show very little signal, demonstrating that SUSI can discriminate between mineral-containing and pure collagen materials.

Imaging and Analysis of Hydroxyapatite Content, Characteristics, and Spatial Distribution

To further demonstrate the ability of spectral ultrasound to determine mineral distribution and particle size in engineered tissues, three different types of HA mineral were added to collagen hydrogels at a concentration of 10.0 mg/ml. In addition, duplicate sets of each gel type were fabricated in which the HA was first sonicated to improve dispersion in the constructs. Figure D.3 shows images of constructs made with each type of HA under both unsonicated (upper panels in each group) and sonicated (lower panels) conditions. The 3D rendered images in the first column of images in Figure D.3 clearly show the morphology of each construct. The second and third columns include the sectional GS images with the MBF and slope values mapped over the right half of the images, to show specific information on each construct type. In

unsonicated HA-R samples, significant settling of the mineral component was suggested by the very high GS signal near the bottom of the constructs. In addition, the MBF signal was mostly absent in the bulk of HA-R constructs except toward the lower bottom of the construct, since the settled mineral was not included in the MBF analysis because it produced a saturated signal. Sonication clearly improved dispersion of the HA-R mineral. Settling was also observable though less pronounced in the HA-M samples, and to a lesser extent in HA-N samples. The slope values showed the expected size difference between HA-R and HA-M (lower slope values correspond to larger particles), though the difference between HA-M and HA-N was not detected, possibly due to the resolution of the imaging system at this frequency. The effect of sonication on HA-M and HA-N was also less marked, though dispersion was improved by sonication in all cases.

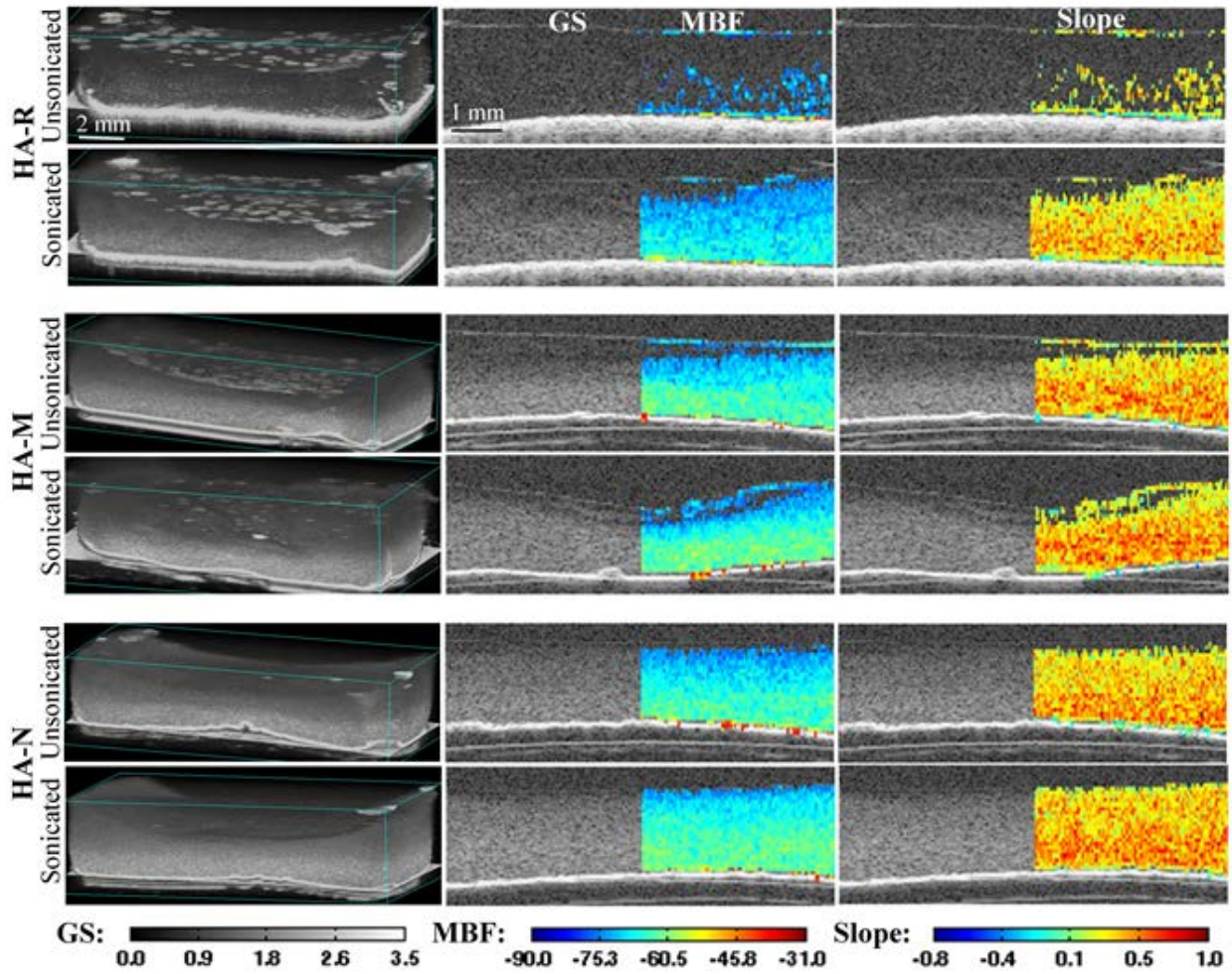

Figure D.3 – Parametric images of collagen-HA constructs made with three different HA grades: reagent (R), micro (M), and nano (N). Constructs were made either without sonication (top row of panels in each set) or with sonication (bottom row of panels in each set). First Column: 3D rendered image of the construct. Second Column: images of GS (left half of image) and MBF (right half of image) in a representative cross-section. Third Column: images of GS (left half of image) and slope parameter (right half of image) in a representative cross-section.

Process	Parameter	HA mineral type		
		R (μ ± σ)	M (μ ± σ)	N (μ ± σ)
Unsonicated	GS (dB)	1.24 ± 0.33	1.45 ± 0.32	1.59 ± 0.39
	MBF (dB)	-72.2 ± 6.1	-69.8 ± 4.2	-67.4 ± 5.5
	Slope (dB/MHz)	0.20 ± 0.18	0.33 ± 0.16	0.37 ± 0.17
Sonicated	GS (dB)	1.68 ± 0.38	1.61 ± 0.37	1.73 ± 0.36
	MBF (dB)	-66.0 ± 5.1	-67.1 ± 5.6	-65.0 ± 4.9
	Slope (dB/MHz)	0.39 ± 0.17	0.38 ± 0.16	0.40 ± 0.16

Table D.2 – Mean and standard deviation of ultrasound parameters correspondence of HA mineral.

To more systematically quantify the effects of HA type and sonication on mineral dispersion in collagen constructs, a 3D volume of 0.5 mm × 5.0 mm × thickness (~2 mm) was analyzed for each treatment. This provided assessment of data from a larger volume of the constructs (as opposed to a single section, as in Fig. D.3). The GS, MBF and slope parameters are plotted as histograms in Figure D.4 and the means and standard deviations of the histogram data are shown in Table D.2. The first column of histograms in Figure D.4 shows a comparison of the HA types using the unsonicated samples, and subsequent columns compare the unsonicated to the sonicated sample for each HA type. Since all constructs contained the same mass of HA mineral, the higher area under the curve and the higher mean of the GS and MBF data are indicative of more homogeneous distribution of the mineral in the construct, since settled HA was not included in the analysis. The lower mean of the slope for HA-R reflects the larger particle size, though the difference between HA-M and HA-N was not clearly discriminated. Sonication improved the distribution of HA-R significantly and the histogram data

suggested better dispersion of HA-M and HA-N as well. The parametric data in Table D.2 also reflect and quantify the observations made from the histogram data.

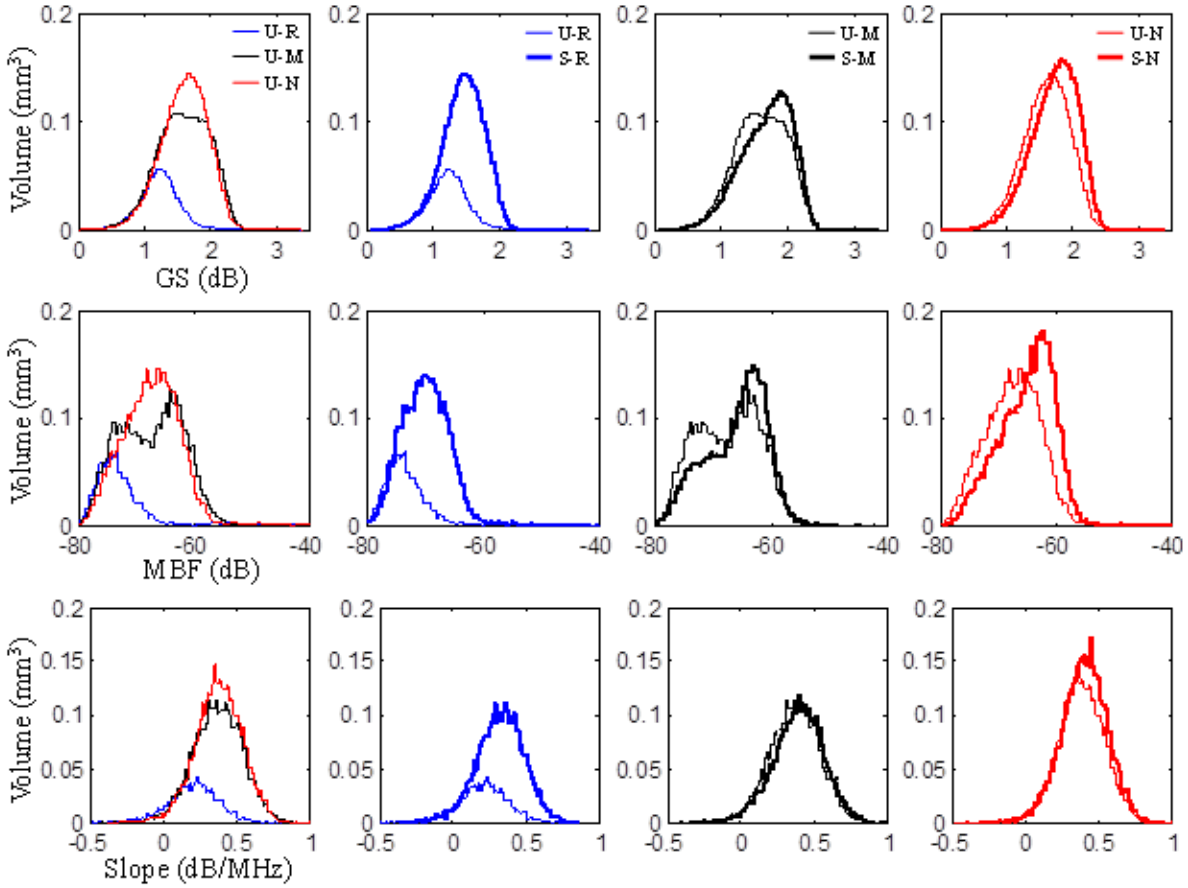

Figure D.4 – Histogram distributions of spectral parameters for unsonicated (U) and sonicated (S) collagen-HA constructs made with reagent (R), micro (M), or nano (N) grade HA. Top row shows gray scale values, middle row shows MBF values, and bottom row shows slope values. First column compares parameters between unsonicated samples. Subsequent columns compare unsonicated and sonicated constructs made with each HA type.

As a further validation of the ability of spectral ultrasound to characterize mineral in 3D collagen gels, a set of constructs with increasing HA concentration (5.0, 10.0 and 20.0 mg/ml) were created. HA-N was used with sonication since these constructs showed the most uniform HA distribution in previous studies. Figure D.5 shows 3D renderings as well as GS, MBF and slope data for these constructs. The intensity of both the GS and MBF signals reflect the increasing HA content, while the slope values remain essentially unchanged. These data reflect

that while the amount of HA in the constructs increased, the size of the HA particles remained the same. Figure D.6 shows correlations between the density of the GS, MBF, and slope parameters and the amount of HA added to the constructs. These data show a strong linear correlation between HA content and both the GS and MBF parameters. In contrast, the slope parameter was minimally affected by the concentration of HA, as would be expected when the particle size remains constant. The linear regression has a slight negative slope (-0.4°), possibly due to aggregation of mineral particles at higher concentration.

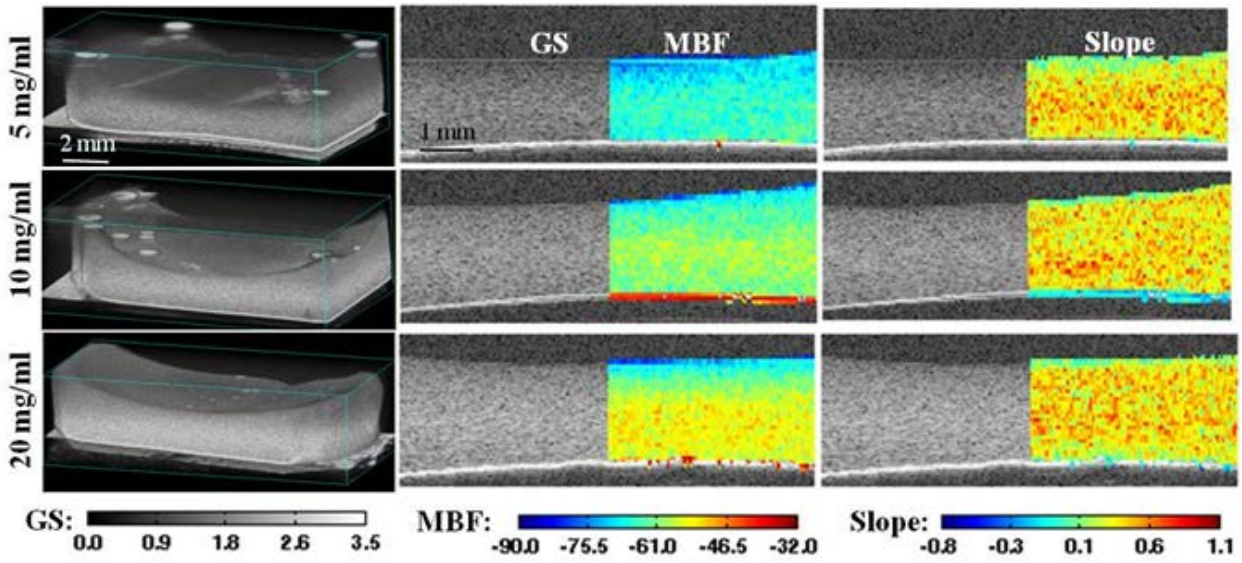

Figure D.5 – Ultrasound imaging of collagen-HA constructs made with three different concentrations of HA-N with sonication. First column shows 3D rendered images, second column shows GS and superimposed MBF, third column shows GS and superimposed slope. Rows show the HA-N concentration used to make the constructs.

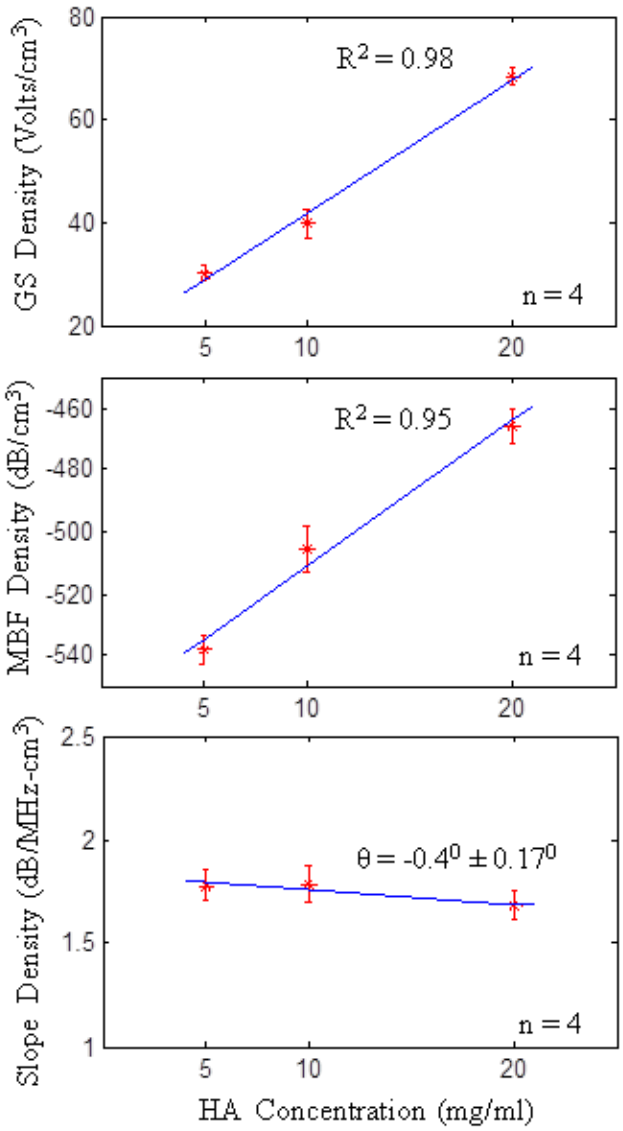

Figure D.6 – Correlation of sonicated HA-N mineral density with GS density, MBF density and Slope density. Nearly flat correlation for slope density is a correspondence of very close mineral sizes. (n=4 for each sample type; error bars represent standard deviation).

Imaging and Analysis of Mineral Deposition over Time

As an alternative to incorporating a mineral phase at the time of construct fabrication, we also promoted progressive mineral deposition over time by incubating constructs in simulated body fluid (SBF). Pure collagen constructs incubated in either PBS (control), 2.5X SBF, or 5X SBF for a period of 21 days were imaged at different days and the resulting spectral ultrasound data at day 21 are shown in Figure D.7. Constructs incubated in PBS showed low signal levels,

indicative of minimal mineral deposition. Constructs incubated in 2.5X SBF showed some mineralization on the surface, although the interior of the material was largely free of mineral. In contrast, the 5X SBF constructs showed robust mineralization and a marked compaction to form a dense and mineral-rich material. The MBF values show the spatial location and the amount of mineral in the constructs, whereas the decreased values of the slope parameter in the 5X constructs suggest that the mineral phase in these constructs was composed of larger particles.

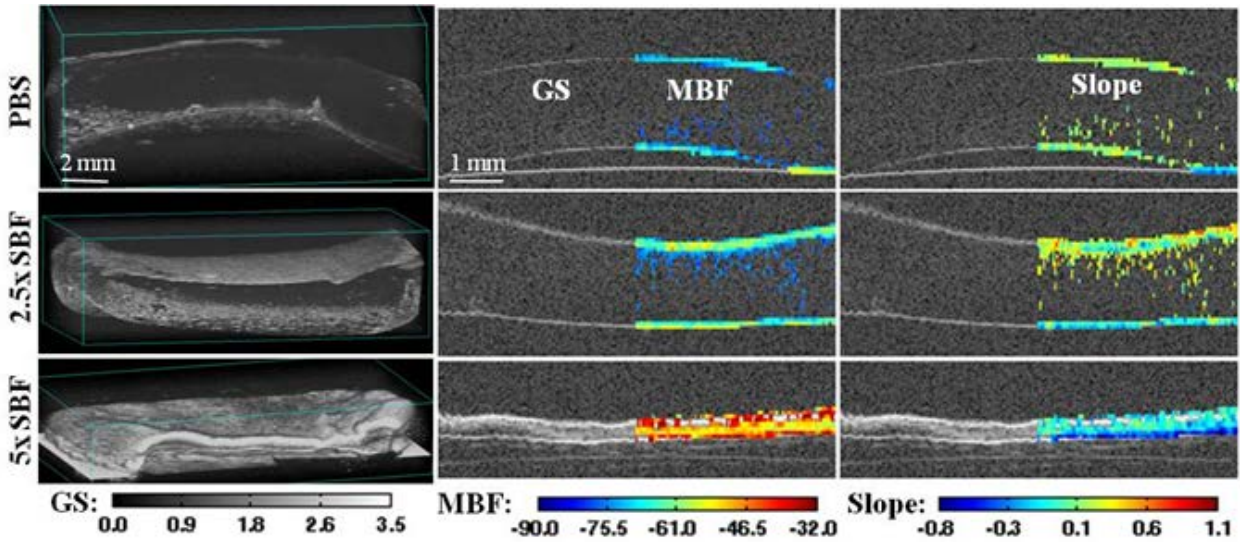

Figure D.7 – Collagen constructs exposed to mineralizing solution imaged at day 21 of incubation. First column shows 3D rendered images, second column shows GS and superimposed MBF, third column shows GS and superimposed slope. Rows show the incubation solution used.

Figure D.8 shows a temporal analysis of mineral deposition, using the 5X SBF constructs as an example because they demonstrated the most robust mineralization. The 3D renderings, GS images and MBF images show the pattern of mineral deposition, which clearly was initiated at the construct surface as early as day 3, and then extended progressively into the interior of the construct. Ultrasound imaging also shows the morphology of the construct as a whole, and in particular the marked compaction in the z-direction that occurred between day 7 and day 10. The slope decreased over time, indicating increased particle size, as would be expected for a mineral deposition process.

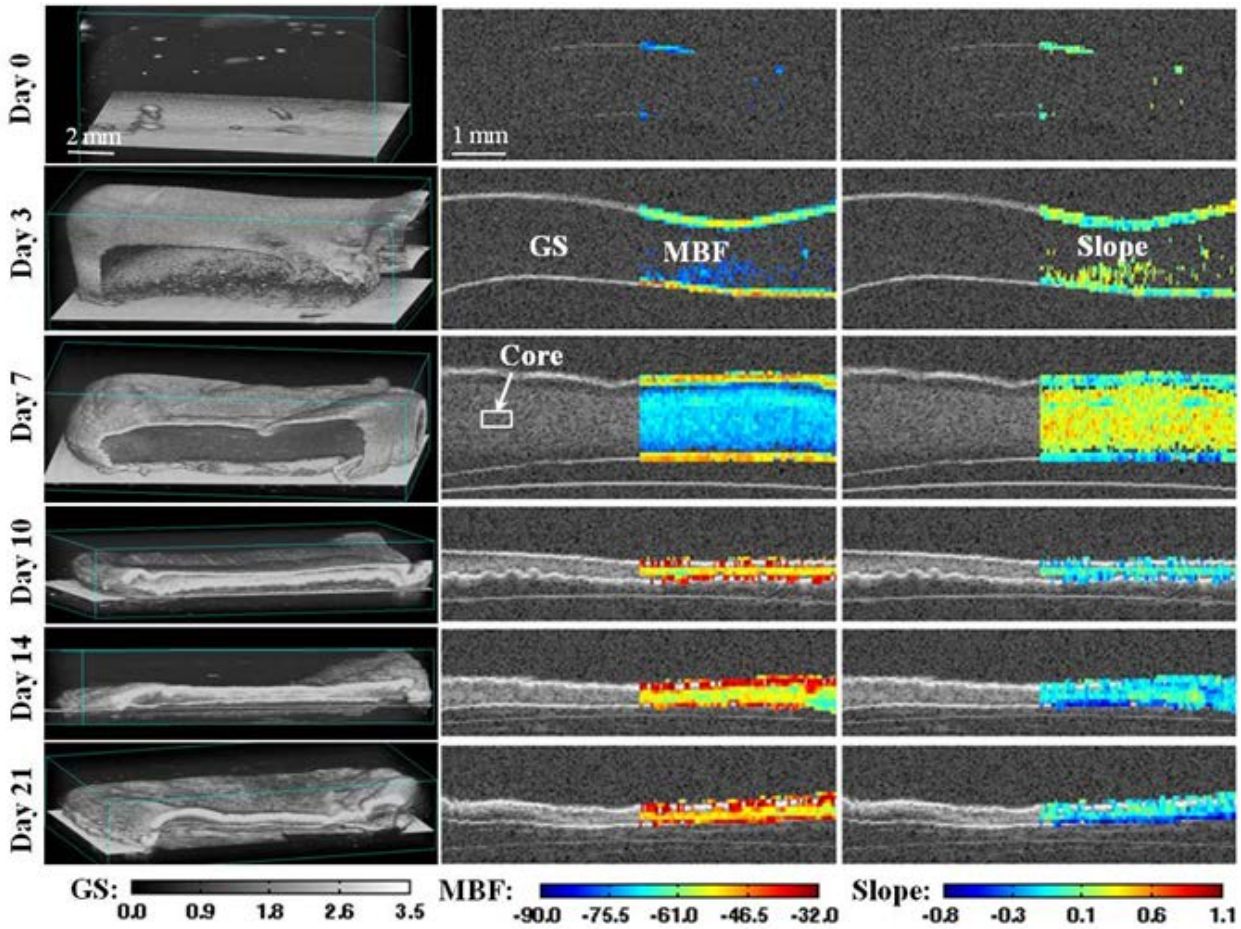

Figure D.8 – Collagen constructs mineralized in 5X SBF and imaged over time. First column shows 3D rendered images, second column shows GS and superimposed MBF, third column shows GS and superimposed slope. Rows show the time point of imaging.

Thresholding on ultrasound images was used to automatically determine construct thickness using Eqn. (2), by averaging the values in a 5.0 mm × 0.5 mm section. This method takes into account changes in construct shape, and therefore can provide an accurate measure of the relevant dimensions at any specific location and time. Figure D.9 shows that constructs in PBS compacted 17.4 ± 6.2 % ($n = 4$, $p<0.05$) over the first week but recovered over time at days 14 and 21. Constructs in 2.5X SBF did not compact significantly (1.8±2.8 % at day 7 with $p = 0.35$) over 21 days of incubation and had similar thickness as the constructs in PBS at day 21. Constructs in 5X SBF compacted markedly to less than a third of their original thickness (1.75 ±

0.06 mm, n = 4 with $p<0.001$) after day 7, and their dimensions remained relatively constant for the remainder of the incubation period.

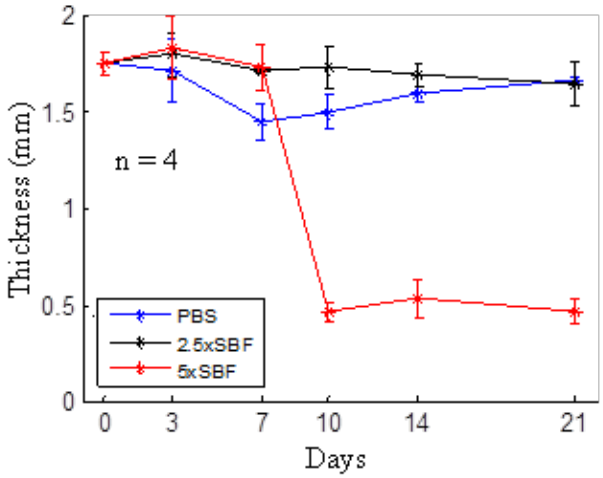

Figure D.9 – Plot of thickness over time of constructs incubated in PBS, 2.5X SBF, or 5X SBF. (n=4 for each sample type; error bars represent standard deviation).

The density of the MBF signal over a 0.5 mm x 5.0 mm x thickness volume of each construct determined using Eqn. (3) was compared with the extent of mineral deposition as measured by calcium content using the OCPC assay. Figure D.10 shows both MBF density and calcium density in constructs over time. Overall, the MBF density matched the measured calcium concentration very closely in all constructs ($R^2>0.95$ in all cases). In PBS, there was essentially no exogenous mineral deposition and the calcium concentration remained below 2 µg/mL. In 2.5X SBF the calcium content remained low and statistically unchanged over the first 14 days of incubation, but then climbed to ~35 µg/mL by day 21, with a corresponding increase in MBF density. The 5X SBF constructs were robustly mineralized and the calcium content increased linearly over the incubation period to a final value above 6000 µg/mL at day 21.

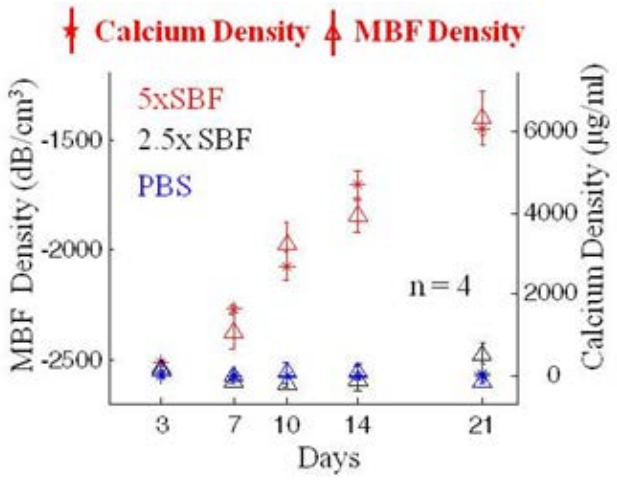

Figure D.10 – Calcium density and calculated MBF density over time in constructs incubated in PBS, 2.5X SBF, and 5X SBF. (n=4 for each sample type; error bars represent standard deviation).

D.4 Discussion

Spectral ultrasound imaging rapidly generated objective and quantitative information about the morphology and composition of 3D collagen constructs. Importantly, the imaging method was noninvasive and could be performed while constructs remained bathed in incubating medium. Since the assay was non-destructive, the same samples could be imaged over time to monitor their development. In addition, 3D imaging allowed sub-volume analysis and comparison of different regions of the imaged constructs through simple processing of the digital data. The use of high frequency ultrasound imaging (≈50 MHz) provided a spatial resolution of approximately 25 µm, which is suitable for characterization of engineered tissue constructs. High frequency imaging resulted in a lower penetration depth than other modalities, but still allowed characterization of the 2 mm thick engineered constructs used in this study. We imaged volumes on the order of 0.5 cm^3, but larger volumes can easily be imaged by increasing the lateral scan dimension. Importantly, the wide bandwidth available at higher frequencies is beneficial for spectral analysis because it provides richer information about the composition of the constructs, relative to conventional gray scale imaging. Taken together, these features make ultrasound

imaging very attractive for biomaterials and tissue engineering research, and potentially for quality assurance purposes as engineered tissues approach the market.

In this study, we focused on mineral-containing materials because of our interest in developing mineralized orthopaedic tissues [19, 20]. Analysis of 3D collagen gels supplemented with different types of hydroxyapatite showed that spectral ultrasound can characterize the concentration, degree of dispersion, and spatial location of the mineral phase in 3D. In particular, 3D ultrasound imaging showed clearly the ability of sonication to enhance dispersion of the larger HA-R particles as well as the much smaller HA-M and HA-N particles. Mineral distribution was best analyzed using the GS and MBF parameters, since both depend primarily on the concentration of scatterers in the sample. The settling and dispersion effects could be assessed by color-coding the parametric images, and could be further quantitatively characterized using histogram analysis. In addition, the relative concentration of samples supplemented with different levels of HA were characterized using ultrasound imaging results, which correlated well with the initial loading level. Achieving good dispersion of hydroxyapatite particles throughout scaffolds and hydrogels is a well-studied problem in developing biomimetic matrices [21], and assessment of dispersion has been a challenge. Our results show that ultrasound imaging has the ability to both qualitatively and quantitatively characterize dispersion in 3D samples, and can be used to compare treatments designed to enhance dispersion.

In the analysis of HA distribution, the GS and MBF data provided similar information. However a key distinction between these parameters is that MBF is independent of both the imaging system used and the scanning power of the ultrasound probe, whereas the GS data is dependent on these factors. Therefore MBF data generated by different users on different systems is comparable, whereas GS data is not. In addition, SUSI uses raw spectral data and no

manual thresholding is required. These features are important advantages of the method, since the ability to generate objective operator- and instrument-independent data makes the method more broadly applicable and appropriate for inter-study comparisons.

The slope parameter is reflective of particle size. In this study, the slope parameter was able to differentiate between HA-R particles (590 μm diameter) and the smaller HA-M (5 μm) and HA-N (<200 nm) particles. However the smaller particle sizes could not be differentiated from each other because of the resolution of the probe used (approximately 25 μm). While the MBF parameter varied with added HA content as the concentration increased, the slope parameter remained relatively constant, as would be expected from adding more particles of the same size. The slope parameter is extracted from the raw RF spectrum and therefore is also instrument-independent.

Simulated body fluid (SBF) was used as way to exogenously mineralize 3D collagen matrices, to observe and characterize the evolution of a mineral phase in constructs over time. SBF treatment has been developed and validated as a method to deposit a bone-like apatite mineral coating throughout scaffolds and hydrogels [22, 23]. Ultrasound imaging revealed the pattern, degree and temporal progression of mineral deposition. There was a clear dose-dependent effect of SBF concentration on mineral development, which was initiated at the surface of the constructs. In the most concentrated SBF solution (5X), the formation of a mineral "shell" around the construct was followed by a dramatic compaction of the material after a week of incubation. Both the mineralization and the compaction processes were tracked over time using ultrasound imaging, which are not possible using current histological techniques. The spectral parameters were used to quantify the degree of mineral deposition and these results correlated well with corresponding data from a destructive calcium quantification assay. The

reason for the marked volume change in highly mineralized constructs is not clear, but may have been due to changes in osmotic pressures caused by the mineral shell or the weight of the mineral deposits. Mineralization by SBF is a crystallization process that proceeds exponentially as new surface area and nucleation sites for crystal growth are provided. The much higher mineral content in the 5X SBF constructs was therefore expected based on the higher ion content in the mineralizing solution and the corresponding exponentially greater mineral deposition.

We have validated SUSI as a method to characterize a developing mineral phase in protein-based hydrogels. This technique therefore can be used to complement existing tissue imaging and characterization methods, and may provide additional information that cannot be obtained using current techniques. Microcomputed tomography (microCT) has been used widely in orthopaedic tissue engineering [24, 25], but is most suited to highly mineralized samples with strong radiographic contrast. Ultrasound is more applicable to soft tissues, and as we have shown it can distinguish mineral phases in such tissues. SUSI offers relatively rapid image acquisition (seconds to minutes for cm sized samples) whereas microCT imaging typically takes much longer. In addition, SUSI can be performed with a small and easily transported probe whereas microCT requires inserting the sample into a larger scanner.

The SUSI technique has other possible extensions and applications in addition to those addressed in this study. More detailed analysis of spectral data from multi-component samples may allow discrimination between material phases, e.g. between different protein types in hydrogels and/or between different types of mineral components. In addition, SUSI may be extended to in vivo characterization of mineralization. Spectral analysis already is performed clinically to assess intravascular plaque formation [26], and is being developed for virtual histological examination of cancerous tissue. Such extensions will be part of future work in the

field, and will enhance the utility of SUSI in accelerating the development of functional engineered tissues.

D.5 References

1. Langer R, Vacanti JP. Tissue Engineering. Science 260, 920, 1993.

2. Fite BZ, Decaris M, Sun Y, Sun Y, Lam A, Ho CK, et al. Noninvasive Multimodal Evaluation of Bioengineered Cartilage Constructs Combining Time-Resolved Fluorescence and Ultrasound Imaging. Tissue Engineering Part C: Methods 17, 495, 2011.

3. Kreitz S, Dohmen G, Hasken S, Schmitz-Rode T, Mela P, Jockenhoevel S. Non-Destructive Method to Evaluate the Collagen Content of Fibrin-Based Tissue Engineered Structures via Ultrasound. Tissue Engineering Part C: Methods 17, 1021, 2011.

4. Oe K, Miwa M, Nagamune K, Sakai Y, Lee SY, Niikura T, et al. Nondestructive Evaluation of Cell Numbers in Bone Marrow Stromal Cell/beta-Tricalcium Phosphate Composites Using Ultrasound. Tissue Engineering Part C: Methods 16, 347, 2010.

5. Rice MA, Waters KR, Anseth KS. Ultrasound monitoring of cartilaginous matrix evolution in degradable PEG hydrogels. Acta Biomater 5, 152, 2009..

6. Walker JM, Myers AM, Schluchter MD, Goldberg VM, Caplan AI, Berilla JA, et al. Nondestructive Evaluation of Hydrogel Mechanical Properties Using Ultrasound. Annals of Biomedical Engineering 39, 2521, 2011.

7. Lizzi FL, Ostromogilsky M, Feleppa EJ, Rorke MC, Yaremko MM. Relationship of Ultrasonic Spectral Parameters to Features of Tissue Microstructure. IEEE T Ultrason Ferr 34, 319, 1987.

8. Lizzi FL, Astor M, Liu T, Deng C, Coleman DJ, Silverman RH. Ultrasonic spectrum analysis for tissue assays and therapy evaluation. International Journal of Imaging Systems and Technology 8, 3, 1997.

9. Golub RM, Parsons RE, Sigel B, Feleppa EJ, Justin J, Zaren HA, Rorke M, Sokil-Melgar J, Kimitsuki H. Differentiation of breast tumors by ultrasonic tissue characterization. J Ultrasound Med 12, 601, 1993.

10. Silverman RH, Folberg R, Rondeau MJ, Boldt HC, Lloyd HO, Chen X, Lizzi FL, Weingeist TA, Coleman DJ. Spectral parameter imaging for detection of prognostically significant histological features in uveal melanoma. Ultrasound Med Biol 29, 951, 2003.

11. Oelze ML, O'Brien WD Jr, Blue JP, Zachary JF. Differentiation and characterization of rat mammary fibroadenomas and 4T1 mouse carcinomas using quantitative ultrasound imaging. IEEE Trans Med Imaging 23, 764, 2004.

12. Feleppa EJ. Ultrasonic tissue-type imaging of the prostate: implications for biopsy and treatment guidance. Cancer Biomark 4, 201, 2008.

13. Nasu K, Tsuchikane E, Katoh O, Vince DG, Virmani R, Surmely JF, Murata A, Takeda Y, Ito T, Ebara M, Matsubara T, Terashima M, Suzuki T. Accuracy of in vivo coronary plaque morphology assessment: a validation study of in vivo virtual histology compared with in vitro histopathology. J Am Coll Cardiol 47, 2405, 2006.

14. Nair A, Kuban BD, Tuzcu EM, Schoenhagen P, Nissen SE, Vince DG. Coronary plaque classification with intravascular ultrasound radiofrequency data analysis. Circulation 106, 2200, 2002.

15. Cummings CL, Gawlitta D, Nerem RM, Stegemann JP. Properties of engineered vascular constructs made from collagen, fibrin, and collagen–fibrin mixtures. Biomaterials 25, 3699, 2004.

16. Murphy WL, Kohn DH, Mooney DJ. Growth of continuous bonelike mineral within porous poly(lactide-co-glycolide) scaffolds in vitro. Journal of Biomedical Materials Research Part A 50, 50, 2000.

17. Hall TJ, Madsen EL, Dong F, Medina IR, Frank GR. Low-reflection-coefficient liquid interfaces for system characterization. Ultrasound Med Biol 27, 1003, 2001.

18. Rao RR, Jiao A, Kohn DH, Stegemann JP. Exogenous mineralization of cell-seeded and unseeded collagen-chitosan hydrogels using modified culture medium. Acta Biomater 8, 1560, 2012.

19. Wang L, Stegemann JP. Thermogelling chitosan and collagen composite hydrogels initiated with β-glycerophosphate for bone tissue engineering. Biomaterials 31, 3976, 2010.

20. Lund AW, Bush JA, Plopper GE, Stegemann JP. Osteogenic differentiation of mesenchymal stem cells in defined protein beads. J Biomed Mater Res B Appl Biomater 87, 213, 2008.

21. Šupová M. Problem of hydroxyapatite dispersion in polymer matrices: a review. Journal of Materials Science: Materials in Medicine 20, 1201, 2009.

22. Gkioni K, Leeuwenburgh SCG, Douglas TEL, Mikos AG, Jansen JA. Mineralization of Hydrogels for Bone Regeneration. Tissue Engineering Part B: Reviews 16, 577, 2010.

23. Kretlow JD, Mikos AG. Review: Mineralization of Synthetic Polymer Scaffolds for Bone Tissue Engineering. Tissue Engineering 13, 927, 2007.

24. Ho ST, Hutmacher DW. A comparison of micro CT with other techniques used in the characterization of scaffolds. Biomaterials 27, 1362, 2006.

25. Jones JR, Atwood RC, Poologasundarampillai G, Yue S, Lee PD. Quantifying the 3D macrostructure of tissue scaffolds. J Mater Sci Mater Med 20, 463, 2009.

26. J. Qian, A. Maehara, G. S. Mintz et al., “Impact of Gender and Age on In Vivo Virtual Histology-Intravascular Ultrasound Imaging Plaque Characterization (from the global Virtual Histology Intravascular Ultrasound [VH-IVUS] Registry),” American Journal of Cardiology 103, 1210, 2009.

APPENDIX E

Noninvasive Quantification of In Vitro Osteoblastic Differentiation in 3D Engineered Tissue Constructs using Spectral Ultrasound Imaging

E.1 Introduction

Bone tissue engineering approaches combine cells, biomaterials, and growth factors to recreate native bone tissue [1]. Traditionally, biochemical and histological assays are performed to monitor cell function and development in these engineered tissues. However, these techniques require sample processing and are destructive in nature, and therefore do not allow for an individual sample to be tracked as it develops. For example, traditional methods for characterizing cell number include manual counting chambers, automated cell counters, spectrophotometers, and flow cytometers [2-4]. These methods require a variety of sample processing steps including disruption of the tissue construct into constituents for counting (destructive in nature) and sample dilution. In addition, they may require specialized equipment and reagents that can be expensive. Importantly, most currently used measurement techniques describe only single timepoint, aggregate characteristics of the sample, and do not provide three dimensional (3D) spatial and temporal information.

Non-destructive approaches based on confocal microscopic imaging to count cell nuclei have been used to provide 3D assessment of cell numbers [5]. However, such techniques require high quality microscopy images, are time consuming, and involve complex processing algorithms to acquire entire spatially registered 3D images of the construct. Magnetic resonance imaging (MRI) and micro-computed tomography (μCT) techniques have been used to estimate

bone mineral densities [6, 7]. However, these methods require the use of calibration phantoms and involve long data acquisition times [8]. Long exposures to X-ray may affect cell-seeded constructs in terms of the structure, viability, and cellular development of the constructs. Conventional MRI imaging systems do not provide the ability to study the microstructural details of 3D engineered tissue constructs due to their low resolution. Therefore there is a need for non-destructive imaging and characterization modalities, capable of providing both spatial and temporal information of engineered tissues as they develop in vitro. Such methods would greatly facilitate the translation of tissue engineering products from the lab to the clinic.

Ultrasound imaging is a widely used non-invasive and non-destructive method that has the potential for quantitative evaluation of tissue development both in vitro and in vivo. It has been reported recently that ultrasound can be used to quantify cell number in BMSC/β-TCP composites using a grayscale equivalent parameter [9]. Fite et al. used an ultrasound method to monitor the chondrogenic differentiation of equine adipose stem cells in 3D poly(lactide-co-glycolide) scaffolds [10] by correlating signal attenuation measured through gray scale image analysis to extracellular matrix (ECM) deposition, which was considered to be a marker of cell differentiation. Kreitz et al. tracked collagen deposition by myofibroblasts in fibrin tissue constructs over an 18 day culture period [11]. Their quantitative analysis correlated observed gray scale values to ECM deposition as measured by hydroxyproline content. Ultrasound has also been used as a tool to measure the mechanical properties of agarose hydrogels as they develop over time [12], by correlating material properties such as elastic modulus with obtained acoustic properties.

Ultrasound propagation and acoustic scattering in a tissue volume depend on tissue microstructure, composition, and physical properties such as density and compressibility.

Therefore, backscattered ultrasound signals may be used to extract information about the structure and composition of the tissue under investigation, as well as its mechanical and physical properties. Although tissue properties such as speed of sound, acoustic attenuation and the tissue volume can be calculated directly from the backscattered radiofrequency (RF) data, tissue microstructural details are not apparent from the raw RF signals. Tunis et al. [13] studied the envelope statistics of ultrasound backscatter signals from cisplatin-treated aggregated acute myeloid leukemia (AML) cells and evaluated the applicability of various statistical distribution functions to model the envelope histograms. They reported that shape parameters of the generalized gamma distribution function were sensitive to structural changes within cells induced by the drug.

Quantitative ultrasound imaging methods using spectral analysis of the RF signals have been developed to extract additional parameters for enhanced tissue characterization. The power spectrum of the backscattered RF data includes information about tissue microstructure, and the spectral regression parameters can be related to scatterer properties such as effective sizes, concentrations and acoustic impedances [14, 15]. Spectral slope has been shown to depend on the scatterer size, whereas mid-band fit (MBF) relates to the size, concentration and relative acoustic impedances of the scattering elements [14]. Spectral analysis has been used in various applications, including characterization of plaque composition by intravascular ultrasound (IVUS) [16, 17], lesions induced by high intensity focused ultrasound (HIFU) [18, 19] and RF ablation [20]. Spectral parameters have also shown the ability to identify changes in tissue state for prostate, breast, pancreas, lymph node, and other cancer types [21-27]. Oelze et al. [22] developed methods to differentiate and characterize rat mammary fibroadenomas and 4T1 mouse

carcinomas by estimating scatterer properties from backscatter RF signals in the spectral domain with a Gaussian form factor model [28].

The use of high frequency (20 – 60 MHz) ultrasound imaging has provided higher spatial resolution than conventional ultrasound imaging (5 – 15 MHz) in diagnostic radiology [23]. Kolios et al. have developed spectral analysis technique to characterize the properties of cell aggregates that were used as simplified models of tumors [23, 29], to detect cellular changes with high spatial resolution and sensitivity after exposure to chemotherapy drug treatments [30]. They found that ultrasound backscatter intensity and spectral slope increased due to treatment, which was interpreted as a consequence of the decrease in effective scatterer size of cell aggregates. The use of higher ultrasound frequency imaging, with corresponding ultrasound wavelengths in the order of 100 μm, permits sensing of changes in cell nuclei and cell structure.
In order to achieve non-invasive and quantitative assessment of engineered tissue constructs with high spatial resolution, we have implemented a high frequency spectral ultrasound imaging (SUSI) technique, and have validated its use to characterize the composition and structure engineered tissue constructs. In previous work, we used the spectral MBF and slope parameters to measure the quantity and spatial distribution of particulate hydroxyapatite in acellular collagen hydrogels [31]. We observed a strong correlation between MBF and mineral concentration, and between the spectral slope and particle size. The amount of mineral deposited from simulated body fluid on acellular collagen constructs over a period of 3 weeks was also studied using spectral parameters, and showed strong correlation with MBF.

The work presented here extends our previous study using high resolution SUSI to quantitatively characterize the osteogenic differentiation of MC3T3 mouse pre-osteoblast cells seeded within 3D collagen-based engineered tissues. MC3T3 cells are a well characterized

mineralizing cell type that can be induced towards the osteogenic lineage with the addition of a defined set of supplements in the culture medium [32]. Collagen is a widely used biomaterial in orthopaedic tissue engineering due to its ability to support cell attachment and proliferation, as well as to serve as an osteoconductive and osteoinductive matrix [33]. In this study we non-destructively quantified the bulk properties of the hydrogels, including speed of sound, acoustic attenuation and volume compaction, and tracked these parameters over time. Microstructural properties of the cell-seeded constructs, including cell size, cell number, and cell differentiation, were also assessed using spectral ultrasound and were compared to data generated by traditional biochemical assays and confocal fluorescence imaging. This study demonstrates that SUSI can be used to non-destructively characterize cell-seeded engineered tissue constructs longitudinally over time with high spatial resolution.

E.2 Materials and Methods

Cell Culture

Mouse pre-osteoblast MC3T3-E1 (generously provided by Dr. R.T. Franchesci, University of Michigan) were cultured in α-MEM without ascorbic acid (Life Technologies, Grand Island, NY) supplemented with 10% fetal bovine serum (FBS; Life Technologies) and 1% penicillin and streptomycin (PS: Life Technologies) and used at passage 8. Media was changed every other day.

Collagen Hydrogel Synthesis

Three-dimensional (3D) collagen hydrogels were created as previously described [31]. Briefly, collagen type I (MP Biomedicals, Solon, OH) was prepared at 4.0 mg/ml in 0.02 N

acetic acid. Collagen hydrogels (2.0 mg/ml final concentration) were formed by mixing 10% Dulbecco's modified Eagle's medium (DMEM; Life Technologies), 10% FBS, 20% 5X-concentrated DMEM (stock concentration), 10% 0.1 N NaOH (Sigma Aldrich, St. Louis, MO), and 50% collagen stock solution. 500 μL of the mixture was then pipetted into a 24-well plate and allowed to gel for 30 mins at 37°C. Cells were encapsulated within the hydrogels at the time of gelation at a concentration of 1.0×10^6 cells/ml.

After gelation, hydrogels were moved into a 6-well culture plate containing α-MEM supplemented with 10% FBS and 1% PS to allow cells to compact their matrices. After 24 hours, the media was changed with either a control media or osteogenic media containing 10 mM beta-glycero phosphate (β-GP; Sigma) and 50 μg/ml ascorbic acid 2-phosphate (Sigma).

Cell Viability

Cell viability was visualized and quantified as previously described [34]. At days 1 and 21, cell-seeded hydrogels were washed 3X in phosphate buffered saline (PBS; Life Technologies) for 5 mins and then incubated in 4 μM calcein-AM (EMD Millipore, Billerica, MA) and 4 μM ethidium homodimer-1 (Sigma) in PBS for 45 mins. Constructs were washed 3X in PBS prior to imaging on a Nikon A1 Confocal Microscope (Nikon Instruments, Melville, NY). Cell viability was quantified using ImageJ software (National Institute of Health, Bethesda, MD).

Fluorescence Staining

At days 1 and 21, cells were stained for their actin cytoskeleton and nuclei. Hydrogels were washed 2X in PBS for 5 mins/wash and then fixed in zinc-buffered formalin (Z-Fix; Battle

Creek, MI) for 10 mins at 4°C. Gels were washed another 2X in PBS and then permeabilized using 0.5% Triton-X 100 (Sigma) in PBS for 20 mins at room temperature. Constructs were washed again 2X, and then incubated in a solution containing 165 nM AlexaFluor 488 phalloidin (Life Technologies) and 10 nM fluorescent DAPI (Life Technologies) in 1% bovine serum albumin (BSA; Sigma) in PBS for 45 mins. Hydrogels were washed again prior to imaging.

Biochemical Assays

Cellular DNA content and calcium were quantified as previously described [35]. For DNA quantification, hydrogels were collected and degraded overnight in 10 mM Tris-HCl (Sigma) containing 0.6 mg/mL collagenase type I (MP Biomedicals), 0.2% IGEPAL (Sigma), and 2 mM phenylmethanesulfonylfluoride (Sigma). DNA was then measured using the PicoGreen DNA assay (Life Technologies). Calcium secretion was assayed by first dissolving the constructs in 1 N acetic acid (Sigma) overnight. The cell-hydrogel lysate was then assayed using the ortho-cresolphthalein (OCPC) method [31].

Phantom Studies

Agar phantoms embedded with Polybead® microspheres (Polysciences, Inc., Warrington, PA) of different diameters at various concentrations were used to validate the size and concentration estimation from SUSI. Polybeads were added to the 2% agar solution at 45^0 C and thoroughly mixed to disperse them uniformly throughout the phantom. Four polybead diameters of interest were chosen: 6, 10, 16 and 25 μm. For each polybead size, phantoms with four different concentrations of polybeads were made. Each phantom was approximately 2000 mm^3 in size.

Ultrasound Imaging and Backscattered Signal Acquisition

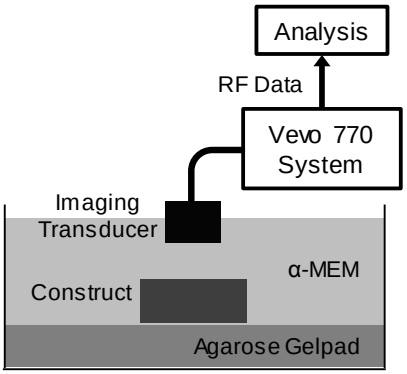

Figure E.1 – Schematic of experimental setup used for spectral ultrasound imaging (SUSI) of engineered tissue constructs.

Figure 1 shows a schematic diagram of the ultrasound imaging setup. A gel slab with 8% agarose (Sigma) was placed at the bottom of a 60 mm Petri dish to reduce ultrasound reflection from the bottom of the dish. The dish was then filled with α-MEM at room temperature and the constructs were placed on top of the agarose gel pad. Ultrasound imaging was performed using a Vevo 770 (VisualSonics Inc., Toronto, Canada) and an RMV 708 imaging probe with a nominal 55 MHz center frequency, 20 - 75 MHz bandwidth (−6 dB), 4.5 mm focal distance, and 1.5 mm depth of focus (− 6 dB). Ultrasound B-mode imaging was performed with the ultrasound beam focus placed 0.5 mm below the top surface of each sample. The interval between adjacent A-lines in the B-scans was set at 31 μm. 3D imaging of the construct was performed by acquiring a series of B-scans with 200 μm interval between adjacent scans across the tissue construct using a computer-controlled automatic translational stage. The 3D image data were used to estimate the volume of the construct. The backscattered radiofrequency (RF) signals of all ultrasound images were acquired at a sampling rate of 420 million samples/s. For estimating the speed of sound and acoustic attenuation of the construct, backscattered RF data with ultrasound focus placed at the gel pad surface were collected with and without the presence of a construct.

Ultrasound Imaging Analysis

1) Construct Volume: A semi-automated segmentation procedure and edge detection algorithm from the Vevo 770 system were used to detect the contour of the construct in a B-image. The volume of the construct was then calculated as the volume within the contours defined from each of B-mode images separated by 200 μm in 3D image data.

2) Speed of Sound in Construct: A grayscale parameter [31] was computed from the RF data of a B-scan. The time of travel of the ultrasound pulse from the imaging transducer to the construct top surface $\left(t_{top}\right)$, bottom surface $\left(t_{bottom}\right)$, and the agar gel pad surface $\left(t_{pad}^{construct}\right)$ was determined based on grayscale thresholding using an automated algorithm. The time of travel to the agar gel pad without the construct $\left(t_{pad}^{ref}\right)$ was also determined and used as the reference. Assuming the speed of sound in the surrounding fluid medium $\left(C_f\right)$ to be 1480 m/s, the thickness of the construct (L) was determined as

$$L = 0.5 C_f \left[\left(t_{bottom} - t_{top}\right) + \left(t_{pad}^{ref} - t_{pad}^{construct}\right)\right], \tag{1}$$

and speed of sound in the tissue construct $\left(C_{tc}\right)$ as

$$C_{tc} = \frac{2L}{t_{bottom} - t_{top}}. \tag{2}$$

3) Attenuation: Frequency dependent attenuation in dB/cm was calculated as:

$$\alpha\left(f\right)_{tc} = \frac{20}{2L}\log_{10}\frac{\left|A\left(f\right)\right|}{\left|A_0\left(f\right)\right|} \tag{3}$$

where $|A(f)|$ and $|A_0(f)|$ are the spectral magnitudes of the RF signal from the gel pad surface with and without (reference) the presence of construct respectively. The slope of α against f was

estimated by a linear fit between 20 - 55 MHz to yield the attenuation coefficient in the construct in dB/(cm-MHz).

SUSI analysis

1) Scatterer Size: The calibrated power spectrum of the RF signals for each A-line was obtained using linear regression to find the spectral parameters, i.e., the slope (*m'*) and the mid-band fit (*MBF'*) within a − 9 dB bandwidth [31]. The spectral parameters were corrected for the attenuation (α, dB/(cm-MHz)) of the tissue construct as $m=m'+2\alpha z$ and $MBF=MBF'+2\alpha z f_c$ where z is the ultrasound propagation distance in the tissue construct. Ultrasonic spectral parameters have been related to the system factors and the physical properties of effective acoustic scatterers in tissue [14]. As described previously [14], spectral slope represents a parameter associated with scatterer radius (a), its geometry (n) and the center frequency of the imaging transducer (f_c) and bandwidth (b), and is given by:

$$m = 26.06\frac{\left[b-\left(1-\frac{b^2}{4}\ln\left(\frac{2+b}{2-b}\right)\right)\right]}{b^3 f_c}n-\left(105.5\,f_c\right)a^2. \tag{4}$$

Thus, the scatterer radius can be calculated as:

$$a=\sqrt{0.25\frac{\left[b-\left(1-\frac{b^2}{4}\right)\ln\left(\frac{2+b}{2-b}\right)\right]}{b^3 f_c^2}n-\frac{m}{105.5\,f_c}}. \tag{5}$$

2) Acoustic Concentration: The spectral MBF depends on an additional parameter, the acoustic concentration (CQ^2),

$$MBF = 4.34\ln\left(Ea^{2(n-1)}CQ^2\right)+g_1\left(f_c,b\right)n+g_2\left(f_c,b\right)a^2, \tag{6a}$$

$$g_1(f_c,b)=4.34\left[\ln\left(f_c\left(1-\frac{b^2}{4}\right)^{1/2}\left(\frac{2+b}{2-b}\right)^{1/b}\right)-1\right], \tag{6b}$$

$$g_2(f_c,b)=-76.9\,f_c^2\left(3+\frac{b^2}{4}\right). \tag{6c}$$

where C is the number concentration of the acoustic scatterers (/mm^3), Q is the relative acoustic impedance, and E is a shape-dependent parameter. Eq. (6) can be rearranged to obtain C as

$$C=\frac{e^{0.23\left(MBF-g_1 n-g_2 a^2\right)}}{Ea^{2(n-1)}Q^2}. \tag{7}$$

The relative acoustic impedance, Q, of MC3T3 cells was estimated from a known number concentration, C, of cells in constructs.

3) Deposited calcium by cells: Differentiation of MC3T3 cells was assessed by detecting and quantifying the mass of the calcium deposited [36]. The mass of calcium at day 21 was calculated by comparing the relative acoustic impedance of the scatterers at day 0 to day 21. The relative acoustic impedance is defined as

$$Q_i=\frac{\rho_i c_i-\rho c}{\rho c}, \tag{8}$$

where ρ and ρ_i are the mass densities of the ECM and scatterers on the i^{th} day, c and c_i are the speed of sound in the ECM and scatterers on i^{th} day respectively. On day 21, the presence of deposited calcium around the cells will increase relative acoustic impedance of the scatterer. With known relative acoustic impedance of the scatterer on day 0 (cell alone without calcium) and day i (cell and calcium), the mass of secreted calcium can be calculated as (derivation in Appendix)

$$M_i^{cal}=N_i\rho c\left(\frac{V_i}{c_i}\left(1+Q_i\right)-\frac{V_0}{c_0}\left(1+Q_0\right)\right), \tag{9}$$

where N_i is the total number of cells on day i and V_i is the volume of the net scatterer on day i and is approximately $\frac{4}{3}\pi a_i^3$.

4) SUSI Parametric Images: The spatial distribution of scatterer features (scatter size and calcium concentration) within a construct was represented as parametric images where each pixel within a B-mode image was marked with a color that corresponded to the values of the scatterer size or calcium concentration.

Statistical Analysis

Analysis of the scatterer size and concentration was carried out in an element volume with dimensions of 0.6 mm x 5.0 mm x thickness (~1 mm) throughout the construct. Results are presented as mean ± standard deviation. Statistical comparisons between any two parameters were performed using Student's t-test for paired samples and the differences were considered significant at a level of $p < 0.05$.

E.3 Results

Validation of SUSI Estimation of Scatterer Size and Concentration

Verification of SUSI technique was performed using agarose phantoms embedded with polystyrene microspheres of known size and concentration. As shown in Supplemental Table SE.1, experiments were performed on phantoms with 4 different concentrations of Polybead® polystyrene microsphere (Polysciences Inc.) of different sizes (6, 10, 16 and 25 μm diameter). The SUSI method was able to detect the scatterer (polystyrene spheres) size and concentration in these phantoms, validating the SUSI estimation protocol. Additional validation of SUSI for estimation of cell size was performed using MC3T3-seeded engineered tissue constructs on day

0 with four known concentrations of cells (Supplemental Figure SE.1). Constructs with a known concentration of cells ($2x10^6$ cells/ml) were used to estimate the relative acoustic impedance of the MC3T3 cells via SUSI analysis, providing a value of approximately 0.6. SUSI was also used to estimate cell size, and the estimated cell diameter was approximately 14 μm (n = 9, range = ≈13.5-15.5 μm). The estimated diameter decreased slightly with increasing cell concentration (Figure S1E), possibly due to increased compaction of the constructs at higher cell concentration. The estimated relative acoustic impedance was then used to estimate the cell concentration of other constructs with prepared at different cell concentration (0.5, 1 and $5x10^6$ cells/ml) at day 0. These data are shown in Figures SE.1E, F, and show a good linear fit between the estimated concentration and the true concentration (R^2 = 0.92). These data confirmed the ability of SUSI to detect particle size and concentration in hydrogel constructs.

Virtual Histology for Longitudinal Monitoring of Tissue Constructs

Imaging using the Vevo 770 system at 55 MHz achieved rapid and non-invasive 3D ultrasound imaging of MC3T3-seeded collagen constructs. During ultrasound imaging, the constructs in α–MEM media were removed from the incubator for less than 20 minutes. Figure 2 shows an example of non-destructive longitudinal monitoring of the progression and development of cell seeded collagen constructs incubated in control and osteogenic media. The 3D rendered ultrasound images at different time-points (day 1, 7, 14 and 21) clearly show a reduction in the volume of the constructs over time ("gel compaction") in both control and osteogenic media. Constructs adopted a symmetrical concave shape from day 1, which is a typical result of cell-mediated gel compaction. In addition, constructs in osteogenic medium

became more echogenic than those in control medium, indicating changes occurring during development in osteogenic medium.

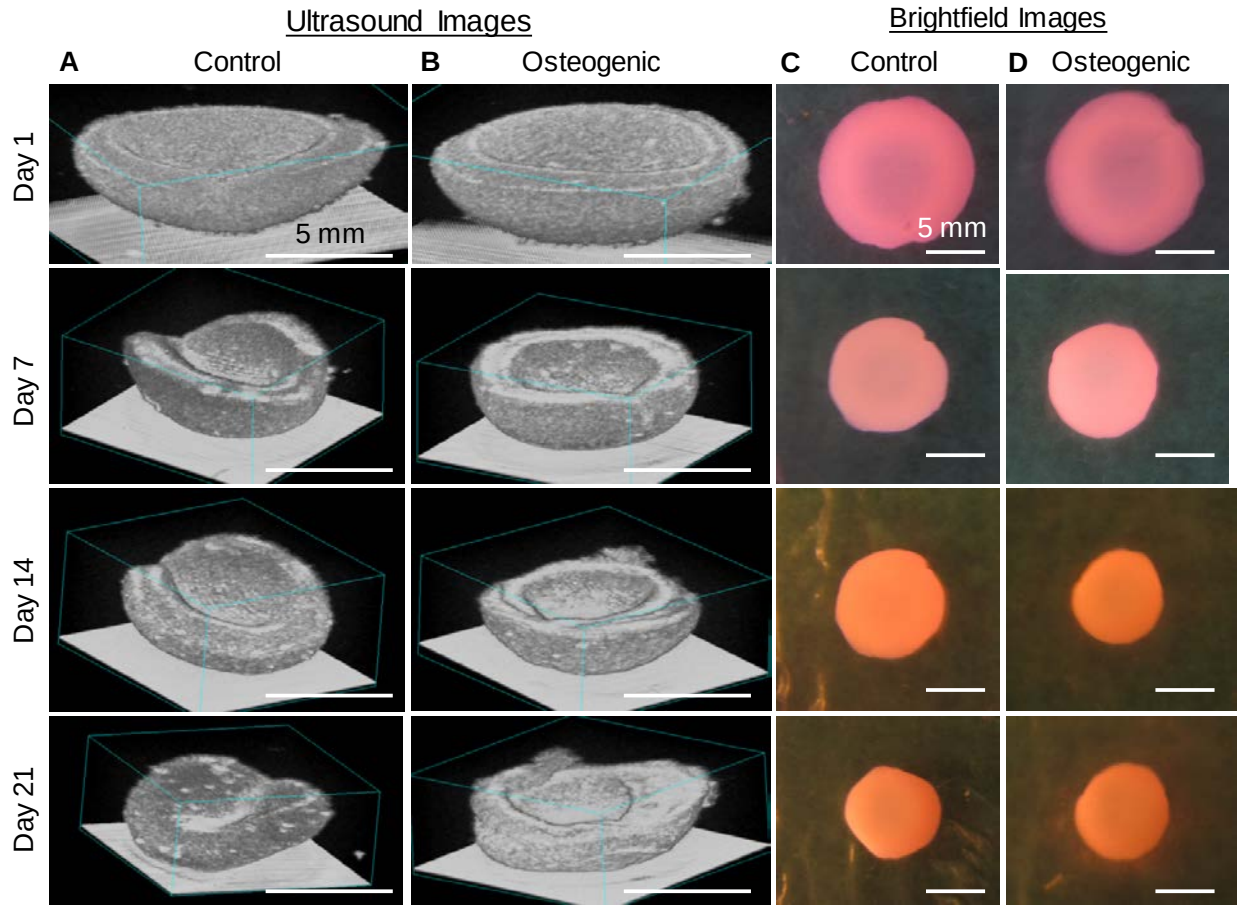

Figure E.2 – Longitudinal monitoring of MC3T3 cells seeded in collagen constructs. 3D rendered ultrasound backscattered images of the constructs in (A) control and (B) osteogenic media on day 1, 7, 14 and 21 of the development process. Brightfield images of corresponding constructs are shown in (C) and (D).

Cell viability in the constructs with and without ultrasound imaging was compared to assess possible effects of ultrasound imaging. As shown in Figure 3, viability was greater than 90% at day 1 in all of the samples and greater than 70% in all samples at day 21. There were no statistical differences between the samples with and without ultrasound imaging at either time point, indicating that exposure to ultrasound imaging did not affect cell viability.

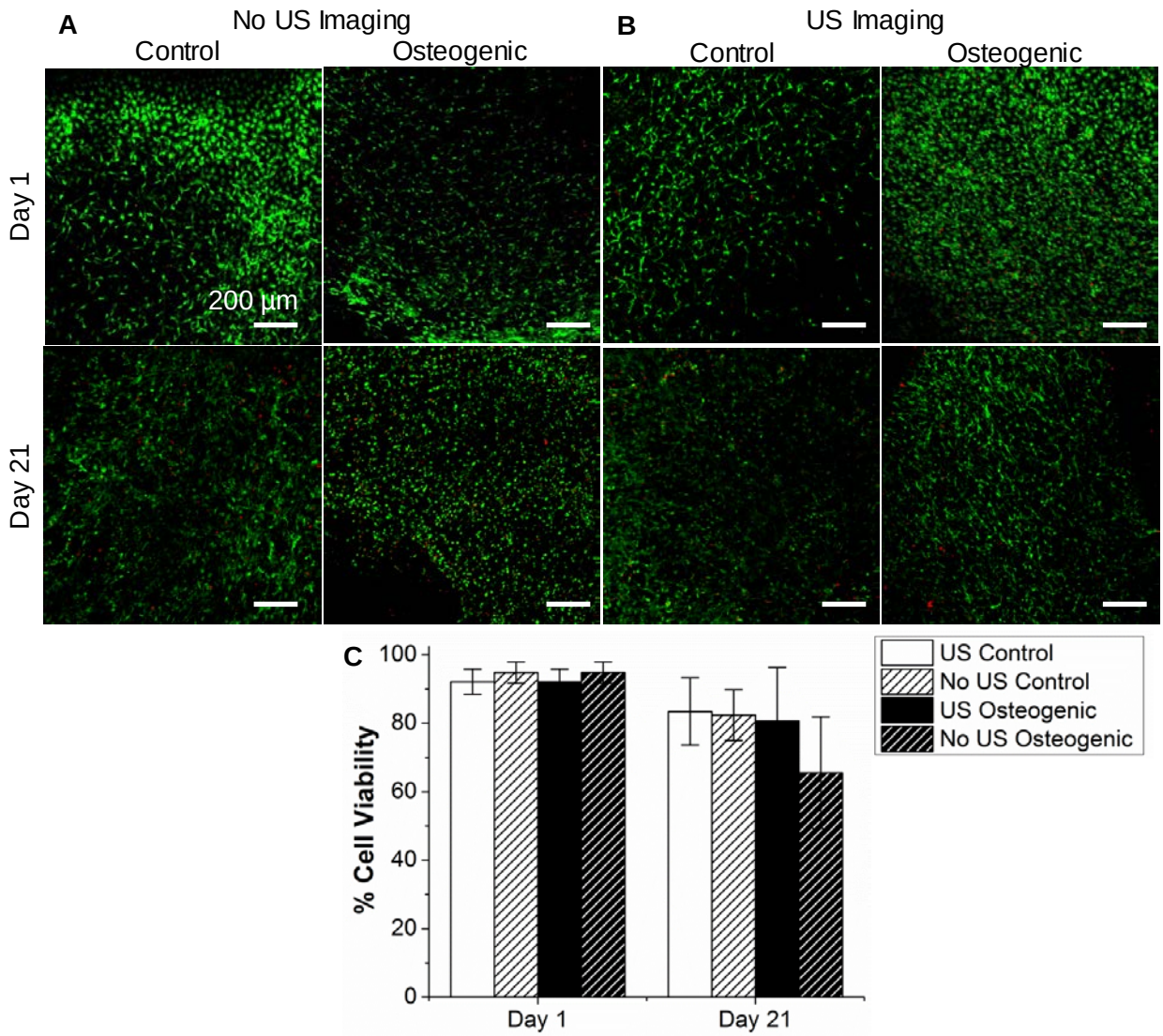

Figure E.3 – Comparison of cell viability at day 1 and 21 of MC3T3 cells seeded in collagen constructs. Constructs in (A) were not imaged using ultrasound, while those in (B) were imaged using ultrasound. Bar plot in (C) shows quantification of cell viability calculated from the images. Scale bar = 200 µm.

Measurement of Construct Volume, Speed of Sound, and Acoustic Attenuation

As shown in Figure 4, a significant decrease in construct volume to about 25-30% of the original volume occurred between days 1 and 7, and the construct volume then stabilized between days 7 and 21. No statistically significant differences in construct volumes were detected between control and osteogenic media at any of the time-points. There was a slight

increase and then plateau in the speed of sound over development time for constructs in both control and osteogenic media. The acoustic attenuation parameter increased almost linearly over development time in culture, with no significant differences between constructs in control and osteogenic media. Since the acoustic attenuation is typically an indicator of increased acoustic impedance and/or scatterer concentration, this increase may indicate cell proliferation and/or mineral deposition. These results of construct volume, speed of sound, and acoustic attenuation were used in further analysis of the constructs including estimation of spectral parameters and calcium deposits by the differentiated cell constructs in osteogenic media.

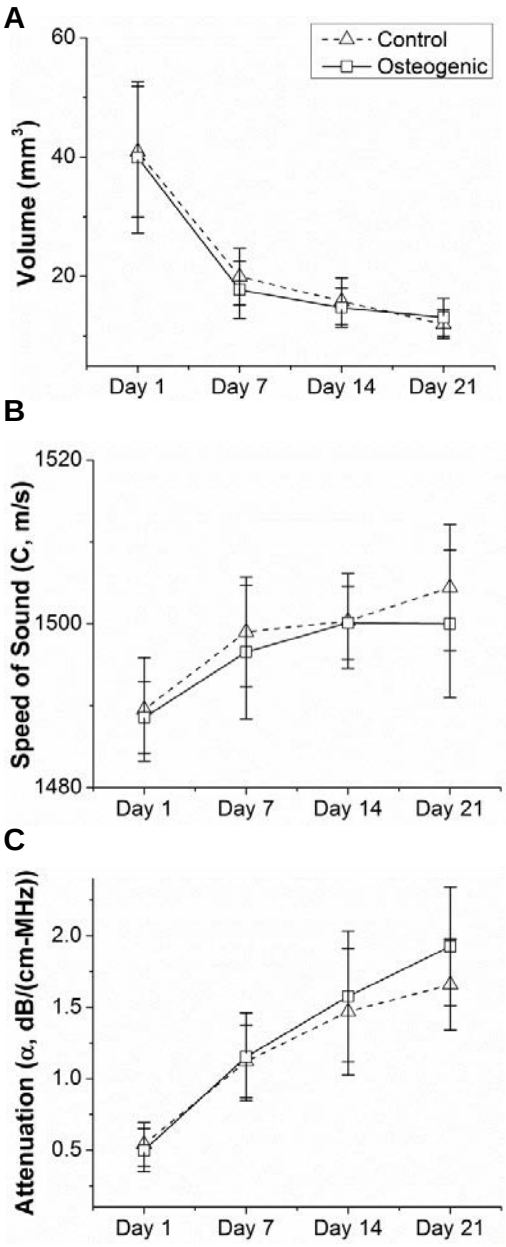

Figure E.4 – Backscatter analysis of MC3T3-seeded constructs in control and osteogenic media over time in culture. Quantification of (A) construct volume, (B) speed of sound, and (C) attenuation at each time-point.

SUSI analysis of Size of Cells or Scatterers in Constructs

Figure 5A-D shows the seeded MC3T3 cells in the collagen hydrogels with the F-actin filaments stained in green and cell nuclei stained in blue. From these images, diameters of the cell nuclei were estimated using a customized MATLAB script to be 6.0 ± 1.0 μm (n = 4) on day

1 and 7.6 ± 1.9 μm (n = 4) on day 21; these values are not statistically different. The effective size of the cells over the three week period was also estimated using the slope parameter obtained from SUSI analysis (Figure 5E). The average diameter for the cells, was approximately 14 μm with a range from about 12-15 μm, and remained essentially unchanged during the three week culture period for constructs in both control and osteogenic media. The significantly higher estimate value for scatterer diameter from SUSI compared to nucleus diameter measurement from DAPI stain suggest that the entire cell may have involved in the scattering of ultrasound, not merely cell nucleus.

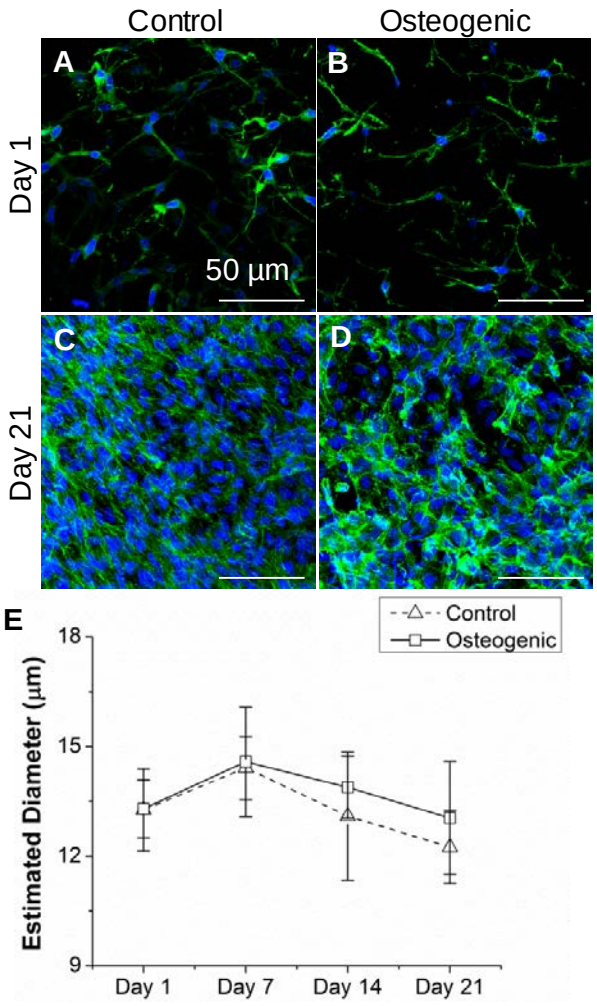

Figure E.5 – Developmental changes in sizes of MC3T3 cells seeded in collagen constructs. (A)-(D) Fluorescence staining of MC3T3 cells embedded in collagen constructs in control and osteogenic media on day 1 and day 21 (actin cytoskeleton is stained green, nuclei are stained blue). (E) Estimated diameter of cells from SUSI analysis over time in culture. Scale bar = 50 µm.

Acoustic Concentration and Calcium Deposition in Constructs

The total amount of DNA in a construct was measured biochemically and converted to the total number of cells by determining the average amount of DNA per cell on a construct at day 0, when the number of cells was known ($0.5x10^6$ cells/construct). As shown in Figure 6A, the number of cells decreased by about 60% from day 1 to day 7 in constructs in both the control and osteogenic groups, indicating probable cell death or migration out of the constructs. Thereafter the number of cells remained constant from days 7 to 21 with no significant

differences between or within media groups. These cell numbers correlated well with the equivalent number of acoustic scatterers, which is the acoustic concentration (CQ^2) estimated by SUSI analysis multiplied by the construct volume, with the exception of the day 21 measurement in the osteogenic group (Figure 6B). The acoustic concentration from SUSI depends on both the relative acoustic impedance of the scatterers (Q) and the actual number of scatterers (C). Thus assuming the actual number of scatterers or cells remained constant, the increased equivalent number of acoustic scatterers (or increased acoustic concentration) can be attributed to an increase of the relative acoustic impedance of the scatterers during the last days of incubation of the constructs (Figure 6C). The significantly increased acoustic impedance on day 21 may therefore be indicative of changes due to the differentiation process in the constructs. Since acoustic impedance depends on the mass density and the speed of sound in scatterers, the increased acoustic impedance may reflect an increase in mass density due to calcium deposition associated with cell differentiation. As calcium is much denser than water, its presence is expected to significantly increase the relative acoustic impedance of the scatterers.

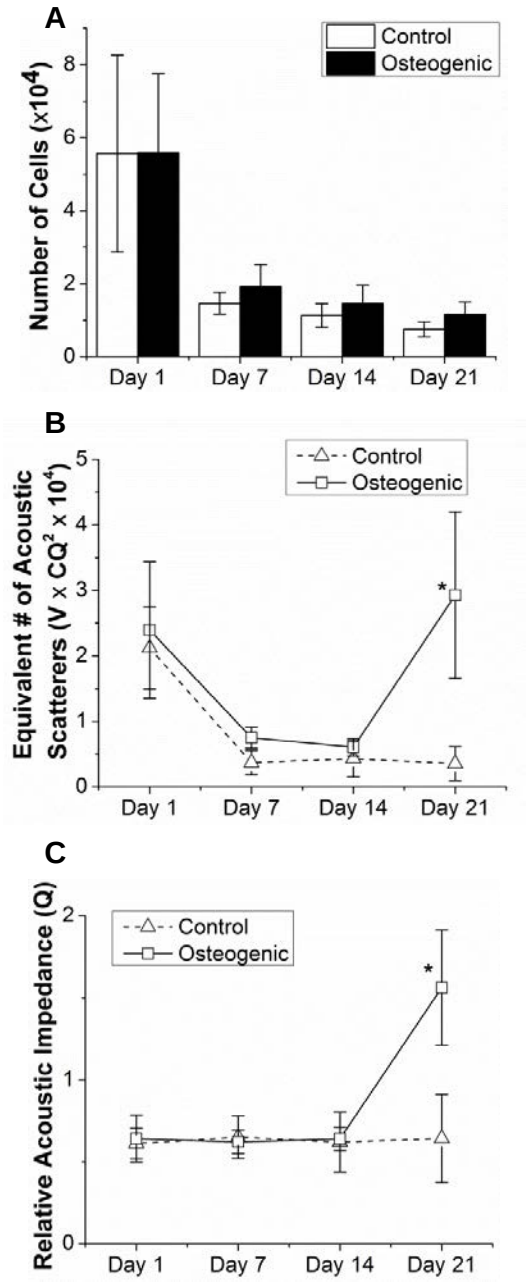

Figure E.6 – Quantified development of MC3T3 cells seeded in collagen constructs (A) Total number of cells as assessed by DNA quantification of MC3T3-seeded collagen constructs in control and osteogenic media over time in culture. (B) Equivalent number of acoustic scatterers as estimated from SUSI analysis. (C) Relative acoustic impedance estimated from (A) and (B).

As a quantitative marker to identify the extent of osteogenic differentiation of seeded MC3T3 cells [36], we estimated the calcium content using both standard biochemical assays (OCPC method) and SUSI. The estimated calcium concentration from SUSI on day 21 was 41.7

± 11.4 µg/ml (n = 9) and was comparable with the measured values of 38.7 ± 16.7 µg/ml (n = 10) from the OCPC method. No statistically significant difference in calcium deposition at day 21 was detected in constructs subjected to ultrasound imaging and those without ultrasound imaging performed (Figure 7B).

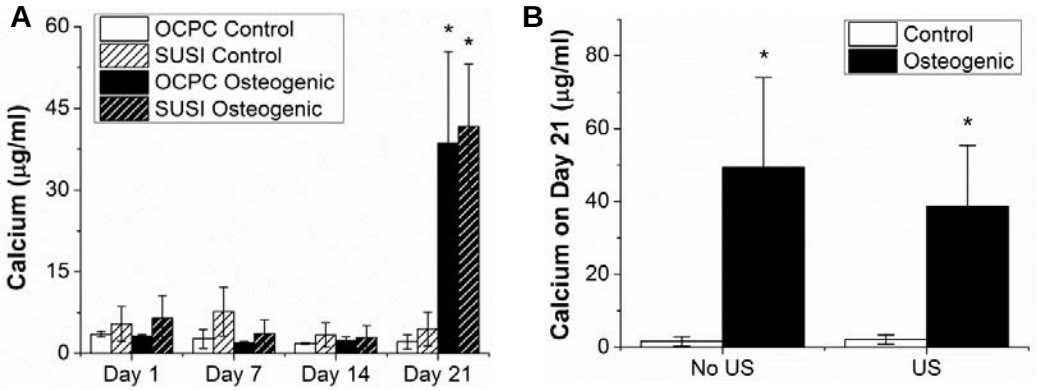

Figure E.7 – Amount of calcium mineral secreted by MC3T3-seeded collagen constructs in control and osteogenic media. (A) Calcium content as determined by OCPC assay and SUSI estimation. (B) Comparison of calcium content between constructs cultured in control and osteogenic media with and without exposure to ultrasound imaging.

Spatiotemporal Evolution of Constructs by Parametric Ultrasound Imaging

The estimated microstructural properties (acoustic scatterer size and secreted calcium concentration) from SUSI analysis were used to generate parametric, color coded images overlaid on B-mode images, allowing visual assessment of the spatiotemporal evolution of constructs during development. As an example, Figure 8 shows the estimated microstructural parameters in a representative region of interest for constructs in control and osteogenic groups throughout the 21 day culture period. Scatterer diameter was uniform within the construct, and did not vary significantly during the development process for constructs in either control or osteogenic medium (Figure 8A). The estimated calcium concentration was relatively constant at low values at all time-points to day 14, but exhibited a significantly higher value in the

constructs in osteogentic medium on day 21. The increase in calcium content is indicative of osteogenic differentiation of MC3T3 cells in the constructs.

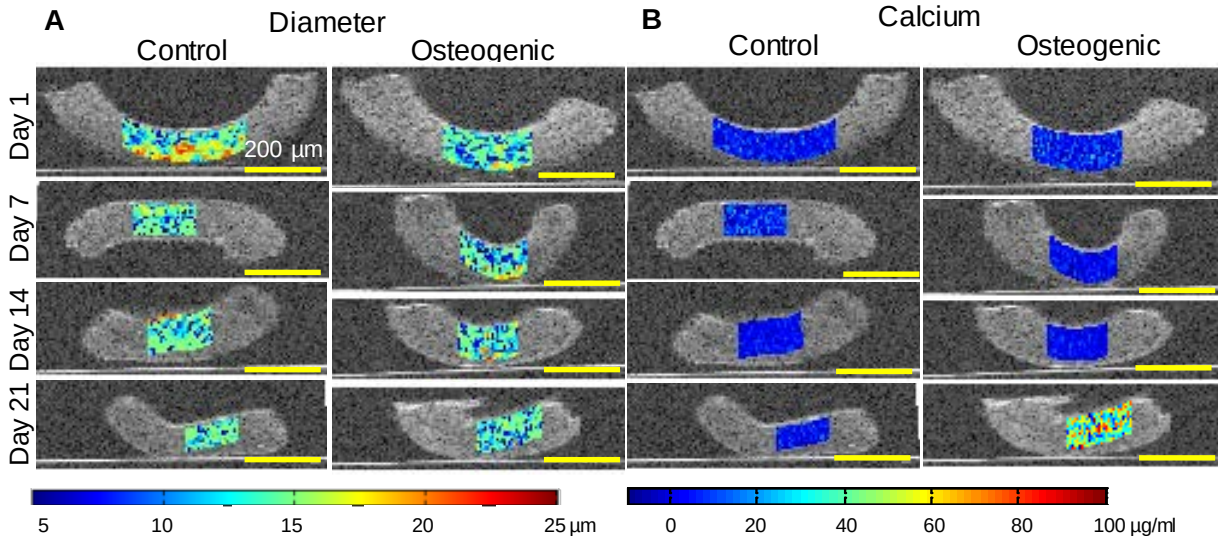

Figure E.8 – Overlaid B-mode (grayscale) and color maps of SUSI parameters. (A) Cell diameter, and (B) mass of calcium deposition of MC3T3 cells embedded in collagen constructs in control and osteogenic media.

E.4 Discussion

In this study, we demonstrated that high resolution ultrasound imaging provided non-destructive monitoring of MC3T3-seeded collagen constructs over 3 weeks. Physical parameters including the volume of each individual construct, speed of sound and acoustic attenuation in the constructs were obtained from simple analysis of the ultrasound RF signals. Notably, SUSI analysis provided estimation and assessment of key microstructural characteristics of the constructs, beyond what can be generated by conventional ultrasound images. These parameters included cell size, acoustic scatterer concentration, cell number, and mineral deposition. Since system-dependent factors are removed from SUSI analysis by calibration, the parameters provided are objective and instrument-independent. Therefore such data have broad utility and are particularly useful for inter-study comparisons. These features make ultrasound imaging and particularly SUSI a very attractive tool for biomaterials and tissue engineering research, and as a

tool in quality assurance as engineered tissues approach the market. Below we discuss implications of our results and limitation of this study.

When embedded in 3D collagen hydrogels, many cell types including fibroblasts, smooth muscle cells, cardiomyocytes and osteoblasts, will remodel the collagen by exerting contractile forces that can align and compact the matrix [37]. These forces are significantly higher than the forces required for cell locomotion and it has been proposed that this force generation is targeted at matrix remodeling, rather than cell migration [38, 39]. This morphogenic phenomenon has been studied widely, and the mechanisms are still not fully understood. Assessment of tissue construct morphology in 3D in a non-invasive method is important to study these changes, and to quantitatively characterize the degree of remodeling. In this study, we showed that high resolution 3D ultrasound imaging could be used to noninvasively track morphological changes in tissue constructs longitudinally, revealing the significant compaction of unconstrained MC3T3-seeded constructs from day 1 to day 7.

We showed that ultrasound imaging provides non-destructive monitoring without affecting the structure or function of the constructs. Cell diameter as determined by SUSI was in the range of 12.5-15.5 μm, which matched the size determined by parallel fluorescent confocal imaging. SUSI analysis also revealed that the total number of acoustic scatterers in unconstrained MC3T3-seeded collagen constructs decreased by approximately 80% over the 21 day culture period in control medium. This result was in agreement with destructive biochemical DNA measurement performed in parallel. The decrease in cell number may have been a result of cell death or migration from the construct, possibly as a result of the decrease in construct volume that resulted from gel compaction. A similar pattern in cell number was observed in a previous

study of unconstrained constructs seeded with undifferentiated mesenchymal stem cells (MSC) [40].

The acoustic concentration is defined as CQ^2, where C is the number concentration of the scatterers and Q the acoustic impedance of the scatterers. The parameter Q depends on the physical and acoustic properties of the scatterer, particularly the mass density and speed of sound. Therefore assessment of the total number of acoustic scatterers (CQ^2 multiplied by construct volume) can provide information regarding changes in the construct microstructure. MC3T3 cells secrete mineral into the surrounding matrix as they undergo osteogenic differentiation [36]. They thereby modify the properties of the acoustic scatterers in the construct by increasing their mass density and thus the relative acoustic impedance. Therefore, relative acoustic impedance can be used as an indicator of changes in cellular state during osteogenic differentiation. In the current study, we qualitatively characterized the differentiation process by monitoring changes in the relative acoustic impedance, and also generated quantitative values of the mass of calcium deposited based on the relative acoustic impedance values. These data matched well with parallel measurement from conventional destructive biochemical tests for calcium content. We therefore have demonstrated that ultrasound imaging can be used to estimate the mass of calcium mineral in 3D collagen constructs as MC3T3 cells differentiate in osteogenic medium.

The current study highlights the advantages of high frequency ultrasound imaging for monitoring of tissue construct development. The use of a high frequency in our study provided high spatial resolution, which allowed detailed characterization of the constructs *in vitro*. However, most *in vivo* and eventual clinical applications will require the use of lower frequency imaging (e.g. 10 MHz) to allow deeper tissue penetration, which will reduce the resolution of the

images. Another limitation of our current method is that our estimation of the relative acoustic impedance in this study required knowledge of the number of cells, which may not be readily available non-destructively. Relative changes to the acoustic concentration, a composite parameter that is obtained directly from SUSI analysis, can be used to noninvasively assess relative changes in the constructs. However, at this stage we are not able to use this parameter to generative an absolute quantitative estimation of calcium deposition without knowledge of the cell number. We assumed that cells and the calcium they deposited were a single scatterer, however future work will examine the ability to resolve different cell types and matrix components using SUSI.

E.5 Supplemental Information, Figures and Tables

The relative acoustic impedance (Q) of the scatterers in the construct on day i is

$$Q_i = \frac{\rho_i c_i - \rho c}{\rho c} \tag{A1}$$

where ρ_i and ρ are the densities of the scatterer and extracellular matrix (ECM), c_i and c are the speed of sound in the scatterer and ECM respectively. Rewriting the expression for density of the net scatterer,

$$\rho_i = \frac{\rho c}{c_i}\left(1 + Q_i\right) \tag{A2}$$

The density of the net scatterer can also be calculated from its total mass and volume. On any specific developmental time-point of the construct, the net scatterer is considered to be a cell along with any secreted calcium mineral. Thus, the total mass of the net scatterer on day i is the sum of the masses of a cell on day 0 and secreted mineral on day i.

$$\rho_i = \frac{V_0\rho_0 + m_i^{cal}}{V_i} \tag{A3}$$

After rearranging the expression for mass of the mineral secreted by each cell, the total mass of calcium on day *i* can be obtained.

$$M_i^{cal} = N_i m_i^{cal} = N_i\left(V_i\rho_i - V_0\rho_0\right) \tag{A4}$$

$$M_i^{cal} = N_i\rho c\left(\frac{V_i}{c_i}\left(1+Q_i\right) - \frac{V_0}{c_0}\left(1+Q_0\right)\right) \tag{A5}$$

where N_i is the total number of cells on day *i* and V_i is the volume of the net scatterer on day *i* which is approximately $\frac{4}{3}\pi a_i^3$.

Size (µm)		**Concentration (x10^4 beads/mm^3)**							
		6 µm		**10 µm**		**16 µm**		**25 µm**	
True	**Est**	**True**	**Est**	**True**	**Est**	**True**	**Est**	**True**	**Est**
6	6.4 ± 0.2	7.1	6.2±0.2	1.4	1.1±0.2	0.6	0.4±0.1	0.22	0.13±0.04
10	10.1 ± 0.6	9.7	9.4±0.4	2.7	2.5±0.4	0.8	0.7±0.2	0.40	0.36±0.08
16	13.4± 1.1	15.4	16.6±0.8	3.9	4.4±0.8	1.5	1.6±0.3	0.52	0.56±0.11
25	24.7 ± 0.2	21.9	23.1±1.4	5.0	5.5±1.1	2.3	2.5±0.5	0.62	0.71±0.15

Supplemental Table E.1 – Tabular values of estimated Polybead® polystyrene microsphere (Polysciences Inc.) bead size and concentration and comparison with their true values.

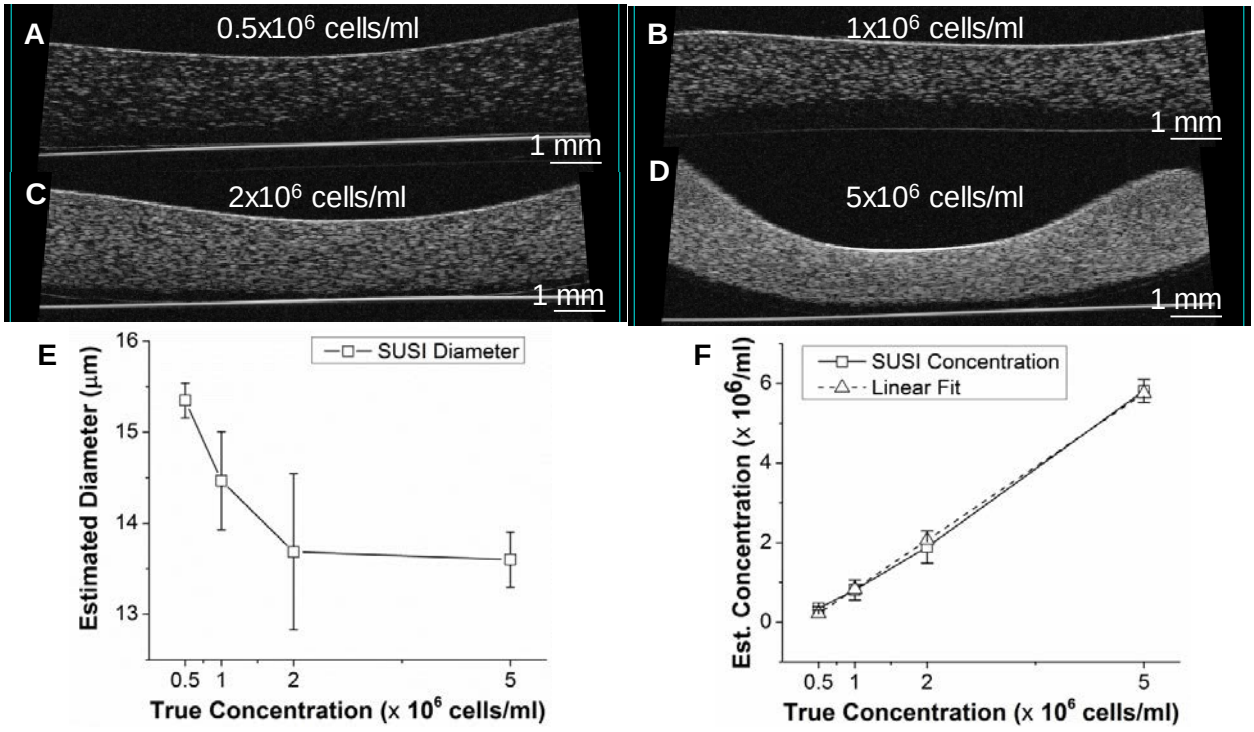

Supplemental Figure E.1 – Experiment for estimation of relative acoustic impedance of MC3T3 cells on day 0 and validation of estimated cell concentration from SUSI analysis. (A)-(D) Ultrasound B-mode (grayscale) images of MC3T3-seeded collagen constructs on Day 0 at 0.5, 1, 2 and 5 x106 cells/ml cell concentrations, respectively. (E) Cell diameter, and (F) cell concentration estimated from SUSI analysis and compared to seeded cell concentration at day 0.

E.6 References

1. Langer R, Vacanti JP. Tissue engineering. Science 260, 920, 1993.

2. Yang SY, Hsiung SK, Hung YC, Chang CM, Liao TL, Lee GB. A cell counting/sorting system incorporated with a microfabricated flow cytometer chip. Meas. Sci. Technol 17, 2001, 2006.

3. Oliver MH, Harrison NK, Bishop JE, Cole PJ, Laurent GJ. A rapid and convenient assay for counting cells cultured in microwell plates: application for assessment of growth factors. J Cell Sci 92, 513, 1989.

4. Butler WB. Preparing nuclei from cells in monolayer cultures suitable for counting and for following synchronized cells through the cell cycle. Anal Biochem 141, 70, 1984.

5. Han JW, Breckon TP, Randell DA, Landini G. The application of support vector machine classification to detect cell nuclei for automated microscopy. Machine Vision and Applications 23, 15, 2012.

6. Ho KY, Hu HH, Keyak JH, Colletti PM, Powers CM. Measuring bone mineral density with fat-water MRI: comparison with computed tomography. J Magn Reson Imaging 37, 237, 2013.

7. Nazarian A, Snyder BD, Zurakowski D, Müller R. Quantitative micro-computed tomography: A non-invasive method to assess equivalent bone mineral density. Bone 43, 302, 2008.

8. Jones AC, Milthorpe B, Averdunk H, Limaye A, Senden TJ, et al. Analysis of 3D bone ingrowth into polymer scaffolds via micro-computed tomography imaging. Biomaterials 25, 4947, 2004.

9. Oe K, Miwa M, Nagamune K, Sakai Y, Lee SY, et al. Nondestructive evaluation of cell numbers in bone marrow stromal cell/beta-tricalcium phosphate composites using ultrasound. Tissue Eng Part C Methods 16, 347, 2010.

10. Fite BZ, Decaris M, Sun Y, Sun Y, Lam A, Ho CK, et al. Noninvasive multimodal evaluation of bioengineered cartilage constructs combining time-resolved fluorescence and ultrasound imaging. Tissue Eng Part C Methods 17, 495, 2011.

11. Kreitz S, Dohmen G, Hasken S, Schmitz-Rode T, Mela P, Jockenhoevel S. Nondestructive method to evaluate the collagen content of fibrin-based tissue engineered structures via ultrasound. Tissue Eng Part C Methods 17, 1021, 2011.

12. Walker JM, Myers AM, Schluchter MD, Goldberg VM, Caplan AI, et al. Nondestructive evaluation of hydrogel mechanical properties using ultrasound. Ann Biomed Eng 39, 2521, 2011.

13. Tunis AS, Czarnota GJ, Giles A, Sherar MD, Hunt JW, Kolios MC. Monitoring structural changes in cells with high-frequency ultrasound signal statistics. Ultrasound Med Biol 31, 1041, 2005.

14. Lizzi FL, Ostromogilsky M, Feleppa EJ, Rorke MC, Yaremko MM. Relationship of ultrasonic spectral parameters to features of tissue microstructure. IEEE Trans Ultrason Ferroelectr Freq Control 34, 319, 1987.

15. Lizzi FL, Astor M, Liu T, Deng C, Coleman DJ, Silverman RH. Ultrasonic spectrum analysis for tissue assays and therapy evaluation. Intl J Imaging Sys Tech 8, 3, 1997.

16. Nair A, Kuban BD, Tuzcu EM, Schoenhagen P, Nissen SE, Vince DG. Coronary plaque classification with intravascular ultrasound radiofrequency data analysis. Circulation 106, 2200, 2002.

17. Qian J, Maehara A, Mintz GS, Margolis MP, Lerman A, et al. Impact of Gender and Age on In Vivo Virtual Histology-Intravascular Ultrasound Imaging Plaque Characterization (from the global Virtual Histology Intravascular Ultrasound [VH-IVUS] Registry). Am J Cardiol 103, 1210, 2009.

18. Gudur MS, Kumon RE, Zhou Y, Deng CX. High-Frequency Rapid B-Mode Ultrasound Imaging for Real-Time Monitoring of Lesion Formation and Gas Body Activity During High-Intensity Focused Ultrasound Ablation. IEEE Trans Ultrason Ferroelectr Freq Control 59, 1687, 2012.

19. Kumon RE, Gudur MS, Zhou Y, Deng CX. High-Frequency Ultrasound M-Mode Imaging for Identifying Lesion and Bubble Activity during High-Intensity Focused Ultrasound Ablation. Ultrasound Med Biol 38, 626, 2012.

20. Siebers S, Schwabe M, Scheipers U, Welp C, Werner J, Ermert H. Evaluation of ultrasonic texture and spectral parameters for coagulated tissue characterization. IEEE Ultrasonics Symposium 1-3, 1804, 2004.

21. Feleppa EJ. Ultrasonic tissue-type imaging of the prostate: Implications for biopsy and treatment guidance. Cancer Biomark 4, 201, 2008.

22. Oelze ML, O'Brien WD Jr, Blue JP, Zachary JF. Differentiation and characterization of rat mammary fibroadenomas and 4T1 mouse carcinomas using quantitative ultrasound imaging. IEEE Trans Med Imaging 23, 764, 2004.

23. Vlad RM, Alajez NM, Giles A, Kolios MC, Czarnota GJ. Quantitative Ultrasound Characterization of Cancer Radiotherapy Effects in Vitro. Int J Radiat Oncol Biol Phys 72, 1236, 2008.

24. Lizzi FL. Ultrasonic scatterer property images of the eye and prostate. IEE Ultrasonics Symposium Proceedings 1 & 2, 1109, 1997.

25. Lizzi FL, Feleppa EJ, Alam SK, Deng CX. Ultrasonic spectrum analysis for tissue evaluation. Pattern Recognition Letters 24, 637, 2003.

26. Kumon RE, Repaka A, Atkinson M, Faulx AL, Wong RC, et al. Characterization of the pancreas in vivo using EUS spectrum analysis with electronic array echoendoscopes. Gastrointest Endosc 75, 1175, 2012.

27. Kumon RE, Deng CX, Wang X. Frequency-Domain Analysis of Photoacoustic Imaging Data from Prostate Adenocarcinoma Tumors in a Murine Model. Ultrasound Med Biol 37, 834, 2011.

28. Insana MF, Wagner RF, Brown DG, Hall TJ. Describing Small-Scale Structure in Random-Media Using Pulse-Echo Ultrasound. J Acoust Soc Am 87, 179, 1990.

29. Kolios MC, Czarnota GJ, Lee M, Hunt JW, Sherar MD. Ultrasonic spectral parameter characterization of apoptosis. Ultrasound Med Biol 28, 589, 2002.

30. Czarnota GJ, Kolios MC, Abraham J, Portnoy M, Ottensmeyer FP et al. Ultrasound imaging of apoptosis: high-resolution non-invasive monitoring of programmed cell death in vitro, in situ and in vivo. Br J Cancer 81, 520, 1999.

31. Gudur M, Rao RR, Hsiao YS, Peterson AW, Deng CX, Stegemann JP. Noninvasive, Quantitative, Spatiotemporal Characterization of Mineralization in Three-Dimensional Collagen Hydrogels Using High-Resolution Spectral Ultrasound Imaging. Tissue Eng Part C Methods 18, 935, 2012.

32. Czekanska EM, Stoddart MJ, Richards RG, Hayes JS. In Search of an Osteoblast Cell Model for in Vitro Research. Eur Cell Mater 24, 1, 2012.

33. Al-Munajjed AA, Plunkett NA, Gleeson JP, Weber T, Jungreuthmayer C, et al. Development of a Biomimetic Collagen-Hydroxyapatite Scaffold for Bone Tissue Engineering Using a SBF Immersion Technique. J Biomed Mater Res B Appl Biomater 90B, 584, 2009.

34. Rao RR, Peterson AW, Ceccarelli J, Putnam AJ, Stegemann JP. Matrix composition regulates three-dimensional network formation by endothelial cells and mesenchymal stem cells in collagen/fibrin materials. Angiogenesis 15, 253, 2012.

35. Rao RR, Peterson AW, Stegemann JP. Osteogenic differentiation of adipose-derived and marrow-derived mesenchymal stem cells in modular protein/ceramic microbeads. J Biomed Mater Res A 101, 1531, 2013.

36. Declercq HA, Verbeeck RM, De Ridder LI, Schacht EH, Cornelissen MJ. Calcification as an indicator of osteoinductive capacity of biomaterials in osteoblastic cell cultures. Biomaterials 26, 4964, 2005.

37. Wakatsuki T, Elson EL. Reciprocal interactions between cells and extracellular matrix during remodeling of tissue constructs. Biophys Chem 100, 593, 2003.

38. Dembo M, Wang YL. Stresses at the cell-to-substrate interface during locomotion of fibroblasts. Biophys J 76, 2307, 1999.

39. Galbraith CG, Sheetz MP. A micromachined device provides a new bend on fibroblast traction forces. Proc Natl Acad Sci U S A 94, 9114, 1997.

40. Zscharnack M, Hepp P, Richter R, Aigner T, Schulz R, et al. Repair of Chronic Osteochondral Defects Using Predifferentiated Mesenchymal Stem Cells in an Ovine Model. Am J Sports Med 38, 1857, 2010.

APPENDIX F

Publications and Presentations

Peer-reviewed articles:

1. **Rao RR**, Vigen ML, Peterson AW, Caldwell DJ, Putnam AJ, Stegemann JP. "Dual-Phase Osteogenic and Vasculogenic Engineered Tissue for Bone Formation." *Tissue Engineering: Part A* (accepted, in press)

2. **Rao RR**, Stegemann JP. "Cell-Based Approaches to the Engineering of Vascularized Bone Tissue." *Cytotherapy* (accepted, in press)

3. Wang L, **Rao RR**, Stegemann JP. "Matrix-Enhanced Stem Cells Embedded in Chitosan-Collagen Microbeads." *Cells, Tissues, Organs* Apr 3:333-343. 2013.

4. **Rao RR**, Peterson AW, Stegemann JP. "Osteogenic potential of ASC and MSC in protein/ceramic microenvironments." *Journal of Biomedical Research Part A* Jun;101(6):1531-8. 2013.

5. Caldwell DC, **Rao RR**, Stegemann JP. "Assembly of Discrete Collagen-Chitosan Microenvironments into Multiphase Tissue Constructs." *Advanced Healthcare Materials* May;2(5):673-7. 2013.

6. Saito E, Suarez-Gonzalez D, **Rao RR**, Stegemann JP, Murphy WL, Hollister SJ. "Use of Micro-Computed Tomography to Non-destructively Characterize Biomineral Coatings on Solid Freeform Fabricated Poly (L-lactic acid) and Poly (ε-caprolactone) Scaffolds *In Vitro* and *In Vivo*." *Tissue Engineering: Part C* (accepted, in press)

7. Gudur MS,* **Rao RR**,* Hsiao YS, Peterson AW, Deng CX, Stegemann JP. "Non-Invasive Quantitative Spatiotemporal Characterization of Mineralization in 3D Collagen Hydrogels Using High Resolution Spectral Ultrasound Imaging." *Tissue Engineering: Part C* Dec; 18(12): 935-946. 2012.

8. **Rao RR**, Peterson AW, Ceccarelli J, Putnam AJ, Stegemann JP. "Matrix Composition Regulates Network Formation by Endothelial Cells and Mesenchymal Stem Cells in 3D Collagen/Fibrin Materials" *Angiogenesis* Jun;15(2):253-64. 2012.

9. **Rao RR,** Jiao A, Kohn DH, Stegemann JP. "Exogenous Mineralization of Cell-Seeded and Unseeded Collagen-Chitosan Hydrogels using Modified Culture Medium." *Acta Biomaterialia* Apr; 8(4): 1560-1565. 2012

*Authors contributed equally to this work.

Presentations (presenter is underlined)

1. Rao RR, Vigen ML, Peterson AW, Caldwell DJ, Putnam AJ, Stegemann JP. "Dual-Phase Osteogenic and Vasculogenic Engineered Tissue for Bone Formation." *Tissue Engineering and Regenerative Medicine International Society (TERMIS) – North America Annual Meeting,* Atlanta, GA, November 2013.

2. Gudur MS, Rao RR, Peterson AW, Hsiao YS, Caldwell DJ, Deng CX, Stegemann JP. "Nondestructive Evaluation of Mineralization and Osteoblast Phenotype in Engineered Tissues using Spectral Ultrasound Imaging." *Tissue Engineering and Regenerative Medicine International Society (TERMIS) – North America Annual Meeting,* Atlanta, GA, November 2013.

3. Gudur MS, Rao RR, Peterson AW, Caldwell DJ, Deng CX, Stegemann JP. "Noninvasive, Quantitative, Monitoring of In Vitro Osteoblastic Differentiation in 3D Engineered Tissues using Spectral Ultrasound Imaging." *Biomedical Engineering Society Annual Meeting,* Seattle, WA, September 2013.

4. Rao RR, Peterson AW, Stegemann JP. "Osteogenic differentiation of ASC and MSC in protein/ceramic microenvironments." *Society for Biomaterials Annual Meeting,* Boston, MA, April 2013.

5. Caldwell DJ, Rao RR, Stegemann JP. "3D Patterned Microenvironments Created Through Assembly of Discrete Collagen-Chitosan Tissue Modules." *Society for Biomaterials Annual Meeting,* Boston, MA, April 2013.

6. Peterson AW, Rao RR, Rioja AY, Putnam AJ, Stegemann JP. "Formation of Endothelial Cell Networks in Hydrogel Scaffolds Assembled from Modular Collagen-Fibrin Microenvironments." *Society for Biomaterials Annual Meeting,* Boston, MA, April 2013.

7. Rao RR, Ceccarelli J, Singh R, Putnam AJ, Stegemann JP. "Hydroxyapatite Affects Endothelial Network Formation in Unconstrained Collagen/Fibrin Composite Hydrogels." *Society for Biomaterials Fall Meeting,* New Orleans, LA, October 2012.

8. Rao RR, Peterson AW, Putnam AJ, Stegemann JP. "Cell Ratio and Matrix Composition Modulate Vasculogenesis in 3D Collagen-Fibrin Composite Matrices." *Tissue Engineering and Regenerative Medicine International Society (TERMIS) – North America Annual Meeting,* Houston, TX, December 2011.

9. Rao RR, Jiao A, Kohn DH, Stegemann JP. "Exogenous Mineralization of Cell-Seeded Collagen-Chitosan Matrices using Modified Culture Medium." *Tissue Engineering and Regenerative Medicine International Society (TERMIS) – North America Annual Meeting,* Houston, TX, December 2011.

10. Rao RR, Wang L, Stegemann JP. "Incorporation of Particulate Hydroxyapatite into Collagen-based, Cell-laden Microbeads." *Society for Biomaterials Annual Meeting,* Orlando, FL, April 2011.

11. L Wang, RR Rao, JP Stegemann. "Moldable and Injectable Chitosan-collagen Microbeads for Bone Repair." *Society for Biomaterials Annual Meeting,* Orlando, FL, April 2011.

12. Jiao A, Rao RR, Kohn DH, Stegemann JP. "Rapid Mineralization of Cell-Seeded Collagen-Hydroxyapatite Composite Scaffolds via a Biomimetic Process." *Society for Biomaterials Annual Meeting,* Seattle, WA, April 2010.